Modelling of the intensified esterification using ozone-rich microbubbles for biodiesel production

Mario Alejandro Guadarrama Alvarez

A thesis submitted in partial fulfilment of the requirements for the degree of Doctor of Philosophy

The University of Sheffield

Faculty of Engineering

Department of Chemical and Biological Engineering

October 2018

i. Preface

This thesis is submitted as a partial fulfilment of the requirements for the degree of Doctor of Philosophy at the University of Sheffield and is available for further library use as learning material. This study has taken place at the Department of Chemical and Biological Engineering in the period from October 2014 to September 2018 under the supervision of Professor William B. J. Zimmerman. The purpose of this thesis is to present a novel computational model for the intensified esterification of vegetable oils via ozone-rich microbubbles.

Hereby, I certify that all the results described in this dissertation are original and have not been submitted in any part or whole for other degrees at this or any other universities.

Mario Guadarrama

The University of Sheffield

October 2018

ii. Short abstract

The aim of this thesis is to model the intensified esterification in order to improve the pretreatment stage of biodiesel production, where the free fatty acids found in vegetable oils are converted to fatty acid methyl esters. The intensified esterification considers the use of a microbubble reactive distillation as an alternative to the acid pretreatment. The proposed set of reactions based on a free-radical mechanism would favour the process towards completion achieving a yield higher than 90%. This is achieved due to the respective water stripping and removal, leading to a higher efficiency of the process and avoiding inhibition caused by products. Both the 0-D irreversible and reversible model are built in order to portray the relevance of the reverse reaction, since it is known that esterification is a reversible reaction of second order. The rate constants obtained in these models are fed into the 2-D model, where the reaction kinetics, mass and heat transfer and surface reactions in the gas-liquid interface are studied.

Some of the results obtained in the 2-D model for the reversible esterification are described below. A higher FAME concentration is obtained due to the free-radical direct injection into microbubbles with plasma and the water removal (Le Chatelier's push and pull). An enhanced reaction kinetics is found with shorter residence times. An increase in temperature would mean an increase in both forward and reverse rate constants, favouring the forward rate constant (Esterification is endothermic). Decreasing the bubble size results in an increase of the FAME production due to the enhanced gas-liquid ratio at the interface and the increased vaporisation and stripping of water. Increasing the concentration of the $O^{\cdot}$ radical results in an increase in the FAME concentration in the liquid domain. A higher bubble temperature results in a higher water concentration inside the bubble, leading to a higher reaction rate and water stripping. These findings are used in order to propose an esterification reversible model using *J. platyphylla*, which accounts shorter residence times lower than $1x10^{-4}$ s, in other words ($\tau_{res}<1x10^{-4}$ s), when the maximum water concentration in the bubble is reached before it reaches the chemical equilibrium.

Keywords: *esterification, microbubbles, free radical, biodiesel, ozone, modelling*

iii. Abstract

In this thesis a computational model was built to analyse the reaction kinetics of the esterification of vegetable oils via ozone-rich microbubbles. The model considers a single fluidic oscillator microbubble comprised of dry-to-bone air and ozone, with a diameter of 200 μm. The spherical bubble shape is maintained due to surface tension and the bubble is rising in an infinite reservoir due to buoyancy at a terminal velocity to simplify calculations. The proposed reaction mechanism takes place on the skin of the bubble and the concentration profile in the liquid phase is not constant.

The proposed computational model is comprised of a single microbubble (gas phase) in a liquid of Free Fatty Acid (FFA) and methanol (bulk liquid). This model is developed and solved numerically using a set of equations for mass and energy transfer and different reaction kinetic parameters. It complements earlier esterification experiments in which (1) ozone-rich bubbles were used to convert 91.16% of the oleic acid to oleic acid methyl ester after 32 h at 60 °C, achieving a final 1.33% of FFA content in used cooking oil and therefore making it feasible for biodiesel production via transesterification; and (2) binary distillation experiments in which an ethanol-water mixture was stripped by hot air microbubbles achieving a volume ethanol from the azeotropic mixture of around 98%.

The ozone present in the microbubble decomposes into O· (atomic oxygen), which then reacts in the proposed three-step reaction mechanism for the intensified esterification of vegetable oils following the Bodenstein steady state approximation. The water formed a by-product of this reaction is stripped by the microbubbles rising in the reservoir and kept in the upper gas phase. This model presents a novel three-step reaction mechanism which takes place on the skin of the bubble and involves free radical (MeO· and HO·) as intermediates for the production of Fatty Acid Methyl Ester (FAME), the reaction described previously evolves on a time scale related to the internal mixing of microbubbles of 10^{-3}s. The predictions obtained with this model for a single microbubble are in good agreement with the experimental data previously mentioned, demonstrating that esterification of vegetable oils is relative to the specific interfacial area and favoured at a higher liquid temperature.

The aim of this study is to propose a computational model robust enough to describe the reaction kinetics of the esterification of vegetable oils. Converting the FFAs to FAMEs is an important pre-treatment stage when producing biodiesel, which is here studied using a microbubble mediated reactive distillation shifting the conventional esterification towards completion from 80% to nearly 95% since the by-product (water) in this case is stripped by the microbubbles and is recovered in the off-gases which are comprised of unreacted ozone and humid air that can be vented. The model fits the rate constants of the third and slowest reaction in the proposed mechanism, by fitting *kf3* and *kr3*

to the data solving for a determined figure of merit and comparing both results following the inverse method using the least squares fitting.

Some relevant features for the 2-D model can be concluded after the respective analysis. The temperature profile is nearly isothermal at 333 K and the water concentration is constant across the bubble at around 5.26×10^{-4} mol/m^3. This pattern is mainly due to the intensive internal mixing found in the inside of the microbubble which favours the homogenisation of both the thermal and chemical fields at short residence times when the bubble rises through the liquid. A rapid increase in temperature is noticed with an turning point around T=330 K. Secondly, a slow increase can be depicted which reaches the liquid temperature T_∞. This would suggest that vaporisation and sensible heat transfer are dominating the first and second regime respectively.

A smaller bubble reaches the thermal equilibrium faster compared to a bubble with a larger radius. In the case of R=1×10^{-4} m, this thermal equilibrium is reached around 9×10^{-3} s compared to 4×10^{-2} s for a bubble five times its size. A higher FAME concentration is found in the liquid mixture at a smaller bubble size. An increase of the FAME concentration from the kinetic side of the process. In terms of the vaporisation of water, this process is thermodynamically favoured with an increase in temperature and therefore would cause an increase in the FAME production. Having said this, the increase of the FAME concentration in the liquid mixture could be attributed to the sum of these two factors which address both the reaction kinetics in the proposed mechanism and the physical advantage posed by the stripping of the produced water. An initial bubble temperature above the initial liquid mixture temperature (T_0 bubble > T_0 liquid), a maximum in the water concentration is found at the turning point previously mentioned. The higher the difference in temperature between these two temperatures, the more rapidly the turning point is reached.

These findings would suggest that the residence time of the microbubble (τ_{res}) rising though the liquid would necessarily be lower than 1×10^{-4} s, in other words ($\tau_{res} < 1 \times 10^{-4}$ s), when the maximum water concentration in the bubble is reached before it reaches the chemical equilibrium. Increasing the concentration of the $O^{\cdot}$ radical results in an increase in the FAME concentration in the liquid domain. For the initial molar ratio $O^{\cdot}$:FFA of 2:1 and 3:1, the FAME concentration reaches a maximum value at 0.1 s of 1.156 and 1.775×10^{-4} mol/m^3. For the esterification reaction here proposed, the forward reaction (esterification) is endothermic and the reverse reaction (hydrolysis) is exothermic. The endothermic direction is known to have a larger activation energy, in other words $Ea_f > Ea_r$. The forward reaction for the third step has an activation energy of E_a = 4.263 kJ/mol and a pre-exponential factor of A = 3.114×10^{-5} $M^{-1}s^{-1}$. The reverse reaction for the third step has an activation energy of E_a = 1.974 kJ/mol and a pre-exponential factor of A = 1.048×10^{-6} $M^{-1}s^{-1}$.

The intensified esterification mechanism here proposed for the use of *Jatropha platyphylla* as feedstock for the biodiesel production has several relevant features. Firstly, evaporative cooling happens at least three orders of magnitude faster than sensible heat transfer for this process. Water concentration rapidly increases reaching a maximum water concentration at $2x10^{-4}$ s of $1.14x10^{-3}$ mol/m^3. This value corresponds to the maximum in the absolute humidity which would mean the maximum efficiency in terms of heat transfer from the bubble to the liquid mixture to vaporise the water without falling into the sensible heat transfer regime. The concentration of FAME is relatively higher compared to the hydroxyl radical. There are nearly two orders of magnitude between the concentrations of these two species. This suggests the radical species is being produced by the forward reaction in the first and third step of the mechanism and then consumed by forward reaction in the second step, so it reaches an equilibrium.

At a bubble temperature of 343.15-393.15 K with intervals of 10 K, the maximum water concentration in the bubble is $6.16x10^{-4}$, $6.38x10^{-4}$, $7.68x10^{-4}$, $8.76x10^{-4}$, $9.97x10^{-4}$ and $11.14x10^{-4}$ mol/m^3 respectively. At long residence times, all these curves would tend to reach the thermal equilibrium in the microbubble when the water concentration is $5.38x10^{-4}$ mol/m^3. A larger temperature difference between the initial bubble temperature and the liquid mixture temperature results in a longer period required to reach this equilibrium. Increasing the concentration of the $O^{\cdot}$ radical results in an increase in the FAME concentration in the liquid domain. For the initial molar ratio $O^{\cdot}$:FFA of 2:1 and 3:1, the FAME concentration reaches a maximum value at 0.1 s of 1.662 and 2.427 mol/m^3. The forward reaction for the third step has an activation energy of E_a = 4.7817 kJ/mol and a pre-exponential factor of A = $7.744x10^{-4}$ $M^{-1}s^{-1}$. The reverse reaction for the third step has an activation energy of E_a = 2.8117 kJ/mol and a pre-exponential factor of A = $1.282x10^{-4}$ $M^{-1}s^{-1}$. All these results are in agreement with the hypothesis that reducing the liquid layer thickness and therefore the residence time of the microbubble rising through the liquid would result in maximising the vaporisation of the produced water. This would then result in an enhanced FAME production, which is an appealing feature when designing an esterification unit.

Keywords: *esterification, microbubbles, free radical, biodiesel, ozone, modelling*

iii. Acknowledgements

Firstly, I would like to thank the National Council for Science and Technology (CONACyT) and the Support Institute for Research and Innovation (INAPI) in Sinaloa for the financial support throughout my studies at the University of Sheffield.

I would like to express my deepest appreciation to my thesis supervisor Professor William B. J. Zimmerman who continually conveyed an excitement in regard to teaching and sharing his knowledge, guidance, encouragement and patience during my studies at the University of Sheffield. Without his help and advice this dissertation would not have been possible.

In addition, a thank you to all my colleagues in the microfluidics group, Dr Chaffin, Dr Holmes, Dr Abdulrazzaq and Dr Desai for the many ideas and suggestions in the making of this thesis project. Furthermore, I would like to thank all the staff in the Department of Chemical and Biological Engineering for always being so helpful and supportive when needed.

Lastly, I would express my appreciation to my family Nita, Armando and Ana Libia for the countless displays of love and affection, and my beloved friends Alejandra, Carly, Paulina and the Mexas group José, Edgar, Pablo, Andrés, Ariel, Joaquín, Rafael, Gerardo, Luis and Alejandro who always have been supportive during my stay in the United Kingdom over the last few years and shared a few pints in our local pub The Red Deer.

Contents

iv. List of figures

v. List of tables

vi. List of symbols

Symbol	Designation	Symbol	Designation
AN	Acid number	Q	Internally generated heat
k_i	Rate constant	Q_p	Work due to pressure changes
htc	Heat Transfer Coefficient	Q_{vd}	Work due to viscous dissipation
KL	Mass Transfer Coefficient	H_{vi}	Latent heat of vaporisation
H	Henry Coefficient	Q_b	Boundary heat source
A	Surface Area	T_∞	Liquid temperature far from bubble
pA	Total pressure	$\dot{m}$	Evaporation rate at interface
R	Universal Gas Constant	C_l	Concentration in liquid domain
g	Gravity	C_g	Concentration in gas domain
r	Radius	H_i	Enthalpy of reaction
u_r	Radial velocity vector	R_{ads}	Reaction rate at interface
u_z	Axial velocity vector	S_i	Entropy of reaction
U_t	Terminal velocity	σ_i	Site occupancy number
T	Temperature	Pe	Peclet number
$\propto$	Thermal diffusivity	Re	Reynolds number
D	Molecular diffusivity	τ	Residence time
ρ	Density	Nu	Nusselt number
c_i	Molar concentration	E_o	Eotvos number
k	Thermal conductivity	N_{bub}	Bubble flux
P_i	Partial pressure	ε	Lennard-Jones energy
x_i	Mole fraction	k_B	Boltzmann's constant
γ_i	Activity coefficient	V_A	Molar volume
μ	Viscosity	$\dot{n}_i$	Evaporation constant at interface
P_i^*	Saturation vapour pressure	v_{ij}	Stoichiometric coefficients
s_i	Molar entropy	h_i	Molar enthalpy
Q_j	Heat source of reaction	Ω_D	Diffusion collision integral

1. Introduction

In this chapter, a brief general background concerning the fundamental concepts explored in this thesis is introduced. Section 1.1 describes the thesis background which contains the key features for the intensified esterification using ozone-rich microbubbles. The aims and scope of this thesis as well as the scope of this project are presented in Section 1.2 and Section 1.3 respectively. Lastly, the thesis outline is introduced in Section 1.4.

1.1. Thesis background

Currently the predicted shortages of fossil fuels and growing environmental concern are the main drivers for the research and development of alternative fuels. One of the most promising substitutes for fossil fuels is biodiesel because its commercial production around the world could significantly decrease the greenhouse gas emissions and therefore reduce air pollution (Srivastava & Prasad, 2000).

Over the last decades, a diverse range of methods have been studied for biodiesel production such as heterogenous, homogeneous, non-catalytic and enzyme catalysed transesterification. Non-catalytic transesterification requires high temperature and pressure operating conditions as well as a high alcohol:oil molar ratio. On the other hand, the enzymatic catalysed reaction is found to be expensive. The best method to produce biodiesel to date is the transesterification using an alkali catalyst. This method has the flexibility of using renewable feedstock such as animal fat, vegetable oil and waste cooking oil (WCO). (Lim & Teong, 2013; Talebian, et al., 2013; Kokoo & Zimmerman , 2018).

Regarding the feedstock, researchers around the world have focused their attention on non-edible oils to overcome environmental problems as well as food competition. Non-edible oils are usually grown in waste lands that are not suitable for agriculture reducing the costs of cultivation and enhancing a high yield without in-depth care. Compared to the average cost of vegetable oil, waste cooking oil (WCO) is three times cheaper which means a significant reduction in terms of the production cost. Having said this, there is a particular interest in developing technologies which consider these types of alternative feedstock in order to make the bioprocess economically feasible (Gui, et al., 2008; Tiwari, et al., 2007; de Araujo, et al., 2013).

Nevertheless, when non-edible oils or waste cooking oil are considered as the feedstock for biodiesel production, the significant Free Fatty Acid (FFA) and water content are seen as a disadvantage due to soap formation caused by the reaction with the catalyst. The soap formation limits the reaction and add more downstream steps. Esterification is used as a pre-treatment stage to avoid this and reduce the FFA content (below 3%) in order to make the feedstock suitable for biodiesel production (Aransiola , et al., 2014).

Considering esterification as a pre-treatment stage has the potential to improve the downstream processing of biodiesel since water removal would take place prior to transesterification. Zimmerman et at proposed a model for the evaporation dynamics of microbubbles where both heat transfer and evaporation on the microbubble are explored. It is believed that at short residence times, vaporisation is favoured, while at long residence times sensible heat transfer governs favouring re-condensation of the vaporised water. In order to achieve a maximum removal of vapour with minimum heat transfer, both the vaporisation layer thickness (few hundred microns) and the contact time need to be accurately estimated. This study proposes a rapid evaporation using hot and dry microbubbles to vaporise and strip the water produced from the reacting mixture. Following Le Chatelier's principle for equilibrium reactions, the proposed reactive distillation is forced to achieve completion (Zimmerman, et al., 2013).

$$O\cdot + MeOH \rightarrow MeO\cdot + HO\cdot$$

$$HO\cdot + HO\cdot \rightarrow H_2O + \frac{1}{2}O_2$$

$$FFA + MeO\cdot \rightarrow FAME + HO\cdot$$

Figure 1 Three-step mechanism proposed for the intensified esterification.

One of the main purposes of this model is to understand and explore the effects of water production and its respective removal. This thesis explores the hypothesis that forces the esterification reaction of FFAs to completion via the microbubble mediated reactive distillation. In this case, ozone-rich bubbles provide the catalyst to this reaction and remove the water product, driving the reaction to completion following Le Chatelier's principle. This approach uses O·, produced from the ozone decomposition, as free radical initiator for the three-step reaction mechanism proposed which takes place on the bubble interface (gas-liquid), the mechanism is shown in Figure 1. The microbubble removes the vapour phase products (water) avoiding product inhibition. When the molecules of produced water are removed by vaporisation, the system undergoes further reaction to produce another molecule to replace it with, therefore driving the reaction to completion.

Abdulrazzaq et al studied the non-equilibrium vaporisation pattern in ethanol-water mixtures based on hot microbubble injection. The driving force is kinetically more rapid at vaporising ethanol than water in all the mixtures. Methanol is more volatile than ethanol, so it would be expected to occupy the bubble vapour phase in the case of the esterification reaction mixture. This means that methanol would be removed preferentially over water. In Figure 1, the effects of water removal in pulling the reaction and excess methanol in pushing the reaction to equilibrium are depicted. By only injecting hot bubbles, the equilibrium is pulled but the push diminished. In order to avoid the likeliness of methanol to vaporise in the esterification reaction, this thesis explores the hypothesis that methanol

becomes immediately reactive in order to achieve an effective water removal. The reaction occurs on the bubble interface where the methanol reacts with the oxygen singlet forming the free methoxy free radical (see Figure 1). Ozone is known to be a free radical initiator, but actually oxygen singlet radicals can be formed and then injected into the bubble by tuning an ozone plasma microreactor which preferentially produces these species by selecting the residence time. Oxygen radicals tend to form hydroxyl radicals in the presence of water, but either species form water when methanol is present by scavenging the hydrogen from the alcohol group resulting in the formation of the methoxy radical. This suggests that ozone-rich bubbles injection into FFA-methanol mixtures (no catalyst present) will drive esterification towards completion by the water removal mechanism previously described and catalysed by the three-step mechanism (free radical chain reaction) (Tran, et al., 2017; Timberlake & Hodges, 1970; Zimmerman, 2011; Rehman, et al., 2016; Lozano-Parada & Zimmerman, 2010).

1.2.Aims and scope

This research project is comprised of multiple models, simulations and their respective estimation of parameters. The main software used for the computational models is COMSOL Multiphysics and MATLAB coupled with Livelink. To explore the time scale of different ozone decomposition methods discussed in Chapter 3 and to calculate and estimate different parameters like thermodynamic properties in Chapter 4, 0-D models in COMSOL are used to input the different reactions mechanisms. When studying this reaction mechanism, both the irreversible and reversible reaction for the slowest step are discussed in Chapter 5. This section includes a deep analysis of the effect of the different rate constants on the water and overall FAME production.

Another important component of this project is chapter 6 and 7 where the 2-D axisymmetric model built in COMSOL for the intensified esterification for both the irreversible and reversible reactions of the slowest step. This model couples heat and mass transfer, surface reactions and reaction engineering modules so both the vaporisation and stripping of produced water and the free radical chain reaction are coupled and then fitted to the experimental data. These two fields are studied separately to explore its relevance and effect on the overall FAME production.

Once the models are built, they are imported to the software COMSOL for MATLAB to be fitted to the experimental data using a list of commands found in Appendix B. in order to fit the curves obtained from the simulation to the experimental data, the least squares method is used.

The main aims of this research are detailed below:

1. To model the ozone decomposition and find its respective time scale using different methods such as, the NFG for Aqueous Ozone Decomposition and the Hoigné and Gordon method.

2. To model the heat exchanger used in the gas inlet and explore the effect of temperature on ozone decomposition for the oxygen singlet radical formation.

3. To estimate the diffusion coefficients for the different species studied in both the liquid and gas phase.

4.To calculate the effect of different physical parameters on the rising of microbubbles and determine the liquid thickness layer and residence time.

5.To compare the flow and surface parameters with dimensionless analysis (Peclet, Nusselt, Reynolds) in terms of microbubbles.

6. To estimate the mass transfer coefficient and gas-liquid interfacial area to be used in the computational model.

7. To explore the effect of the forward rate constant (*kf2*) on both water and overall FAME production using the 0-D model.

8. To fit the resulting 0-D models to the experimental data, so the right values of the rate constants (*kf3* and kr3) for the slowest step are determined.

9. To explore the effect of the proposed mechanism for the water vaporisation and stripping from the reacting mixture.

10. To fit the 2-D model to the experimental data, including the mass and heat transfer, surface reactions and reaction engineering module.

11. To determine the kinetic parameters for the built models and find the optimum operating conditions varying temperature, species concentration and physical parameters.

12. To explore the effect of the bubble temperature and size, oxygen singlet concentration and liquid mixture temperature on the reaction kinetics and physics of the intensified esterification.

1.3.Objective

The main objective of this thesis is to build a semi-empirical model for the intensified esterification reaction proposed mechanism using ozone-rich microbubbles. The experimental data used for this study explores the effect of both temperature and FFA initial content on the overall biodiesel production. Once the computational model is built with the respective heat and mass transfer definitions and surface reactions mechanism proposed in this work, the reaction kinetics are explored using parametric sweeps to analyse the impact on the overall FAME production. Some variants of the computational model are used in order to explore the isolated effect of reactions kinetics and the water mass transfer by convection. The resulting model should be robust enough, so the user is able

to explore the effect of changing physical and chemical parameters such as, the bubble size, methanol:oil ratio, temperature of the liquid, temperature of the microbubble and the oxygen singlet radical concentration. Since the chain reaction mechanism here proposed is not selective for the feedstock, vegetable oils with a FFA content value ranging 10-20% can be modelled using this work.

1.4. Thesis outline

The thesis here presented is comprised of eight chapters. In Chapter 1, a brief introduction to the thesis is presented with its respective background, aims, scope and objective. Chapter 2 includes a comprehensive literature review of biodiesel production, ozone generation and the intensified esterification using microbubbles. In Chapter 3, it can be found the experimental data used for to be fitted with the models, and the 0-D models for the ozone decomposition and a 2-D model for the heat exchanger to study the thermal decomposition of ozone in COMSOL Multiphysics. Chapter 4 presents the estimation of the diffusion coefficients, the calculation of different physical parameters on the rising of microbubbles, a comparison of the flow and surface parameters with dimensionless analysis (Peclet, Nusselt, Reynolds) in terms of microbubbles and an estimation the mass transfer coefficient and gas-liquid interfacial area.

Chapter 5 explores the effect of the forward rate constant (*kf2*) on both water and overall FAME production using the 0-D model and show the fit of the resulting 0-D models to the experimental data. Chapter 6 and 7 explore the effect of the proposed mechanism for the water vaporisation and stripping from the reacting mixture, the inversion method fit the 2-D model to the experimental data including the mass and heat transfer, surface reactions and reaction engineering module, and the kinetic parameters for the built models, irreversible and reversible respectively. In Chapter 8, the conclusions and suggested future work are presented.

2. Literature review

In this chapter some of the relevant features are presented for the ozone free radical initiated mechanism. The comprehensive literature review is divided into three main parts: The biodiesel production, ozone generation and the intensified esterification using microbubbles. The biodiesel production considers the current global scenario, a description of the biodiesel properties and potential feedstock as well as the current technologies in terms of the esterification reaction. The ozone generation section is comprised of relevant features regarding the properties, applications and stability of ozone, as well as the different technologies for ozone and free radical generation using micro plasma. Lastly, the intensified esterification reaction describes the main features of the mechanism proposed in this thesis such as, the fluidic oscillator, evaporation dynamics and heat transfer, the Bodenstein steady state assumption, the free radical reaction mechanism and the microbubble generation. All of these subjects take part in this literature review which is aimed to provide the reader with enough background to understand the proposed reaction mechanism proposed in this thesis.

2.1.Biodiesel production

In this section are presented some of the main subjects regarding the biodiesel production. Some of these features are the current global scenario, fuel properties, vegetable feedstock used in the biodiesel production suggesting the use of a Mexican species for one of the next chapters, current production technologies in terms of the esterification reaction and the potential use of microbubbles for this reaction. The main importance of this section is to highlight the main technologies used by other researchers and point out their strengths and weakness, in order to point out the gap to be fulfilled by the ozone free radical initiated esterification.

2.1.1. Current global scenario

Currently the predicted shortages of fossil fuels and growing environmental concern are the main drivers for the research and development of alternative fuels. The world energy demand is mainly supplied by petrochemical sources, natural and coal respectively in this order; but due to their current usage rate they will be consumed soon. In this context, there is special focus on diesel fuels since they play a vital role in the industrial economy of developing countries due to its importance for transport of industrial and agricultural goods (Srivastava & Prasad, 2000).

Major economic events and scientific evidence emerging in 2008 had significant contributions for biofuels in terms of government and industry aspirations. The use of biofuels, such as bioethanol and biodiesel, as a substitute for transport fuels is mainly justified since they could reduce greenhouse gas emissions enhancing rural incomes and achieving fuel security. Many of the key events in 2008 which

impacted upon the supply, demand and sustainability of biofuels were: the increase in food commodity prices (important biofuel feedstock), increase in oil prices, global financial crisis and publication of several scientific studies concerning biofuels like the UK's Gallagher Review (Join Nature Conservation Committee, 2009).

Biofuels such as biodiesel are indeed partial substitutes for petrol fuels and fossil diesel. Nowadays there are a small percentage of vehicle engines which can use near pure biofuels but most of the world's vehicles simply cannot utilise more than a 10% biofuels component. This technical limitation derived from the engine design creates the well-known "blending ceiling" which will keep limiting the biofuel demand until the new generation of engines becomes accessible around the world. Having said this, the total diesel consumption and this blending ceiling will determine the biodiesel consumption over the coming decade. According to the European Union standards a 10% biofuel substitution target for 2020 has been set and the International Energy Agency has estimated substitution levels from 3% for Africa to 14% for the Americas by that time. In 2008 the global biofuels substitution was 2.85%, in the Americas a level above 10% was possible due to increased blending ceiling in the USA and the use of flex fuel vehicles in Brazil (Join Nature Conservation Committee, 2009).

The depletion of fossil fuels could have significant effects in our lifestyle, forcing many dependent industries on fuels, such as the agricultural and automobile, to close down; having negative effects on the economic growth of developed and developing countries. Having said this, a practical and suitable approach to the problems previously mentioned will be the usage of an alternative fuel obtained from renewable sources free of sulphur content. One of these alternative fuels is biodiesel which has gained a good reputation amongst the well-known renewable sources due to its reduced toxic emissions, when blended with mineral diesel, for its respective use in conventional engines (Bharathiraja, et al., 2014; Harrington & D'Arcy, 1985).

Amongst the top biodiesel producing countries are Germany, Brazil, Argentina, Indonesia and France. Both Philippines and Taiwan are the only countries where the biodiesel production has met the country's mandate. Based on the traded and exported processed plant oils and animal fats per country, in 2006 a review was published reporting the top five countries (Malaysia, Indonesia, Argentina, USA and Brazil) to have the potential to produce this biofuel. European countries lead the world production of biodiesel with Germany being top, whereas Indonesia is the only Asian country to make to the top five producing countries. It can be noticed there is a large gap between the biodiesel demand and the production capacity, suggesting there is room for improvement by means of thorough research to meet the demands. Table 1 shows the top consuming countries being the USA, Germany, Brazil, France and Spain. It is interesting to point out that not all the top producers are the largest consumers of this biofuel (Woo, et al., 2016; Johnston & Holloway, 2007).

Table 1 Top five countries in production and consumption of biodiesel in 1x106 litres per year (Woo, et al., 2016).

Producing countries	Produced (demand)	Consuming countries	Consumed (ML)
Germany	3097(2507)	USA	3356
Argentina	3018(816)	Germany	2750
Brazil	2747(1864)	Brazil	2611
France	2673(1819)	France	2350
Indonesia	1973(350)	Spain	1857

On the 6th August 2015, the UK Government published the Renewable transport fuel obligation report which stated that 3.29% of total road and non-road mobile machinery fuel was supplied by 1,671 million litres of renewable fuel. 84% of the total of renewable fuel (1,397 million litres) met the sustainable requirements established by the UK government and 50% of the total was comprised of biodiesel. In terms of biodiesel, waste cooking oil was the most widely reported source in the UK reaching an annual supply of approximately 115 million litres, accounting for 17% of biodiesel and 8% of total fuel production in the UK throughout 2015. Around one third of the biofuel produced (30%) was sourced from UK feedstock. On the other hand, the most widely reported source for bioethanol was wheat from the UK with an annual supply of 144 million litres, accounting for 21% of bioethanol and 10% of total fuel production in the UK. It was also stated that almost half of the fuel produced (48%) between April 2014 – April 2015 came from non-agricultural residues meaning a greenhouse gas saving of 69% compared to conventional fossil fuels. It is important to mention that 99% of the biofuel was sourced via a voluntary scheme such as ISCC at 83% of biofuel (Department for Transport, 2015).

The United States Energy Information Administration (USEIA) reported that for every 42 gallons of crude oil, 10 gallons of diesel are produced (circa 24%). Diesel is mainly used as transportation fuel but there is a wide spectrum for its use including energy generation. It has been estimated that one barrel of biodiesel is equivalent to 0.88 barrel of crude oil, suggesting that the world diesel consumption would need to increase by 14% if biodiesel were to replace mineral diesel. Nowadays countries around the world aim to utilise biodiesel in transportation at blends of 2-20%. Table 2 illustrates the biodiesel feedstock mandates and production of different countries/regions (Woo, et al., 2016; U.S.E.I.A., n.d.; BP, 2013).

As reported by the US EPA, greenhouse gas emissions are reduced by 57-86% when using 100% biodiesel compared to mineral diesel. In addition, major tailpipe pollutants from petroleum diesel are reduced by biodiesel. Mineral diesel blended with biodiesel, known as B20 due to its proportions, can be sourced by many organic oils limited to those one with a low level of free fatty acids, usually below 4%. Waste greases typically contain 10-25% of FFAs which is beyond the level that can be converted

using the alkaline-catalysed reaction. In order to reduce the level of FFAs, pre-esterification processes are required but it incurs in additional costs.

Table 2 Biodiesel feedstock, mandates and production of different countries (Lane, 2014).

Country/region	Feedstock	Blend (%)	Crude oil (Mt)	Diesel (Mt)	Required biodiesel (Mt)
Brazil	Soybean, Palm	5-6	125.6	29.9	1.6
European Union	Rapeseed/Sunflower	7.5	611.3	145.5	12.2
USA	Soybean, Waste oil	10-20	819.9	195.2	21.7
Indonesia	Palm, *Jatropha*	2-2.5	71.6	17.0	0.3
Argentina	Soybean	10	28.2	6.7	0.7

The novel approach proposed in this research project intends to make all waste greases potential feedstock sources for biodiesel production. Presently, the Greater London Authority (GLA) is examining the use of 30% biodiesel (B30), and has reported that the biodiesel cost is 75 p/L compared to petroleum diesel of 52 p/L. The biodiesel consumption for 2014 was of 280m litres, with 49bn litres for transport, from which 0.57% accounts for UK transport consumption. European production of biodiesel is running at only 55% of capacity, and particularly the UK is at 30% (Department for Transport, 2015).

From 1992 to 2012, the world production of vegetable oils has increased by nearly 100 million tons in terms of annual production. The world edible oil production from 1992 2012 is shown in Figure 2. According to the Food and Agriculture Organisation of the UN Statistics Division, nearly 60% of the oil produced every year is used as food supply. If the waste cooking oil is then recovered and treated, this could potentially mean around 80 million tons of biodiesel produced by these means. This potential amount of biodiesel would be enough to meet the world present world demand that has been estimated to be circa 63 million tons (Woo, et al., 2016; FAOSTAT, 2014).

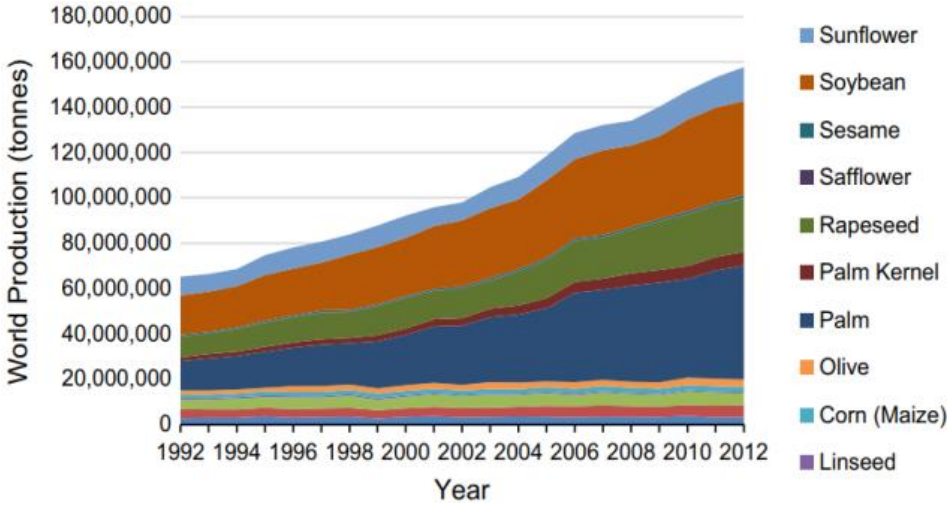

Figure 2 World edible oil production from 1992 to 2012 (FAOSTAT, 2014).

A part of this research project a microbubble intensified esterification kinetic model is proposed in order to be implemented with the use of cheap feedstock, such as *Jatropha platyphylla*, to produce biodiesel from the free fatty acids (FFAs). Nowadays blended biodiesel is only profitable due to RTFCs. In the USA, subsidies for biodiesel production became too expensive due to its growth in volume and mainly because the fee-in tariff was not renewed. The US market crashed since it is not profitable to produce biodiesel without subsidy. Increasing profitability by cheaper feedstock sources and decreasing processing costs are the main driver to develop new approaches for biodiesel production (Bharathiraja, et al., 2014; Department for Transport, 2015).

2.1.2. Fuel properties

One of the most promising substitutes for fossil fuels is biodiesel because its commercial production around the world could significantly decrease the greenhouse gas emissions and therefore reduce air pollution. Presently biodiesel is obtained from a vast range of livestock like algae, animal fat, vegetable oils and waste cooking oils; via the conversion of fatty acids into fatty acid methyl esters (FAMEs). Biodiesel by definition is described as an alternative fuel derived from either vegetable oil or animal fat, comprised of mono-alkyl esters of long chain fatty acids. This type of biofuel has several advantages which have been outlined when compared to mineral diesel, some of them are: it reduces CO_2 emissions from vehicle engines, the high purity avoids the future use of lubricant, it involves a more efficient production process compared to petroleum, it is derived from renewable sources, and it provides a high cetane number which enhances the engine performance (Su & Wei, 2008; Fukuda, et al., 2001).

Biodiesel is produced by a conventional process which involves a catalysed transesterification reaction of oils with methanol. As described before, triglycerides from a vegetable oil or animal fat react with an alcohol in the presence of a catalyst that speeds up the reaction producing free fatty acid methyl esters (FAMEs) known as biodiesel and glycerol. In Figure 3 is shown the chemical reaction formula for the transesterification of vegetable oils into biodiesel.

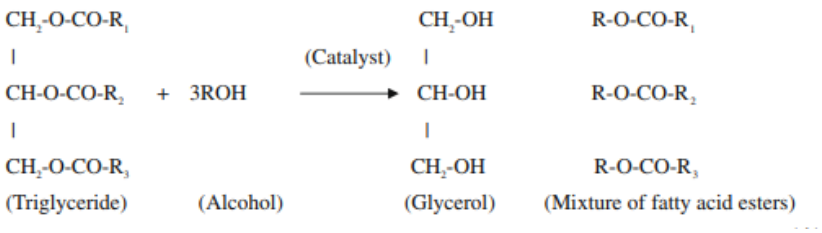

Figure 3 Simplified form of the transesterification reaction (Leung, Wang 2010).

In order to produce biodiesel two important aspects to be considered are the desired quality of the end product and the properties of the feedstock since the operating parameters and process design will depend on them. The commercial production of biodiesel from soybean in the United States of

America and from rapeseed in the European Union have promoted the respective characterisation of this alternative fuel and development of new technologies to optimise its production. In Table 3, the corresponding values for biodiesel of the European, German and the USA standards are shown (Leung, et al., 2010; Devi, et al., 2006).

Table 3 Biodiesel values of European, German and American standards (Achten, et al., 2008).

Variable	EN 14214-2003	DIN V 51606	ASTM D6751
Density (g cm^{-3})	0.86-0.90	0.87-0.90	--
Flash point (°C)	Min 120	Min 110	Min 130
Cetane value	Min 51	Min 49	Min 47
Viscosity at 30°C (cSt)	3.5-5.0a	3.5-5.0a	1.9-6.0a
Iodine number (mg iodine g^{-1})	Max 120	Max 115	Max 115
Acid number (mg KOH g^{-1})	Max 0.5	Max 0.5	Max 0.5
Carbon residue % (kg kg^{-1}) $x10^2$	Max 0.3	Max 0.3	Max 0.05
Sulphur content % (kg kg^{-1}) $x10^2$	Max 0.01	Max 0.01	Max 0.015
Sulphated ash % (kg kg^{-1}) $x10^2$	Max 0.02	Max 0.03	Max 0.02
Water % (kg kg^{-1}) $x10^2$	Max 0.5	Max 0.3	Max 0.5
Free glycerol % (kg kg^{-1}) $x10^2$	Max 0.02	Max 0.02	Max 0.02
Total glycerol % (kg kg^{-1})$x10^2$	Max 0.25	Max 0.25	Max 0.24

2.1.3. Feedstock

There is a vast diversity of lipid feedstock sources which can be used for biodiesel production. **Error! Reference source not found.** shows some examples of these sources, mainly they are divided into algae, palm fruits, seeds and waste oil. In spite of the fact that when using palm fruits, the productivity reaches its highest, the most common feedstock sources for biodiesel production are seeds from different plants such as *Jatropha*, sorghum, peanut, sunflower and rapeseed. Climatic, agricultural and geographical conditions determine the choice for a selected feedstock, but at the same time is important to consider the different feedstock properties. As an example, the fatty acid content and oil saturation of oilseed species tend to vary considerably. A higher cetane number and improved oxidative stability are characteristic in biodiesel produced from highly saturated oils. Having said this, pure plant oil containing a high degree of saturation is more suitable in warmer climates. In the next section some of these plants will be described in more detail focusing on oilseed crops particularly *Jatropha*, since it is the feedstock source chosen for this research particularly the Mexican species *Jatropha platyphylla* to be considered in Chapter 8 for a proposed model of the intensified mechanism (Worldwatch Institute, 2006).

The goal set by the Brazilian government for 2008 led to a net production of 800 million litres of biodiesel. By 2006, the installed biodiesel production capacity in Brazil doubled reaching a production

of around 1,180 million litres per year. On the other hand, in South East Asia there is an increasing interest in palm biodiesel. Countries such as Malaysia, Indonesia and Thailand have recently started the production of biodiesel from palm oils but faced a growing competition for food at the same time since this source belongs to the edible crops type. Nevertheless, non-edible crops like *Jatropha* are drawing attention due to their suitability to be produced on lands with variable quality. In India, *Jatropha* biodiesel production is being held as a strategy regarding wasteland reclamation. Finally, the use of oil-bearing seeds, such as like starch-based alcohol fuels, for biodiesel production is limited from the perspective of carbon emissions reduction and petroleum substitution (Climate Change Central, 2006; Government of India Planning Commission, 2005; Gonsalves, 2006).

2.1.4. Vegetable oils used for biodiesel production

From the vast diversity of different sources used as feedstock for biodiesel production, this research project focuses on the use of vegetable oils. Vegetable feedstock for biodiesel production is a suitable source since it is produced on a large scale considering environmental issues and is renewable in nature. Vegetable oils include both edible and non-edible ones, almost 95% of the vegetable sources used to produce biodiesel come from edible oils since their capacity to be produced in most of the arable regions around the world and the properties of the end product meet the standards for them to be used as a substitute for mineral diesel. In spite of that, producing biodiesel from edible oils have disadvantages such as the competition with the edible oil market which usually leads to an increased cost of edible oils and therefore biodiesel (Antolin, et al., 2002; Gui, et al., 2008; Sahoo & Das, 2009).

The great majority of the biodiesel produced around the world uses soybean oil, methanol and an alkaline catalyst to speed up the reaction. Since soybean oil is a food product, the current food competition makes production face several challenges. Nevertheless, there is a large amount of low-cost oils and fats such as animal fats and restaurant waste that could be used and then converted to biodiesel. A problem related with the processing of these low-cost sources is that usually the have a high content of free fatty acids that cannot be converted using alkaline catalysts (Canakci & Van Gerpen, 2001; Demirbas, 2003; Demirbas, 2008).

In order to compare the proposed feedstock source for this project, *Jatropha platyphylla*, with many other oilseed crops, a detailed description of some of the main feedstock sources is provided like rapeseed, soybean, palm oil, sunflower and *Jatropha* species. Firstly, rapeseed, also known as colza or canola, belongs to the family of the Brassicacea and is characterised by a high content of erucic acid (50%), toxic compound which may cause liver and heart damage. High content of monounsaturated oleic acid and low levels of both polyunsaturated and saturated acids are mainly found in rapeseeds. Some of the advantages of using rapeseed as the feedstock source are its oxidative stability, combustion characteristics and cold temperature behaviour. China is considered the largest rapeseed

producer in the world with an designated for its cultivation expanding rapidly; around the world this cultivation area is growing 2% annually. In 2005 1.4 million hectares were cultivated in Europe, half of this production was in Germany followed by other countries such as France, Poland and Czech Republic (Mittelbach & Remschmidt, 2004; Worldwatch Institute, 2006).

In Table 4 the fuel properties of methyl esters produced from different feedstock sources are compared to a biodiesel blend B20 and mineral diesel. These fuel properties are important because they dictate the biofuel characteristics. The physical and chemical properties stated below are included and need to be met by any biodiesel producer according to the different International standards that regulate its production.

Table 4 Fuel properties of methyl esters from vegetable oils (Helwani, et al., 2009).

Biodiesel	Cetane number	Cloud point (ºC)	Pour point (ºC)	Flash point (ºC)	Density ($g.cm^{-3}$)
Soybean	45	1	-7	178	0.885
Rapeseed	54	-2	-9	84	--
Palm	62	13	--	164	0.88
Sunflower	49	1	--	183	0.86
B20	51	--	-16	128	0.859
Diesel	50	--	-16	76	0.885

Soybean is the most popular biodiesel feedstock source in the United States and is the most produced vegetable oil worldwide and the dominant oilseed crop cultivated. Regarding its production, the United States, Brazil and Argentina are the main producers of soybean oil where biodiesel is growing rapidly due to its abundance rather than a specific desirability. Although it is an abundant feedstock in these countries, only a small fraction of the supply is converted to biofuels. Biodiesel produced from rapeseed oil has been discussed to meet the biodiesel standards with iodine values similar to sunflower oil ranging 121-143 gI2/100g. Although soybean crops tend to generate a low yield of biodiesel per hectare when compared to other oilseed crops; it can grow in both tropical and temperate conditions, it has the ability to stock soil nitrogen reducing the amount of fertilizer needed generating a positive energy balance (Rutz & Janssen, 2007).

Palm oil is one of the two main palm trees used for oil production, specifically in South Asia. Malaysia and Indonesia are the largest producers of palm oil with a rapid growth in the last decade. The second largest planted area of palm oil is located in Nigeria and Brazil is considered to play an important role regarding palm oil cultivation in the next decade. Presently the majority of the palm oil is used by the food industry but the demand of palm oil Europe for biodiesel production is expected to increase significantly. The Netherlands is the largest importer of palm oil in the European Union followed by the United Kingdom which imports doubled to 914,000 tons between 1995 and 2004,

representing 23% of the EU imports. Palm oil contains a high amount of monounsaturated and medium-chain saturated fatty acids. Traditional alkali-catalysed biodiesel production is affected by a high content of fatty acids in the feedstock, forcing producers to include acid-catalysed pre-esterification and deacidification steps (Mittelbach & Remschmidt, 2004).

Sunflower oilseeds oil is the fifth largest oilseed crop in the world, accounting for almost all the remaining biodiesel feedstock in Europe right after rapeseed. It has a significantly higher yield compared to soybean but similar when compared to rapeseed. Sunflower crops require less fertilizer and water making it acceptable as a suitable feedstock source by the public. Its use for fuel production is limited due to the high contents of linoleic acid, poor oxidative stability and high iodine values not suitable for fuels (Rutz & Janssen, 2007).

Table 5 Physicochemical properties of vegetable oils used in the models (Kokoo & Zimmerman , 2018; Makkar, et al., 2010).

Property	Used cooking oil	*Jatropha platyphylla oil*
Density (kg/m^3)	916	908
Dynamic viscosity (cSt)	40.2	31.5
Acid value (mg KOH g^{-1})	2.1	0.43
Water content (mg/kg)	1560	326
Flash point (°C)	286	274
Average molecular weight (g/mol)	882	876

For the purpose of this thesis, modelling of the intensified esterification using microbubbles for biodiesel production considers two different feedstocks. In chapters 7 and 8, the feedstocks considered for the model are the used cooking oil and *Jatropha platyphylla* oil. In Table 5, the main physico-chemical properties for both oils are illustrated. These features are adapted for each of the respective models in order to obtain a more accurate model.

2.1.5. *Jatropha* species and *J. platyphylla,* the Mexican feedstock source

One of the objectives of this research project is to come up with a computational model that helps understanding the reaction kinetics of the esterification reaction in vegetable oils in order to be used with one of the species from the genus *Jatropha*, the Mexican species *J. platyphylla*. The Mexican government is interested in analysing its properties and feasibility as a feedstock source for biodiesel production in the North of Mexico. The genus *Jatropha* belongs to the Euphorbiaceae family, plants found in this family are known for their toxicity. The majority of the *Jatropha* species studied, have been found to produce several toxins such as nutritional factors (phytates, lectin, trypsin inhibitor) and phorbol esters. The most famous species and also widely promoted as a feedstock source for biodiesel production is *Jatropha curcas*. In this chapter both *J. curcas* and *J. platyphylla* are described in order to

compare their properties focusing in their feasibility as feedstock sources for biodiesel production (Makkar, et al., 2010).

Jatropha curcas, also known as physic nut, is one of the 150 species in the family of the Euphorbiaceae. *J. curcas* is the most famous species from this family since it has the most research and studies conducted. This oilseed crop grows well on semi-arid and marginal lands. The bushes are usually harvested twice a year and can remain productive for decades. In India where nearly 64 million hectares of land are considered to be uncultivated or wasteland, *Jatropha* has been identified as one of the most propitious feedstocks for large-scale biodiesel production. At the same time, this oilseed is well suited for biofuel production at the village level or small-scale (Rutz & Janssen, 2007).

It has been reported that in *J. curcas* seeds from different agroclimatic regions in Mexico contain a crude protein and lipid content of around 31-35% and 55-58%, respectively. Regarding the fatty acid composition of *J. curcas* found in these Mexican regions (Castillo de Teayo, Pueblillo, Coatzacoalcos and Yautepec) was comprised mainly of oleic, linoleic, palmitic and stearic acid. The coastal samples analysed registered higher levels of oleic acid, on the other hand samples from the center of Mexico contained high levels of linoleic acid. This variation can be related to the differences in soil and climatic conditions. Overall, the *J. curcas* samples were composed mainly of unsaturated fatty acids and similar to the one reported from different countries like India, Indonesia and Malaysia (Martinez-Herrera, et al., 2006).

The seed yield has a high impact determining the viability of biodiesel from *Jatropha*, it has been reported a reasonable amount of variability in yield for *Jatropha* which is attributed to differences in plantation practices, climatic conditions, and germplasm quality. Some yield estimates have been estimated based on extrapolation of yields from small demonstration plots and individual plants instead of being from block plantations. In India, researchers have estimated that 15 billion litres of biodiesel could be produced by cultivating *J. curcas* on approximately 11 million hectares of wasteland by 2020 (Worldwatch Institute, 2006).

Jatropha platyphylla is another species in the family of the Euphorbiaceae, found in the pacific coast from Sinaloa to Michoacan states in Mexico. *J. platyphylla* is restricted to warm areas with temperatures fluctuating around 20-29ºC and is normally found around deciduous forests. It has a physical appearance of this 2-5 meters high plant which is resistant drought. It has round lobes, 15-35 cm long peltate leaves across with broad and round seed as well. Physically the appearance of these seeds is similar in shape and size to Macadamia nuts (Makkar & Becker, 2009).

Seeds of *J. platyphylla* are circular with a diameter of 1.5cm, while the toxic and non-toxic genotypes of *J. curcas* are elliptical (length 1.7cm, width 0.8 cm). The average seed, shell and kernel mass of *J. platyphylla* is 2.3-, 3- and 2-folds higher than those of *J. curcas*. The shells of *J. platyphylla*

are responsible for more than 50% of the total weight of the seeds, whereas for *J. curcas* this value fluctuates around 32-39%. Regarding the oil and protein contents, in *J. platyphylla* kernels the oil and crude protein content do not differ significantly. But the high oil content in *J. platyphylla* (60%) makes this species a valuable and suitable source for oil and therefore biodiesel production. Although the oil content is slightly higher in *J. platyphylla*, since the proportion of kernels in its seeds is lower than that in *J. curcas* the oil content would be lower; the same would be true for the crude protein content (Oyeleye, et al., 2011; Gosselink, et al., 2004).

Table 6 Composition of kernels and defatted kernel meal from J. platyphylla and J. curcas (Oyeleye, et al., 2011).

J. platyphylla		***J. curcas***	
		Toxic	**Non-toxic**
Kernel			
Crude protein	27.1 ± 2.0	26.6 ± 1.12	26.8 ± 1.25
Oil	60.3 ± 3.54	57.4 ± 0.50	57.5 ± 0.69
Ash	3.9 ± 0.09	4 ± 0.67	4.5 ± 0.56
Deffated kernel meal			
Crude protein	66.4 ± 2.0	63.7 ± 1.11	62.4 ± 2.65
Ash	9.0 ± 0.58	9.4 ± 1.01	9.1 ± 1.04

The composition of kernels and defatted kernel meal from *J. platyphylla* and from toxic and non-toxic genotypes of *J. curcas* are shown in Table 6. Regarding the fatty acid composition, in *J. platyphylla* the saturated fatty acid levels are similar to that of *J. curcas*. Oil in both species is composed mainly of unsaturated fatty acids (linoleic and oleic acid), a higher linoleic acid level is found in *J. platyphylla* which could be beneficial for human consumption but at the same time shows the potential of this plant as a suitable feedstock source in the semi-arid coastal areas of Mexico. In Table 7 is shown the fatty acid composition of both species in order to compare the fatty acid composition and highlight any difference between them. As mentioned before, *J. platyphylla* contains more than 50% of polyunsaturated fatty acids from which the predominant one is linoleic acid, 18:2n-6. The monounsaturated fatty acids comprise 25% of the total being the most predominant oleic acid 18:1n-9 and, oleic acid 18:1n-7 and palmitoleic acid, 16:1n-7 respectively.

Lastly, the monosaturated fatty acids are found in less proportion of around 21%, from which palmitic, 16:0 and stearic acid 18:0 are the most predominant ones. *J. platyphylla* in comparison to *J. curcas* has a higher amount of polyunsaturated fatty acids due to the abundance of linoleic acid, which is higher than that of *J. curcas*. But concerning monounsaturated fatty acids, *J. platyphylla* has a lower composition than *J. curcas* due to the lower presence of oleic acid, 18:1n-9 (Oyeleye, et al., 2011; Makkar, et al., 1998).

Table 7 Fatty acid composition of J. platyphylla and J. curcas (Oyeleye, et al., 2011).

Fatty acid composition (%)	***J. platyphylla***	***J. curcas***	
		Toxic	**Non-toxic**
Myristic, 14:0	0.2	0.2	0.1
Palmitic, 16:0	13.2	13.4	15.3
Stearic, 18:0	7.5	6.4	6.6
Arachidic, 20:0	0.2	0.2	0.2
Total saturated	21.1	20.3	22.3
Palmitoleic, 16:1n-7	0.7	0.8	0.9
Oleic, 18:1n-9	23.1	36.5	41.0
Oleic, 18:1n-7	1.0	Not detected	Not detected
Total monounsaturated	25.0	37.3	42.0
Linoleic, 18:2n-6	53.7	42.1	35.3
α-linoleic, 18:3n-3	0.1	0.2	0.3
Total polyunsaturated	52.8	42.3	35.7

As mentioned before *J. platyphylla* has been studied in order to analyse its feasibility as a feed ingredient for fishes such as Tilapia. Researchers have found that fish species are particularly sensitive to *Jatropha* toxins. Deactivation of the trypsin inhibitor and lectins is achieved by heating *J. platyphylla* kernel meal; this meal is included in a standard diet containing 36% of crude protein in order to replace 50% of the fish meal protein. Results indicated that fishes fed with or without this kernel substitution had normal blood biochemical parameters within the normal ranges. Having said this, both kernels and kernel meal of *J. platyphylla* could serve as a supplement in aquaculture and as part of a diet for malnourished children in the pacific coastal areas of Mexico. It could also be used to produce biofuels using conventional inter species cross breeding in order to maximise its physical and chemical properties as a feedstock source. Considering the high levels of oil contained in this plant and its abundance in the semi-arid coastal areas of Mexico, *J. platyphylla* is a suitable Mexican feedstock source for village-level and small scale biodiesel production (Makkar & Becker, 2009; Kumar, et al., 2010; Akinleye , et al., 2011).

2.1.5.1. Esterification reactions

One of the many possible methods to produce biodiesel from waste cooking oils is a two-step process involving the esterification of FFA and the transesterification with methanol of the mixture using a basic catalyst. Waste cooking oils are known to have high concentrations of FFA. In this section several technologies and open challenges concerning esterification reactions are discussed. As mentioned in the previous section, the most common way to produce biodiesel from refined vegetable oils is the transesterification of triglycerides using methanol and a basic homogeneous catalyst such

as, KOH, NaOH and CH_3ONa. These catalysts cannot be used with unrefined or waste oils since they tend to have a high concentration of FFA. In order to obtain a high yield, there is a requirement of a maximum of 1 wt% of FFA (Lee, et al., 2014; Ma & Hanna, 1999).

Table 8 contains a list of different waste and non-edible oils that are mainly used in biodiesel production. A potential solution for this problem could be the use of a homogeneous acid catalyst for both the esterification and transesterification. Nevertheless, the second step (transesterification) has a low reaction rate and the recovery of the catalyst is desired. When using a heterogenous acid catalyst, high reaction temperature and pressure are necessary. A major challenge for catalysis researchers involves the identification and characterisation of solid materials capable of carrying out the FFA esterification and transesterification simultaneously (Di Serio, et al., 2008; Lee, et al., 2014)

Table 8 FFA concentration in waste and non-edible oils (Vitiello, et al., 2017).

Waste oil	Acidity (% oleic acid)
Sunflower	4
Olive frying oil	7.8
Jatropha	14.9-19.5
Commercially refined macroalgae (Kelp) lipid	17.5
Mahua	3.4

A solution to this problem is the esterification of the FFA present in the oil by an esterification with methanol producing Fatty Acid Methyl Esters (FAME) in the presence of a catalyst given by the reaction in Figure 4, followed by the transesterification of the residual glycerides using an alkaline catalyst. However, the chemical equilibrium of the reaction results in a technical constraint when feedstock with high FFA (20%) is used. This is explained by the difficulties faced when a FFA concentration lower than 1% is aimed for. A few aspects regarding the catalytic aspects of the esterification reactions are then explored since they represent the main driver in the utilisation of feedstock with high FFA content (Vitiello, et al., 2017).

Figure 4 Esterification reaction of FFA with methanol (Vitiello, et al., 2017).

The esterification reaction is mainly catalysed by either Lewis or Bronsted acids. The Lewis acid or addition of a proton to the carboxylic group results in a more reactive electrophilic group which then favours the nucleophilic attack of the methanol. This is mainly described as an equilibrium reaction and its yield is reduced by the presence of water. The Bronsted acids are preferred for the esterification reaction since they are more active and resistant to the inhibition caused by the presence of water (Di Serio, et al., 2008).

As an example of a catalysed esterification, the most commonly used method uses sulfuric acid as the homogeneous catalyst (1-3% w/w) with a reaction temperature of 40-95°C. In order to favour the forward reaction an excess of methanol is used. Chai et al reported an optimal methanol:FFA molar ratio of 40:1 (Chai, et al., 2014).

Different approaches have been studied to avoid the inhibition of the esterification by the presence of water. Stacy et al carried out the esterification of FFA with methanol using a bubble column as the reactor with an operating temperature of 120°C and atmospheric pressure. This resulted in the vaporisation of the methanol and stripping of the produced water. This reactor showed a good performance even with pure FFA. Using 0.1% w/w of sulfuric acid and a molar ratio 4:1, a sample of 95% pure oleic was esterified in 60 minutes. Nevertheless, using homogeneous acid catalysts like sulfuric acid has many disadvantages such as, the neutralisation of the acid catalyst before transesterification, plant corrosion and downstream processing to remove traces of sulphur from the catalyst. These issues could potentially be solved using a heterogeneous catalyst (Stacy, et al., 2014; Su, 2013).

Two main classes of catalysts are pointed out, the inorganic metal oxide-based superacid and the sulfonic functionalised solids. Nowadays, technologies have focused on the use of strong cation exchange resin for its commercialisation. This particular interest is based solely in the performance of strong cation exchange resin in terms of stability and activity for industrial applications. Another aspect is their low cost when compared to other catalysts, they can be obtained from styrene and several amounts of divinyl benzene (DVB) (Vitiello, et al., 2017).

These resins can have an internal structure characterised by no discreet pores (gel-type resins) or a porous structure (macroreticular resins). Their activity is highly related to the degree of sulfonation and the structure. As mentioned before, an increase in the temperature is followed by an increase in the reaction rate of the esterification. When this type of catalyst is used, the maximum temperature is linked to the thermal stability of the resin used, circa 150°C. Heterogeneous catalysts face the equilibrium limitation as well, this is counteract using an excess of methanol usually (1:6 to 1:20). It is important to mention that in the case of sulfonic resin, the inhibition due to the presence of water can be stronger. Resins undergo a swelling phenomenon when they are in contact with polar solvents like water or methanol. Having said this, the composition in both the adsorbed and liquid phase depends on the partitioning coefficients of the mixture species (Tesser, et al., 2010).

On the other hand, the macroreticular resins do not show this swelling dependency. This is the main reason why their activity is still kept at low methanol concentrations. Nevertheless, their maximum activity is considerably lower compared to the gel-type resins since not all the mass in the resin is “swellable”. For methanol concentrations above 10%, their reaction rate decreases. This phenomenon

was reported by Jerabek et al who found that low methanol concentrations, the activity of methanol-occupied sulfonic groups is lower than those which remain unreacted (Jerabek, et al., 2010).

Overall the stability of the resins under the operating conditions here discussed is good. However, one of the main drawbacks is the presence of cations that can potentially dissolve in waste oils when using ion-exchange resins. This means a pre-treatment of the feedstock needs to be performed which could be the use of a metal adsorption column before the esterification, used in industrial applications (Russbueldt & Hoelderich, 2009).

In terms of different acid solids used for the esterification of FFA, some of the most widely used compounds are tin oxide, titanium oxide, ion-exchange resin, sulfonic modified silica, zirconium oxide and heteropoly acids. Lately, a big emphasis has been made in the use of aluminosilicates, cation-exchange resins and zirconium oxides as heterogeneous acid solids (Borges & Diaz, 2012).

Zatta et al reported the esterification of lauric acid with methanol and ethanol, using raw halloysite catalyst. The molar ratio (alcohol:lauric acid) and catalyst proportion were explored at a reaction temperature of 160°C during 2 hours in a steel reactor. The lauric acid conversion achieved was 87.11 and 95.02% for the esterification with ethanol and methanol respectively. The results show the halloysite catalyst as an inexpensive and reusable catalyst option for esterification of fatty acids (Zatta, et al., 2011).

The use of H-Mordenite treated with phosphoric acid as an alternative to homogeneous acid catalyst for the esterification of FFA in neem oil was reported by Sathyaselvabala et al. The treatment is used to increase the weak acid sites which lead to a better esterification. The FFA content in the neem samples was reduced from 24.4 to 1.8 mg KOH/g oil. The optimum parameters were a methanol:oil molar ratio of 6:1 with a reaction temperature of 60°C and a catalyst loading of 1% (Sathyaselvabala, et al., 2010).

The use of zirconium oxides as a heterogeneous catalyst for the esterification reactions is the most widely explored. The main reason for this is due to its high number of Bronsted acid sites. This number is a relevant criterion when selecting an efficient compound. Tungsten oxide zirconia has been examined as a catalyst for vegetable oils conversion using methanol, which resulted in no leaching and a high activity. Amongst the tungstated zirconia catalysts with an extra loading of tungsten of 10-30 wt%, the 20wt% showed the highest catalytic activity. The high catalytic activity of this catalyst is related to its strong acidity (Lee & Saka, 2010; Park, et al., 2010).

A zirconia supported metaloxide was developed by Kim et al, used in the production of biodiesel from brown grease. A high FAME yield was achieved resulting in a total acid number for the product of 12 mg KOH/g, meaning a FAME yield of 78%. Rattanaphra et al reported the esterification of myristic

acid with methanol using a sulphated zirconia as catalyst. This catalyst is classified as a heterogeneous superacid catalyst and has strong acid properties, having a higher acid strength than heteropoly acids and sulfonic ion-exchange resins. Nevertheless, after the catalyst was used several times the leaching of the sulphate groups became noticeable (Rattanaphra, et al., 2011; Kim , et al., 2011).

Although the zirconium oxide catalysts show a good performance for the esterification reaction when using inexpensive feedstock with high levels of FFA, its cost is relatively high for biodiesel production since zirconium is a costly and rare metal. Having said this, there is a need to find a feasible and cheaper alternative for this type of reaction. In general, the esterification reaction requires high reaction temperatures to obtain a better yield this is why the esterification via microbubbles is studied in this thesis to come up with a feasible alternative to produce biodiesel from high FFA content feedstock using a reaction mechanism enhanced by free radicals and the vaporisation of the produced water.

2.1.5.2. Esterification via microbubbles

A microbubble mediated esterification computational model using ozone-rich microbubbles is proposed in this research project to obtain biodiesel from vegetable oils. Based on experimental data gathered by previous doctoral student on ozonolysis of oleic acid, olive oil and used cooking oil, a proper analysis of the reaction kinetics and modelling using COMSOL Multiphysics® Software were carried out.

In 2012-2013, the United Kingdom produced 40% of the world total waste cooking oil-derived biodiesel, around 128 m litres. 95% of this waste cooking oil can be free fatty acids, in conventional esterification a methanol: oil above 70:1 in order to achieve approximately a conversion of 90%. On the other hand, microbubble intensified esterification promises a full conversion of FFAs to biodiesel with 1:1 stoichiometric feed (Department for Transport, 2015).

In 2013 Talebian-Kiakalaieh et al carried out the transesterification of waste cooking oil with heterogeneous acid catalyst and methanol. Using the acid-catalysed reaction, several operating parameters were controlled such as methanol: oil ratio, temperature, catalyst loading and reaction time. Solid acid catalysts are really active for heterogeneous reactions and have several advantages like the following: no washing for product (FAME), able to catalyse transesterification and esterification simultaneously, insensitive to FFA content, easier separation steps, higher yield obtained, requires lower catalyst loading compared to other processes, and the catalyst can be reused. The highest conversion obtained by Talebian-Kiakalaieh et al was 88.6% at the optimum temperature of 65 ˚C, methanol: oil ratio of 70:1, 10wt% catalyst load during a total reaction time of 14 hours (Talebian-Kiakalaieh, et al., 2013).

Kokoo (Sheffield University PhD student) and Zimmerman (Sheffield University Professor,2014) carried out the intensified esterification of olive oil (<1% FFA), waste olive oil (20% FFA) and oleic acid (FFA) with ozone-rich microbubble injection (0.1-0.2 L/min and 600 μm size) in a 1 litre vessel using 1:1 methanol loading, GC-MS analysis were conducted on the reacting mixture after 8, 16, 20, and 24 hours. Olive oil broke was intended to be susceptible for a second acid-catalysed stage, but it reacted forming FAMEs and ti completion. Oleic acid and waste olive oil were completely converted to FAME at 60 ˚C after 8 and 20 hours. Ozone microbubbles used remarkably a lower volume of excess methanol to achieve a complete conversion of FFA to FAME. This intensified esterification process can be 10 times faster when compared to conventional esterification of waste cooking oils to biodiesel (Kokoo & Zimmerman , 2018).

Microbubbles produced by a fluidic oscillator are generated with 1000 fold less energy dissipation compared to the ones produced by saturation/nucleation mechanism, meaning a 90% decrease in capital cost. Oxidation yields found in microbubble dispersal are twice those for fine bubble dispersal, suggesting autocatalysis by microbubbles is enhanced by strongly exothermic oxidation reactions, which produce free radicals. For 100 μm diameter bubbles, the time scale for internal mixing is 1ms. Secondly, increased vaporisation rates over fine bubbles by a factor of 7 were caused by the microbubble evaporation/distillation principle, due to more rapid internal mixing. Following LeChatelier's principle, water produced by esterification in the bubble is removed, therefore driving the reaction to completion. This concept has been proven in the lab, with neither base nor acid catalysts, but ozone rich microbubbles. Immediate efflux from the plasma reactor into a microbubble for oxidising is tested as potential ozone generators for pilot scale (Zimmerman, et al., 2013).

In the previous section, several techniques used in the esterification of FFA were presented. Although some of them present an alternative for this process, they require a high operating temperature, resulting in a more complicated and less efficient reaction. Both the homogeneous and heterogeneous acid catalysed esterification represent a valid alternative. Chai et al reported the use of sulfuric acid for the esterification of a used vegetable oil with using a methanol:FFA molar ratio of 20:1 and a catalyst loading of 5% resulting in a good performance for a FFA range of 15-35%, an activation energy for the esterification reaction of 20.7 kJ/mol was calculated (Chai, et al., 2014).

The biodiesel production from *Jatropha* oil has been explored using a novel magnetic carbonaceous acid. The acid showed high stability and activity, and it was easy to recover (96.3 recovery rate) after the reaction was carried out yielding 90% conversion. It was found that the catalyst had a high acid density of 2.8 mmol/g and strong magnetism, ideal for direct production of biodiesel from vegetable oils with a high acid value (17 mg KOH/g). A non-edible oil (Calophyllum inophyllum) with a FFA of 15%

was used for the biodiesel production using a sulphonated carbon catalyst showing a conversion of 99% (Zhang, et al., 2015; Dawodu, et al., 2014).

As mentioned before, both the heterogeneous and homogeneous acid catalyst have the requirement of methanol in excess, a high temperature and catalyst loading. This separation requirement in the pre-treatment stage would be significant in the feasibility of the process in terms of industrial applications since it means the use of large vessels with the capability to separate and then recycle the excess methanol to make the process economically viable. Another matter of importance is the separation of the acid catalyst before transesterification, since an alkaline catalyst is used to achieve rapid kinetics. If the acid catalyst is not removed, it would mean the production of salts and water. Unreacted FFA would then react with the alkaline catalyst, meaning further downstream processing and a surplus of the alkaline provision to substitute the spent catalyst. The downstream separation for methanol and water would then require vacuum distillation to be carried out and potentially an ion-exchange resin to purify the glycerol and remove the produced salts. All the steps here mentioned are classified as energy intensive accounting for a significant part of the cost of the process (Kokoo & Zimmerman , 2018; Talebian, et al., 2013).

Having said this, the esterification of FFA seen as a pre-treatment stage could represent an improvement for the downstream processing if the produced water were removed before the subsequent step, the transesterification. Zimmerman et al reported a methodology for the rapid evaporation with hot, dry microbubbles, which successfully stripped the water from the reacting mixture. The direct contact microbubble evaporation always achieved 100% relative humidity, observing an absolute humidity decrease and a vapour temperature reduction with contact time increase. The process is considered to operate under isothermal conditions with low contact times and a high selectivity for vaporisation over sensible heat transfer was achieved (Zimmerman, et al., 2013).

Therefore, introducing dry microbubbles would favour the stripping of water from the reacting mixture. In theory, the proposed reactive distillation can potentially achieve completion according to LeChatelier's principle for an equilibrium reaction. Removing the produced water by means of vaporisation would drive the esterification reaction to completion, as a new molecule of water would need to be produced in order to replace the one previously removed. Regrettably, the injection of microbubbles alone in the reactive mixture of the acid esterification reported by Talebian et al with high excess methanol did not achieve the anticipated effect. The operating conditions varied in this study were the methanol:oil ratio, catalyst loading, reaction temperature and time. The highest conversion of 88.6% was then achieved at a molar ratio of 70:1 at 65°C, with a catalyst load of 10wt% and a reaction time of 14 hours (Talebian, et al., 2013).

Abdulrazzaq et al reported the separation of azeotropic mixtures using air microbubbles generated by a fluidic oscillator. It was reported a strongly non-equilibrium preference for the vaporisation of ethanol in mixtures containing water-ethanol when hot microbubbles were injected. In the following modelling of the experimental data is described that the non-equilibrium driving force studied in the mixtures is more rapidly achieved vaporising ethanol in the different liquid proportions studied (Abdulrazzaq, et al., 2015; Abdulrazzaq, et al., 2016).

Methanol is known to be more volatile than ethanol, this is why it would be expected to vaporise and then occupy the vapour phase in the bubble domain in the esterification reacting mixture. Suggesting that both water and methanol would be removed from the mixture, but preferentially methanol. Excess methanol is needed to push the equilibrium favouring the forward reaction (esterification) whereas water removal would pull it, injecting hot microbubbles would pull the equilibrium but weaken the push. It is clear that something more than just the injection of hot microbubbles is needed to avoid the vaporisation of methanol. Kokoo and Zimmerman proposed the methanol present in the esterification as immediately reactive in order to make the water removal more effective. The reaction mechanism is set to be on the bubble interface, where the produced water can joing the dry bubble and the methanol residue remains in the liquid domain as part of the FAME produced. In order to overcome the vaporisation of the methanol, this species forms the methoxy free radical whenever a methanol molecule reaches the surface of the bubble (Kokoo & Zimmerman , 2018; Timberlake & Hodges, 1970).

Microbubbles can potentially be injected with ozone in order to generate ozone-rich microbubbles. In fact, ozone is known to be a free radical initiator. It has been reported by Lozano-Parada and Zimmerman that it is possible to tune an in-situ ozone plasma microreactor to preferentially produce oxygen singlet radicals by adjusting the residence time and then injecting them directly into the bubble. At $1x10^{-2}$ s, the ozone production found its maximum and for the oxygen singlet the maximum yield was found at $1x10^{-3}$ s. This means a 10x throughput can be produced by tuning the microreactor at the appropriate operating conditions (Lozano-Parada & Zimmerman, 2010; Zimmerman, 2011; Rehman, et al., 2016).

It has been reported that the oxygen radicals would form hydroxyl radical in the presence of water. In the presence of methanol, these radical species could potentially scavenge the labile hydrogen from the alcohol group and form the methoxy radical. Kokoo and Zimmerman proposed the ozone-rich bubbles injection into methanol-FFA mixtures without any catalyst present, suggesting the reaction is driven towards completion of esterification by the water removal mechanism previously described, but dramatically enhanced by the free radical chain reaction (Kokoo & Zimmerman , 2018).

Presently, there are no claims that the esterification of FFA can be free radical catalysed. Abdul-Majeed et al reported an unconventional flying jet DBD plasma torch for the esterification of used cooking oil when compared to conventional transesterification, suggesting that plasma activation can successfully catalyse transesterification as well as esterification. Nevertheless, a plasma jet does not provide a route for the water vaporisation, meaning one would not expect the esterification to go to completion but only being catalysed using this method (Abdul-Majeed, et al., 2016).

2.2.Intensified esterification using microbubbles

In this section are discussed the most relevant aspects of the intensified esterification method proposed such as the microbubble generation and its size effect, the fluidic oscillator technology, the coalescence between microbubbles, the Dielectric Barrier Discharges for plasma generation, the Criegee mechanism of fatty acids, the reaction kinetics of this method, the hydroxyl and methoxy radical kinetics the steady state approximation and the heat and mass transfer aspects of the mechanism proposed. All of these features are used in the next chapters, in order to build a robust model that is informed in experiments and then validated. The main importance of this section relies on describing the physical and chemical parameters studied in the intensified esterification in order to ease the calculations understanding of the proposed models.

2.2.1. Microbubbles generation and size effect

The importance of bubbling systems in diverse industrial processes is related to the gaseous exchange of heat and mass transfer from the gas to the liquid phase and vice versa. The microbubble dispersal application in engineering is called surface aeration, commonly used in the design of bioreactors. The higher surface area to volume ratio of microbubbles improves the efficiency of these processes where a gaseous exchange takes place. One of the main benefits of microbubbles is the transport behaviour in terms of momentum, mass and heat transfer at the interface (skin of the bubbles) influenced by the interfacial surface area. The interphase mass transfer flux *(J)* is given by:

$$J = K_l \cdot a\,(c_g - c_l) \qquad (1)$$

where a is the interfacial area, K_l is the mass transfer coefficient (mol s^{-1}), c_g and c_l are the molar concentrations of the gas and liquid phase respectively. Regarding the heat transfer flux *(Q)*, there is an analogy where the concentrations are replaced by temperature that is the Newton's Law of cooling (Zimmerman, et al., 2008).

Concerning the effect in momentum transfer, the mass transfer flux is taken by the force *(F)* in the vertical direction due to changes in the velocity in the horizontal direction, this behaviour follows Newton's Law of viscosity given by:

$$F = -\mu a \frac{\delta w}{\delta x} \tag{2}$$

The momentum transfer is increased by a cloud of rising bubbles because the surface area of the cloud drags more of the surrounding liquid with it compared to one larger bubble with less surface area. Instinctively it could be thought that smaller bubbles rise slower than a single large bubble matching the volume. In Figure 5, the rise velocity of microbubbles is shown based on experimental data and theoretically. From the slope in Figure 5 can be deducted that bubbles three times smaller stay in the liquid domain ten times longer, this means they have a longer time to transfer the same momentum rate. Transfer rates in microbubbles increase inversely proportionally to the size of the bubble, but the difference in velocity rises proportionally to the bubble size. Having said this, it could be expected for the momentum transfer by the cloud to be comparatively constant. Nevertheless, due to the finite height in terms of the liquid layer the momentum transferred should be larger when using smaller bubbles. (Zimmerman, et al., 2008; Liger-Belair, et al., 2004).

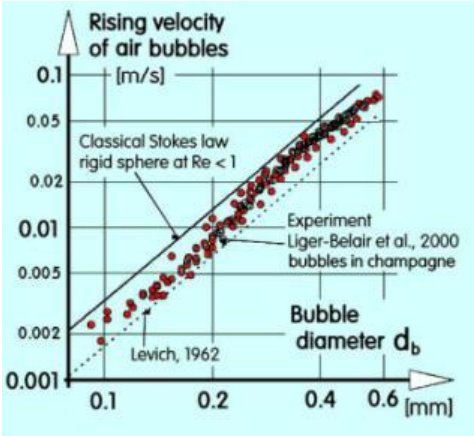

Figure 5 Rise velocity of microbubbles (Levich, 1962).

Geometrically speaking the surface area to volume ratio of a bubble (sphere) increases inversely to the radius given by:

$$\frac{S}{V} = \frac{4\pi r^2}{\frac{4}{3}\pi r^3} = \frac{3}{r} \tag{3}$$

Regarding the bubble phase, if the total volume V_0 is set to be constant then:

$$S = \frac{3}{r} V_0 \tag{4}$$

For example, if 1 L of air is dispersed in 100 μm bubbles the interfacial area increases significantly to 10 m^2, which is greater than a tank open to the atmosphere with a reasonable sized air-liquid interface. It may result difficult to calculate the mass transfer coefficient when studying one single bubble since it depends on the environment, properties of the medium and hydrodynamics of bubble rise. Generally, the mass transfer is dominated by convection and be fitted to a phenomenological

equation like the interphase mass transfer flux stated previously in this section where the interfacial area is proportional to the overall flux. In other words, heat or mass flux are enhanced when decreasing the bubble size (Desphande & Zimmerman, 2005; Zimmerman, et al., 2009).

Dividing a determined volume into *N*, smaller and equal in size, objects results in additional surface area which scales with the cube root of *N*. The notorious effect of using smaller bubbles is depicted in Figure 6, the bubble volume scales as the cube of the bubble size *l*, but the transfer rate and surface area scale with its square. Hence, any transfer coefficient that is proportional to the surface area to volume ratio will increase by a factor of 2. This means that if a bubble reduces in size the process efficiency is enhanced due to better mass or heat transfer (Brittle, et al., 2015).

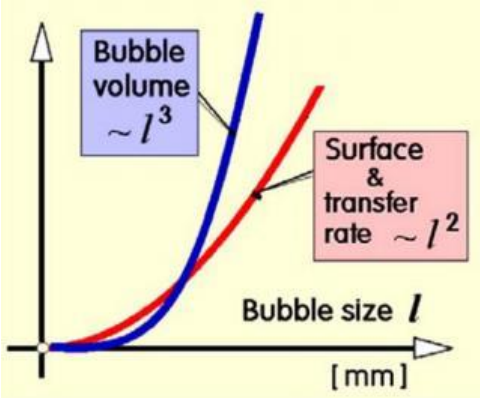

Figure 6 Surface area and bubble volume scaling in microbubbles (Zimmerman, et al., 2008).

As a result of the behaviours pointed out previously, Figure 7 shows that the total transfer rate across surface scales inversely with the bubble size. A rising cloud comprised of smaller bubbles lead to greater transfer rate when compared to the number of bubbles adjusted to keep the gas phase volume at a constant value. Following the Stokes regime, if nonlinearity is neglected then the stirring effect by the rising cloud of smaller bubbles surpasses that of a single larger bubble.

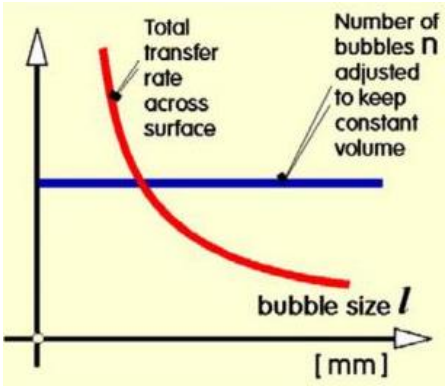

Figure 7 Total transfer rate across surface (Zimmerman, et al., 2008).

The residence time of a microbubble in a viscous liquid can be calculated using the Stokes Law, where as a result of the squared diameter *(d^2)* it can be inferred that residence times for smaller bubbles are longer for the same height of the liquid layer.

$$U_{stokes} = \frac{2}{9}\frac{g\Delta\rho d^2}{\mu} \quad (5)$$

This means smaller bubbles have more time for momentum transfer to the liquid dragged along with them, even if they have less momentum to be transferred. Momentum is transferred as well for the $\frac{S}{V}$ ratio of a bubble defined previously by shear stress across the surface area. Consequently, when using smaller bubbles, the flux of momentum is increased by the $\frac{S}{V}$ ratio. Microbubbles appear to have a *dragging ability* which is higher when rising with the same volume of fluid holdup. This is relevant for improved mixing in a riser region of a bioreactor, if bubbles are produced energetically efficiently. In order to achieve an equivalent mixing level with microbubbles, a lower volumetric flow rate is used. This means a higher holdup at lower volumetric flow rates due to a longer residence time in the liquid phase. In 2006, Shi studied this behaviour in laboratory experiments demonstrating an 8-fold increase in the transfer of dissolved oxygen when using 8-fold smaller bubbles with oscillatory flow compared to the same volumetric flow rate through the same nozzle bank (Zimmerman, et al., 2009; Shi, 2006).

Burns et al compared three commonly used mechanisms used in bubble generation. Air spraying, electroflotation and Dissolved Air Flotation (DAF) are then discussed in terms of surface area and bubble size produced per time as a function of the power input. This study showed that DAF resulted in the finest bubble size distribution with largest average bubble size but assured the highest surface area/power/unit time when compared to the other two methods. This method also showed a small improvement of bubble size when the pressure was increased to 60-90 psi in order to produce 46-57 μm bubbles (Zimmerman, et al., 2008; Burns, et al., 1997).

The ultrasonic method to produce microbubbles uniformly with a diameter of 4-15 μm at a constant rate was reported by Makuta et al. The produced bubbles from the tip of a needle were oscillated using ultrasonic waves and projections for the surface waves were formed to produce a continuous stream of small bubbles. One of the main bubble generation constraints was the gas viscosity of around 20 μPa s in a viscous liquid with a high kinematic viscosity ranging between 5-100 $mm^2\ s^{-1}$ and a surface tension of 20-34 mNm^{-1} (Makuta, et al., 2006).

In the previously described processes for microbubble generation, the high value added to the compound obtained justifies the use of high-power technologies to generate microbubbles. However, it is desired to explore new alternatives to generate microbubbles that do not require a high power. The microbubble generation could then potentially benefit from innovations on the energy efficiency whilst achieving the same holdups and same bubble size distribution (Zimmerman, et al., 2008).

2.2.2. Fluidic oscillator

The esterification approach is controlled by the microbubble surface are and bubble flux. In previous trials at pilot and industrial scale implementations carried out by Zimmerman, less than 100 μm average bubble size can be obtained, whilst lab bench usually achieves a size of around 600 μm. Having said this, the kinetics of larger scale trials should be faster and better mixed than lab bench trials.

Microbubbles are mainly produced by three methods, the most commonly used one involves the compression of a gas to nearly 6 bar to be then released through a nozzle. Another method for microbubble generation is ultrasound. Nevertheless, these techniques would require a high-power density to generate small bubbles. Lastly, microbubbles can potentially be generated oscillating the fluid by mechanical vibration or using a fluidic oscillator. This device offers a cheap alternative and has a low maintenance requirement since there a no moving parts that could suffer damage (Zimmerman, et al., 2008; Zimmerman & Tesar , 2013).

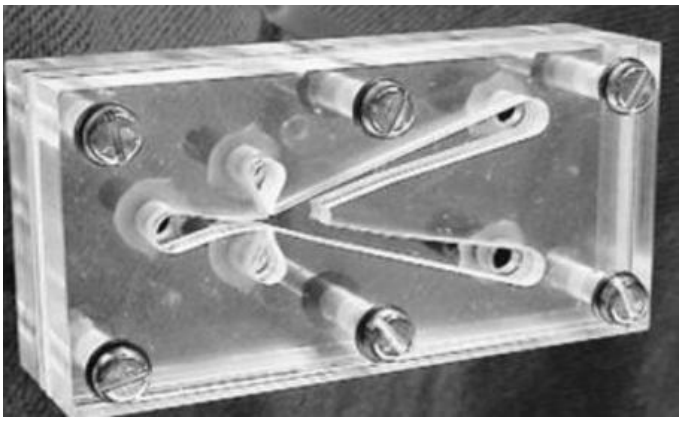

Figure 8 Fluidic oscillator (Zimmerman, et al., 2009).

The fluidic oscillator is comprised of two main components, an amplifier and a feedback loop. Figure 8 shows a fluidic oscillator made by laser cutting in acrylic plates. The amplifier is made of CNC acrylic glass plates designed to form a cavity. The feedback is used to connect the two control terminals of the amplifier. When the fluid enters the main cavity through a nozzle, it arises as a jet causing the fluid to travel from either side of the jet. Around the walls of the device, low pressure regions start developing causing the jet to attach to one side of the cavity explained by the Coanda Effect. This results in a pressure difference throughout the control terminal generating a pressure wave in the feedback loop which then diverts the jet to the other outlet and vice versa. An important parameter when operating the fluidic oscillator is the oscillation frequency which depends on the flow rate and the length of the feedback loop (Rehman, et al., 2015).

Zimmerman et al reported an energy efficient mechanism for microbubbles generation on the size of the pore used to disperse the bubbles using a fluidic oscillator. This approach decreases the friction

losses in the pipe network and nozzle/diffuser due to the boundary layer disruption, this results in an energetic consumption saving when compared to steady flow. The bubble cloud generated using this technique is of the scale of the pore when the distribution of the antechamber gives a good distribution and the frequency of oscillation is high enough. Another parameter that has influence on the size of bubbles generation is the surface wetting properties. A thin water film between the pore material and the bubble is often seen in hydrophilic surfaces, and when using a hydrophobic gas like air no adhesion to the solid surface is experienced. In this case the bubbles emerge like bullets from the pores, instead of the conventional (steady flow) slow pushing out from the pore. Having said this, the air pulses has an impact on the bubble size (Zimmerman, et al., 2008; Zimmerman, et al., 2009).

A relevant application of the wave dynamics theory involves the length of the pulse. The linear velocity of the fluid is related to the speed of the carrier, and if divided by the frequency of oscillation it gives the wavelength of the pulse. In this case, the linear flow rate should be as small as possible and the frequency as large as possible in order to produce smaller bubbles in the order of magnitude of $1x10^{-6}$ to $1x10^{-9}$. A fluidic oscillator achieves frequencies of 1-100 Hz, it has been reported that the smallest bubbles are generated at higher harmonics of the oscillation when using the fluidic oscillator (Zimmerman & Rees, 2004; Hool & Schuchardt, 2011).

An increase in the oscillations is related to the miniaturisation of the fluidic oscillator and resulting in oscillations in kHz required if nanobubbles were to be produced. It is important to mention that the oscillatory flow differs from classical calculations of bubble mass, and it based on the Tate's law instead defined by:

$$W = 2\pi r\gamma \tag{6}$$

where W is the weight of the bubble and is calculated using the surface tension and the pore size. The density of a gas is known to be relatively small when compared to a liquid, this law states that a larger diameter bubble diameter than the pore radius (*r)* is obtained unless the surface tension (γ) is dramatically small. It is relevant to mention that one key feature when working with water is its large surface tension, therefore wetting effects are inherently different when microbubbles are generated in a fluidic oscillator than in the conventional steady flow generator (Zimmerman, et al., 2011).

As mentioned before, this research project focuses on the use of microbubbles to carry out an intensified esterification using cheap organic oils. Microbubbles have several industrial applications due to their higher surface to volume ratios compared to that of fine bubbles. Advantages such as efficient mixing and increased mass transfer rate are obtained when working with microbubbles. Presently, there are three main microbubbles production methods: injection of compressed air into the liquid phase, ultrasonic waves, and the fluidic oscillator driven microbubbles. The last one is the preferred approach for this research project since it is a low-power generation method using a porous

material. Zimmerman et al in 2009 introduced a fluidic oscillator, this device is connected to a steady air supply that in conjunction with a set frequency, generates uniform microbubbles with the same size as the pore. This microbubble production method has several advantages, such as robustness, non-electrical dependence, and low operating costs. In addition to the higher surface area per unit volume ratio observed when using microbubbles compared to that of fine bubbles, their residence time is also longer meaning more time for microbubbles to react with the components in the liquid phase around them (Zimmerman, et al., 2009).

In spite of this, a lower transfer momentum has been reported in experiments. In Figure 8, a photo of the assembled fluidic oscillator previously described is shown. Its ability to divert the flow passing through the supply nozzle is controlled by terminals A and B. The frequency of oscillation is controlled by adjusting the supply flow rate and the length of the feedback loop. The surface of the pore has also influence on the size of the bubbles, when using hydrophilic surfaces, a thing water film is developed between the bubble and the pore material. When using hydrophobic gases, a bullet shape is observed since they do not stick to the pore surface (Zimmerman & Rees, 2009; Zimmerman, et al., 2011; Tesar, et al., 2006).

As part of this research project, fluidic oscillator driven microbubbles in conjunction with plasma microreactor is used to inject ozone-rich microbubbles to enhance the proposed intensified esterification. Presently, there are several techniques to produce ozone, such as electrolytic technique, ultraviolet light and non-equilibrium plasma. The electrolytic technique is expensive due to the high potential and current needed to electrolyse water. The ultraviolet light requires a great amount of energy and achieves only small yields of ozone. Lastly, non-equilibrium plasma is the preferred ozone production method in this research project. This method has several advantages like: discharge generated from AC power, atmospheric pressure, and moderate gas temperature. Some examples of non-equilibrium plasmas are corona discharge, glow discharge and dielectric barrier discharge (DBD). This last one is the most common technique for ozone production around the world and an schematic of this device is shown in Figure 10 (Eliasson & Kogelschatz, 1991; Conrads & Schmidt, 2000).

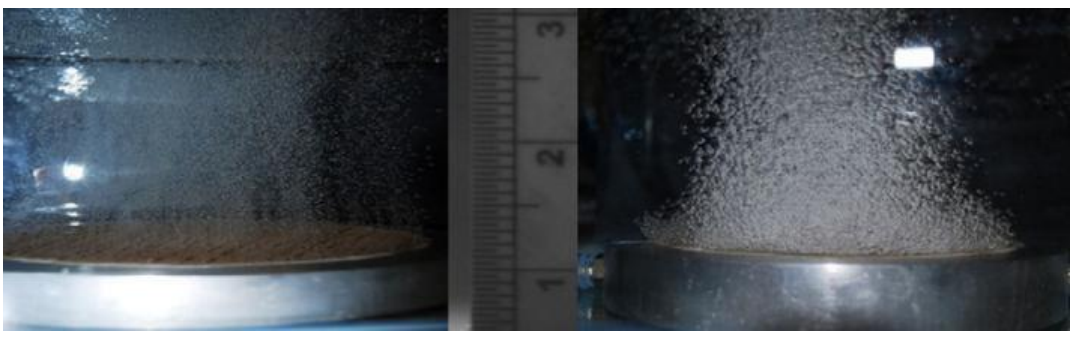

Figure 9 Comparison of microbubble generation using the fluidic oscillator (Zimmerman, et al., 2011).

A brief comparison of the microbubble generation using the fluidic oscillator is illustrated in Figure 9. On the right side of the figure, the resulting microbubbles at a steady flow through a 15 cm diameter microporous diffuser considering a pore size of 20 µm size pore. The bubbles here observed have a size of 500 µm which is much larger than the pore due to coalescence effects. On the left side, the microbubbles generated using the same fluidic oscillated considering a fast oscillation of nearly 90 Hz and a flow rate tuned to the Stokes rise velocity are shown. These operating conditions result in non-coalescent and uniformly dispersed microbubbles with a size of 20-100 µm. There are multiple applications where high transfer rates at low volumetric flows and low-energy processes are desired. Having said this, microbubble generation even for high flow rates could potentially be achieved using this technique. When operating at the same temperature, the bubble size obtained using a fluidic oscillator is smaller than a system operating without it, this is due to the pulsejet stream. Typically, decreasing the buoyant forces results in a bubble size increase, which is a function of the liquid density. Kokoo and Zimmerman reported that the density of oleic acid decreased slightly with an increase of the liquid temperature resulting in larger bubbles. The bubble size decreases when the liquid temperature is increased due to the reduction of the fluid viscosity (Zimmerman, et al., 2011; Kokoo & Zimmerman , 2018; Ma, et al., 2012)

2.2.3. Low power consumption plasma microreactors

The production of ozone and the oxygen related radicals is limited by high-power consumption, high voltage and vacuum operation. In the past years, Zimmerman et al reported different plasma microreactors operating under atmospheric pressure, room temperature and low voltage. A plasma reactor onto microchips has been developed with a built-in plasma source and impedance matching network, resulting in a greater operational flexibility when compared to conventional plasma sources. This set up achieved a low power consumption when operating plasma microreactor for ozone formation by taking advantage of the rapid kinetics of the chemical reaction. For greater throughput, a prototype dosing lance complex was developed for the plasma reactor, leading to high dispersal rates of the ozone when delivered to the microbubble. It is relevant to point out that ozone is highly reactive, and microbubbles have a low carrying capacity suggesting the possibility to tune the production and dispersal of the ozone and oxygen radicals found in the sample. This eradicates the need for costly further processing of unspent ozone destruction (Lozano-Parada & Zimmerman, 2010; Zimmerman, 2011).

Zimmerman reported the development of a microreactor operation with its respective plasma source and matching network optimisation. It was found that ozone production can be carried out developing a glow discharge with a low voltage (170 VC AC) at room temperature and atmospheric pressure using an electric field of 100 Hz AC. Conventional plasma sources operate at 13.56 MHz to

maintain the plasma continuously. Using a low frequency like 100 Hz, this operation requires one tenth the specific power for ozone yield when compared to conventional ozone generation. This phenomenon is mainly attributed to the kinetics of the ozone formation reaction. It was demonstrated that 99% of the ozone and oxygen singlet equilibrium yield was obtained $1x10^{-2}$ and $1x10^{-3}$ s. The reactor used in this experiment had a length of 1 cm and with a superficial velocity of 1 and 10 m/s, the residence times for each species can be calculated. This method allows low power operation simply to power the plasma only while the reaction is taking place and then provide fresh reactants to a process. There is one potential drawback for this method, the extinction of the plasma at the walls. Ions in the plasma are estimated to have a diffusion velocity of 1 cm/s, and the time to extinction is around 0.1 s considering the electrodes are 800 μm apart from each other. Suggesting that by that time the reaction is already over, and the products can be used without worrying about their extinction at the walls. Conventional plasma reactors walls are far apart in order to minimise the extinction of the plasma (Zimmerman, et al., 2011).

Dielectric-Barrier Discharges (DBD) are presently used in large industrial scale since they combine the advantages of non-equilibrium plasma properties with operating atmospheric pressure. One important feature of this technology is the relatively simple scalability from laboratory to industrial scale (MW input power). They consider a frequency that lies between 1 kHz and 10 MHz with a pressure ranging between 10-500 kPa. Some of the main applications include pollution control, surface treatment, ozone generation and CO_2 lasers. The operating conditions and the application have an influence when choosing the desired discharge with a filamentary structure or a diffuse appearance (Kogelschatz, 2003).

Non-equilibrium plasma is the preferred ozone production method in this research project. This method has several advantages like: discharge generated from AC power, atmospheric pressure, and moderate gas temperature. Some examples of non-equilibrium plasmas are corona discharge, glow discharge and dielectric barrier discharge (DBD). This last one is the most common technique for ozone production around the world and an schematic of this device is shown in Figure 10 (Eliasson & Kogelschatz, 1991; Conrads & Schmidt, 2000).

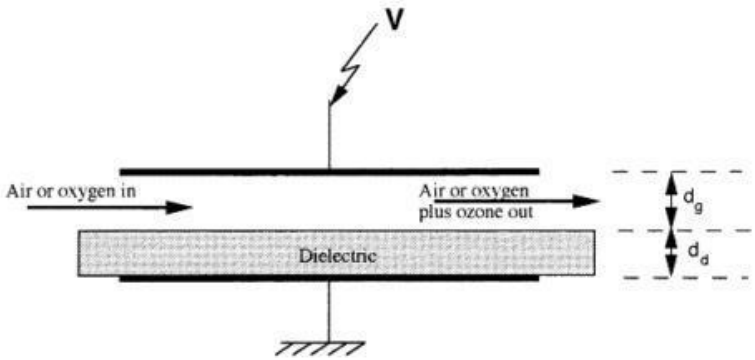

Figure 10 Ozone generation using dielectric barrier discharge (DBD) (Chalmers, et al., 1998).

In a DBD device, at least one of the surfaces is covered by a dielectric layer (quartz, ceramic, glass, polymers) and uses one of the three types of silent discharge (volume, coplanar and surface). DBD devices can be run using AC power supply with a frequency of 50-1 MHz, voltage of 1-10 kV, a gap between layers of milimetres range and operated at high pressure of 1-3 bar. Having said this, DBD is suitable for large scale production using as the reactant source either air or pure O2. This method does not require a vacuum pump or air compressor, resulting in less operating costs and higher active processing volumes (Becker, 2005; Pietsch & Gibalov, 1998).

2.2.4. Reaction kinetics

There are several factors affecting the yield of biodiesel, such as the alcohol quantity, reaction time, and reaction temperature. From the factors listed above, the molar ratio of alcohol to triglyceride seems to be one of the main factors. Theoretically for the transesterification reaction, 3 mol of alcohol and 1 mol of triglyceride are required to produce 3 mol of fatty acid ester and 1 mol of glycerol. In biodiesel production, an excess of alcohol is used to ensure that oils will be converted to esters, and a higher alcohol triglyceride ratio can result in a greater ester conversion in a shorter period of time. Yield of biodiesel is increased when alcohol triglyceride ratio is raised beyond 3, reaching a maximum. The molar ratio associated with the type of catalyst used, and usually the molar ratio used in most investigations is 6:1. When the content of FFAs in the oils is high, a molar ratio as high as 15:1 is needed when using the acid-catalysed reaction (Leung, et al., 2010).

The conversion rate of fatty acid esters increases with reaction time. Firstly, the reaction happens slowly due to the dispersion and mixing of alcohol into the oil. The reaction proceeds in a faster pace after a while, usually the yield reaches a maximum at a reaction time of 90 minutes, remaining constant with a further increase in the reaction time. A reduction in the product yield could be cause by an excess reaction time, due to backward reactions resulting in a loss of esters. On the other hand, a higher reaction temperature decreases the viscosity of oils resulting in an increased reaction rate, reducing the reaction time. If the temperature increases beyond the optimal level, the yield of biodiesel decreases due to the acceleration of secondary degradation reactions. The reaction

temperature should always be less than the boiling point of the alcohol, ensuring that the alcohol is not lost through vaporisation. Temperatures normally range from 50 to 60 ˚C (Leung, et al., 2010).

Tesser et al in 2010 reported a kinetics model for HBr dissociation when considering the esterification reaction, they stated that the uncatalyzed reaction (no acid added) is consistent with second order kinetics in FFA concentration. The main reason for this is because FFAs serve as both the substrate and H+ donor. According to this statement, the concentration of H+ depends on the FFA concentration whether the reactions is catalysed or not. The production of H+ depends on the dissociation of the acid in the catalysed reaction. It is assumed that bromide ions are only produced in stoichiometric ratio with H+ and that aqueous dissociation reaches equilibrium really fast. HBr does not dissociate strongly in methanol solution as sulphuric acid giving a weaker acid catalysed esterification. Therefore, the introduction of water vapour in the microbubble aids the dissociation of HBr. Having said this, the forward reaction depends on the concentration of water and the role of FFA in the hydrolysis reverse reaction is also acid catalysed. It is important to acknowledge that exists a methanol concentration dependency and varying the methanol concentration increase the curves for acid values. This model proposes that the greatest source of H^+ is the dissociation of HBr in water, showing the dependency of the forwards reaction on the presence of water (Tesser, et al., 2010; Berrios, et al., 2007).

As mentioned before, in this research project one of the aims is to explore the effect of the oxygen singlet in the ozone free radical initiated esterification. This reaction is hypothesised to happen on the bubble interface. In the reacting mixture, both the methanol and FFA can be found to then notice the increase in FAME production as the product of interest. To avoid the propensity of the methanol to vaporise, it is assumed that methanol becomes immediately reactive this means the water removal would be more effective. In order to make the methanol reactive, it is assumed to form the methoxy radical in the presence of oxygen singlet, this is the first step of the reaction mechanism here proposed.

The methoxy group is known to be a substituent with a large negative σ^+ value of 0.78. Timberlake and Hodges described the methoxy group as stabilising group with good resonance towards carbonium ion centres. The hydrogen abstraction from ethers rates and stabilisation energies of methoxy substituted methyl radicals are in agreement with the stabilisation of radical centres by the methoxy group (Timberlake & Hodges, 1970).

Kokoo reported the esterification of oleic acid using methanol as the protic solvent, since it increases the production of FFA specifically 1-nonanal, when compared to ethanol, n-propanol, iso-propanol and butanol. Methanol was reported to have a lower reactivity with ozone, this means methanol loss due to its oxidation by ozone is relatively low. The Henry's Law constant and diffusion coefficient reported for FFA-methanol mixtures are higher when compared to the mixtures with the

other solvents. This would favour the generation of smaller bubbles in the reacting mixture, increasing the interfacial area and hence the mass and heat transfer. The main drawback reported by this study was the already known low boiling point of methanol which is here overcome by the high reactivity of this species in the proposed reaction mechanism (Kokoo & Zimmerman , 2018).

Kokoo and Zimmerman reported that in the presence of water, the oxygen radicals produce hydroxyl radicals to then form water in the presence of methanol by scavenging the labile hydrogen from methanol to form the methoxy radical. Therefore, the reaction mechanism is based on the hypothesis that ozone-rich bubbles can be injected to the reacting mixture and tuned in to obtain the maximum oxygen singlet generation, so this free radical initiated esterification would be driven towards completion by the removal of water caused in the microbubble stripping but enhanced by the free radical chain reactions. One of the advantages of this mechanism is that no acid or basic catalyst is used, instead the free radical species act as the catalysts. Avoidance of downstream processing to eliminate and neutralise the catalysts is then obvious, reducing the operational cost of this process compared to the conventional esterification process. It is important to state that the effect of varying the oxygen singlet concentration is here studied in order to determine the its overall effect on the esterification reaction (Kokoo & Zimmerman , 2018).

2.2.5. Proposed three-step mechanism reaction

Kokoo and Zimmerman proposed the methanol present in the esterification as immediately reactive in order to make the water removal more effective. The reaction mechanism is set to be on the bubble interface, where the produced water can join the dry bubble and the methanol residue remains in the liquid domain as part of the FAME produced. In order to overcome the vaporisation of the methanol, this species forms the methoxy free radical whenever a methanol molecule reaches the surface of the bubble. This reaction is given by the equation below. (Kokoo & Zimmerman , 2018; Timberlake & Hodges, 1970).

$$O\cdot + MeOH \rightarrow MeO\cdot + HO\cdot \quad (7)$$

Microbubbles can potentially be injected with ozone in order to generate ozone-rich microbubbles. In fact, ozone is known to be a free radical initiator. It has been reported by Lozano-Parada and Zimmerman that it is possible to tune an in-situ ozone plasma microreactor to preferentially produce oxygen singlet radicals by adjusting the residence time and then injecting them directly into the bubble. At $1x10^{-2}$ s, the ozone production found its maximum and for the oxygen singlet the maximum yield was found at $1x10^{-3}$ s. This means a 10 times faster throughput can be produced by tuning the microreactor at the appropriate operating conditions (Lozano-Parada & Zimmerman, 2010; Zimmerman, 2011; Rehman, et al., 2016).

By feeding the free radicals generated in the plasma microreactor directly into microbubbles, one avoids the three “Ds” that would significantly slow ozone kinetics in water and wastewater. Firstly, dispersion is related to the fact that nearly half of the ozone produced does not mixt into the substrate liquid, so it must be destroyed. Secondly, dissolution refers to the solubility of ozone in water is very low and expected to be similar in methanol-FFA mixtures, which results in dissolution rates with a small driver resulting in an inherently slow reaction. Lastly, dissociation of ozone into hydroxyl radicals in water is also slow (Beltran, 2003).

Having said this, the use of microbubbles which are directly fed the oxygen singlet results in hydroxyl radicals which can then react with the methanol in the liquid mixture. This reaction is set to happen in the gas-liquid interface, the skin bubble. The thesis here presented models the effect of increasing the oxygen singlet concentration in order to speed up the overall reaction kinetics of the intensified esterification.

$$HO\cdot + HO\cdot \rightarrow H_2O + \frac{1}{2}O_2 \quad (8)$$

$$FFA + MeO\cdot \rightarrow FAME + HO\cdot \quad (9)$$

It has been reported that the oxygen radicals would form hydroxyl radical in the presence of water. In the presence of methanol, these radical species could potentially scavenge the labile hydrogen from the alcohol group and form the methoxy radical. Kokoo and Zimmerman proposed the ozone-rich bubbles injection into methanol-FFA mixtures without any catalyst present, suggesting the reaction is driven towards completion of esterification by the water removal mechanism previously described, but dramatically enhanced by the free radical chain reaction. The esterification reactions are known to be second order reversible reactions. (Kokoo & Zimmerman , 2018).

The reaction mechanism here proposed is then summarised in the overall reaction equation which is described below:

$$FFA + MeOH + O\cdot \leftrightarrow FAME + H_2O + \frac{1}{2}O_2 \quad (10)$$

The microbubbles generated with a fluidic oscillator have an initial concentration for the free radical $O\cdot$ of [$O\cdot$]= 4500 ppm which corresponds to the initial concentration of [$O\cdot$]= 281.25 mol/m^3 used in these models. The production rate of the biodiesel is then maximised by producing a high amount of $O\cdot$ using an advanced oxidation plasma reactor.

In the models here proposed the effect of important parameters such as bubble size, initial bubble temperature and the initial oxygen singlet concentration are studied on the production of FAME in the ozone free radical initiated esterification. These predictions are of high importance not only for the design of the system but also for the optimisation of the bioprocess operating parameters here described.

2.2.5.1. Free radicals in microbubbles

Mulakhudair et al reported the production of free radicals in aqueous solution for the decomposition of lignin in order to enhance the digestibility of lignocellulosic biomass. The degradation of polyvinyl alcohol by collapsing microbubbles has been reported as well, describing microbubbles as a strong degradation/oxidizing agent. Li et al reported a reduction in phenol of around 60% in 2 hours by the application of microbubble collapse to treat wastewater. In this case, the use of oxygen microbubbles resulted in the highest rate constant of 1.6 h^{-1} suggesting the hydroxyl radicals enhance the phenol decomposition process. Oxygen microbubbles decomposed more phenol when compared to the nitrogen microbubbles, suggesting the oxygen enhances the formation of hydroxyl radicals to then speed up the decomposition process. It has been reported that oxygen species like superoxide anion radical, hydroxyl and hydrogen peroxide radicals are generated during the reduction of molecular oxygen to water (Mulakhudair, et al., 2017; Li, et al., 2009).

Microbubble boundaries are known to be highly charged interfaces which could carry and release free radicals into the medium. When in contact with a liquid, they deposit and attack the surface causing degradation of the physical structure or potentially initiation chemical reactions. Ranger et al reported that hydroxyl radicals degraded lignin by removing the hydrogen atom from the methyl groups or a carbon in its structure. The degradation was influenced by the bubble and particle size, carrier gas and the surface charge magnitude. The radicals generated by collapsing microbubbles are mainly hydroxyl and superoxide radicals which are known to attack hydrogen bonds in biomass (Ragnar, et al., 1999; Mulakhudair, et al., 2017).

Chu et al reported that microbubbles have the potential to accelerate the production of hydroxyl radicals during the ozonation of simulated dyestuff wastewater. These results are of relevance concerning the treatment of hazardous wastewater since this type of radicals have a relatively higher standard redox potential of 2.8 V than oxidants lie hydrogen peroxide or ozone (1.77 and 2.07 V respectively). This suggests that direct oxidation is relatively slower than radical oxidation. The hydroxyl radicals showed an unselective and rapid reactivity with most of the organic compounds found in wastewater (Chu, et al., 2007).

Microbubbles with a high internal pressure could potentially induce the decomposition of ozone and therefore contribute to the generation of hydroxyl radicals. According to the Young-Laplace equation given by:

$$\Delta P = \frac{2\gamma}{r} \tag{11}$$

where ΔP is the pressure difference, r is the radius of the bubble and γ is the surface tension. This suggests that the internal pressure would be higher for bubbles with a smaller radius (Chu, et al., 2007).

Han et al reported the generation of free radicals by collapsing microbubbles using th Electron-Spin Resonance (ESR) spin-trap method. The presence of short-term free radicals was successfully monitored using 5,5-dimethyl-1-pyroroline-N-oxide (DMPO) as the spin-trap reagent, which is commonly used for the identification of oxygen-centered radicals like OH and superoxide. Takahashi et al reported the free radical generation during microbubble collapse and shrinkage without any dynamic stimulus. The reaction rate was increased when the reaction temperature was raised, hence accelerating the production of more radicals from microbubbles (Han , et al., 1998; Takahashi, et al., 2007).

2.2.6. Heat transfer and evaporation dynamics

The injection of hot bubbles in a cold liquid causes the energy to be transferred to the surrounding mixture either by means of latent heat of vaporisation or sensible heat transfer. The latent heat of vaporisation results in the evaporation of the liquid mixture from the surface to the interior of the bubble. Whereas, the sensible heat transfer causes an increase in the temperature of the liquid mixture. It has been reported by recent experiments that when decreasing the residence time of microbubbles in a liquid mixture, vaporisation dominates over heat transfer. At longer residence times, heat transfer dominates over vaporisation and the liquid evaporated in the first place is recondensed and returned to the liquid mixture from the inside of the bubble (Zimmerman, et al., 2013).

The recondensation process is connected to a release of sensible heat to the liquid mixture leading to an increase in temperature. In order to control these features, the residence time of bubbles is determined by the liquid bed height through which the microbubbles rise through. In the case of a thin liquid layer, vaporisation is favoured leading to maximum separation efficiency. On the other hand, if the bed height is increased then the sensible heat transfer becomes more relevant to the process and leads to a reduced vaporisation and increase of the liquid mixture (Abdulrazzaq, et al., 2015).

Abdurazzaq et al reported the effect of the depth of the liquid layer on the separation efficiency of azeotropic mixtures. Increasing the liquid depth resulted in an increase of the final concentration of ethanol in the liquid mixture, at 1cm almost no azeotropic separation occurred. This suggests the separation of the azeotrope is better at lower bed heights and it can be attributed to the residence time of the microbubbles in the liquid. At longer residence times, the microbubbles start cooling down and as they rise recondensation of the vapours takes place leading to the transport of these species back to the liquid mixture. On the other hand, at lower residence times, this behaviour can be prevented, and vaporisation favoured (Abdulrazzaq, et al., 2016).

The molecules in the liquid mixture need to have enough kinetic energy to escape from the liquid to the gaseous phase. The kinetic energy varies directly with temperature, this means that vaporisation should happen more rapidly at higher liquid temperatures. An increase in the injected microbubbles

temperature would increase the energy carried by the gas phase resulting in an increase of the liquid temperature since more sensible heat is transferred. It is important to point out that higher liquid temperatures would increase the kinetic energy of the molecules contained in the mixture, this would lead to an increase in the vaporised liquid to the inside of the bubble (Abdulrazzaq, et al., 2015).

The effects of microbubbles for physico-chemical processes have remained unstudied, phenomena such as evaporation and heat transfer on the microbubble interface have significant relevance when working at the microscale. In this research project using computational modelling supported by experimental evidence, both evaporation and heat transfer on the microbubble interface are explored. These two processes are thought to be inherently transient, when dealing with short residence time vaporisation tends to be favoured, whilst at longer residence times sensible heat transfer is considered to mainly dominate resulting in re-condensation of the vaporised liquid. The main purpose is to address how thin a layer thickness (expected to be a few hundred microns) will give the maximum absolute vaporisation, after which the vapour is condensed by sensible heat as the bubble cools. When reaching the maximum vaporisation in conjunction with the appropriate contact time, a vaporising system with minimum heat transfer which removes the maximum of vapour is achieved. Between sensible heat transfer of the liquid element and vaporisation on the skin of the microbubble, vaporisation governs in right in the beginning. Then the liquid reaches its equilibrium concentration of vapour on the surface layer. When working with microbubbles, the internal mixing is essential and in very short time, on the order of 10-3s, the maximum absolute humidity is achieved (Zimmerman, et al., 2013).

Greater heat transfer rates are expected when using greater surface area per unit volumes. Having said this, less vaporisation would occur with microbubbles due to less heat available for the latent heat of vaporisation to be paid. Energy is split between latent heat of vaporisation and heat transfer to the liquid when microbubbles are introduced with turbulent flow. Introducing microbubbles with a fluidic oscillator gently introduces bubbles into the liquid using so much less energy density considering a laminar flow around the bubbles. In 2012, Hanotu et al reported energy densities 1000-fold smaller than those for conventional microbubble generation when using fluidic oscillator driven microbubbles. In this process, vaporisation is much faster in the beginning but with a slow heat transfer. By controlling the contact time of the microbubbles is possible to achieve a more effective vaporisation without sensible heat transfer to the liquid. Some of the results of the experiments carried out by Hanotu et al are: vapour temperature reduction with contact time increase, higher liquid temperature with contact time increase, and absolute humidity decrease with contact time increase. Microbubble evaporation has potential applications like chemical synthesis with reactive extraction, such as condensation reactions e.g. esterification (Zimmerman, et al., 2013; Hanotu, et al., 2012).

In order to achieve more vaporisation, a different approach could be used in order to conduct the process far from equilibrium. It is possible to raise the gas temperature very high with the same amount of heat energy since both the density and calorific value for water are 3 orders of magnitude larger than that for the gas phase. Zimmerman et al reported the use of a uniform cloud of microbubbles which were described as non-convergent (monodisperse). This approach is believed to increase the interfacial area which can potentially speed up both evaporation rates and sensible heat transfer since the typical model for rate laws are proportional to the gas-liquid surface area. Preliminary experiments have reported that the absolute level of humidification can be a controlled parameter and varies significantly with the bed height of the liquid that the microbubble rises through. One would think that the greater the residence time, the greater the vaporisation achieved. (Zimmerman, et al., 2008; Zimmerman, et al., 2011; Zimmerman, et al., 2009)

There are two recent studies were coarse bubbles were used for the humidification-dehumification process by bubbles. Narayan et al reported the potential of this process (solar-driven) desalination and modelled a bubble column for the condensation at high concentrations of non-condensable gas using bubbles greater than 3 mm with heat transfer coefficients estimated by correlation (Narayan, et al., 2013).

Zimmerman et al reported that because of the greater surface are per unit volume of microbubbles, a greater heat transfer rate is expected. When microbubbles are introduced under a turbulent flow, the energy is then diverted into the latent heat of vaporisation and the heat transfer to the liquid. The microbubbles are introduced gently using a fluidic oscillator into the liquid resulting in a reduction of the energy density when compare to conventional microbubbles. This is could be attributed to the fact that energy densities are 1000-fold smaller than the nozzle exit regime for conventional microbubble generation. Having said this, it is known that heat transfer is slow, but vaporisation is much faster in the beginning. This suggests that one can preferentially achieve a more effective vaporisation avoiding sensible heat transfer to the liquid by controlling the contact time (Zimmerman, et al., 2013)

Experiments have been conducted using a bubble column and injecting hot and dry air in four different liquids (tap water, methanol-water and ethanol-water binary mixtures, and food particles in aqueous solution). The microbubbles were generated using a fluidic oscillator and the major features obtained were: a higher liquid temperature and an absolute humidity decrease with residence time increase, a vapour temperature reduction was observed as well with a residence time increase. A 100% humidity was always achieved and up to a 95% selectivity for vaporisation over sensible heat transfer when the bed height of the liquid was tuned. Lowering the liquid bed height from 5 cm to 2cm and then 1cm resulted in an increase of the absolute humidity and outlet gas temperature. This means that in the competition between sensible heat transfer and vaporisation, vaporisation is favoured

immediately. In other words, the liquid would flash to its equilibrium concentration of vapour on the surface layer. When using finer bubbles (coarse), this rapid flash has no significant importance since the internal mixing of the bubble is too slow to make the most of the preferential vaporisation. When using finer bubbles, the effect is considerable since the internal mixing is stronger. The maximum absolute humidity is achieved in a very short residence time in the order of 10^{-3} s, this means a several bubble lengths (few hundred microns) for the residence time to be achieved. This is the main driver to introduce a microbubble internal mixing that occurs on a time scale of 10^{-3} s, so the condensing vapour or evaporating mixture should obey a rate law that evolves on this rapid time scale (Zimmerman, et al., 2013).

In the models here proposed the effect of important parameters such as bubble size, initial bubble temperature and the initial oxygen singlet concentration are studied on the production of FAME in the ozone free radical initiated esterification. These predictions are of high importance not only for the design of the system but also for the optimisation of the bioprocess operating parameters here described.

2.3.Conclusions

The esterification of FFA seen as a pre-treatment stage could represent an improvement for the downstream processing if the produced water were removed before the subsequent step, the transesterification. Introducing dry microbubbles would favour the stripping of water from the reacting mixture. In theory, the proposed reactive distillation can potentially achieve completion according to LeChatelier's principle for an equilibrium reaction. Removing the produced water by means of vaporisation would drive the esterification reaction to completion, as a new molecule of water would need to be produced in order to replace the one previously removed.

Methanol is known to be more volatile than ethanol, this is why it would be expected to vaporise and then occupy the vapour phase in the bubble domain in the esterification reacting mixture. Suggesting that both water and methanol would be removed from the mixture, but preferentially methanol. Excess methanol is needed to push the equilibrium favouring the forward reaction (esterification) whereas water removal would pull it, injecting hot microbubbles would pull the equilibrium but weaken the push. Methanol present in the esterification as immediately reactive in order to make the water removal more effective. The reaction mechanism is set to be on the bubble interface, where the produced water can join the dry bubble and the methanol residue remains in the liquid domain as part of the FAME produced. In order to overcome the vaporisation of the methanol, this species forms the methoxy free radical whenever a methanol molecule reaches the surface of the bubble.

Microbubbles can potentially be injected with ozone in order to generate ozone-rich microbubbles. In fact, ozone is known to be a free radical initiator. It has been reported by Lozano-Parada and Zimmerman that it is possible to tune an in-situ ozone plasma microreactor to preferentially produce oxygen singlet radicals by adjusting the residence time and then injecting them directly into the bubble. At $1x10^{-2}$ s, the ozone production found its maximum and for the oxygen singlet the maximum yield was found at $1x10^{-3}$ s. This means a 10x throughput can be produced by tuning the microreactor at the appropriate operating conditions.

It has been reported that the oxygen radicals would form hydroxyl radical in the presence of water. In the presence of methanol, these radical species could potentially scavenge the labile hydrogen from the alcohol group and form the methoxy radical. This suggests the reaction is driven towards completion of esterification by the water removal mechanism previously described, but dramatically enhanced by the free radical chain reaction. Having outlined the main features of the literature review in terms of the esterification reaction, in the next chapter the methodology followed to build the proposed models for this reaction is shown. It is important to consider the thought process between understanding the theoretical frame in order to be implemented and applied to the computational models.

3. Methodology

This chapter is comprised mainly of the experimental data and the procedure followed to be able to build the proposed models found in the following chapters. Some of the main aspects studied in this chapter are the acid number and FAME calculations and the model description for the 2-D axisymmetric models presented in chapters 7 and 8. It is important to point out that in this chapter the raw data is processed in order to be used in the computational models which are aimed to describe both the physics and the reaction kinetics in terms of the ozone free radical initiated esterification here studied. Some of the assumptions and theories stated in the literature review are here used to ease calculations. There is no ultimate answer for this process, but the assumptions and theory formulated in the previous chapter is helpful to propose a reaction mechanism based and informed on experimental data, which is then validated by fitting the experimental data and the computational model.

3.1. Experimental data used

The methodology to generate microbubbles for the esterification unit has been reported by Kokoo et al using two different techniques (with and without a fluidic oscillator). When the fluidic oscillator was used, a dry air flow of 60 L/min at 20°C and 15 psi was fed into the fluidic oscillator designed by Zimmerman et al which has been previously described in Chapter 2. One of the main features of this fluidic oscillator is that it generates a pulse-jet stream. The dry air is purged so only 0.1 L/min is fed into a plasma ozone generator (OZ500, Dryden Acqua). These operating conditions apply for both techniques (Kokoo & Zimmerman , 2018; Zimmerman, et al., 2009).

The resulting gas mixture from the ozone generator had a concentration of 1500 ppm, this mixture is then fed into the glass bubble reactor. The reactor has a diameter of 7.5×10^{-2} m and is filled with a total liquid mixture of 0.325 L for each run. The initial concentration of ozone was measured using the iodometric method. The glass reactor is comprised of a thermocouple, a sampling tube and a diffuser made of borosilicate glass 3.3 with a radius of 1.1 cm (ROBU Glasfilter-Gerate GmbH). A heating mantle was used to control the liquid mixture temperature at each run.

In order to recover the vapour products, a glass condenser was used with a surface area of around 200 cm^2, water at room temperature was used as the cooling medium. The schematic diagram for the esterification unit used in Chapter 7 is shown in Figure 11. It is important to mention that all the connections and tubing used in this experiment were PTFE, stainless steel or glass in order to guarantee the resistance to ozone. The experiments were carried out at atmospheric pressure and a reaction temperature of 20, 40 and 60°C, and the samples for further analysis were collected every 4 hours for 36 h and kept in a 4°C refrigerator.

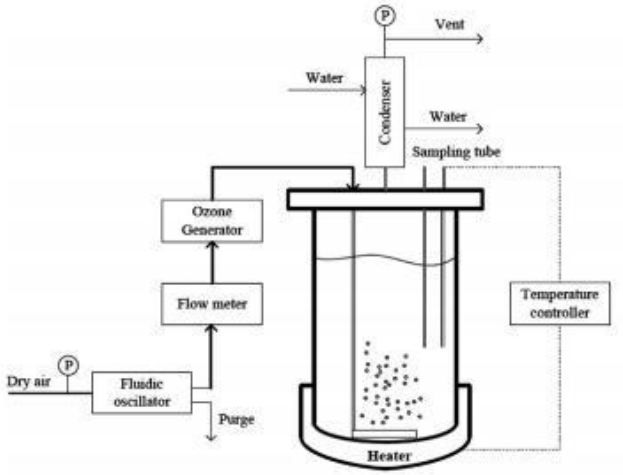

Figure 11 Schematic diagram for the esterification unit (Kokoo & Zimmerman , 2018).

It can be noticed from the time scale of the experimental data, that the ozonolysis reaction of the used cooking oil is slow. This behaviour can be attributed to the use of "off the shelf" ozone generator instead of a plasma microreactor that feeds into microbubbles. The process was not yet optimised, since the sparger for microbubbles by fluidic oscillation was not adequately designed to fit the purpose. Having said this, the major role of the modelling here presented is to explore the parameters previously mentioned without building the reactor by validating the model with actual experiments.

3.2.Acid number and Free Fatty Acid calculation

In order to quantify the Free Fatty Acid (FFA) content in the samples and analyse the results, endpoint data was gathered from Dr Kokoo doctoral thesis "*Upgrading of oleic acid, olive oil, and used cooking oil via bubbling ozonolysis*". The standard test method for Acid and Base number by colour-indicator titration (ASTM D974) was used to determine the acid number of the samples comprised of Used Cooking Oil (UCO) and methanol after ozonolysis. The analysis of the Acid number is important since it can be associated with the FFA percentage in samples and therefore used to calculate the Fatty Acid Methyl Ester (FAME) concentration. T

ASTM D974 method is usually used to determine the acidic of basic constituents in lubricants soluble in mixtures of toluene and isopropyl, and petroleum products. It is able to determine acids or bases whose dissociation constants in water are larger than 10^{-9}, weak acids or bases with a lower dissociation constant do not interfere. Organic and inorganic acids, resins, lactones and salts of heavy metals are considered to have acidic characteristic, which can be successfully measured in both new and used oils following the ASTM D974 method.

Reagent preparation

1. Titration solvent: It is prepared by mixing toluene, water and anhydrous isopropyl alcohol following a volumetric ratio of 100:1:99.
2. Naphtolbenzein indicator: It is a solution of naphtolbenzein in titration solvent with a concentration of 10$\pm$0.01 g/L.
3. Potassium hydroxide solution, Standard alcoholic (0.1 M): It is prepared by adding 6 g of solid KOH in 1 L of anhydrous isopropyl alcohol. The mixture is then boiled for 10-15 minutes and stirred to avoid a solid conglomeration at the bottom. Then, 2 g of barium hydroxide are added, and the mixture again boiled for 5-10 minutes. The solution is filtered through a sintered-glass and stored in a chemically resistant bottle.

Method

1. Used cooking oil (0.2-2 g) is added to 0.1 L of the titration solvent and 0.5 mL of the indicator solution. The mixture is properly stirred until solutes are dissolved, the solution should give an orange-yellow colour because of the acid content.
2. The mixture is immediately titrated using the KOH solution, the process reaches an end when the mixture changes to a green colour.
3. A blank titration is performed using 100 mL of the titration solvent and 0.5 mL of the indicator solution, and then titrated using the KOH solution.

Acid number and FFA calculation

The acid number in the samples after ozonolysis is calculated using the equation below, stated in the ASTM D974:

$$AN, mg\ of\ KOH/g = \frac{(A-B)\cdot M \times 56.1}{W} \tag{12}$$

where A is the KOH solution used for the titration of the sample (mL), B is the KOH solution used for the titration of the blank (mL), M is the molarity of the KOH solution, and W is the sample used (g).

The acid number calculation can be associated to the FFA percentage in a sample defined by:

$$\frac{FFA\%}{28.2} = \frac{(A-B)\cdot M}{W} = \frac{AN}{56.1} \tag{13}$$

The Free Fatty Acid (FFA) result from the breakdown of biodiesel or oil. The Acid Number (AN) is usually used to describe the FFA content of finished biodiesel, while the FFA% is commonly used to describe the FFA content of oils and corresponds to the weight to weight ratio of FFA in the oil sample. From the equation above, the relationship between the AN and FFA% can be deducted by solving both equations for common values giving:

$$AN = 1.99 \times FFA\% \quad (14)$$

The Acid Number values for the 10% FFA are shown in Figure 12 for the three different temperatures (20, 40 and 60°C) which the experiments were carried out. The initial acid number value for the 10% FFA samples was 21.11 mg of KOH/g. When comparing the values obtained for the different treatments, the lowest value is observed at a higher temperature. For example, after 12 hours of ozonolysis the acid number values at 20, 40 and 60°C were 18.70, 18.01 and 17.3 mg of KOH/g respectively. The acid number values after 24 hours for the samples at 20, 40 and 60°C were 16.95, 16.46 and 16.17 mg of KOH/g in that order. The final value for the acid number after 36 hours show a value of 16.28, 16.05 and 15.79 mg of KOH/g for the samples at 20, 40 and 60°C. The difference between the highest (60°C) and lowest temperature (20°C) in terms of acid number is notoriously higher in the first 12 hours of the process than after 36 hours. After 36 hours the 60°C treatment showed the biggest decrease (25.2%) regarding the acid number. This suggests a rapid conversion of the FFA into FAME in a short period of time. After 32 hours of the process, the acid number seems to have reached a plateau suggesting a steady state has been achieved even across the different temperature treatments.

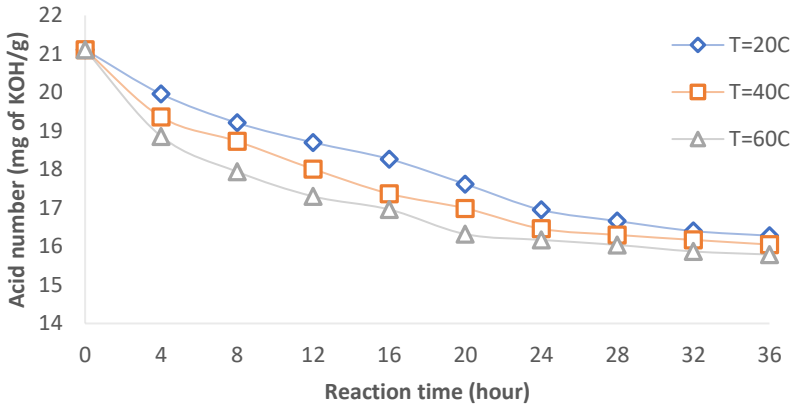

Figure 12 Ozonolysis of used cooking oil at 10% FFA (Kokoo & Zimmerman , 2018).

Figure 13 contains the acid number values for the 15% FFA. The initial acid number value for the 15% FFA samples was 31.13 mg of KOH/g. At 15% FFA the trend that at a higher temperature the acid number is lower still applied. After 12 hours of ozonolysis the acid number values at 20, 40 and 60°C were 28.99, 27.92 and 26.94 mg of KOH/g respectively. The acid number values after 24 hours for the samples at 20, 40 and 60°C were 27.47, 26.65 and 25.53 mg of KOH/g in that order. The final value for the acid number after 36 hours was 26.8, 25.48 and 24.61 mg of KOH/g for the samples at 20, 40 and 60°C. The difference between the highest (60°C) and lowest temperature (20°C) in terms of acid number does not seem to change dramatically during the process for the 15% FFA. After 28 hours of the process, the acid number seems to have reached a plateau suggesting a steady state has been achieved even across the different temperature treatments. After 36 hours the 60°C treatment showed the biggest decrease (20.94%) regarding the acid number.

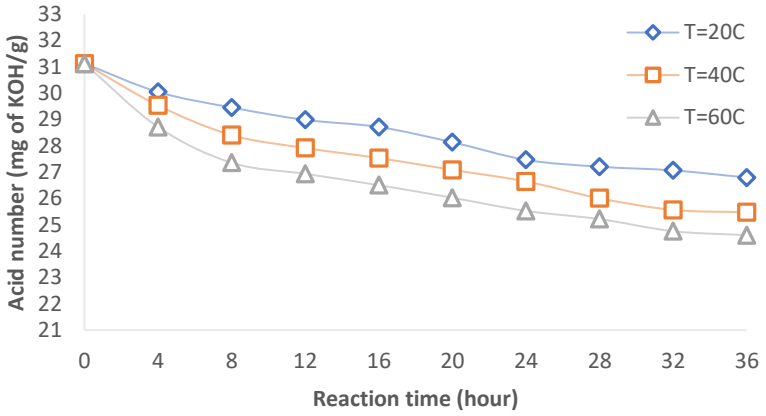

Figure 13 Ozonolysis of used cooking oil at 15% FFA (Kokoo & Zimmerman , 2018).

Lastly, Figure 14 shows the trend for the acid number values for the 20% FFA. The initial acid number value for the 20% FFA samples was 43.63 mg of KOH/g. After 12 hours of ozonolysis the acid number values at 20, 40 and 60°C were 35.58, 33.45 and 30.34 mg of KOH/g respectively. The acid number values after 24 hours for the samples at 20, 40 and 60°C were 33.31, 29.88 and 28.57 mg of KOH/g in that order. The final value for the acid number after 36 hours was 31.07, 29.18 and 28.69 mg of KOH/g for the samples at 20, 40 and 60°C. The difference between the highest (60°C) and lowest temperature (20°C) in terms of acid number is notoriously higher in the first 12 hours of the process than after 36 hours.

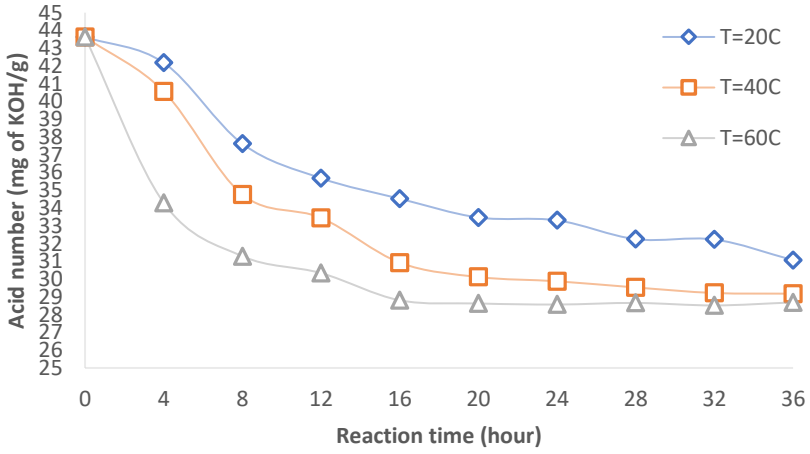

Figure 14 Ozonolysis of used cooking oil 20% FFA (Kokoo & Zimmerman , 2018).

After 20 hours of the process, the acid number seems to have reached a plateau for the curve at 60°C suggesting a steady state has been achieved and it was this treatment the one showing the biggest decrease (34.24%) regarding the acid number. Once the values for the acid number are obtained, the FAME production can be calculated using these graphs. Knowing the acid number for each treatment at a certain, it is possible to correlate this value to the FFA%. The liquid mixture has an equimolar condition for methanol and FFA, this means a ratio of 1:1 methanol to FFA. The molar concentration is then calculated using the molecular weight of the species and the volume of the liquid mixture. In

Table 9, the results from the calculations followed for the FFA content of 20% at 60°C are presented. The rest of the results obtained for these calculations are shown in Appendix A.

Table 9 Values for the content and concentration at FFA 20% at 60°C.

Time (h)	Acid number (mg of KOH/g)	FFA %	FFA (mol) x10^{-2}	[FFA] (mol/m^3)	FAME (mol) x10^{-2}	[FAME] (mol/m^3)
0	43.63	21.924	10.743	330.555	0	0
4	34.3	17.236	8.445	259.868	2.297	70.687
8	31.29	15.723	7.704	237.063	3.038	93.492
12	30.34	15.246	7.470	229.866	3.272	100.689
16	28.81	14.477	7.093	218.274	3.649	112.281
20	28.63	14.386	7.049	216.910	3.693	113.645
24	28.57	14.356	7.034	216.456	3.708	114.099
28	28.66	14.402	7.056	217.137	3.686	113.417
32	28.52	14.331	7.022	216.077	3.720	114.478
36	28.69	14.417	7.064	217.365	3.678	113.190

Once the molar concentration for the product of interest calculated, this could be used to generate a plot for the fame production over time. For the models presented in Chapter 5 and 6, a concentration profile over time like the one shown in Figure 15. This accounts for the average concentration found in the reactor, and the molar concentration was used in order to ease calculations with the software used.

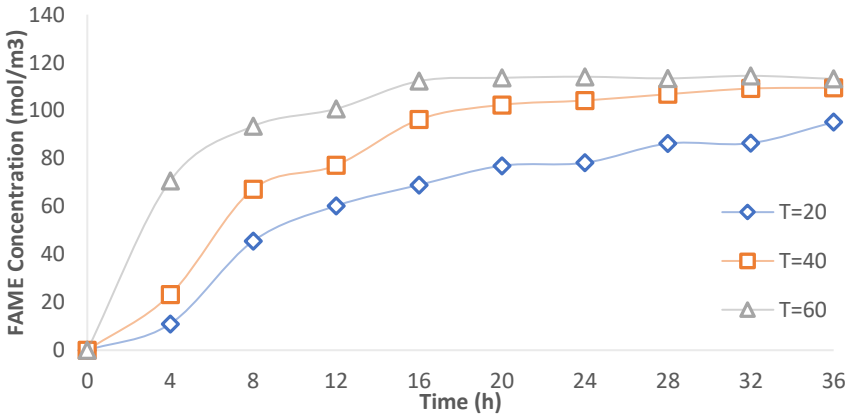

Figure 15 FAME concentration profile at 20% FFA and 60°C.

For chapters 7, the FAME production was fitted using the amount of FAME produced in moles over time shown in Figure 16. This accounts for the single bubble approach used to correlate the experimental data and computational model. The computational model was fitted using the formula below:

$$T = \bar{F} \cdot \dot{B} \cdot \tau \qquad (15)$$

where T is the amount of FAME produced at certain time step defined by the user, $\bar{F}$ is the amount of FAME produced per bubble rising through the liquid (mol), $\dot{B}$ is the bubble flux defined in the system (bubbles/s) and τ is the time step defined by the user. As a first guess and considering the experimental data gathered, the time step used was 4 hours. The gradient for both FFA and FAME is then obtained after the time step. It is important to mention that the production of FAME in the time step is assumed to be linear described by a straight line. Once the gradient is defined, the amount of FFA and FAME found in the time step is then fed into the code to be used as initial conditions for the next iterations, and this loop is repeated until the final measurement is reached. By changing the initial conditions every time step, the curve starts showing a curvature related to the consumption and production of FFA and FAME respectively. Once the computational model is run for the whole duration of the experiment, the predicted FAME production (y^p) is a function of time (t) and the forward (k_f) and reverse (k_r) rate constants, defined by:

$$y^p = F(t_i; k_f, k_r) \tag{16}$$

Having built the function for FAME production over time, it is possible to interpolate smaller time steps in order to obtain a better fitting of the model if not satisfied with the time step resolution. The time step that satisfied this condition for the proposed model in Chapter 7 was 20 minutes.

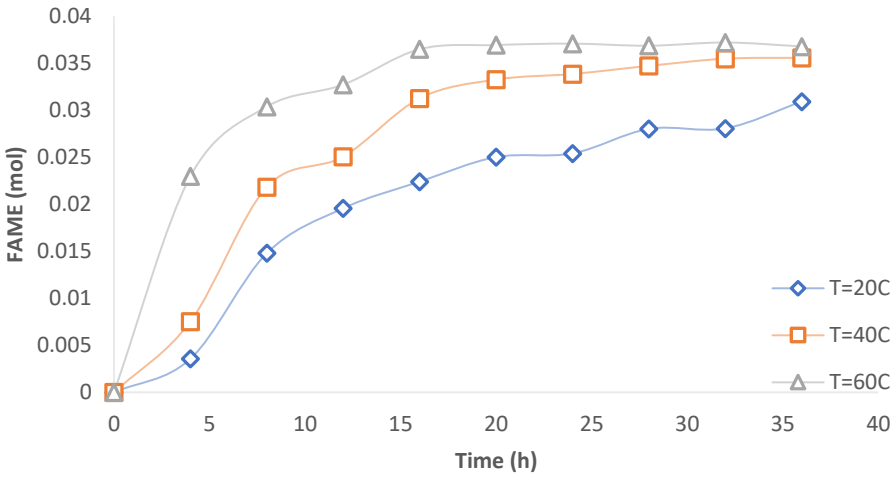

Figure 16 Number of moles of FAME over time at 20% FFA and 60°C.

From the figures previously shown, it can be concluded that the acid number decrease is directly related to the reaction temperature. The lowest value for the acid number is observed at the highest reacting temperature of 60°C, while the acid number is relatively higher compared to lower reacting temperatures of 20-40°C. Over the first 12 h, the acid number suffers a decrease across the different treatments. The acid number trend followed at 10 and 15% FFA content is relatively similar, compared

to the more pronounced curvature observed at 20% FFA content. The reduction of FFAs is due to the esterification of both saturated and unsaturated FFAs, which is exploited in this thesis in order to propose a reaction mechanism to describe the behaviour here observed. The ozone free radical initiated esterification could potentially describe this trend and be applied as an alternative for biodiesel production as a pre-treatment stage before the transesterification.

3.3.Computational model

In this thesis four computational models are presented, all of these models were built using COMSOL Multiphysics software. The first two models account for the irreversible and reversible reaction mechanism modelled using a 0-D approach. These two models only consider and analyse the reaction kinetics of the set of reactions proposed for the intensified esterification. The description for both models can be found at the beginning of Chapter 5 and 6 respectively. On the other hand, the other two models use a 2-D axisymmetric approach which includes the heat and mass transfer, surface reactions, transport of diluted species and reaction engineering modules available in the software previously mentioned. When comparing the 0-D and 2-D axisymmetric inferred rate constants, it is important to stress that the 2-D axisymmetric model is for interfacial interaction only. The 0-D model presumes homogeneous reaction and the 2-D model is heterogeneous. Inherently, this distinction is a massively different mechanistic approach. Conceptually, the 2-D model can make predictions that are testable to distinguish between heterogeneous and homogeneous catalysis. For instance, the layer depth is extremely important to avoid re-condensation in the 2-D model, whereas the 0-D model has no such mechanism so would be monotonically varying with layer depth. In the next section, the model description for the 2-D axisymmetric model backbone used in Chapter 7 and 8 is described.

3.3.1. 2-D axisymmetric model description

A 2-D axisymmetric computational model of a dry-to-bone air and ozone microbubble is developed using COMSOL Multiphysics. The system to be investigated is comprised of a dispersed phase being the single fluidic oscillator air microbubble with a diameter of 200 μm rising in an infinite reservoir of methanol-oil mixture due to a buoyancy force. A simulation study is carried out for the system previously described using a time dependent model for the concentration and temperature profile inside the microbubble, considering circulation patterns inside and around the bubble correlated to the bubble motion. According to the operating conditions set in Chapter 3, the liquid bed height is 8.44 cm which corresponds to a residence time of 19.26 s for the microbubble to rise through the liquid mixture. The model here described is based on the operating conditions defined in the experimental set up, this is in order to validate the model with the data gathered.

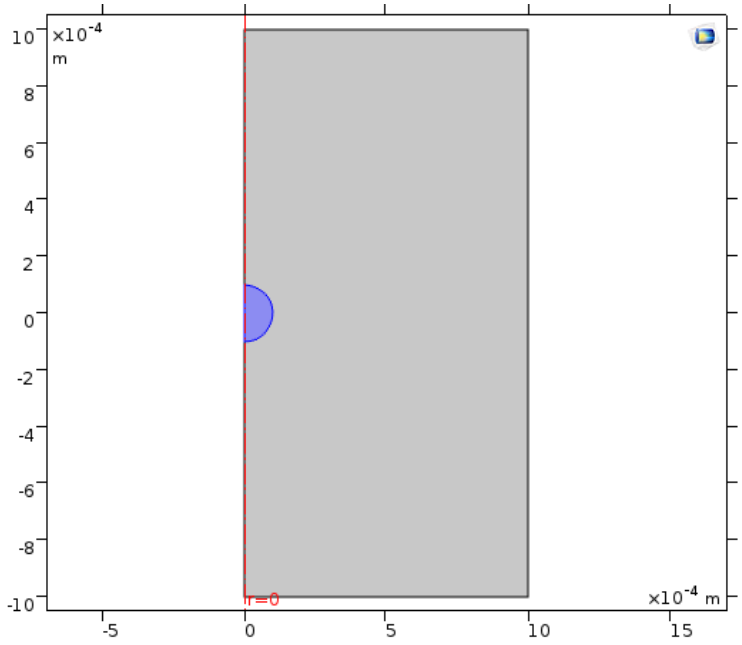

Figure 17 Single microbubble in infinite reservoir for biodiesel production.

Figure 17 shows a 2-D axisymmetric view of the single microbubble model. As mentioned before the bubble has a radius of 100 μm and its shown as the blue domain in the middle of the image. The infinite reservoir has sides ten times bigger than the radius $1x10^{-3}$ m and is shown in the image as the grey domain. The values and formulas used in this model for the thermal conductivity, the heat capacity at constant pressure and density are found Table 10 and Table 11. These tables are comprised of the physico-chemical properties and parameters used in the computational model, some of which are temperature dependent and either the value or equation for the regression is shown.

Table 10 Properties and parameters relevant to the computational model.

Parameter	Name	Value
Initial bulk liquid temperature (K)	T0_liq	293.15-333.15
Bubble initial temperature (K)	T0_bub	293.15
Reaction 3 rate constant forward ($m^3/(s{\cdot}mol)$)	kf3	--
Reaction 3 rate constant reverse ($m^3/(s{\cdot}mol)$)	kr3	--
Heat transfer coefficient ($W/m^2{\cdot}K$)	htc	0.1
Mass transfer coefficient (m/s) $x10^{-5}$	KL	2
Henry coefficient $x10^{-2}$	Henry	3.18

In Table 11 a list of the different variables used in this computational model is shown in order to model the different physical and chemical processes happening in the microbubble and its surroundings.

Table 11 Variables used in the model.

Variable	Name	Expression
Radial bubble velocity	ur_bub	(Ut*r*z)/Rad^2
Axial bubble velocity	uz_bub	Ut*(1-z^2/Rad^2-2*r^2/Rad^2)
Radial bulk liquid velocity	ur_liq	(-1/r)*(-0.75*r^2*Rad*Ut*z*(r^2-Rad^2+z^2))/(r^2+z^2)^2.5
Axial bulk liquid velocity	uz_liq	0.25*Ut*(6*Rad/(r^2+z^2)^0.5-4-(2*Rad^3)/(r^2+z^2)^1.5-3*(Rad*r^2)*(r^2-Rad^2+z^2)/(r^2+z^2)^2.5)
Surface area	A	4*pi*Rad^2
Water vapour pressure	pstarwat	10^(8.07131-1730.63/(233.426-273.15+T[1/K]))[Pa]
Air heat capacity	cp_air	(1075.5-0.5505*T[1/K]+0.0013*T^2[1/K^2]-0.0000007*T^3[1/K^3])[J/kg/K]
Water saturation concentration	csatwater	pstarwat*x2/(T*R)
Water heat vaporisation	Hwat	(46238+19.796*T[1/K]-0.0926*T^2[1/K^2])[J/mol]
Bubble thermal conductivity	thermcond_bub	(0.0239+0.00007*T[1/K])[W/m/K]
Water heat capacity	Cp_water	(1*10^-07)*T^3-0.0001*T^2+0.0375*T-2.0304
Oil heat capacity	Cpoil	(1868.8-1.5794*T[1/K]+0.0037*T^2[1/K^2])[J/kg/K]
Total pressure (Pa) $x10^5$	pA	1.0133
Universal gas constant (J/(mol·K))	R	8.314
Gravity (m/s^2)	g	9.806
Bubble radius (m) $x10^{-4}$	Rad	1
Bulk liquid density (kg/m^3)	Rho_liq	916
Bulk liquid dynamic viscosity (Pa·s)	mu_liq	0.1075
Air density (kg/m^3)	Rho_bub	1.225
Terminal velocity (m/s)	Ut	(g*Rad^2*(Rho_liq-Rho_bub)/mu_liq/3)

3.3.1.1. Governing equations

In this system both mass and heat transfer take place at the same time leading to vaporisation and heating of the water present in the liquid phase. Having said this, the simultaneous solution of the mass and energy transfer governing equations inside the microbubble are a key element to obtain the concentration and temperature profiles. The vaporisation of the water and its removal are taking place at the same time as the free radical initiated esterification. Taking in consideration the simplifications mentioned, the equations for mass and heat transfer are considered the main governing equations in the model and are shown below:

$$\frac{\delta T}{\delta t} + u \cdot \nabla T = \alpha \nabla^2 T \tag{17}$$

$$\frac{\delta c_i}{\delta t} + u \cdot \nabla c_i = D \nabla^2 c_i \tag{18}$$

In the case of the heat transfer equation *T* is the temperature of the bubble field, u is the velocity inside the bubble and α is the thermal diffusivity of the air. Concerning the mass transfer equation $c_i$is the molar concentration of species *I*, and *D* is the molecular diffusivity. Gas molecular diffusivities and gas density are considered constant dependent. The gas properties such as heat capacity, thermal diffusivity and thermal conductivity are considered temperature dependent and each value is calculated using polynomial empirical correlations.

To calculate the internal velocity field of the bubble in this model, an equation adopted for small spherical bubbles rising under buoyancy force is used. Hadamard and Rybcynski's equation is the solution of the Navier-Stokes equation calculated by Hill's spherical vortex and the stream function is shown below, including the dimensionless radial (r) and axial (z) velocity components derived from it (Abdulrazzaq, et al., 2016; Zimmerman, et al., 2013).

$$\Psi = \frac{1}{2} U_t R^2 \left(\frac{r}{R}\right)^2 \left[1 - \left(\frac{z}{R}\right)^2 - \left(\frac{r}{R}\right)^2\right] \tag{19}$$

$$u_r = -\frac{1}{r}\frac{\delta \Psi}{\delta z} \tag{20}$$

$$u_z = \frac{1}{r}\frac{\delta \Psi}{\delta r} \tag{21}$$

Both dimensionless velocity components and the terminal velocity are computed to be:

$$u_r = U_t \frac{r}{R}\frac{z}{R} \tag{22}$$

$$u_z = U_t \left(1 - \left(\frac{z}{R}\right)^2 - 2\left(\frac{r}{R}\right)^2\right) \tag{23}$$

$$U_t = \frac{1}{3}\frac{gR^2}{\mu}\Delta\rho \tag{24}$$

where *R* is the radius of the bubble, u_r and u_z are the velocity vectors in radial and axial coordinates respectively, U_t is the terminal velocity of a bubble rising, *g* is the gravitational acceleration, μ is the viscosity of the liquid phase and $\Delta\rho$ is the density difference.

On the other hand, the velocity field outside the bubble is calculated using the dimensionless Stokes stream function equation assuming a uniform far-field flow.

$$\Psi = -\frac{1}{2} U_t r^2 \left[1 - \frac{3}{2}\frac{R}{\sqrt{r^2 + z^2}} + \frac{1}{2}\left(\frac{R}{\sqrt{r^2 + z^2}}\right)^3\right] \tag{25}$$

The radial and axial velocity components are calculated the same way as for the internal velocity field, both dimensionless velocity components and the terminal velocity outside the bubble are computed to be

$$u_r = \frac{3}{4} r R U_t z \frac{(r^2 - R^2 + z^2)}{(r^2 + z^2)^{\frac{5}{2}}} \tag{26}$$

$$u_z = \frac{1}{4} U_t \left(\frac{6R}{(r^2 + z^2)^{\frac{1}{2}}} - 4 - \frac{2R^3}{(r^2 + z^2)^{\frac{3}{2}}} - 3r^2 R \frac{(r^2 - R^2 + z^2)}{(r^2 + z^2)^{\frac{5}{2}}} \right) \tag{27}$$

This approach assumes all the bubbles are small enough that the surface tension would oppose deformation from the spherical shape, and the time for the bubble to encounter laminar flow is infinitesimally short after it has been injected and released into the liquid mixture. Having said this, the fluid dynamics can be studied analytically so the main focus is on the mass and heat transfer dynamics (Zimmerman, et al., 2013).

3.3.1.2. Initial and boundary conditions

The microbubbles used in the computational model are injected at an initial temperature T_0, it is important to mention that the initial concentration for water inside the bubble is zero. For the methanol-oil (liquid domain) the initial temperature varies between 293, 313 and 333 K for the calculations. Boundary conditions are set for both mass and heat transfer. In this computational domain, the side walls are set to a temperature matching the temperature of the liquid depending on the experiment (293, 313 and 333 K). In the case of this system, the Langmuir law for evaporation can be used to calculate the mass flux for the different species at the interface since the system is working far from equilibrium conditions (Abdulrazzaq, et al., 2016).

$$\dot{n}_i = k_i A (x_i \gamma_i P_i^* - P_i) \tag{28}$$

where $\dot{n}_i$ represents the evaporation rate for each species found at the interface, k_i is the evaporation constant describing the amount of component evaporated per unit time per unit pressure per unit area, *A* is the liquid-gas contact area, x_i is the mole fraction, γ_i is the activity coefficient, P_i^* is the saturation vapour pressure at the liquid-gas interface, and P_i is the partial pressure of the vapour inside the bubble for each species. This simplified equation states that at equilibrium conditions the activity coefficient $\dot{n}_i = 0$, evaporation or condensation is purely driven by the difference of the interfacial partial pressure and the predicted Raoult's Law (Zimmerman, et al., 2013).

For the gas-liquid interfacial dynamics, a common assumption is that the interface flashes to equilibrium. In the case of air in contact with water, this is equal to fixing the partial pressure of water to the saturation pressure found at the interface temperature. In order to convert the partial pressure

of water into its molar concentration, the ideal gas law can be used (Zimmerman, et al., 2013; Maccines, et al., 2012).

The ideal gas law is used to calculate the partial pressure of the vapour species in the bubble, since the operating conditions taken into account being high temperature and low pressure, resulting in the equation below:

$$C^* = \frac{P^* x_i}{RT} \tag{29}$$

According to Himus and Hinchley, the evaporation parameter for pure water evaporated using air has a value around $2x10^{-5}$ m/s, used in the calculations for this model. The boundary condition for the heat transfer in this computational model is given by Fourier's Law where the normal heat flux at the interface is equal to the evaporation rate $\dot{n}_i$ weighted by the latent heat of vaporisation H_{vi} for each one of the species. In the equation below $\hat{n}$ is the normal vector, *K* is the thermal conductivity (Abdulrazzaq, et al., 2016; Himus & Hinchley, 1924).

$$\hat{n} \cdot K \nabla T = \sum \dot{n}_i \Delta H_{vi} \tag{30}$$

3.3.1.3. Heat transfer in the bubble and bulk liquid domain

In COMSOL Multiphysics, the heat transfer in the bulk liquid and bubble domain is described using the Heat Transfer in Fluids module. This module is used to model heat transfer by convection and the fluid model is active by default on all domains. The temperature equation defined in fluid domains corresponds to the convection-diffusion equation that may contain additional contributions like heat sources. In this case, the computational model considers a time dependent study given by the set of equations given by:

$$\rho C_p \frac{\delta T}{\delta t} + \rho C_p \boldsymbol{u} \cdot \nabla T + \nabla \cdot \boldsymbol{q} = Q + Q_p + Q_{vd} \tag{31}$$

$$\boldsymbol{q} = -k \nabla T \tag{32}$$

where Q represents the internally generated heat (W/m^3), Q_p and Q_{vd} refer to the work due to pressure changes and viscous dissipation respectively. The heat transfer in the bubble domain considers an absolute pressure of 1 atm, and the velocity fields for both the axial and radial dimensions. In Figure 18, the axial symmetry used for the heat and mass transfer calculations is represented by the dark blue boundary located on the left-hand side of the model. The red boundaries represent the thermal insulation in the system and have a value of $-\boldsymbol{n} \cdot \boldsymbol{q} = 0$, assuming no heat is lost beyond this boundary.

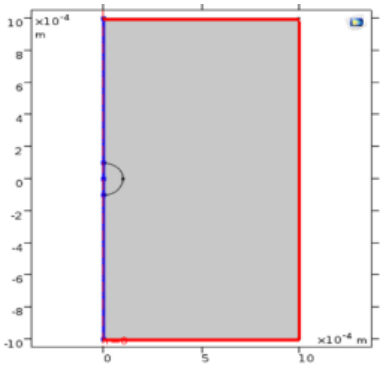

Figure 18 Axial symmetry for model.

The heat transfer in the bulk liquid domain considers an absolute pressure of 1 atm, and the velocity fields for both the axial and radial dimensions. The physico-chemical properties used to describe the essential features of the model can be found in Table 11. The red boundaries shown in Figure 18 are used to define the thermal boundaries of the system and set to a temperature equal to temperature of the liquid.

The system considers a boundary heat source on the surface of the bubble, this heat source is defined by the use given by the equation below:

$$Q_b = \hat{n} \cdot k\nabla T \tag{33}$$

where Q_b represents the boundary heat source and in the case of this computational model follows the expression:

$$Q_b = h(T - T_\infty) - \dot{m}\Delta H_v(T) \tag{34}$$

This is an adaptation of Fourier's Law to compute the normal flux component, which is equated to the Newton's Law of Cooling and the latent heat of vaporisation of water ($\Delta H_v(T)$) at a certain temperature weighted by the evaporation rate on the interface ($\dot{m}$). In the Newton's Law of Cooling, *h* is the local heat transfer coefficient and T_∞ is the temperature of the liquid domain far from the bubble. This equation is the analogous of the two-film theory of mass transfer resistance proposed by Lewis and Whitman, used for sensible heat transfer. It is important to point out that this equation is not fundamental, in terms of microscale distillation with mass and heat transfer effects a traditional McCabe-Thiele diagrams approach is used for analysis, but not kinetics are considered (Lewis & Whitman, 1924; Zimmerman, et al., 2013).

$$\dot{m} = J = -\hat{n} \cdot D\nabla C \tag{35}$$

Regarding the evaporation rate, it is noticed that the conservation of mass states that the evaporative flux must be equal to the diffusive flux produced from the reaction mechanism, from the bubble surface inwards into the bubble described by Fick's Law. The microbubble is injected dry or in other words with an initial water concentration of 0 mol/m^3 (Zimmerman, et al., 2013).

3.3.1.4. Transport of diluted species in both domains

In this model the mass transfer is defined using the Transport of Diluted Species module which is usually used to compute the concentration field of a dilute solute in a solvent and model multiple species transport. Transport and reactions of the species dissolved in a gas and liquid can be computed. The driving forces for transport can be diffusion by Fick's law, convection, when coupled to fluid flow. This time dependent study considers convection and diffusion inside the bubble domain using the concentration of the different species as dependent variables, described by the set of equations:

$$\frac{\delta C_i}{\delta t} + \nabla \cdot (-D_i \nabla C_i) + \boldsymbol{u} \cdot \nabla C_i = R_i \quad (36)$$

$$\boldsymbol{N_i} = -D_i \nabla C_i + \boldsymbol{u} C_i \quad (37)$$

In terms of diffusion, the coefficient is defined by the user in the magnitude of 1x10^{-9} m^2/s. In this time dependent model, there is a no flux condition on the surface of the microbubble with a value of $-\boldsymbol{n} \cdot \boldsymbol{N_i} = 0$. The initial concentration for water is assumed to be really low and a consequence of the instantaneous first reaction described later in the three-step mechanism for this model, with an initial value of 1x10^{-5} mol/m^3. The concentration profile for the water formed inside the bubble follows the expression:

$$C_w = \frac{P^* \cdot x_i}{RT} \quad (38)$$

The transport of the water produced as a consequence of the surface reactions is described by a general inward flux given by:

$$N_{cw} = KL \cdot a\left(C_l - H \cdot C_g\right) \quad (39)$$

where the liquid -gas film theory for mass transfer coefficients is used. The mass transfer is proportional to the concentration driving force at the interface and the interfacial area. C_l is the concentration of the gas in the liquid domain, C_g is the concentration that results in equilibrium with the initial gas concentration in the bubble. *KL* is the mass transfer coefficient, *H* is the dimensionless Henry constant for this particular case, and *a* is the surface area. In terms of diffusion, the coefficient is defined by the user and are found using the SEGWE method presented Evans et al in 2013 for molecules with a weight below 1000g/mol (Evans , et al., 2013; Evans , et al., 2018).

Table 12 Diffusion coefficients and initial concentrations of the species in the bulk liquid.

Component	Diffusion coefficient (m^2/s) x10^{-9}	Initial concentration (mol/m^3)
FAME	3.460	0
FFA	3.546	301.54
MeOH	11.38	301.54
H_2O	15.97	0
O_2	11.39	0

In this time dependent model, there is a no flux condition on the surface of the microbubble and the red boundaries shown in Figure 18 with a value of $-\boldsymbol{n} \cdot \boldsymbol{N_i} = 0$. The initial concentrations for the species in the bulk liquid are shown in Table 12. A general inward flux is set on the surface of the bubble for each one of the species in the bulk liquid. There is an outflow condition set at the bottom red boundary that follows the equation $-\boldsymbol{n} \cdot D_i \nabla C_i = 0$.

3.3.1.5. Proposed reaction mechanism

In this computational model, the esterification of vegetable oils is studied mediated by ozone rich and dry-to-bone air microbubbles. The proposed mechanism considers a set of three chemical reactions involving free radicals. As mentioned before the microbubbles, around 100 μm radius in size, are injected at the bottom of the esterification unit. The bubbles are injected with an initial oxygen singlet concentration of 1500 ppm or 281.25 mol/m^3, nitrogen N_2 is considered as an inert gas for this model. It is important to mention that the bubble is injected dry, with an initial water concentration of 0 mol/m^3. For this model the esterification of the FFAs in the vegetable oil into FAMEs require the presence of another reactant such as methanol.

In order to define the chemical reactions happening in the mechanism previously described both the chemistry and surface reactions models are used. The Chemistry module provides an extensive library of chemical reactions for use by any physics interface and the kinetic expressions for reaction rates, reaction heat sources, and also species transport properties, that can be used by other physics interfaces.

The initial composition of the liquid phase is comprised of FFAs and methanol, and as soon as the reaction is carried out the FAMEs start to appear. At the surface of the bubble, where the reaction mechanism takes place the free radicals such as MeO·, HO·, and O· can be found. As mentioned previously the initial composition of the gas phase (inside the bubble) only considers air and ozone, when the reaction is carried out one of the by-products is the water which is then stripped by the bubbles whilst rising through the liquid phase in order to avoid product inhibition.

The first two reaction proposed in this mechanism are considered to be instantaneous, and according to the Bodenstein steady state approximation. These two reactions are in equilibrium and follow the next expression:

$$k_{eq} = k_{eq0} \qquad k_{eqj} = \frac{\prod_{i=1}^{Qp} C_i^{v_{ij}}}{\prod_{i=1}^{Qr} C_i^{-v_{ij}}} \tag{40}$$

For each reaction the enthalpy (H_j), entropy (S_j) and heat source of reaction is calculated automatically in the model and given by:

$$H_j = \sum_{i=1}^{Q_p} v_{ij} h_i - \sum_{i=1}^{Q_r} (-v_{ij}) h_i \quad (41)$$

$$S_j = \sum_{i=1}^{Q_p} v_{ij} s_i - \sum_{i=1}^{Q_r} (-v_{ij}) s_i \quad (42)$$

$$Q_j = -r_j H_j \quad (43)$$

From the reaction mechanism previously mentioned, the surface species are the radicals $O\cdot$, $MeO\cdot$ and $HO\cdot$. The species found in the bulk liquid domain are the MeOH, FFA and FAME. Lastly, the species found in the bubble domain are H_2O and O_2. For each one of the species here discussed the molar mass was entered into the computational model, and the charge (*z)* was assumed to be z=0.

The reaction rate for the surface species ($O\cdot$, $MeO\cdot$ and $HO\cdot$) is calculated with the following equation at the surface of the microbubble:

$$R_{ads} = \sum_j R_{ads,\,j} \quad (44)$$

For the remaining bulk species either in the bubble or the bulk liquid domain, the reaction rate was calculated using equation 39 and the following reaction rate:

$$R = \sum_j R_j \quad (45)$$

The surface reactions interface is used to model the chemical reactions of surface and bulk species on a boundary. Surface species can be transported in the tangential direction of the surface by Fick's law whereas bulk species are assumed to be immobile on the surface. These assumptions are made in order to simplify the calculations when solving the computational model.

In this model there are three surface (adsorbed) species ($O\cdot$, $MeO\cdot$ and $HO\cdot$). In the time dependent study, these species are defined by the following set of equations in terms of mass transfer and reaction kinetics:

$$\frac{\delta C_{sj}}{\delta t} + \nabla_t \cdot \left(-D_i \nabla_t C_{sj}\right) = R_{sj} \quad (46)$$

$$\boldsymbol{N}_{sj} = -D_i \nabla_t C_{sj} \quad (47)$$

$$\Theta_i = \frac{\sigma_i C_{sj}}{\Gamma_s} \quad (48)$$

$$\frac{\delta C_{bj}}{\delta t} = R_{bj} \quad (49)$$

Regarding the surface properties, the density of sites has a value of $2\text{x}10^{-5}$ mol/m^2. And all the three radical species found on the surface have a site occupancy number of σ_i=1. In Table 13 are shown the

diffusion coefficients and initial surface concentration values for the radical species found in the interface.

Table 13 Diffusion coefficients and initial concentration for the surface species.

Species	Diffusion coefficient (m^2/s) x10^{-8}	Surface concentration (mol/m^2) x10^{-8}
MeO·	1.16	1
HO·	1.652	1

The rate of reaction for the instantaneous reactions in this mechanism are shown below

$$k_1 = \frac{[MeO\cdot][HO\cdot]}{[MeOH][O\cdot]} \tag{50}$$

$$k_2 = \frac{[H_2O][O_2]^{\frac{1}{2}}}{[HO\cdot]^2} \tag{51}$$

The rate of reaction in terms of the product of interest being FAME is given by the equation

$$r_{FAME} = k_f[FFA][MeO\cdot] - k_r[FAME][HO\cdot] \tag{52}$$

In order to come up with an equation that does not consider the intermediary free radicals, the term $[MeO\cdot]$ and $[HO\cdot]$ are isolated in equations 35 and 36 respectively given

$$[MeO\cdot] = k_1\frac{[MeOH][O\cdot]}{[HO\cdot]} \tag{53}$$

$$[HO\cdot] = \frac{\left([H_2O][O_2]^{\frac{1}{2}}\right)^{\frac{1}{2}}}{k_2{}^{\frac{1}{2}}} \tag{54}$$

Then the term $[HO\cdot]$ from equation 39 is substituted in equation 38, and then substituted in the rate of reaction for FAME in order to obtain an equation that does not include the intermediary free radicals, but only the radical $[O\cdot]$ which is a reagent in this mechanism.

$$r_{FAME} = k_f k_1 k_2{}^{\frac{1}{2}}[FFA]\frac{[MeOH][O\cdot]}{[H_2O]^{\frac{1}{2}}[O_2]^{\frac{1}{4}}} - k_r[FAME]\frac{[H_2O]^{\frac{1}{2}}[O_2]^{\frac{1}{4}}}{k_2{}^{\frac{1}{2}}} \tag{55}$$

3.4.Conclusions

The acid number calculations here presented are a good estimation for the FAME production in the esterification reaction. This allows the reader to understand and follow the thought process. Regarding the model description included in this chapter, it is important to mention that most of the theoretical background here presented is used in chapters 7 and 8, for the 2-D axisymmetric models. The assumptions and theories stated in the comprehensive literature review are used in this chapter for

some of the calculations, and to facilitate the analysis of the models discussed in the following chapters.

The main relevance of this chapter relies on showing the raw data and showing the link and the procedure to come up with results that are informed and could potentially be validated from experiments. The model description shown in Section 3.3 illustrates one example of how the theoretical background discussed in Chapter 2 is then applied to the proposed models in order to ease calculations and achieve building a robust model which describes the reaction kinetics and dynamics of the ozone free radical initiated esterification proposed in this thesis.

Once the experimental data is gathered, it is useful to analyse some of the key parameters happening in terms of the reaction kinetics and dynamics of the process. Having said this, it is relevant to explore the effect of parameters such as temperature, diffusion coefficients and reactions kinetics of the main species found in the system. In the next chapter, several aspects of the reaction kinetics and dynamics are explored using the appropriate approach. All these estimations are carried out in order to point out the regimes and operating conditions that would favour the intensified esterification. This is one of the main reasons to conduct dimensionless calculations, stability analysis and diffusion estimations for the different species found in the system.

4. Estimation of different parameters

In the following chapter some of the key parameters are estimated and discussion for its respective use in the computational models. Some of the main aspects here discussed are the diffusion coefficient for the species of interest and a detailed analysis of the effect of the bubble size on the dimensionless numbers including the Peclet, Nusselt and Reynolds number. The physical properties and transport calculations for the oxygen singlet in different medium in the gas phase are included in this chapter. The effect of the bubble size on the internal pressure and residence time using different liquid mixtures is also included in this chapter. The diffusion coefficients for ozone in both the liquid mixture and gas phase are estimated and related to the diffusion time, in case diffusion governed the process. A brief analysis of the ozone stability and the liquid-phase mass transfer coefficient is showed in this chapter as well. Lastly, a couple of ozone decomposition models are included (HSB and TFG) and one last model for the temperature dependence of ozone in a heat exchanger. The results obtained after analysing these parameters are fed into the computational models in order to convey in a robust model that successfully describes the physics happening in the intensified esterification.

4.1. Diffusion coefficient and dimensionless analysis

In order to build the computational model, some of the physics regarding the relevant species in the system are needed. The oxygen singlet radical is hypothesised to enhance the ozone free radical initiated esterification. It is relevant to study its behaviour and some of its properties in different medium to explore the possible limitations of the model and the regime that best describes the operating conditions of the system. Having said this, the diffusion coefficients reported by Morgan and Schiff are used as a reference in order to estimate several dimensionless parameters such as, the Peclet, Nusselt and Reynolds number. Table 14 shows the physical properties and behaviour of the oxygen singlet in different medium to be considered in the gas phase (microbubble domain). Some of the main features analysed in this table are the diffusion coefficient, Peclet and Reynolds number, density and viscosity and the diffusion time.

Table 14 Physical properties of the oxygen singlet in inert gases and air (Morgan & Schiff, 1964).

System	D_o ($cm^2\ s^{-1}$) $x10^{-2}$	Pe L $x10^{-2}$	ρ ($kg\ m^{-3}$)	μ (Pa s) $x10^{-5}$	Re $x10^{-3}$	t (s) $x10^{-3}$
O/He	7.000	0.397	0.164	1.960	0.232	0.714
O/Ar	2.090	1.330	1.784	2.230	2.225	2.392
O/N_2	2.180	1.275	1.251	1.760	1.977	2.293
O/O_2	2.220	1.252	1.429	2.040	1.948	2.252
O/Air	2.187	1.271	1.225	1.818	1.873	2.285

From the table above, it can be noticed that the Peclet number is considerably lower than 1. This would suggest that convection is the dominant mean of mass transport in the gas phase. Although

convection is known to happen faster than diffusion, for very small volumes (microbubbles) the more efficient means of transport occurs by diffusion. This is the main driver to introduce a microbubble internal mixing that occurs on a time scale of 10^{-3} s, so the condensing vapour or evaporating mixture should obey a rate law that evolves on this rapid time scale. In terms of the Reynolds number, microfluidic systems are known to have a characteristic length is so small that the Reynolds number are mostly always less than 1 as it can be seen in Table 14. This would suggest that the system falls into the category of laminar flow which poses the advantage of fluids that can be manipulated very precisely and the molecules in the fluid can be controlled to form predictable gradients due to the steady streamlines. In the last column the approximation for diffusion time is shown, it can be noticed that for all the gas mixtures, if diffusion dominated means of mass transfer, the diffusion time fall into the order of magnitude of $1x10^{-3}$ s (Zimmerman, et al., 2013; Morgan & Schiff, 1964).

Once the physical properties of the gas phase are discussed, it is relevant to carry out a dimensionless analysis of the regimes found in the system. The estimation for the liquid-side heat transfer coefficient used in the system considers contributions from both the Nusselt and Peclet number. It is assumed for the purpose of this computational model that the bubbles are injected into the liquid at a controlled rate with a significant excess of kinetic energy. As mentioned before, the microbubbles are rising in the liquid mixture under buoyancy only. Kumar et al reported a value for the heat transfer coefficient of 1080 $W/m^2 \cdot K$ when using coarse bubbles of 2cm diameter. Since in this system the bubbles are relatively smaller, it is sensible to expect that convection would be the major contribution to heat transfer and would scale with the Peclet number. One would expect that the heat transfer for a bubble with a radius of $1x10^{-4}$ m would be six orders of magnitude smaller compared to a 1 cm radius bubble. If the dimensional analysis does not follow a proportionality, the Nusselt number could be used (Kumar, et al., 1992)

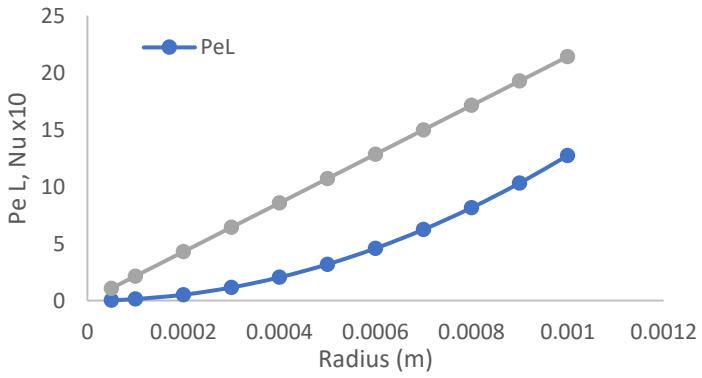

Figure 19 Variation of the Peclet and Nusselt number with bubble size.

The variation of both the Peclet and Nusselt number with bubble size is shown in Figure 19. The Nusselt number is calculated using the correlation reported by Zimmerman et al for fine and coarse bubbles given by:

$$Nu = f(Pe) = 0.6\,Pe^{0.5} \tag{56}$$

This correlation suggests that the heat transfer coefficient follows $h \approx d^{0.5}$. Assuming there are not contributions to convective heat transfer with microbubbles and using the size dependence equation with the Eotvos and Reynolds number regimes given by:

$$Eo = \frac{gd^2}{\sigma}\Delta\rho$$

It is reasonable to suggest that in the microbubble regime, laminar flow dominates the heat transfer and hence the Nusselt number is directly proportional to the Peclet number. This results in a correlation for the heat transfer of $h \approx d^2$, and a heat transfer that is four orders of magnitude smaller for 1x10^{-4} m radius bubbles. After using these arguments, the proposed valued for the heat transfer coefficient is 0.1 W/m^2·K, which is similar to the one reported by Zimmerman et al (Zimmerman, 2011; Zimmerman, et al., 2013; Kumar, et al., 1992).

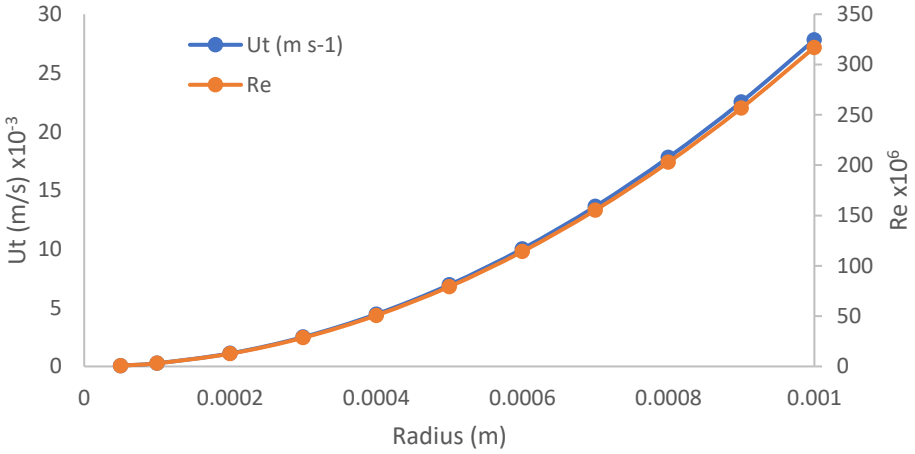

Figure 20 Reynolds number and terminal velocity variation with bubble radius.

Figure 20 illustrates the effect of the bubble size on the terminal velocity and the Reynolds number. It is clear that an increase of the bubble radius means an increase in the terminal velocity and therefore the Reynolds number. In the ozone free radical initiated esterification, a microbubble with a radius of 1x10^{-4} m rising through the liquid mixture, would rise at a terminal velocity of 2.781x10^{-4} m/s and have a Reynolds number 3.17x10^{-6}. This value suggests that the laminar flow is expected in the rising of the microbubble for the esterification unit. It is clear that smaller bubbles have a lower terminal velocity and therefore its residence time would be higher compared to coarse bubbles.

Microbubbles are characterised for having a high internal pressure which results from the surface tension at the gas-liquid interface. The relationship between the pressure and the diameter of the microbubble is given by the Young-Laplace equation found below:

$$P = P_1 + \frac{4\sigma}{d_b} \tag{57}$$

where σ is the surface tension of the liquid and d_b is the diameter of the bubble. According to this equation, the pressure found in a 1 μm would be about 389.325 kPa at 298 K, nearly four times the atmospheric pressure. It can be noticed in Figure 21 that mostly all the bubble sizes tend to be similar to the atmospheric pressure. For bubbles with a diameter less than 50 μm, the internal pressure increases dramatically to a certain extent when decreasing the bubble diameter. In this figure the internal pressure is shown for the case of water or oil as the liquid mixture. It is clear that water has a higher surface tension due to the hydrogen bonding, this results in a higher internal pressure found in the microbubble. The internal gas pressure increases when the microbubbles are smaller, and it is important to point out that the rate of increase is inversely proportional to the bubble size (Pan , et al., 2009).

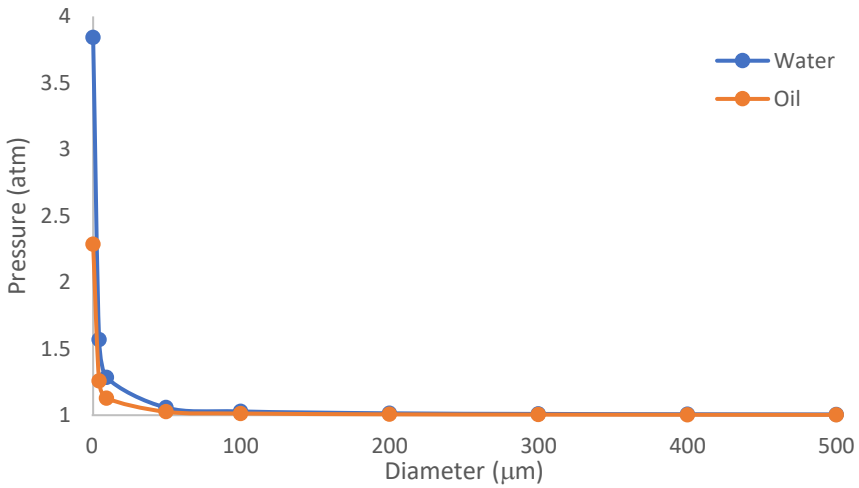

Figure 21 Variation of the microbubble internal pressure with diameter.

The effect of the bubble size on the residence time for a microbubble rising through the liquid mixture for varying liquid layer thickness is shown in Figure 22. Increasing the liquid layer thickness causes an increase in the residence time for the microbubble to rise through the liquid. A bubble one order of magnitude smaller rises at a terminal velocity two orders of magnitude slower. For the proposed models in this thesis, the liquid layer domain considered in the computational model is ten times bigger compared to the radius of the bubble. This would mean that a microbubble with a radius of $1x10^{-4}$ m rising at a terminal velocity of $2.781x10^{-4}$ m/s would take 3.592 s to rise through the liquid mixture.

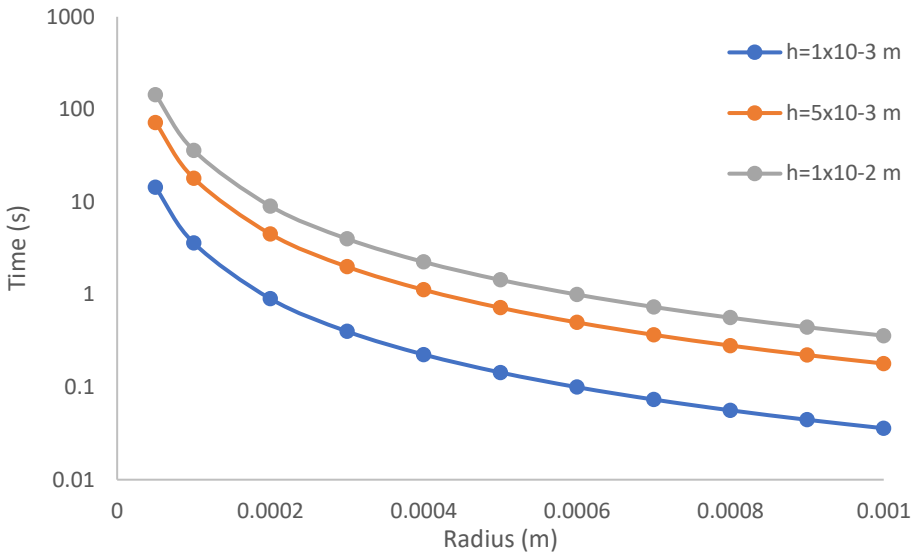

Figure 22 Variation of the residence time with bubble size.

From the experimental data, the volumetric flow used for comparison between the experiments and the computational model has a value of 0.1 L/min. As expected both the bubble flux and the oxygen single molar inlet flow are directly proportional to the volumetric flow.

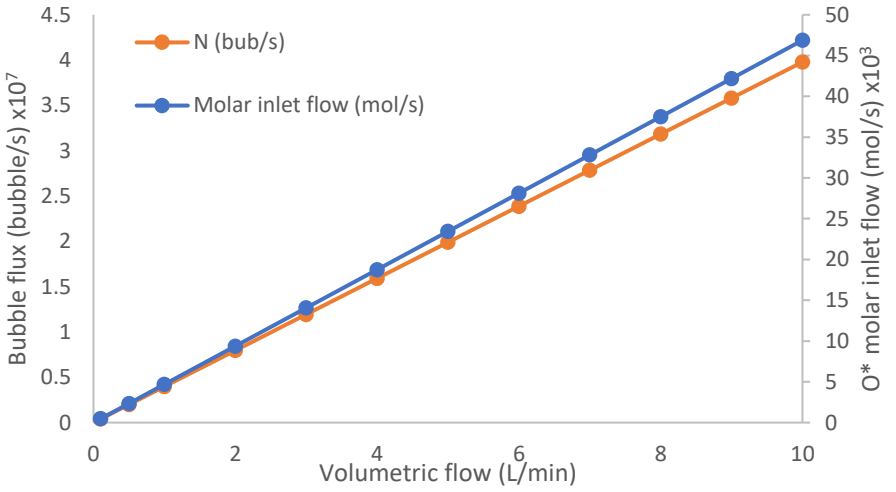

Figure 23 Variation of the bubble flux and molar inlet flow with the volumetric flow.

This figure is shown in the potential case that a further increase of the volumetric flow is required to provide the system with a higher amount of the free radical. Having said this, the bubble flux is then used to correlate the FAME production between a single microbubble and the cloud of bubble. In Figure 24, the bubble flux over time is shown. This parameter is fitted with a quadratic equation given by $N=0.2114 + 4.0553t - 0.0049\ t^2$ ($R^2=0.9998$). It is important to mention that this function of the bubble flux can potentially be used for residence times $t < 20$ s, which is the case for both models presented in Chapter 7 and 8.

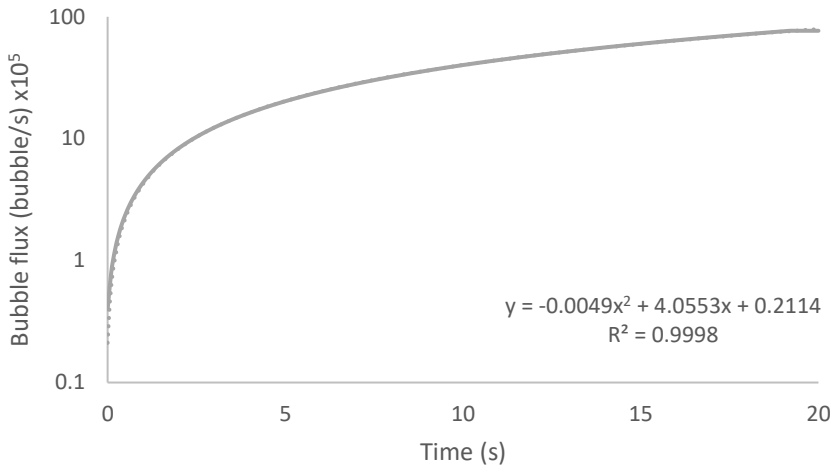

Figure 24 Bubble flux function in time for the fitting of the model.

4.2.Ozone and free radical species

The production rate of the biodiesel can potentially be maximised by producing a high amount of $O\cdot$ using an advanced oxidation plasma reactor. It has been reported by Zimmerman and Lozano Parada that it is possible to tune a plasma reactor under specific conditions, so a maximum of $O\cdot$ at $1x10^{-3}$ s it then produced. This means there is no need to form the ozone species for then to be decomposed in $O\cdot$, but by tuning the device a set amount of this species can be produced (Lozano-Parada & Zimmerman, 2010).

For instance, it is important to explore the behaviour that both the oxygen singlet and ozone would have in the microbubble with the variation of the temperature. It is known that the plasma reactor produces ozone molecules as well that potentially would react with the Free Fatty Acids under the Criegee mechanism. This is the main driver to analyse the total time that this molecule would take to go through both the gas and liquid phase if present, this would suggest if the alternative mechanism could potentially be detrimental to the reaction mechanism here proposed. The total time for the ozone to reach the liquid can be considered as the addition of: i) the diffusion from the centre of the bubble to the interface and ii) the diffusion from the interface to the liquid mixture. It is important to point out that due to the nature of the oxygen singlet, the total time for the radical species is relatively smaller compare to the ozone time. This could be attributed to the difference in the molecular weight between the two species. To explore the variation of the residence time with temperature, the diffusion time and residence time needs to be calculated for both the gas and liquid domain, the procedure followed by Kokoo et al is here described (Kokoo & Zimmerman , 2018).The diffusion time of ozone in the gas phase is defined by:

$$\tau_{O3,air} = \frac{r^2}{2D_{O3,air}} \tag{58}$$

where *r* is the radius of the bubble and $D_{O3,air}$ is the diffusivity of ozone in air. This diffusion coefficient can be calculated by the equation given by:

$$D_{O3,air} = \frac{0.00266T^{1.5}}{PM_{O3,air}^{0.5}\sigma_{O3,air}^{2}\Omega_D} \quad (59)$$

where P is the pressure (bar) and the term *M* is the average molecular weight, *σ* is the characteristic length (A°) and Ω is the diffusion collision integral, these terms are defined by the equations below.

$$M_{O3,air} = \frac{2}{\frac{1}{MW_{O3}} + \frac{1}{MW_{air}}} \quad (60)$$

$$\sigma_{O3,air} = \frac{\sigma_{O3} + \sigma_{air}}{2} \quad (61)$$

$$\Omega_D = \frac{1.0603}{T^{*0.156}} + \frac{0.193}{e^{0.476T^*}} + \frac{1.0358}{e^{1.529T^*}} + \frac{1.764}{e^{3.894T^*}} \quad (62)$$

where T^* is temperature considering the Lennard-Jones energy ε and the Boltzmann's constant k_B ($1.381x10^{-23}$ J/K). The term T^* and the Lennard-Jones energy is described by the equation:

$$T^* = \frac{k_B T}{\varepsilon_{O3,air}} \quad (63)$$

$$\varepsilon_{O3,air} = (\varepsilon_{O3}\varepsilon_{air})^{0.5} \quad (64)$$

The Lennard-Jones energy and characteristic length for ozone and air needed to carry out the calculations are shown in Table 15.

Table 15 Lennard-Jones energy and characteristic length for ozone and air (Ivanov, et al., 2007).

Species	σ	ε
Ozone	3.875	208.4
Air	3.711	78.6
Ozone-Air	3.793	127.985

For the diffusion time of ozone in the liquid, a unidirectional mass transfer is assumed since the diffusive length (20 nm) of ozone in the oil (oleic acid used as an example) is relatively smaller than the radius of the bubble. Therefore, the diffusion time in the liquid can be estimated using the equation below:

$$D_{O3,oil} = \frac{\delta^2}{2D_{O3,oil}} \quad (65)$$

$$D_{O3,oil} = 7.4x10^{-8}\frac{(\phi_s MW)^{0.5}T}{\mu_s V_A^{0.6}} \quad (66)$$

where μ_s is the viscosity of the liquid (cP), V_A is the molar volume of ozone at its boiling temperature (35.5 cm^3/mol) and ϕ_s=1. Figure 25 illustrates the effect of the temperature on the ozone diffusion in both the gas and liquid domain. It is clear that the temperature has a higher impact on the liquid

mixture compared to the gas phase, this is mainly to the changes in the physical properties like the viscosity when varying the temperature. Another relevant observation is that the diffusive length here considered for the liquid is relatively small, this results in a diffusion coefficient seven orders of magnitude smaller compared to the one obtained in the gas domain.

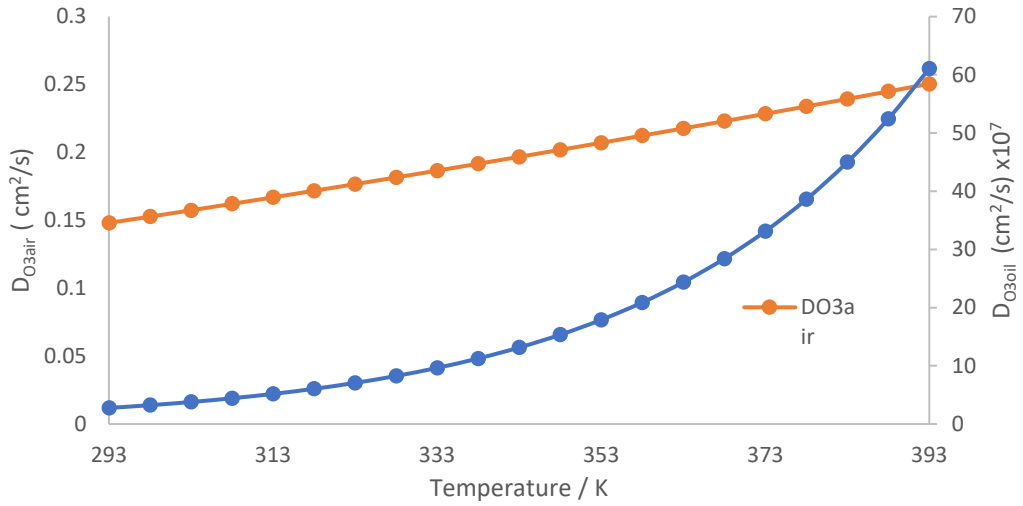

Figure 25 Diffusion coefficients for ozone in both the gas and liquid domain.

The diffusion times in both domains are intrinsically related to the diffusion coefficients, this is the main driver to analyse the time required for each domain. Figure 26 illustrates the variation of the diffusion time with different temperatures. It is important to point out the different orders of magnitude between the diffusion times, this suggests that the diffusion time if possible in the system is mainly determined by the diffusion time of ozone in the gas domain (inside the bubble).

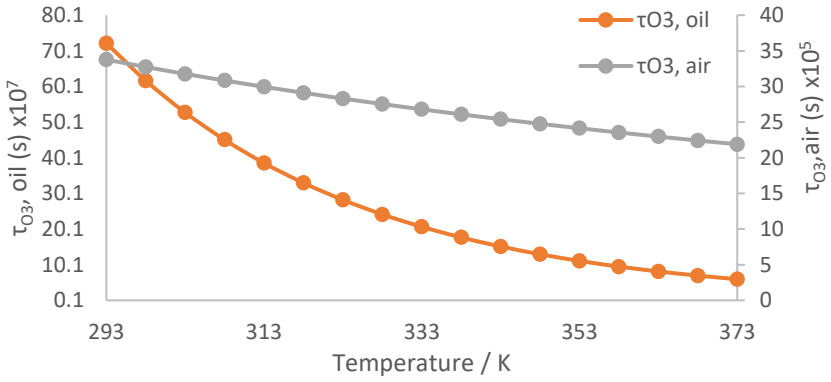

Figure 26 Ozone diffusion time in both the gas and liquid domain.

In the computational models here proposed, the microbubble internal mixing occurs on a time scale of 10^{-3} s, so the condensing vapour or evaporating mixture should obey a rate law that evolves on this rapid time scale. It can be depicted from Figure 26 that if diffusion were to be the determining mean of mass transfer, both the oxygen singlet and ozone would reach the gas-liquid interface in $1x10^{-4}$ s for the case of a microbubble with a radius $1x10^{-4}$ m.

4.3.Ozone stability

When producing ozone in plasma reactors, it has been reported the relative concentration of the oxygen singlet with respect to ozone in pure dry air results. This results in the equation given by:

$$[O]/[O_3] \approx 3 \times 10^8 \cdot \exp(-11750\ K/T_0) \quad (67)$$

It is important to mention this ratio is given here a reference in the event that the oxygen singlet was to be produced from the decomposition of ozone due to the effect of parameters like temperature or the initial concentration. For the computational models proposed in this thesis, the oxygen singlet is described by the results reported by Lozano-Parada and Zimmerman that it is possible to tune an in-situ ozone plasma microreactor to preferentially produce oxygen singlet radicals by adjusting the residence time and then injecting them directly into the bubble. At $1x10^{-2}$ s, the ozone production found its maximum and for the oxygen singlet the maximum yield was found at $1x10^{-3}$ s. This means a 10x throughput can be produced by tuning the microreactor at the appropriate operating conditions (Lozano-Parada & Zimmerman, 2010; Zimmerman, 2011; Rehman, et al., 2016)

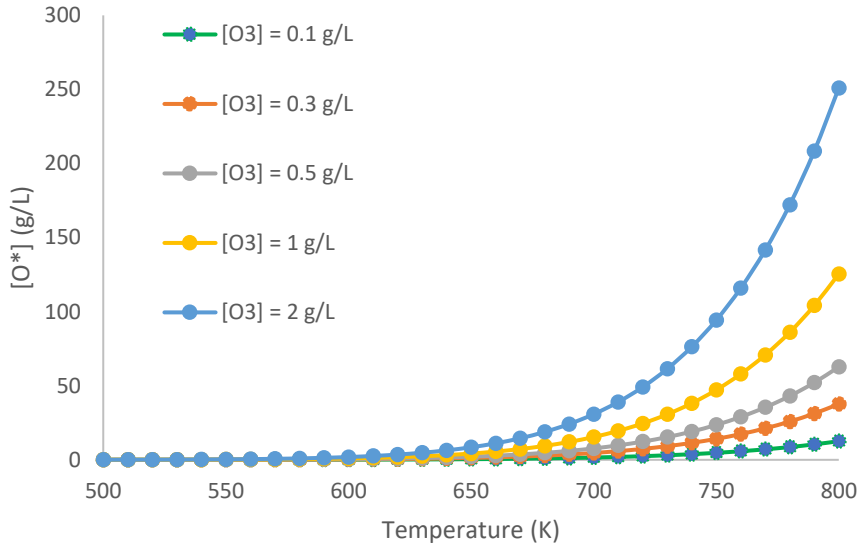

Figure 27 Relative oxygen concentration of oxygen singlet with respect to ozone.

Around a temperature of 100°C, the ozone decomposition is already intensive, and its time of dissociation fluctuates around 1 s. The reverse reaction of the ozone formation is significantly faster and the oxygen singlet concentration at this condition could be neglected $[O^*]/[O_3]=1x10^{-5}$. According to the equation stated previously for the relative concentration of the oxygen singlet, and as it can be depicted from Figure 27 this value becomes comparable at a gas temperature of around 300°C. It is relevant to mention that this data is only valid outside of plasma, where the oxygen singlet is produced solely from ozone decomposition. The actual losses of ozone related to thermal decomposition take place in the rapid reaction of ozone with the oxygen singlet (Fridman, 1953).

The characteristic time for the thermal decomposition of ozone, assuming a stationary ratio for [O*]/[O_3] is given by:

$$\tau_{O_3} = \frac{5 \cdot 10^{-18} s}{\alpha_{O_3}} \cdot exp\left(\frac{14050K}{T_0}\right) \quad (68)$$

As mentioned in Chapter 2, the ozone decomposition has a strong exponential dependence not only on the temperature but also on the initial concentration of this species. The factor α_{O_3} refers to the ratio between the ozone concentration and the total gas density. Diluted ozone is known to be stable at low temperatures. At a relative concentration of 0.2%, ozone decomposes in around 1 s at an operating temperature of 145°C.

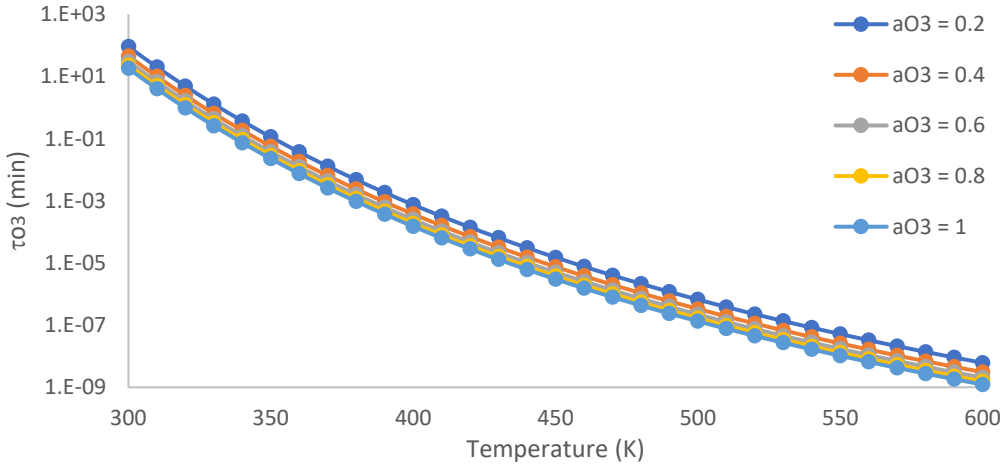

Figure 28 Characteristic time of ozone thermal decomposition (Fridman, 1953).

On the other hand, at a gas temperature of 125°C and a relative concentration of 1% is equally 1 s. An increase in both the gas temperature and the initial ozone concentration would cause a rapid ozone decomposition. It is important to mention that thermal decomposition of ozone is a highly exothermic process and a fast process could potentially lead to overheating and thermal explosion (Fridman, 1953).

4.4.Liquid-phase mass transfer coefficient

The mass transfer coefficient for a microbubble is relatively smaller compared to the value obtained when analysing coarse bubbles. This could be attributed to a much thicker liquid-phase boundary film than coarse bubbles. The liquid-phase mass transfer coefficient could be estimated using the theoretical equation of Levich given by:

$$k_L = 0.65\left(\frac{D_L u_R}{d}\right)^{0.5} \quad (69)$$

where D_L is the diffusivity (m^2/s), u_R is the rising velocity of the bubble (m/s) and d is the bubble diameter. For a microbubble with a diameter of $2x10^{-4}$ m, the mass transfer coefficient has a value of

9.686 x10^{-5} m/s. Figure 29 illustrates the variation of the mass transfer coefficient for different bubble sizes, it is clear that the order of magnitude for this value matches the one used by Abdulrazzaq et al in the purification of bioethanol. In the case of the proposed models in chapters 7 and 8, a value of 2 x10^{-5} is used for the evaporation parameter of water. A small value of the water vaporisation parameter (2x10^{-7}) would result in a slower mass transfer, mainly found in isothermal systems.

A large value of this parameter would result in systems that flash to equilibrium characterised by a rapid vaporisation followed by recondensation as the bubble reaches the second regime. In this study a value of 2x10^{-5} has been used in order to guarantee nonequilibrium dynamics that are rapid enough. This value is in agreement with previous values reported by Abdulrazzaq et al in the purification of bioethanol in binary mixtures (Abdulrazzaq, et al., 2016; Zimmerman, et al., 2013).

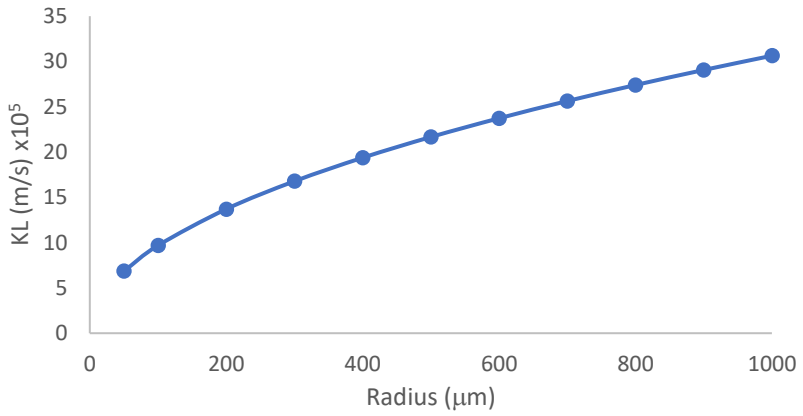

Figure 29 Mass transfer coefficient variation with bubble size using Levich equation.

Another approach to estimate the liquid-phase mass transfer coefficient is the empirical equations of Calderbank and Moo-Young, for a diameter smaller than 600 μm is given by:

$$k_L(v_L D_L)^{\frac{2}{3}} = 0.31[\frac{(\rho_L - \rho_g)\mu_L g}{{\rho_L}^2}]^{\frac{1}{3}} \quad (70)$$

where v_L is the kinetic viscosity of the liquid, ρ_L is the liquid density, ρ_g is the gas density, μ_L is the liquid viscosity and *g* is the gravitational acceleration. It can be noticed that the empirical equations of Calderbank have no dependency on the bubble size. The liquid-phase mass transfer coefficient is then calculated from physical properties like density, viscosity and diffusivity.

4.5. Ozone decomposition models

The decomposition of ozone in an aqueous solution is a very complex process, commonly defined as a radical type chain reaction which is extremely sensitive to the operating conditions. Trace amounts of impurities could potentially act as scavengers or promoters in this reaction, and the effect of the pH or a change in the ionic media have a significant effect on the lifetime of ozone in aqueous solution.

As mentioned before, the ozone decomposition in an aqueous solution involves the formation of radical species. This process has been mainly described by two different mechanisms, by Hoigné-Staehelin-Bader (HSB) and Tomiyasu-Fukutomi-Gordon (TFG). In the following sections, these two methods are discussed and the key features of each one of them are shown.

4.5.1. HSB model

The HSB model states an oxygen-atom transfer from ozone to a hydroxide ion as the initial step of the mechanism, and then a reverse one-electron transfer. On the other hand, the TFG model only states the oxygen-atom transfer. In both models, the fundamental reaction is the initial step, this occurs when the ozone reacts with the hydroxyl radical. The speed of ozone decomposition is slowed down by the removal of the hydroxyl radical, O_2^- and superoxide anion radical in the chain reaction. Having stated this initial step, the stability of the ozone solution is highly dependent on pH and suffers a decrease when alkalinity rises. At a pH above 8, the initiation rate has been reported to be proportional to the concentration of ozone and the hydroxyl radical. Nevertheless, for an acidic solution the reaction with the hydroxyl radical cannot be the initial step (Eriksson, 2004).

In the mechanism, the oxygen singlet reacts with water, and the propagating products diffuse and react with ozone in the bulk liquid continuing the chain reaction. The half-life of ozone is about 2 minutes at room temperature and 1 M NaOH solution, compared to 40 minutes in 5 M or 83 hours in 20 M solutions. This observed decrease could be attributed to the formation of ozonide, which then reacts with the hydroxyl radicals resulting in the reformation of ozone. There are several factors affecting the ozone decomposition. For instance, at a higher temperature ozone depletion happens at a more rapid pace. This model describes the reaction of ozone in an aqueous solution as a direct/indirect reaction, shown in Figure 30.

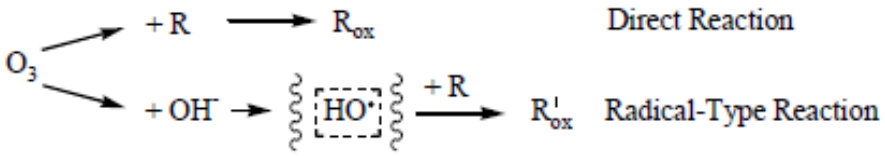

Figure 30 SHB mechanism for ozone reaction.

The direct reaction is selective towards specific functional groups and compounds, this results in the cyclo-addition to unsaturated bonds by the Criegee mechanism forming ozonides. The reactivity of ozone is enhanced by groups that donate electrons, and in the case of electron-withdrawing groups, ozone would act as a nucleophile. The reactions and rate constants for the SHB model are shown in Table 16.

Table 16 Reactions and rate constants for the HSB model (Eriksson, 2004).

Reaction	Rate constant
$O_3 + OH^- = HO_2 + O_2^-$	70
$HO_2 = H^+ + O_2^-$	$10^{-4.8}$
$O_2^- + O_3 = O_3^- + O_2$	1.6×10^9
$O_3^- + H^+ = HO_3$	5.2×10^{10}
$HO_3 = HO^* + O_2$	1.1×10^5
$HO^* + O_3 = HO_4$	2×10^9
$HO_4 = HO_2 + O_2$	2.8×10^4

The concentration profile over time for different species is illustrated in Figure 31. An initial concentration for all the species of 10 mol/m^3 is here used. It can be depicted from this figure that the ozone decomposition occurs in an order of magnitude of 1 x10^{-3} s. The ozone decomposition takes longer in this mechanism and it can be seen that takes a few steps in order to achieve a decay in time.

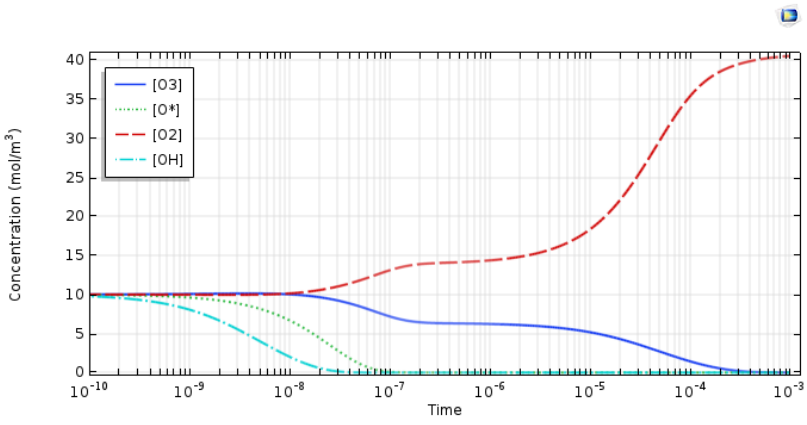

Figure 31 Concentration profile over time for different species in the Hoigé and Gordon model.

The hydroxyl radical and oxygen singlet are nearly consumed at around 1x10^{-8} and 1x10^{-7} s respectively. The production of the molecular oxygen is clearly depicted in this figure, nearly achieving a concentration four times greater than the initial one. In order to contrast both models, the TFG model is presented in the following section.

4.5.2. TFG model

Tomiyasu, Fukutomi and Gordon (TFG) proposed a kinetic model for the aqueous decomposition of ozone. The TFG model predicts a slow ozone decomposition, but when the set of rate constants are modified the new TFG model can predict the lifetime of ozone within an order of magnitude over the neutral-alkaline pH region. The modified set of reactions and rate constants of the extended TFG model for the aqueous ozone decomposition is shown in Table 17. In this table, second, first and zeroth order rate constants are expressed in $M^{-1}s^{-1}$, s^{-1} and Ms^{-1} respectively. This extended model gives an accurate

description of ozone decomposition in alkaline solution. It has been reported that this model describes well the trends observed in the kinetic traces as a function of the pH in the range 10.4-13.2.

Table 17 Reactions and rate constants for the TFG model (Nemes, et al., 2008).

Reaction	Rate constant
$O_3 + OH^- = HO_2^- + O_2$	140
$HO_2^- + O_3 = O_3^- + HO_2$	5.5×10^6
$O_2^- + O_3 = O_3^- + O_2$	3×10^8
$O_3^- + OH = O_2^- + HO_2$	2×10^{10}
$O_3^- + OH = O_3 + OH^-$	8.3×10^9
$OH + O_3 = HO_2 + O_2$	2.5×10^7
$0^- + HO_2^- = 0_2^- + OH^-$	3.2×10^9
$0^- + O_2^- (+ H_20) = 0_2 + 20H^-$	1.8×10^8
$0_3^- = O_2 + 0^-$	5×10^3
$H0_3 = O_2 + OH$	1.1×10^5
$H0_2 + OH^- = O_2^- (+ H_20)$	1×10^{10}
$H_2O_2 + OH^- = HO_2^- (+ H_2O)$	1×10^{10}
$OH + OH^- = O^- (+ H_20)$	4×10^{10}
$H0_3 + OH^- = O_3^- (+ H_20)$	5.2×10^{10}
$H^+ + OH^- = (H_20)$	1×10^{11}

The concentration profile over time for different species is illustrated in Figure 32. An initial concentration for oxygen 42.24 mol/m^3 is here used and for the rest of the species like ozone, hydroxyl radical and the oxygen singlet an initial concentration of 10 mol/m^3 is used. It can be depicted from this figure that the ozone decomposition occurs in an order of magnitude of 1 x10^{-6} s.

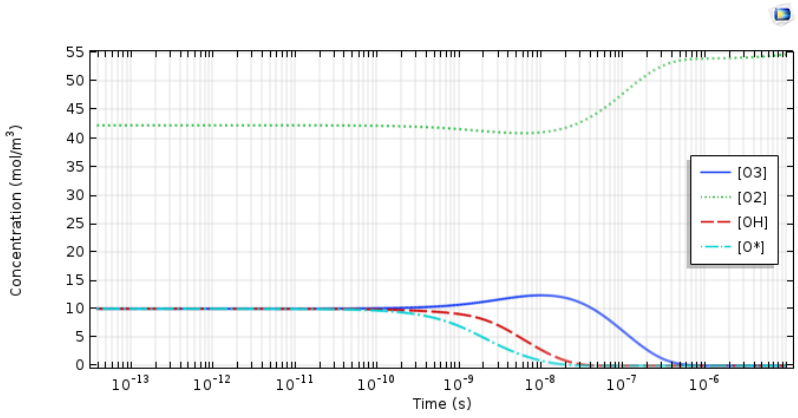

Figure 32 Concentration profile over time for different species in the TFG model.

It is clear that before the rapid decay, a small increase in the ozone concentration occurs at the same time as the radical species start being consumed. The hydroxyl radical and oxygen singlet are consumed relatively faster than ozone in around 1 x10^{-8} s. The ozone decomposition in aqueous

solution results in the production of the oxygen molecule due to its stability and the rate constant of the reaction in charge.

4.5.3. Heat exchanger model

Regarding the ozone free radical initiated esterification, the effect of the temperature on the production of FAME is a matter of importance in order to explore the temperature dependency of the reaction and estimate the temperature that results in a maximum production. Both the bubble and liquid mixture are important parameters explored in chapters 7 and 8. Regarding the bubble temperature, a heat exchanger is designed for the respective use to pre-heat the gas phase before being injected into the microbubble. The heat exchanger here modelled and designed for the intensified esterification is based on a previous device use in the microfluidics group at the University of Sheffield.

It is important to mention that this process air heater is not included in the bioreactor shown in experimental rig used in Section 3.1. The process air heater here described is used in the Microfluidics group at the Kroto Research Institute. The figure below shows the schematic diagram for the process air heater, illustrating some of the key features. The air heater is the RS Pro AH75-6MF, a 750 W heater with the capacity of heating up to 813 K. In Figure 33 the key features of this process air heater are shown, with a heated length *A* of 88.9 mm, a total chamber *B* of 101.6 mm and a tubing "T" with dimensions *C* and *D* of 33.3 mm. The sheath material and T piece are made of stainless steel and copper respectively (RS, 2016).

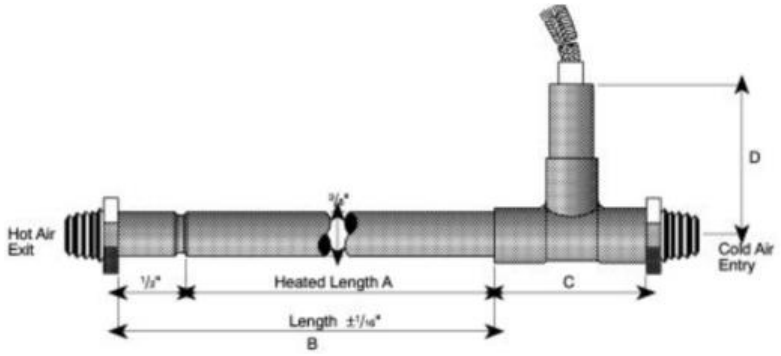

Figure 33 Schematic diagram for the process air heater (RS, 2016).

The process air heater has an internal diameter of 9.52 mm and length of nearly 10 times the radius, resulting in a cross-sectional area of 2.85 $x10^{-4}$ m^2. The gas inlet flow used for the modelling in this section has a value of 0.1 L/min. The linear velocity of the gas mixture in the heat exchanger is calculated to have a value of 8.488 $x10^{-2}$ m/s, giving a residence time of 0.294 s. The gas mixture is in the process air heater operates at a Reynolds number of 142.93 which belongs to the laminar regime (Re<2300). The temperature of the wall and the gas mixture inlet is set to 673.15 and 293.15 K. In this section can be found a brief analysis of the velocity and temperature gradient in the process air heater,

the concentration profile for the species of interest has already been discussed previously in this chapter.

4.5.3.1. Temperature profile

The ozone decomposition has an important temperature dependency. This is the main driver to analyse the temperature profile in the process air heater. Some features like the internal diameter and the inlet flow are important features when designing a process air heater.

In Figure 34, the temperature gradient across the process air heater is illustrated. It can be depicted from this figure that in around 0.1 s, the temperature of the gas in the process air heater shows an isothermal behaviour, reaching a temperature of 673.15. This means that under the operating conditions stated previously, at around 0.1 s the gas reaches a thermal equilibrium with the walls of the process air heater. If the gas mixture is left for a bit longer compared to this thermal equilibrium, this results in assuring the outlet gas temperature to be similar to the one set initially to the process air heater.

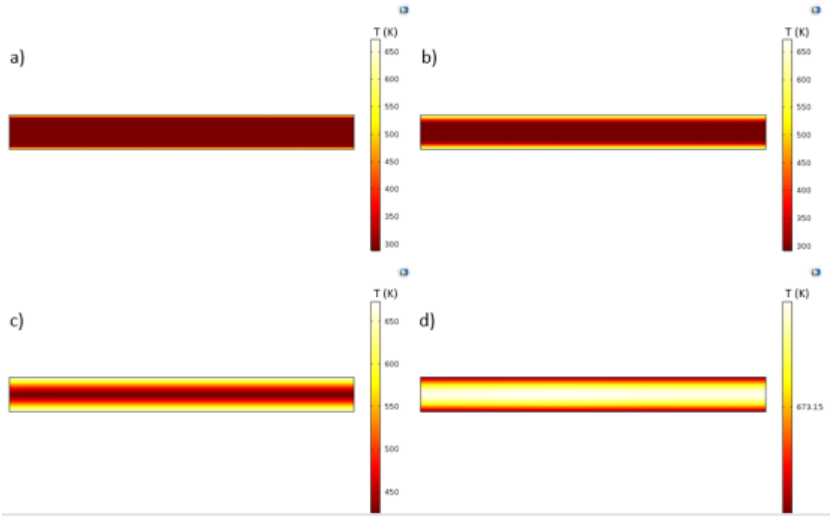

Figure 34 Temperature profile in K across the process air heater over time (For a-d, t=0.0001, 0.001, 0.01 and 0.1 s).

Before 0.001 s, the temperature of the gas mixture does not show much of a temperature gradient. It is until 0.01 s, when the gas mixture flowing in the middle of the air heater rises it temperature to 450 K and the temperature around the walls is highly influenced by the operating conditions set. Having said this, the gas mixture shows a significant increase in temperature around 0.01 s. This would then lead to the thermal equilibrium previously mentioned at around 0.1 s.

4.5.3.2. Velocity gradient

One of the relevant aspects to be analysed in a process air heater is the velocity gradient, which is defined by several parameters set at the beginning of its design such as the internal diameter and the

length of the device. The velocity gradient across the process air heater over time is shown in Figure 35.

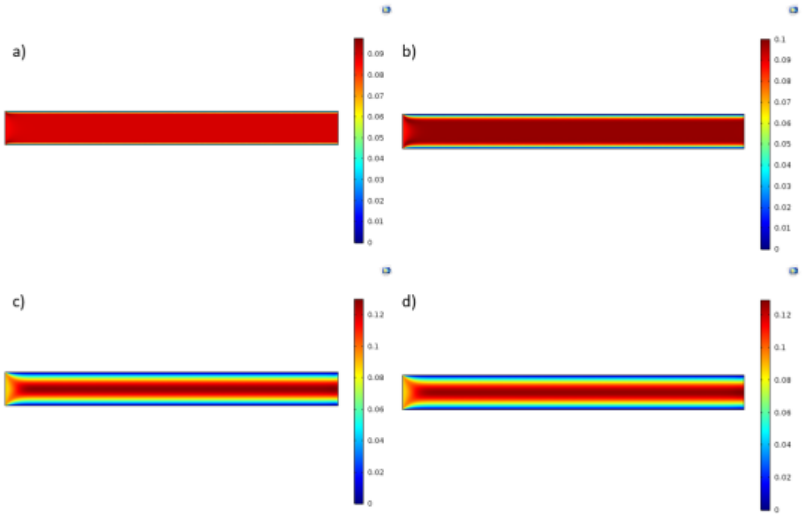

Figure 35 Velocity gradient across the process air heater over time (For a-d, t=0.0001, 0.001, 0.01 and 0.1 s).

These features result in a characteristic Reynolds number which then governs the fluid dynamics and dictates the flow pattern experienced by the gas mixture in the process air heater. In this case, the gas phase flowing in the process air heater has a Reynolds number of 142.93 which falls into the laminar flow. It can be depicted from this figure that around 0.0001 s, the velocity across the air heater fluctuates around 0.08 m/s and tends to zero the closer it gets to the walls of the device. After 0.001 s the velocity profile becomes apparent showing a gradient from 0.1 m/s right at the centre of the pipe, whereas the velocity at a close proximity with the walls becomes apparent slowing the fluid in this section. After 0.01 s, the velocity profile shows a maximum velocity of 0.12 at the centre of the pipe and the velocity gradient is well defined. It is clear that at 0.1 s, the same velocity profile is shown for this system. This suggests that after 0.01 s, the gas phase flowing in the process air heater is well mixed and shows a laminar behaviour dictated by its previously calculated Reynolds number.

4.6.Conclusions

The Peclet number is considerably lower than 1. This would suggest that convection is the dominant mean of mass transport in the gas phase. Although convection is known to happen faster than diffusion, for very small volumes (microbubbles) the more efficient means of transport occurs by diffusion. This is the main driver to introduce a microbubble internal mixing that occurs on a time scale of 10^{-3} s, so the condensing vapour or evaporating mixture should obey a rate law that evolves on this rapid time scale. In terms of the Reynolds number, microfluidic systems are known to have a characteristic length is so small that the Reynolds number are mostly always less than 1. In terms of the diffusion time falls into the order of magnitude of $1x10^{-3}$ s

In the ozone free radical initiated esterification, a microbubble with a radius of $1x10^{-4}$ m rising through the liquid mixture, would rise at a terminal velocity of $2.781x10^{-4}$ m/s and have a Reynolds number $3.17x10^{-6}$. This value suggests that the laminar flow is expected in the rising of the microbubble for the esterification unit. It is clear that smaller bubbles have a lower terminal velocity and therefore its residence time would be higher compared to coarse bubbles. Mostly all the bubble sizes tend to be similar to the atmospheric pressure. For bubbles with a diameter less than 50 μm, the internal pressure increases dramatically to a certain extent when decreasing the bubble diameter.

The internal gas pressure increases when the microbubbles are smaller, and it is important to point out that the rate of increase is inversely proportional to the bubble size. A bubble one order of magnitude smaller rises at a terminal velocity two orders of magnitude slower. For the proposed models in this thesis, the liquid layer domain considered in the computational model is ten times bigger compared to the radius of the bubble. This would mean that a microbubble with a radius of $1x10^{-4}$ m rising at a terminal velocity of $2.781x10^{-4}$ m/s would take 3.592 s to rise through the liquid mixture. The diffusion time if possible in the system would be mainly determined by the diffusion time of ozone in the gas domain (inside the bubble).

Around a temperature of 100°C, the ozone decomposition is already intensive, and its time of dissociation fluctuates around 1 s. The reverse reaction of the ozone formation is significantly faster and the oxygen singlet concentration at this condition could be neglected $[O^*]/[O_3]=1x10^{-5}$. A large value of this parameter would result in systems that flash to equilibrium characterised by a rapid vaporisation followed by recondensation as the bubble reaches the second regime. In this study a value of $2x10^{-5}$ has been used in order to guarantee nonequilibrium dynamics that are rapid enough.

Regarding the ozone decomposition models, the HSB model occurs in an order of magnitude of 1 $x10^{-3}$ s. The ozone decomposition takes longer in this mechanism and it can be seen that takes a few steps in order to achieve a decay in time. On the other hand, the TFG model occurs in an order of magnitude of 1 $x10^{-6}$ s.

For the process air heater model, the operating conditions stated previously, at around 0.1 s the gas reaches a thermal equilibrium with the walls of the process air heater. If the gas mixture is left for a bit longer compared to this thermal equilibrium, this results in assuring the outlet gas temperature to be similar to the one set initially to the process air heater. After 0.01 s, the velocity profile shows a maximum velocity of 0.12 at the centre of the pipe and the velocity gradient is well defined. It is clear that at 0.1 s, the same velocity profile is shown for this system. This suggests that after 0.01 s, the gas phase flowing in the process air heater is well mixed and shows a laminar behaviour dictated by its previously calculated Reynolds number.

5. 0-D with irreversible reaction for the esterification of FFA

In this chapter the irreversible 0-D model is presented for the analysis of the reaction mechanism proposed in this thesis. The 0-D model is chosen since it has no spatial dependency, it is defined to be time dependent. The models are given by ordinary differential equations, since the model is a function of only one variable (time). The main purpose of this approach is to explore the behaviour of the three-step mechanism on its own, in order to have a concrete idea of the kinetics and therefore understanding the role of the different parameters in this set of reactions. It is important to isolate the reactions in order to analyse the timescale and respective values for the rate constants which will be used to fit the model to experimental data. The relevant data calculations and estimations presented in both chapter 3 and 4 are here considered.

The importance of this model relies on maximising the production rate of the biodiesel by increasing the initial concentration of oxygen singlet ($O\cdot$) which is thought to catalyse the proposed reaction mechanism and take the reaction to completion. The model does not take into account heat transfer on the surface, phase changes or transport of diluted species since they are set in a 0-D model. The irreversible mechanism is considered for this chapter since esterification is known to be a reversible reaction of second order. In this chapter the reader can find the model description, determination of rate constants, least squares fitting of the model and the appropriate results for the variation of different parameters such as, temperature and the initial concentration for both methanol and oxygen singlet.

5.1. Model description

The 0-D model for the chemical reactions involved in the proposed three-step mechanism is built using COMSOL Multiphysics. For the purpose of this chapter, the 0-D model is set to be located on the surface of the microbubbles, where all the species interact following the reaction mechanism. The oxygen singlet ($O\cdot$) reacts with methanol forming free radicals such as, the methoxy radical ($MeO\cdot$) and the hydroxyl radical ($HO\cdot$). Right after this happens, the hydroxyl radicals recombine producing water (H_2O) and oxygen (O_2). Lastly, the Free Fatty Acids (FFA) react with the methoxy radical forming the Fatty Acid Methyl Ester (FAME) and hydroxyl radical, in which is assumed to be the slowest step of the mechanism. The set of equations used in the model are shown below:

$$O\cdot + MeOH \rightarrow MeO\cdot + HO\cdot \tag{71}$$

$$HO\cdot + HO\cdot \rightarrow H_2O + \frac{1}{2}O_2 \tag{72}$$

$$FFA + MeO\cdot \rightarrow FAME + HO\cdot \tag{73}$$

To model the set of equations, the Reaction Engineering module is used considering a time dependent study and a batch reactor type which is defined by the following equation:

$$\frac{d(C_i V_r)}{dt} = V_{liq} R_i \quad (74)$$

where V_{liq} is the liquid volume. For the model here described, a batch reactor is used with a volume of V_{liq}=3.25x10^{-4} m^3. The first two reactions in the proposed mechanism are assumed to be in equilibrium and the last step is the slowest one, dictating the timescale for the overall reaction rate. In this chapter irreversible reaction mechanism is studied. When the reactions are input in the modelling software, the fact that there are two equilibrium reactions containing the hydroxyl radical ($HO\cdot$) caused issues when solving for the concentrations of the different species. Having said this, the reaction rate for the second step is set to be so fast that it feels like equilibrium compared to the final reaction. The initial values for the volumetric species concentration are shown in Table 18, traces of some of the species have been added to the model to get the simulation running. FFA and methanol have the same initial molar concentration in the liquid, this is in agreement with the stoichiometric ratio for these two species equal to 1:1. Having said this, the initial concentration for both methanol and FFA is given by:

$$[FFA]_i = [MeOH]_i \quad (75)$$

The calculations for the initial concentration values are shown in chapter 4. The resulting value for the $[FFA]_i$= 301.53 mol/m^3. In terms of the initial concentration of $O\cdot$ used for the fitting of the model to the experimental data, the calculations are shown in the previous chapter. The resulting value for the $[O\cdot]_i$= 281.25 mol/m^3.

Table 18 Volumetric species initial concentration values used in the 0-D model.

Species	Concentration (mol/m^3)
O·	281.25
MeOH	301.53
MeO·, HO·, H_2O, O_2, FAME	1x10^{-4}
FFA	301.53

The first step described by the reaction $O\cdot + MeOH \rightarrow MeO\cdot + HO\cdot$ is set to be in equilibrium following the equation $k_{eq} = k_{eq0}$, where k_{eq0} is equal to 1. For the second step in this reaction mechanism $HO\cdot + HO\cdot \rightarrow H_2O + \frac{1}{2}O_2$, the reaction is to be reversible where the rate constants are given by $k^f = k^r \cdot k_{eq0}$ and k_{eq0} is equal to 1. Lastly, the third step $FFA + MeO\cdot \rightarrow FAME + HO\cdot$ is set to be irreversible where the forward rate constant *kf3* is studied to illustrate the importance of the reaction kinetics of this mechanism, and then be fitted to the experimental data. In order to analyse the effect of different rate constants and the initial concentration of $O\cdot$, parametric sweeps are carried out changing the value at different orders of magnitude of the parameters shown Table 19.

In the next sections of this chapter, the determination of the rate constants *kf2* and *kf3* are described and the variation of different operating conditions is studied for the irreversible mechanism.

Table 19 Parameters used in the irreversible 0-D model.

Parameter	Name
Forward rate constant Reaction 2	kf2
Forward rate constant Reaction 3	kf3
Initial concentration of O·	rado

The reaction type is kept as irreversible and the concentration of the different species involved in the mechanism is given by:

$$\frac{dC_i}{dt} = v_i r \tag{76}$$

where the third step defined by the reaction $FFA + MeO\cdot \rightarrow FAME + HO\cdot$, the forward rate constant is described by the parameter *kf3*.

The reaction mechanism described earlier in this section can be separated into two stages for its analysis. The first stage involves the first two reactions where the oxygen singlet reacts with methanol on the surface, and the resulting hydroxyl radical recombines forming water and oxygen. This stage is carried in preparation for the second stage which involves the reaction on the methoxy radical with the free fatty acid in order to form the fatty acid methyl ester. In order to determine the heat of reaction for each one of the three steps proposed in this mechanism, the heats of formation for each species are shown in Table 20.

Table 20 Heats of formation for selected species at 25°C and 100kPa (Cox, et al., 1989).

Species	Heat of formation (kJ/mol)
O·	438.05
MeOH	-201.6
MeO·	17.15
HO·	37.2
H_2O	-241.826
O_2	0
FFA	-764.8
FAME	-727.64

The heats of reaction for each step in the mechanism are shown in Figure 36. The two reactions considered in the first stage of the mechanism have a negative value, indicating they are exothermic. On the other hand, the reaction in the second stage (esterification) theoretically has a value of 57.21 kJ/mol which indicates an endothermic reaction.

$$O\cdot + MeOH \rightarrow MeO\cdot + HO\cdot \qquad \Delta H_{rxn} = -182.1\ kJ/mol$$

$$HO\cdot + HO\cdot \rightarrow H_2O + \frac{1}{2}O_2 \qquad \Delta H_{rxn} = -316.22\ kJ/mol$$

$$FFA + MeO\cdot \leftrightarrow FAME + HO\cdot \qquad \Delta H_{rxn} = 57.21\ kJ/mol$$

Figure 36 Heats of reaction for the proposed mechanism.

The heats of reaction are discussed in more depth in the discussion section of this chapter. It is important to mention that models proposed in chapter 5 and 6 do not consider any heat transfer in fluids or transport of diluted species, they strictly focus on understanding and exploring the impact of the rate constants in the reactions considered in the proposed mechanism.

5.2. Determination of rate constants

In order to explore the kinetics of the first two steps (instantaneous) in this mechanism, the third reaction is disabled in the computational model. A parametric sweep is carried out for the forward rate constant (*kf2)* to explore the time scale and effects of the spontaneous reactions with an initial time step of 1x10^{-8} s, an initial concentration for $[FFA]_i$= 301.53 mol/m^3 and an initial concentration for $[O\cdot]_i$= 281.25 mol/m^3. The different time scales at which the spontaneous reactions (reaction 1 and 2) reach equilibrium at three different values of *kf2* are illustrated in Figure 37. For a value of the forward rate constant (*kf2)* of 1, 1x10^5, 1x10^6 and 1x10^7 m^3/(s·mol), the reaction reaches equilibrium at a time scale of 1x10^{-1}, 1x10^{-6}, 1x10^{-7} and 1x10^{-8} s respectively.

Once the third reaction is enabled, the effect of *kf2* can be studied by using another parametric sweep to explore the differences this may have in the water concentration. For this sweep, *kf3* is kept constant with a value of 1 m^3/(s·mol). *kf2* controls the time scale that takes for the spontaneous reactions to reach equilibrium. After 1x10^{-6} s there is no discernible difference between the three values for this parameter ranging 1x10^5-1x10^7 m^3/(s·mol), so the value of *kf2*= 1x10^5 m^3/(s·mol) is chosen as a set value throughout the studies.

To demonstrate the effect of this parameter in the water concentration, a new value of *kf2*=1 is introduced in the parametric sweep, which shows a discernible difference when compared to values of kf2=1x10^5-1x10^7 m^3/(s·mol). Using the right value for *kf2* is important since this parameter dictates how much water is being produced and therefore transferred into the bubble. This suggests that the value of *kf2* needs to be big enough to describe the spontaneous reactions but increasing its value above 1x10^5 m^3/(s·mol) has no significant impact since equilibrium is reached before the third step takes place.

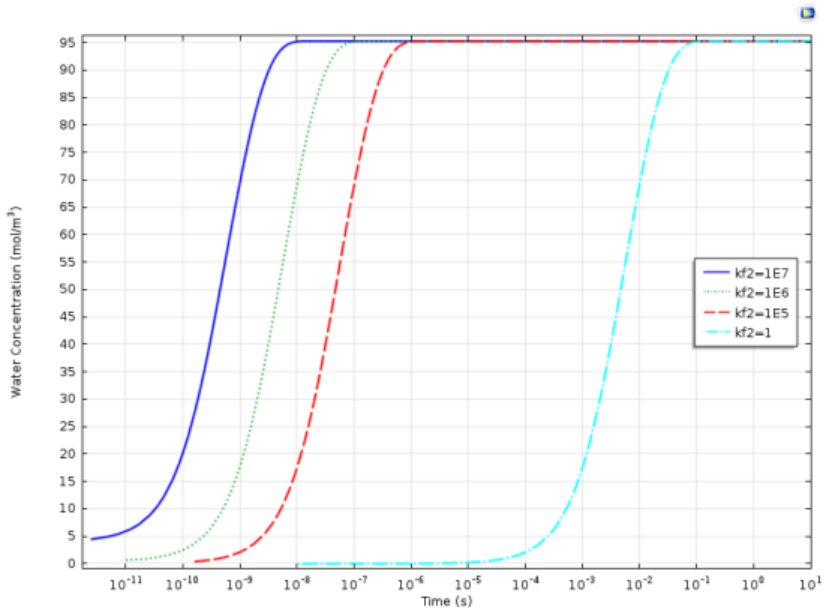

Figure 37 kf2 effect on the water concentration for the spontaneous reactions.

In Figure 38 is shown time scale at which both the spontaneous and the slow step in the proposed mechanism reach equilibrium when a value for *kf2* above 1E5 $m^3/(s \cdot mol)$ is used, being in the order of $1x10^{-6}$ and 1 s respectively. The water concentration at equilibrium is 254.46 mol/m^3.Additionally, when *kf2* has a value of 1 $m^3/(s \cdot mol)$ the overall mechanism reaches equilibrium in the order of 1s. In this scenario, the spontaneous reactions do not reach equilibrium before undergoing to the third reaction, that explains why the curve only exhibits one plateau after 1s. Plots used in this model consider an x-axis log scale since different time scales are explored.

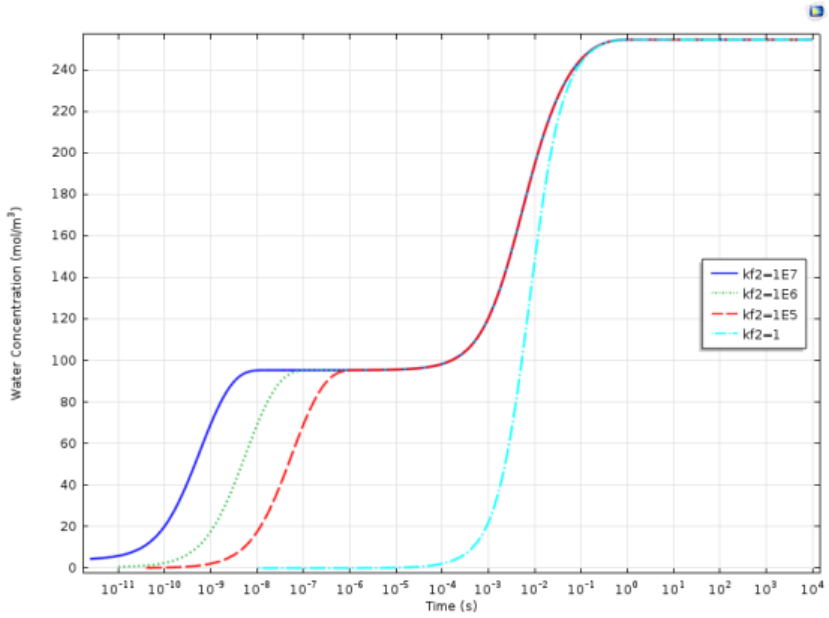

Figure 38 kf2 effect on the water production for the overall mechanism.

Regarding the effect of *kf2* in terms of FAME production, a sensitivity study is conducted by using a parametric sweep of *kf2*. In Figure 39, the parameter *kf2* shows no effect on the FAME concentration.

To magnify the potential differences between the values of *kf2*, a double log plot is used where no differences are depicted between the range of values for *kf2* of 1-1x10^{7} m^{3}/(s·mol). The y-axis log scale is used to elucidate if there are differences in the FAME concentration at the beginning of the reaction (t<1x10^{-6} s) due to a variation in the parameter *kf2* but for all the values tested of this parameter no significant difference is depicted. In other words, no sensitivity to *kf2* on FAME production is shown.

Figure 39 shows that the FAME production is completely independent on *kf2*, but since this parameter affects the water production, *kf2* should not have a value of 1 m^{3}/(s·mol) since this model is interested in how much water is entering the microbubble. Although it is not possible to see changes in FAME concentration caused by varying *kf2,* there is an impact in terms of water production.

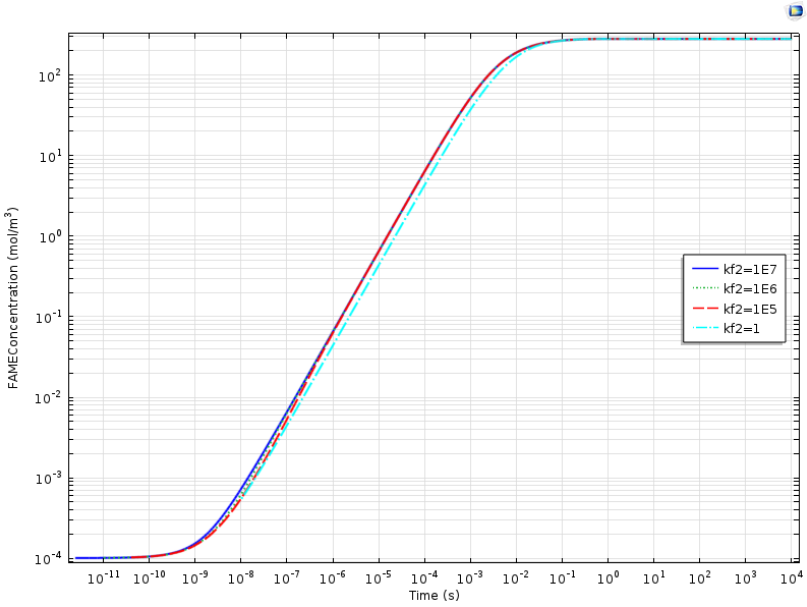

Figure 39 Sensitivity to kf2 on FAME production.

Having completed the parametric sweep for the rate constant *kf2* and established the correct order of magnitude, having a value of 1x10^{5} m^{3}/(s·mol), the next step is to set explore the appropriate values for the rate constant *kf3* for the slowest reaction ($FFA + MeO \cdot \rightarrow FAME + HO \cdot$) in the mechanism. In Figure 40, the effect of the rate constant *kf3* on the FAME production is shown.

The aim of the parametric sweep is to find the appropriate order of magnitude for *kf3,* so it is in agreement with the experimental data. According to the experimental data gathered, the three-step mechanism should reach equilibrium around 20 h. For a value of the forward rate constant of 1x10^{-5}, 1x10^{-6} and 1x10^{-7} m^{3}/(s·mol), the reaction reaches equilibrium at a time scale of 10, 1x10^{2} and 1x10^{3} h respectively. The three rate constants reach equilibrium with a FAME concentration of 281.25 mol/m^{3}, this means for all the treatments here studied the reaction is taken to completion. Having said this, the most appropriate value for *kf3* is 1x10^{-5} m^{3}/(s·mol) since it matches the correct order of magnitude when the three-step mechanism reaches equilibrium.

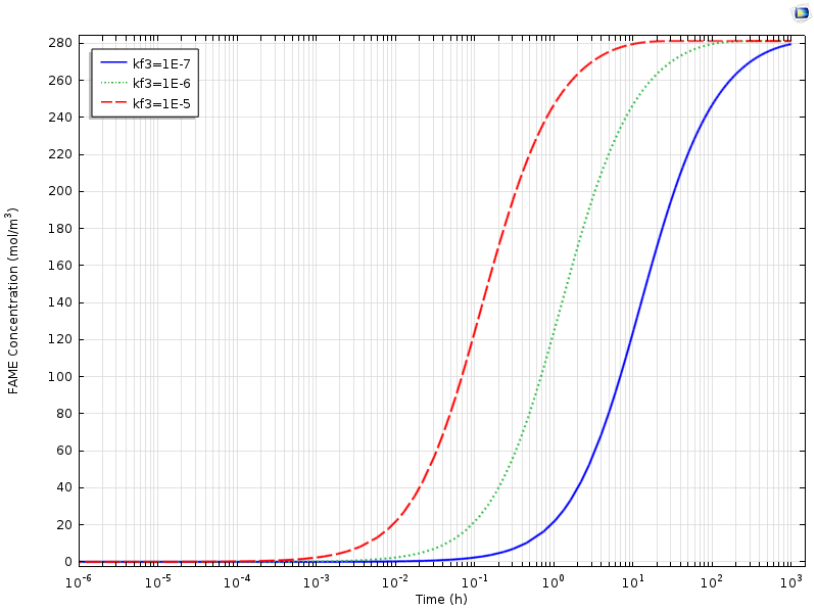

Figure 40 kf3 effect on the overall FAME production using kf2=1x10^5 m^3/(s·mol).

In Figure 41, the initial concentration of $[O\cdot]$ effect of on FAME production is shown. The values for *kf2* and *kf3* were set to 1x10^5 and 1x10^{-5} m^3/(s·mol). It can be depicted that increasing the initial concentration for the species $O\cdot$ increases the FAME production until it reaches a maximum when $[FFA]_i = [O\cdot]_i$. For an initial concentration of $[O\cdot]$ of 10, 100 and 281.25 mol/m^3, the final FAME concentration is equal to the initial concentration of $[O\cdot]$.

But for values when the initial concentration of $O\cdot$ is greater than that of FFA, the FAME concentration reaches a maximum value of 301.53 mol/m^3. This means that the amount of FAME produced in this set of reactions is limited by the initial concentration of $O\cdot$, in other words the species $O\cdot$ is the limiting reagent. The reaction reaches an equilibrium in the correct order of magnitude of 10 h, this is when $O\cdot$ is totally consumed and the reaction is taken to completion achieving a resulting concentration of FAME of 301.53 mol/m^3. This combination of rate constants is then used for the least squares fitting for the 0-D irreversible model.

The mechanism achieves a conversion for FFA of 93.27% and when equilibrium is reached the final concentration of FAME is 281.25 mol/m^3. In other words, the final concentration of FAME in the irreversible reaction mechanism is taken to completion and is equal to the initial concentration of $O\cdot$, following the equation below:

$$[O\cdot]_i = [FAME]_f \tag{77}$$

It is important to mention that this condition only applies when the initial concentration of $O\cdot$ is smaller than the one for FFA. This is because the species $O\cdot$ is the limiting reagent in the proposed reaction mechanism, this condition is stated by:

$$[O\cdot]_i < [FFA]_i \tag{78}$$

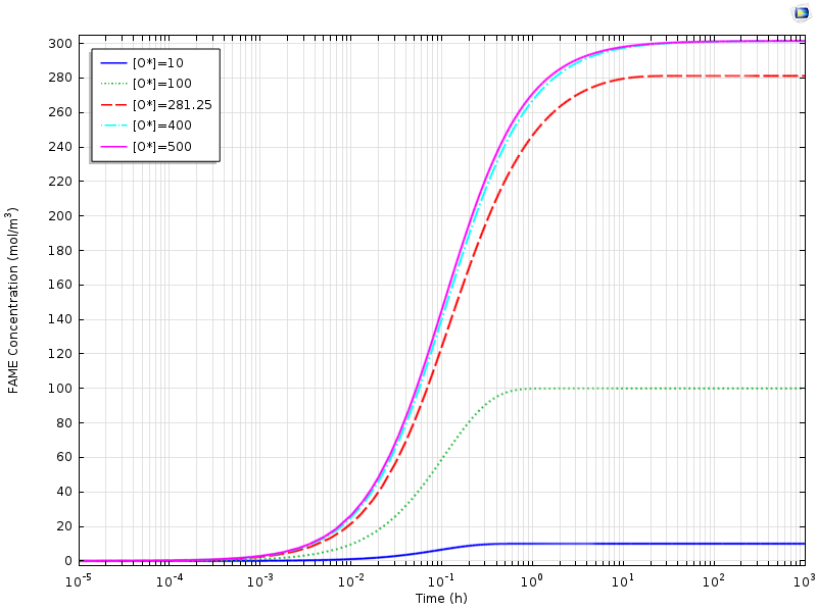

Figure 41 $O\cdot$ initial concentration effect on FAME production.

The concentration profile for FFA, FAME and water is shown in Figure 42. This profile is obtained using an initial concentration for water, FFA and $[O\cdot]$ of $1x10^{-4}$, 301.53 and 281.25 mol/m^3. The value for the forward rate constant *kf2* is $1x10^5$ m^3/(s·mol) and the forward rate constant *kf3* has a value of $1x10^{-5}$ m^3/(s·mol). The resulting irreversible reaction mechanism reaches equilibrium at 10 h, which is the correct order of magnitude for the experimental data. In terms of water production, the concentration profile exhibits two plateaus, the first one for the spontaneous reactions at $1x10^{-10}$ h and the second one for the third step at 10 h.

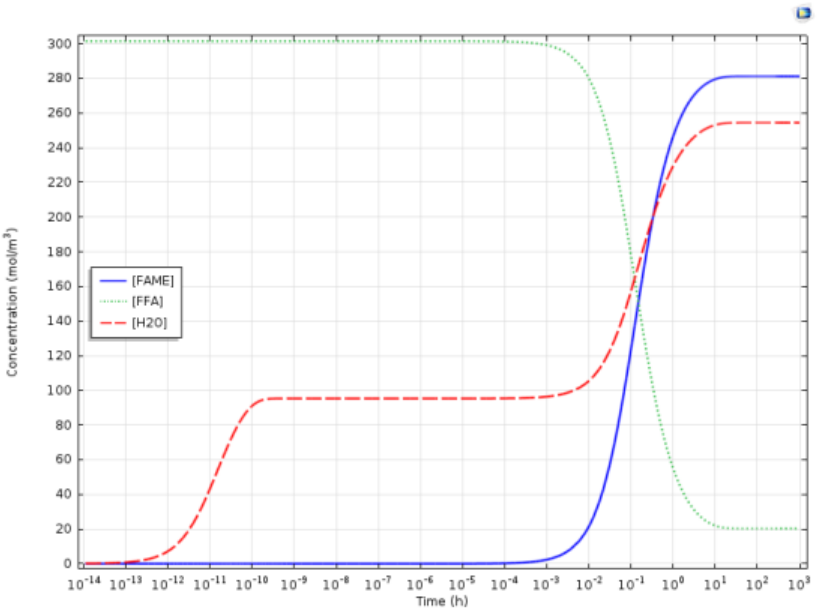

Figure 42 FAME, FFA and water concentration profile in time.

For these two plateaus the concentration reached at equilibrium is 95.29 and 254.46 mol/m^3 respectively. The production of FAME reaches a plateau at equilibrium with a concentration of 281.25

mol/m^3. With the parameters previously mentioned, a conversion of 93.27% of FFA is achieved at equilibrium resulting in a production of 25.82 and 23.36 g for FAME and H_2O respectively.

5.3.Least squares fitting for 0-D irreversible model

The irreversible 0-D model used in Section 5.2 follows a reaction rate for FAME described by the following equation:

$$r_{FAME} = k_f[FFA][MeO\cdot] \tag{79}$$

$$r_{FAME} = k_{f3}k_1k_2^{\frac{1}{2}}[FFA]\frac{[MeOH][O\cdot]}{[H_2O]^{\frac{1}{2}}[O_2]^{\frac{1}{4}}} \tag{80}$$

where *kf* is the combination of different rate constants. The procedure describing how this rate constant is calculated is described in Chapter 7 in more detail. The forward rate constant for the irreversible reaction of the slowest step is therefore defined by:

$$k_f = k_{f3}k_1k_2^{\frac{1}{2}} \tag{81}$$

In Figure 43, one of the curves from the experimental data is shown and it can be depicted that the experimental points do not follow a linear behaviour, so a non-linear regression method is needed to compare the curvature of these lines. After fitting the curves to a 2nd order polynomial trendline, the curvature of the three temperatures is determined by the 2nd derivative. At 20, 40 and 60°C, the value for the second derivative is -0.1728, -0.2796 and -0.8738 suggesting that a higher temperature, the line produced from plotting the FAME production in time show a more pronounced curvature. The experiment was carried using different FFA content with values of 10, 15 and 20%. These curves belong to the FFA treatment with an initial content of 20% using waste cooking oil at 20, 40 and 60°C.

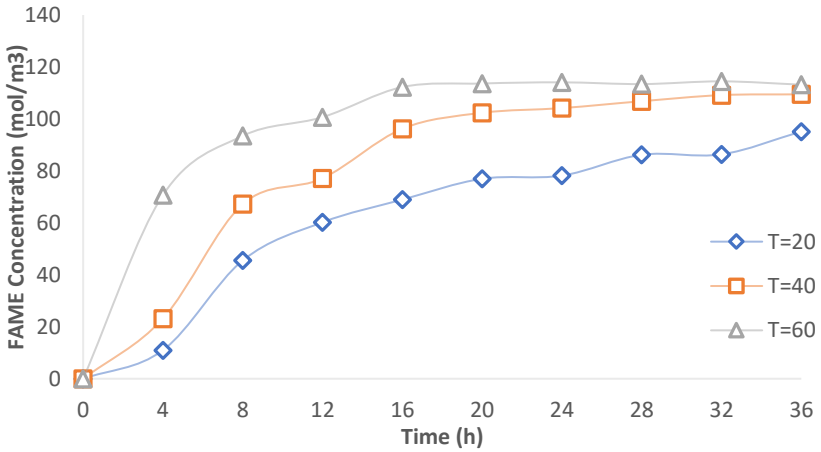

Figure 43 FAME production over time from the experimental data.

The reaction mechanism here proposed is then summarised in the overall reaction equation which is described below:

$$FFA + MeOH + O\cdot \leftrightarrow FAME + H_2O + \frac{1}{2}O_2 \quad (82)$$

As mentioned in Section 3.1, the microbubbles generated with a fluidic oscillator have an initial concentration for the free radical $O\cdot$ of [$O\cdot$]= 4500 ppm which corresponds to the initial concentration of [$O\cdot$]= 281.25 mol/m^3 used in these models. The production rate of the biodiesel is then maximised by producing a high amount of $O\cdot$ using an advanced oxidation plasma reactor. It has been reported by Zimmerman and Lozano Parada that it is possible to tune a plasma reactor under specific conditions, so a maximum of $O\cdot$ at 1x10^{-3} s it then produced. This means there is no need to form the ozone species for then to be decomposed in $O\cdot$, but by tuning the device a set amount of this species can be produced (Lozano-Parada & Zimmerman, 2010).

COMSOL with MATLAB is used for the least squares fitting of this model. This is a mathematical procedure used to find the best-fitting curve to the given set of experimental points. In principle the fitting minimises the sum of the squares of the offsets of the points from the curve. The least squares fitting is given by the equation:

$$R^2 = \sum (y^p - y^m)^2 \quad (83)$$

where y^p is the predicted value from the model, y^m is the measured value from the experimental data. In the case of the irreversible reaction for the proposed mechanism, the predicted FAME production (y^p) is a function of time (t) and the forward rate constant (kf), defined by:

$$y^p = F(t_i; k_f) \quad (84)$$

Once the model has been fitted to the experimental data, the values for the forward rate constant for the irreversible reaction of the slowest step (k_f) can be used to elucidate the dependence of the rate constant (k_f) on the absolute temperature for the proposed reaction mechanism. The Arrhenius equation is given by:

$$k = Ae^{-\frac{E_a}{RT}} \quad (85)$$

where k is the chemical reaction rate in s^{-1} and M^{-1}s^{-1} for first and second order rate constants, A is the pre-exponential factor in the same units as the rate constant used, E_a is the activation energy in J/mol, R is the gas constant (8.314 J/(mol K)) and T is the temperature in K. If the rate constant for a reaction obeys this equation, a plot of ln(k) versus 1/T gives a straight line given by:

$$\ln(k) = -\frac{E_a}{RT} + \ln(A) \quad (86)$$

where the slope of the straight line is ($-\frac{E_a}{R}$) and the intercept $\ln(A)$. In Table 24 are shown the different values for the rate forward constant ($kf3$) at 20, 40 and 60°C from the experimental data.

5.4.Results and discussion

The least squares method is carried out to fit the predicted data from COMSOL Multiphysics to match the experimental data. COMSOL with MATLAB is used to perform the fitting of the curves following the code found in Appendix B. It is important to mention that before running the code for each treatment, the initial concentration of [FFA] and the y^m are set to the respective value.

Once the code is run, it gives the value for *kf3* that satisfies the condition of having the least squared error and the values for the new predicted y^p. The values for the rate constant *kf3* for each treatment are found in Table 21. In Section 5.1 a prediction for the right order of magnitude when the reaction mechanism reached equilibrium gave a value for the forward rate constant *kf3* of $1x10^{-5}$ $m^3/(s\cdot mol)$ with a set value of *kf2* of $1x10^5$ $m^3/(s\cdot mol)$. This value of *kf3* is then used as an initial guess for the fitting. The resulting order of magnitude for majority of the fitted curves is $1x10^{-7}$ $m^3/(s\cdot mol)$, in Table 21 the resulting values of *kf3* are shown in $(M^{-1}s^{-1})$ to ease further calculations. Once the values for the rate constant *kf3* are found for all the treatments, the least square statistical analysis is carried out to discuss the overall quality of the fit. The effect of temperature can be easily described in Table 21, an increase in temperature means an increase in the forward rate constant for the three different FFA contents.

Table 21 Rate constant kf3x10^{-4} (1/M.s) values for each treatment.

		Free Fatty Acid %		
		10%	**15%**	**20%**
Temperature (K)	**293.15**	1.6631	0.8855	0.8930
	313.15	1.9970	0.9602	1.2679
	333.15	2.5311	1.2625	2.6740

The least squares method used to fit the predicted and measured data finds the best fitting straight line in a set of points by finding the minimum of the sum of the squares of the vertical deviations. For the iterations used in this method, a condition to find only positive numbers is used since the order of magnitude is $1x10^{-7}$ and the solver could return negative values. The tolerance for the parameter *kf3* in the iterations is set to $1x10^{-10}$ to return values with significant figures.

Table 22 Statistical analysis of the fitted curves.

FFA %	Temperature (K)	Sxx x10^2	Syy x10^2	Sxy x10^2	Cov (x,y)	R^2	S_{error}
10	293.15	4.617	8.040	5.952	66.1321	0.9769	2.2917
	313.15	6.407	7.917	7.043	78.2590	0.9890	1.5765
	333.15	9.932	10.05	9.949	110.5428	0.9957	1.1163

15	293.15	5.074	6.981	5.830	64.7770	0.9796	2.0066
	313.15	8.911	10.85	9.673	107.4807	0.9836	2.2441
	333.15	23.16	21.76	22.28	247.5875	0.9927	2.1304
20	293.15	196.8	216.0	204.5	2272.5366	0.9921	6.9772
	313.15	379.3	425.1	399.5	4438.8676	0.9949	7.8622
	333.15	597.4	592.3	594.7	6607.6516	0.9998	2.0281

Table 22 is comprised of the different terms calculated for the least squares method and its respective quality. *Sxx* and *Syy* are the corrected sum of squares for y^p and y^m respectively. *Sxy* corresponds to the corrected sum of cross products, *Cov(x,y)* is the covariance and S_{error} is the standard deviation of the error. The correlation coefficient R^2 is the parameterised value for the overall quality of the fit.

All the fitted curves have a correlation coefficient greater than 0.97 which suggests that the method used to fit the curves has a high overall quality. For each FFA content (10, 15 and 20%), the highest value for R^2 is achieved at 60°C, since the experimental data shows the plateau behaviour at higher temperatures. As discussed in Section 4.4, the FAME production curves obtained from the experimental data exhibit a more pronounced curve at higher temperatures. This behaviour could be attributed to the effect of temperature in a chemical reaction, since it is known that a higher temperature a reaction occurs more rapidly. In other words, the exponential growth in terms of production of FAME at the beginning of the reaction is more noticeable at higher temperatures. The best fit was achieved at a temperature of 60°C and 20% FFA with a R^2=0.992, the iteration returned a value for the forward rate constant 2.6740×10^{-4} $M^{-1}s^{-1}$. In terms of comparison, the curve with the lowest R^2 was the 10 FFA% at 293.15 K. The treatment 10 FFA% at 293.15 K obtained a forward rate constant of 1.6631×10^{-4} $M^{-1}s^{-1}$(R^2=0.976). In the next chapters, this treatment will be used for further comparison since the change and hence improvement of the fitting of the respective model can be depicted.

From the results obtained in Figure 43, it can be depicted that there is a significance difference in FAME production by changing the temperature. In order to determine if there are any significant differences between the forward rate constants obtained at Free Fatty Acid contents of 10, 15 and 20%, the one-way analysis of variance (ANOVA) with a significance level of α=0.05 is used. For the test a null and alternative hypothesis need to be stated. The null hypothesis to be tested in this case involves the average of the forward rate constants obtained for different FFA contents which is given by:

$$H_o: \mu_1 = \mu_2 = \mu_3 \quad (87)$$

On the other hand, the alternative hypothesis H_a states that at least one mean is different. It is important to mention that this test does specify which specific groups are statistically different from each other. Table 23 show the results obtained for the ANOVA analysis with the relevant values between and within treatment groups. Since the $F_{value}<F_{crit}$ (2.14<5.14), we fail to reject the null hypothesis meaning there is no significant difference between the three groups for the FFA content 10, 15 and 20%. In other words, the forward rate constants that are inferred in this model are not significantly different for the change of FFA content, but they are for the temperature.

Table 23 ANOVA results for the forward rate constant.

	df	SS x10^{-8}	MS x10^{-9}	F	Fcrit
Treatment	2	1.591	7.958	2.144	5.14
Residuals	6	2.226	3.710		
Total	8	3.817			

Having concluded there is no significant different between the groups accounting for the Free Fatty Acid%, the values for the forward rate constant *kf3* are used in the Arrhenius equation to obtain the activation energy (E_a) and pre-exponential factor (*A)* for the forward reaction of the third step. Table 24 contains the value for the average forward rate constant *kf3* at each temperature. By plotting ln(*k*) against 1/T, it is possible to determine E_a and *A.*

Table 24 Linear regression parameters used for Arrhenius equation parameters.

Temperature (K)	Rate constant x10^{-4} (M^{-1}s^{-1})	1/T x10^{-3} (K^{-1})	ln(k)
293.15	1.1472	3.4112	-9.073
313.15	1.4084	3.1934	-8.868
333.15	2.1559	3.0017	-8.442

From the data gathered in the previous table, Figure 44 exhibits a curve that could be fitted by a linear regression. The slope of this curve equates ($-E_a/RT$) and the intercept ln(*A*). The linear regression has a slope m=-1526.7 and an y-intercept=-3.9057. Having said this, the forward reaction for the third step has an activation energy of E_a = 12.692 kJ/mol and a pre-exponential factor of *A* = 2.0127x10^{-2} M^{-1}s^{-1}. These values were calculated using the linear regression with a R^2=0.9453.

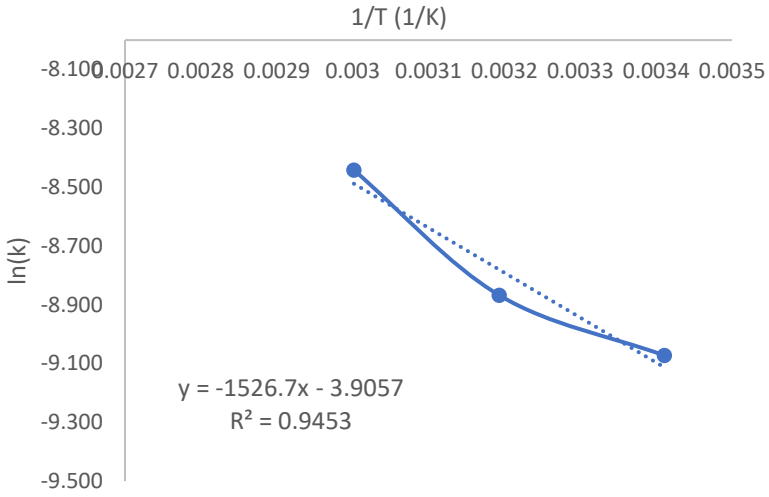

Figure 44 Ln(k) against 1/T plot for the forward rate constant.

The forward rate constant for the third irreversible reaction can be expressed then using the Arrhenius equation, when this expression is combined with the reaction rate for the third step, it is possible to define a new equation for the forward rate constant that contains the parameters previously calculated in the Arrhenius equation, defined by:

$$k_f = k_{f3} k_1 k_2^{\frac{1}{2}} = 0.020127 e^{\frac{-1526.7}{T}} \tag{88}$$

It is important to point out that the first reaction in the proposed mechanism is in equilibrium (k_{eq}=k_{eq0}) with an equilibrium constant k_{eq0}=1, the second reaction is set to be reversible with a forward rate constant *kf2*=1x10^5 m^3/(s·mol), and the third step has a predicted forward rate constant given by the equation:

$$k_f = 0.20127 e^{\frac{-1526.7}{T}} \tag{89}$$

The equation shows an exponential decay law which involves the magnitude of the rate constant as a function of the exponent ($-\frac{E_a}{RT}$). The term RT is used to describe the average kinetic energy, so the exponent is the ratio of the activation energy to the average kinetic energy. A larger ratio will give a smaller rate constant. A low activation energy combined with a high temperature operating conditions will favour larger rate constants and consequently speed up the reaction. Since the terms here discussed occur in an exponent, the effect on the rate constant is considerable (Laidler, 1984).

The effect of the activation energy on the rate constant can be depicted in Figure 45. In this case a modest activation energy difference of 15kJ/mol reduces the rate constant by a factor of 10^2. This exponential term considered in the Arrhenius equation suggests that the forward rate constant decreases exponentially when the activation energy increases, and the rate of reaction would decrease as well since it is directly proportional to the rate constant. It can be noticed that an increase in the FFA content means an increase in the activation energy since the esterification is needed to reach the

activation stage. A reaction with a low activation energy should proceed faster when compared with one that considers a larger activation energy. The intensified esterification reaction here studied showed a value for the activation energy of E_a = 12.692 kJ/mol.

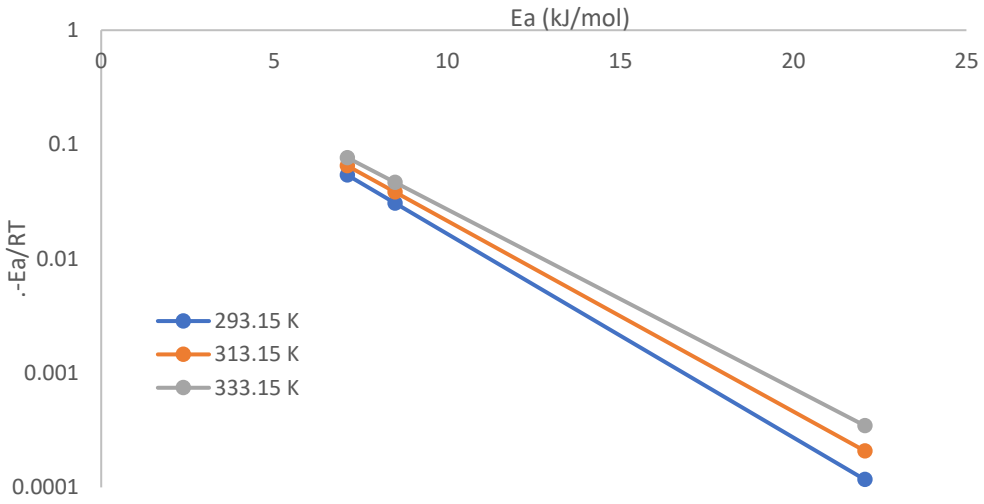

Figure 45 Semi-log plot of -Ea/RT against Ea for the forward reaction.

Ahmed et al reported an activation energy of 16.988, 34.576 and 46.601 kJ/mol for systems with varying molar ratios of ethanol to acetic acid of 10, 30 and 50 respectively. Suggesting the reaction mechanism here proposed has a lower activation energy than conventional esterification (Logan, 1982; Ahmed, et al., 2010).

5.4.1. Variation of temperature

Once the parameters for the Arrhenius equation are obtained, they can be used in COMSOL to run the irreversible mechanism to explore the effect of temperature on FFA, FAME and water production. Consequently, a parametric sweep is performed to explore the effect of varying the temperature in the range 283.15-343.15 K by using the Arrhenius equation when calculating the forward rate constant for the third step. Before the third step in the proposed irreversible mechanism, there is no discernible difference between the curves which could be explained since the Arrhenius equation is only considered in the last step.

In Figure 46, it is easy to appreciate the difference in time between the reaction at the highest and lowest temperature. When compared at a same time, the highest temperature always shows a higher FAME production right after the third step takes place. An initial concentration of $[O\cdot]$=281.25 mol/m^3 and [FFA]=301.54 mol/m^3 are used in this sweep.

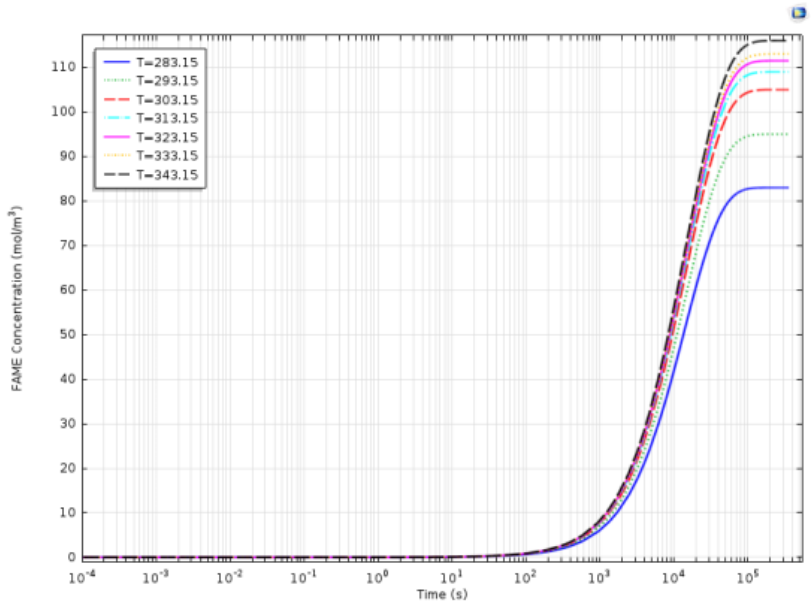

Figure 46 Temperature (K) effect on FAME production.

When the temperature is varied in the range 283.15-343.15 K, intervals of 10 K, the reaction mechanism reaches a final FAME concentration of 82.91, 95.03, 104.63, 109.37, 111.62, 113.15 and 116.65 mol/m^3 respectively. As soon as the third reaction takes place, the curves for each temperature start separating in the exponential phase. It is the curve at 70°C the one showing the highest FAME production. With the parameters previously mentioned, a FAME percentage yield of 31.558, 36.307 and 37.537% is achieved at 273.15, 293.15 and 313.15 K.

Even though at a temperature of 70°C the FAME production shows a more rapid reaction rate, the boiling point of methanol it is a matter of importance. Methanol at standard conditions has a boiling point 64.7°C, this suggests that if the reaction mechanism is carried a temperature higher than the boiling point evaporation of this component will take place. In the proposed model in Chapter 7, the evaporation of methanol could potentially mean that this species is found in the vapour phase inside the bubble. If so, the methanol could react with the oxygen single found in this domain producing the methoxy radical and hydroxyl radicals which then react on the surface with the other reactants (Zimmerman, et al., 2013).

From the Arrhenius equation, it can be inferred that the rate constant of an uncatalysed reaction is more affected by the operating temperature than a catalysed reaction. This behaviour is explained since the catalysed reaction has a smaller activation energy than the corresponding uncatalysed reaction. The exponential term of the Arrhenius equation includes the activation energy and the temperature as the numerator and denominator respectively, meaning a smaller activation energy would result in less of an impact on the forward rate constant compared to a larger activation energy (Laidler, 1984; Logan, 1982).

$$\ln\left(\frac{k_2}{k_1}\right) = -\frac{E_a}{R}\left(\frac{1}{T_2} - \frac{1}{T_1}\right) \quad (90)$$

In order to analyse the effect of temperature in the forward rate constant, the Arrhenius equation is used. When the temperature is raised ($T_2 > T_1$), then the right side of the equation is positive. Consequently, the value of *k2* would be greater than *k1*. It can be inferred from this equation that the effect of temperature on the rate constant is proportional to the activation energy (E_a). For the reaction mechanism here proposed, the forward rate constant *kf3* has a value of 1.1472×10^{-4}, 1.4084×10^{-4} and 2.1559×10^{-4} $M^{-1}s^{-1}$ at 273.15, 313.15 and 333.15 K. The behaviour followed by the forward rate constants is in agreement with the effect of temperature on rate constants. Considering that the third step in this mechanism, the esterification, has a heat of reaction of $\Delta H_{rxn} = 57.21$ kJ/mol, the reaction is defined as endothermic which means the system absorbs energy from the surroundings. If the forward reaction of the esterification is endothermic, the other direction (reverse reaction) is exothermic.

The results from the forward rate constants suggest an endothermic behaviour with an increase in the rate constant when the temperature is increased. This pattern has been reported by Camara and Aranda with the esterification of palmitic and lauric acid using ethanol and a niobium oxide catalyst for the production of biodiesel. Marchetti et al also reported an endothermic behaviour studying the heterogeneous esterification of oleic acid and soybean oil with acid resins and anhydrous ethanol (Marchetti, et al., 2007; Camara & Aranda, 2011).

In terms of water production, the concentration profile exhibits two plateaus, one for the first two spontaneous reactions and the last one for the third step (esterification).

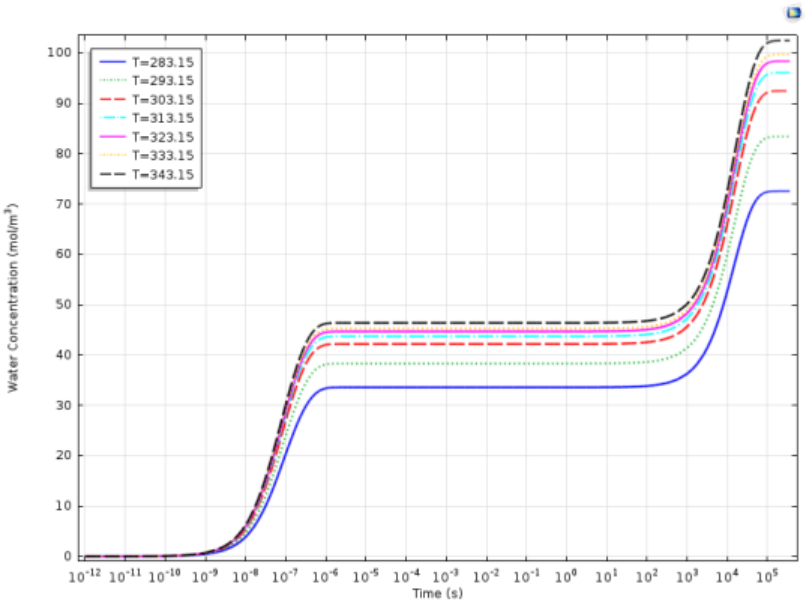

Figure 47 Effect of temperature on water production.

After the first plateau is reached, when the temperature is varied in the range 283.15-343.15 K, intervals of 10 K, the reaction mechanism reaches a water concentration of 33.51, 38.37, 41.17, 43.36, 44.27, 45.18 and 46.42 mol/m^3 respectively. When the same temperature values are used, the final water concentration reaches a value of 72.46, 83.24, 92.47, 96.08, 98.47, 99.41 and 102.38 mol/m^3 respectively. Figure 47 shows the effect of temperature on the water production for the irreversible mechanism.

If the temperature is increased, both the forward and reverse rates increase but it is important to mention that the rate of the endothermic reaction is increased more. Following Le Chatelier's principle, equilibrium will then shift in the endothermic reaction therefore the added heat is consumed. In terms of the equilibrium constant (K_{eq}), raising the temperature would increase the equilibrium constant for an endothermic reaction and the opposite effect for an exothermic reaction (Vallance, 2016).

5.4.2. Variation of initial methanol concentration

The importance of the alcohol in the esterification reaction relies on the fact that the reaction is reversible. Therefore, the efficiency of this reaction is affected by the amount of alcohol used. The reverse reaction can be reduced by using an excess of methanol in the oil:alcohol molar ratio. Abbas and Abbas reported the effect of varying from 1:1 to 1:6 the molar ratio of oleic acid to ethanol. The oleic acid conversion to the ester increased from 0.61 to 0.87 between the treatments of 1:1 and 1:6 respectively after 180 minutes using sulfuric acid as the catalyst at 70°C. Marchetti and Errazu reported a maximum conversion of free fatty acid of 0.96 with a molar rate of 1:6.126 after a reaction time of 240 minutes at 55°C (Abbas & Abbas, 2013; Marchetti & Errazu, 2008).

The use of an excess of alcohol for the esterification incurs in an increase of the process cost. Therefore, in the proposed mechanism the molar ratio oil:methanol is set to 1:1. The main difference between the reaction mechanism in this thesis and the previous set-ups previously discussed is that the proposed mechanism considers a free radical stage which catalyses the reaction. Following the three-step mechanism described in Section 5.1, it can be noticed that one mole of the free radical $O\cdot$ reacts with one mole of methanol to form the methoxy radical and hydroxyl radical. The limiting reactant in this mechanism is the $O\cdot$, which is related to the methoxy radical in the esterification step.

To explore the effect of methanol on FAME production, an initial concentration of [$O\cdot$]=281.25 mol/m^3 and [FFA]=301.54 mol/m^3 is used in this sweep at 333.15 K. The overall concentration profile for water, methanol, oxygen, FFA and FAME over time is found in Figure 48. In terms of methanol and oxygen production, the concentration profile exhibits two plateaus, the final concentration reached for methanol and oxygen is 188.39 and 49.96 mol/m^3. After the spontaneous reaction reached equilibrium, the concentration for methanol and oxygen is 196.22 and 22.65 mol/m^3. This results in a production of 4.586 g of oxygen.

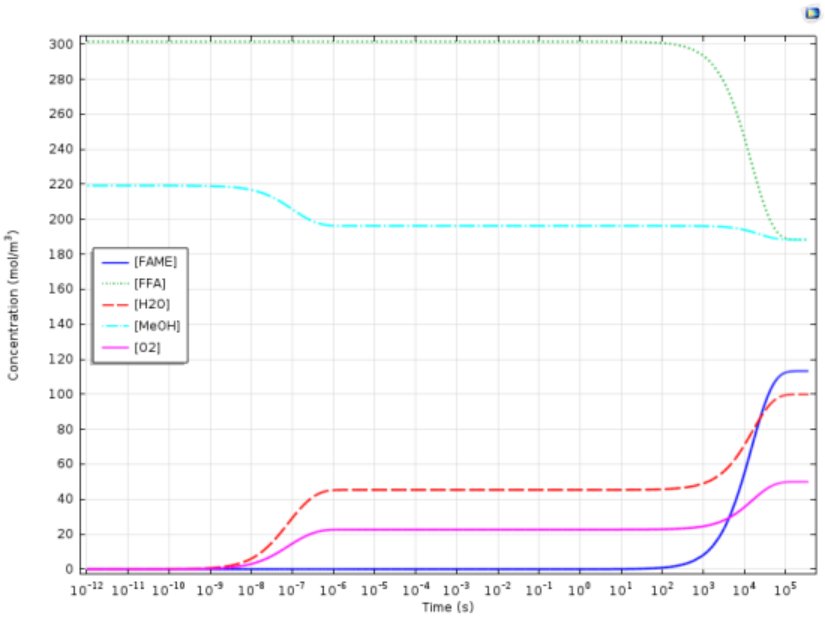

Figure 48 Concentration profile for selected species.

From Figure 48 here studied, it can be depicted that the initial concentration for methanol exhibits an initial value of 220 mol/m^3. This is nearly two thirds of the initial concentration that was set into the model. It is important to mention that the initial condition used in Figure 48 considered an equimolar concentration for both methanol and FFA. It can be noticed that the initial concentration reported from COMSOL is 220 mol/m^3. This change in the initial condition is then attributed to the default solver when finding consistent initial conditions, since the system is considered to be stiff which is fairly common in time integration numerical analysis. This type of system is generally found when computing dynamics that are different orders of magnitude from each other or an incongruity of the time scales explored in the model. In this case, the system considers kinetics happening at a very rapid and slow rate. Having said this, the system needs to get results on the "slow" time scale that properly model the fast reaction kinetics.

In order to study the effect of the initial concentration of methanol on the FAME production and the FFA conversion with an initial concentration of $[O\cdot]$=281.25 mol/m^3, a parametric sweep for different concentrations of methanol is carried out. Figure 49 illustrates the effect of the initial methanol concentration on the FFA conversion and FAME production. This figure shows a comparison between the theoretical FAME production and the experimental data at different initial concentrations of methanol. Theoretically, when the methanol concentration is lower than the initial concentration of $O\cdot$, all the methanol is used and turned into methoxy radicals which then react to form FAME, in other words $[MeOH]_i = [FAME]_f$. But when the initial concentration of methanol is higher than the one of $O\cdot$, $[O\cdot]_i = [FAME]_f$. This suggests that the $O\cdot$ is the limiting reactant in the three-step mechanism. Therefore, no need for an excess of methanol is required in this mechanism since the governing factor for FAME production is the initial concentration of $O\cdot$ (Kastratović & Bigović, 2017).

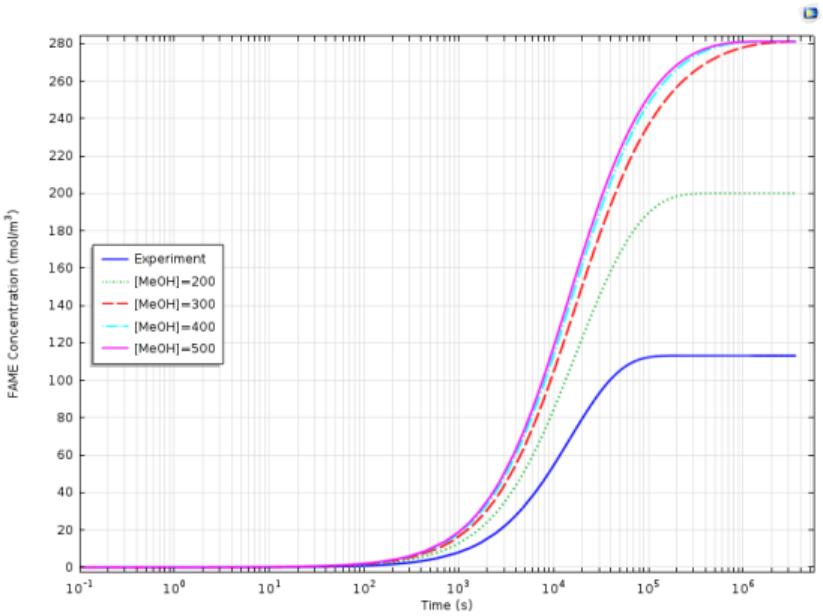

Figure 49 Methanol concentration effect on FAME production and FFA conversion.

In the irreversible mechanism can be noticed that the initial concentration of $O\cdot$ will limit the reaction forcing to achieve a maximum percentage yield for FAME production of 93.274%. This is the main driver to explore the effect of the $O\cdot$ concentration in order to maximise the FAME production. As it can be noticed from the graph the experimental data is far from being similar to the theoretical, but this means there is room for improvement. This could be attributed to the fact that the experiments were carried out using a considerable large layer thickness for the liquid domain and consequently condensation of water is favoured since the microbubble cools down before reaching the surface.

5.4.3. Variation of the initial O· concentration

The limiting reactant in the proposed mechanism is the initial $O\cdot$ concentration. This is why one of the main purposes of this thesis is to maximise the production rate of the biodiesel by producing a high amount of $O\cdot$ using an advanced oxidation plasma reactor. It has been reported by Zimmerman and Lozano Parada that it is possible to tune a plasma reactor under specific conditions, so a maximum of O_3 is produced at $1x10^{-2}$ s and $O\cdot$ at $1x10^{-3}$ s. This means there is no need to form the ozone species for then to be decomposed in $O\cdot$, but by tuning the device a set amount of this species can be produced (Lozano-Parada & Zimmerman, 2010; Rehman, et al., 2016).

The intensified esterification mechanism is catalysed by the oxygen singlet ($O\cdot$) and uses this species as the limiting factor for the reaction to be taken into completion. The maximum yield for FAME production is seen when the $O\cdot$ is put in excess in the system. In order to study the effect of $O\cdot$ on the FAME production, t is important to analyse what happens to the radical species during the mechanism. Figure 50 illustrates the concentration profile for the radical species $O\cdot$, $HO\cdot$ and $MeO\cdot$ over time.

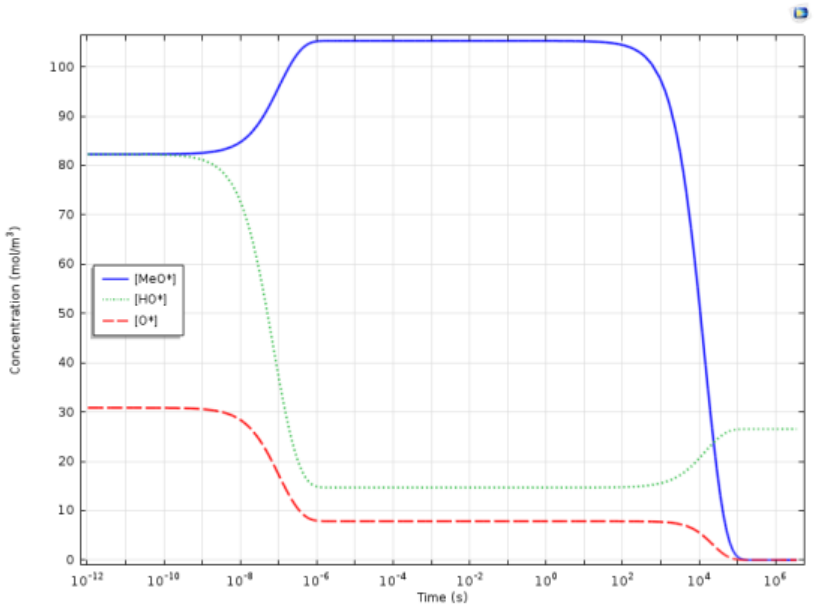

Figure 50 Radical species concentration profile over time.

It can be noticed in this figure that both the methoxy radical and the hydroxyl radical have an initial concentration of 82.27 mol/m^3, and the oxygen singlet has a concentration of 30.88 mol/m^3. Both the methoxy and hydroxyl radical are produced in the first reaction which is set to be at equilibrium. When the second step of this mechanism reaches an equilibrium around 1x10^{-6} s, the methoxy, hydroxyl and oxygen singlet radicals show an intermediate concentration of 105.27, 14.68 and 7.87 mol/m^3. Once the third step has reached equilibrium, all the methoxy radical and oxygen singlet are used to produce to produce FAME. The third step in this mechanism considers the production as well of hydroxyl radical, when this step reaches equilibrium the final concentration of hydroxyl radicals is 26.56 mol/m^3.

The effect of the initial concentration of the oxygen singlet on the FFA conversion and FAME production is illustrated in Figure 51. This figure shows a comparison between the theoretical FAME production and the experimental data at different initial concentrations of the oxygen singlet. As mentioned before, it is believed that the oxygen singlet catalyses the first stage of the proposed mechanism and by increasing the initial concentration of this species a higher yield of FAME production can be achieved. When the $O\cdot$concentration is comparatively lower than the initial concentration of FFA, all the $O\cdot$ is used and turned into methoxy and hydroxyl radicals which then react to form FAME, in other words $[O\cdot]_i = [\text{FAME}]_f$.

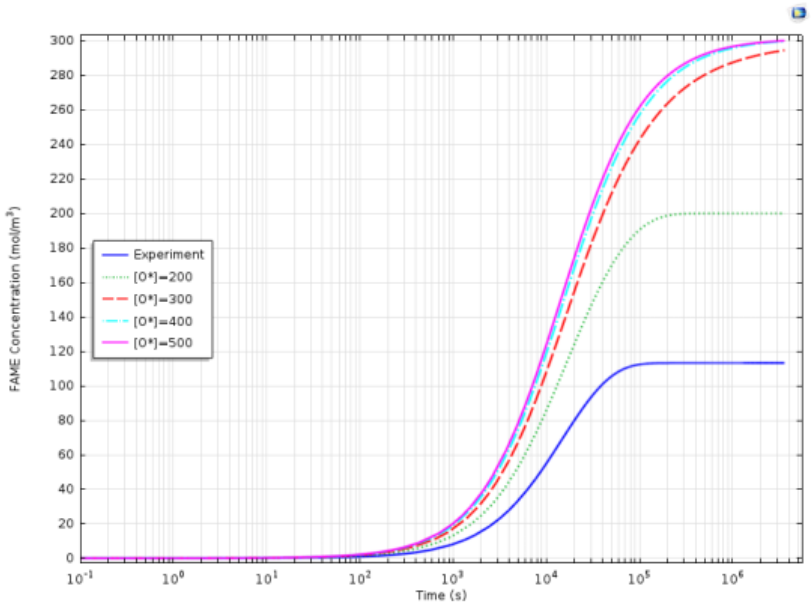

Figure 51 O· Initial concentration effect on FAME production.

On the other hand, when the initial concentration of $O\cdot$ is fairly similar or higher to the initial concentration of FFA, the reaction tends to completion. For an initial concentration of 300, 400 and 500 mol/m^3, the FAME percentage yield achieved has a value of 96.678, 99.459 and 99.592%. Therefore, increasing the initial $O\cdot$ concentration increases dramatically the FAME production to a certain extent. For initial concentrations higher than 500 mol/m^3, the room for improvement is less than 0.51% so there is no need to input more $O\cdot$ since it would only incur in an elevated cost for its production making the first stage of this mechanism fairly feasible. This is why for the irreversible mechanism the question is how much of the $O\cdot$ would be needed to be input into the system so the reaction is still economically feasible.

As mentioned earlier, the experimental data is far from being similar to the theoretical, but this means there is room for improvement. The effect of varying different operating conditions such as temperature and the initial $O\cdot$ and methanol concentration for the reversible mechanism will be discussed in the 0-d model in the next chapter. A discussion in more depth is presented for both the forward and rate constants for the three-step mechanism.

5.5.Conclusions

It can be noticed that an increase in the FFA content means an increase in the activation energy since the esterification is needed to reach the activation stage. A reaction with a low activation energy should proceed faster when compared with one that considers a larger activation energy. The forward reaction for the third step has an activation energy of E_a = 12.692 kJ/mol and a pre-exponential factor of A = 2.0127x10^{-2} M^{-1}s^{-1}. The highest temperature always shows a higher FAME production right after the third step takes place.

The forward rate constant *kf3* has a value of 1.1472×10^{-4}, 1.4084×10^{-4} and 2.1559×10^{-4} $M^{-1}s^{-1}$ at 273.15, 313.15 and 333.15 K. The behaviour followed by the forward rate constants is in agreement with the effect of temperature on rate constants. Considering that the third step in this mechanism, the esterification, has a heat of reaction of $\Delta H_{rxn} = 57.21$ kJ/mol, the reaction is defined as endothermic which means the system absorbs energy from the surroundings. If the forward reaction of the esterification is endothermic, the other direction (reverse reaction) is exothermic.

When the methanol concentration is lower than the initial concentration of $O\cdot$, all the methanol is used and turned into methoxy radicals which then react to form FAME, in other words $[MeOH]_i = [FAME]_f$. But when the initial concentration of methanol is higher than the one of $O\cdot$, $[O\cdot]_i = [FAME]_f$. This suggests that the $O\cdot$ is the limiting reactant in the three-step mechanism. When the $O\cdot$concentration is comparatively lower than the initial concentration of FFA, all the $O\cdot$ is used and turned into methoxy and hydroxyl radicals which then react to form FAME, in other words $[O\cdot]_i = [FAME]_f$. When the initial concentration of $O\cdot$ is fairly similar or higher to the initial concentration of FFA, the reaction tends to completion.

Therefore, increasing the initial $O\cdot$ concentration increases dramatically the FAME production to a certain extent. For initial concentrations higher than 500 mol/m^3, the room for improvement is less than 0.51% so there is no need to input more $O\cdot$ since it would only incur in an elevated cost for its production making the first stage of this mechanism fairly feasible. Having analysed the key features of the irreversible mechanism, it is important to explore the effect of the reverse reaction in the third step. This is the main driver to develop a new 0-D model to understand the influence of the reverse reaction in terms of the produced water but mainly the production of FAME.

6. 0-D with reversible reaction for the esterification of FFA

In the previous chapter, the irreversible model was presented for the reaction mechanism here studied. It is important to mention that this chapter follows on the use of a 0-D model to analyse and discuss the reaction kinetics. The main feature of the model here presented is that it considers the reverse reaction in the third step, acknowledging the esterification reaction as a reversible reaction of second order. The importance of the reversible model relies on maximising the production rate of the biodiesel by increasing the initial concentration of oxygen singlet ($O\cdot$) which is thought to catalyse the proposed reaction mechanism and take the reaction to completion. The relevant data calculations and estimations presented in both chapter 3 and 4 are here considered.

This model considers the same operating conditions stated in Chapter 5 and does not take into account heat transfer on the surface, phase changes or transport of diluted species since they are set in a 0-D model. The reversible mechanism is considered for this chapter since esterification is known to be a reversible reaction of second order. In this chapter the reader can find the model description, determination of rate constants, least squares fitting of the model and the appropriate results for the variation of different parameters such as, temperature and the initial concentration for both methanol and oxygen singlet.

6.1. Model description

For the purpose of this chapter, the reversible 0-D model considers the same operating conditions stated in the previous irreversible model and it is defined by the set of reactions described below:

$$O\cdot + MeOH \rightarrow MeO\cdot + HO\cdot \tag{91}$$

$$HO\cdot + HO\cdot \rightarrow H_2O + \frac{1}{2}O_2 \tag{92}$$

$$FFA + MeO\cdot \leftrightarrow FAME + HO\cdot \tag{93}$$

The first step described by the reaction $O\cdot + MeOH \rightarrow MeO\cdot + HO\cdot$ is set to be in equilibrium following the equation $k_{eq} = k_{eq0}$, where k_{eq0} is equal to 1. For the second step in this reaction mechanism $HO\cdot + HO\cdot \rightarrow H_2O + \frac{1}{2}O_2$, the reaction is to be reversible where the rate constants are given by $k^f = k^r \cdot k_{eq0}$ and k_{eq0} is equal to 1. Lastly, the third step $FFA + MeO\cdot \rightarrow FAME + HO\cdot$ is set to be reversible where the forward and reverse rate constant *kf3* and *kr3* are studied to illustrate the importance of the reaction kinetics of this mechanism, and then be fitted to the experimental data. In order to analyse the effect of different rate constants and the initial concentration of $O\cdot$, parametric sweeps are carried out changing the value at different orders of magnitude of the parameters used in this model shown in Table 25.

In the next sections of this chapter, the determination of the rate constants *kf2* and *kf3* are described and the variation of different operating conditions is studied for the reversible mechanism.

Table 25 Parameters used in the reversible 0-D model.

Parameter	Name
Forward rate constant Reaction 2	kf2
Forward rate constant Reaction 3	kf3
Reverse rate constant Reaction 3	kr3
Initial concentration of O·	rado

The forward rate constant is described by the parameter *kf3* and the reverse rate constant is defined by *kr3*. It is important to mention that the reversible model here described, shows the same behaviour compared to the irreversible model when the parametric sweep for *kf2* was performed to analyse its effect on water production for the spontaneous reactions but it differs from the irreversible mechanism once the third step is enabled at values for *kf3* and *kr3* of 1 $m^3/(s\cdot mol)$.

6.2. Determination of rate constants

In Figure 52 the effect of *kf2* is studied in order to explore its effect on the water production. For the purpose of this sweep, both *kf3* and *kr3* are kept constant with a value of 1 $m^3/(s\cdot mol)$. As seen in the irreversible mechanism after $1x10^{-6}$ s there is no discernible difference between the three values for this parameter ranging $1x10^5$-$1x10^7$ $m^3/(s\cdot mol)$, so the value of *kf2*=$1x10^5$ $m^3/(s\cdot mol)$ is chosen as a set value throughout the studies.

When *kf2*= $1x10^5$-$1x10^7$ $m^3/(s\cdot mol)$, the curves exhibit a plateau after $1x10^{-6}$ and $1x10^{-2}$ s. When these values for *kf2* are compared to *kf2*=1 $m^3/(s\cdot mol)$, this new curve shows a discernible difference since it only exhibits only one plateau $1x10^{-1}$ s. As discussed before for the irreversible mechanism, a value of *kf2* needs to be big enough to describe the spontaneous reactions but increasing its value above $1x10^5$ $m^3/(s\cdot mol)$ does not have a significant impact since equilibrium is reached before the third step takes place.

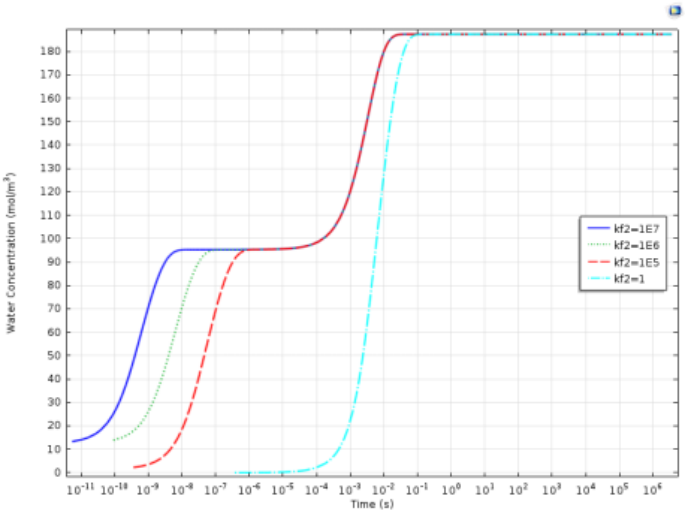

Figure 52 kf2 effect on the water production for the overall reversible mechanism.

The water concentration at equilibrium is 187.34 mol/m^3, which is smaller when compared to the irreversible mechanism value of 254.46 mol/m^3. This means a 26.37% decrease in the water production between the irreversible and reversible models. This behaviour can be explained since the reverse reaction for the third step competes with the second reaction, the equations involved are given by:

$$HO\cdot + HO\cdot \rightarrow H_2O + \frac{1}{2}O_2 \tag{94}$$

$$FAME + HO\cdot \rightarrow FFA + MeO\cdot \tag{95}$$

where both reactions consider the radical species $HO\cdot$ as a reagent. Even though the spontaneous reaction has a rate constant *kf2* (1x10^5 m^3/(s·mol)) higher than *kr3* (1x10^{-8} m^3/(s·mol)) by several orders of magnitude, the reverse reaction for the third step does show an effect in the overall water production. This is due to the fact that $HO\cdot$ produced in both the first spontaneous reaction and the third step is then reacted with FAME undergoing through the reverse reaction mechanism.

Regarding the sensitivity to *kf2* on the FAME production, the reversible reaction shows no effect on the FAME concentration. A double log plot was used for the reversible model as well, showing no sensitivity to *kf2* on FAME production.

Having said this, a value for *kf2* of 1x10^5 m^3/(s·mol) is used to explore the appropriate values for the rate constant *kf3* and *kr3* for the slowest reaction in the mechanism. In Figure 53 is shown the parametric sweep performed to find the right combination for these rate constants.

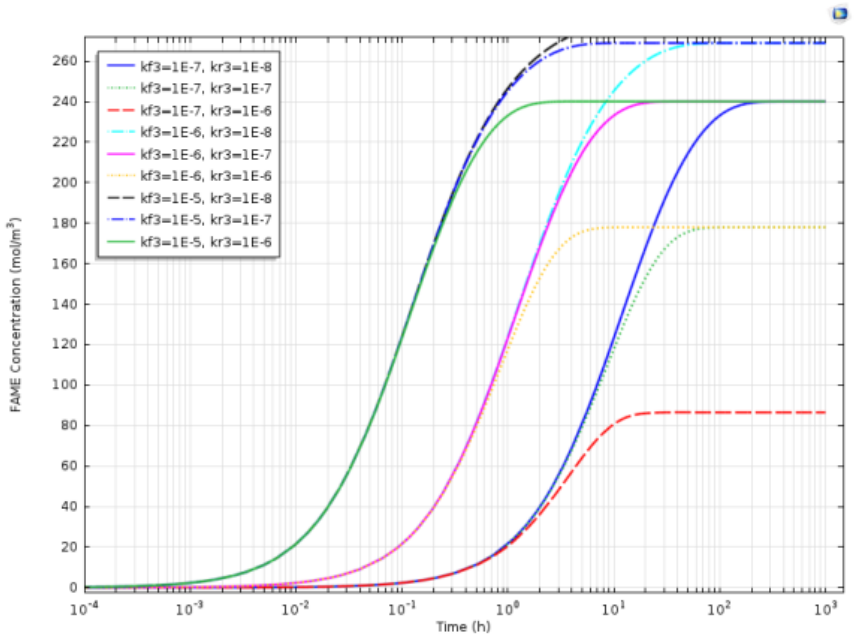

Figure 53 kf3 and kr3 effect on FAME production.

The sweep was carried out using all the possible combinations when *kf3*= 1x10^{-7}, 1x10^{-6} and 1x10^{-5}, and *kr3*= 1x10^{-8}, 1x10^{-7} and 1x10^{-6} m^3/(s·mol). From the different curves obtained in Figure 53, the two pairs that satisfy the correct order of magnitude condition are *kf3*=1x10^{-6} and *kr3*=1x10^{-7} m^3/(s·mol), and *kf3*=1x10^{-6} and *kr3*=1x10^{-8} m^3/(s·mol). The time scale for these two pairs of *kf3* and *kr3* to reach equilibrium between 1-100 h which matches the experimental data. These two pairs are shown in Figure 54 for comparison purposes.

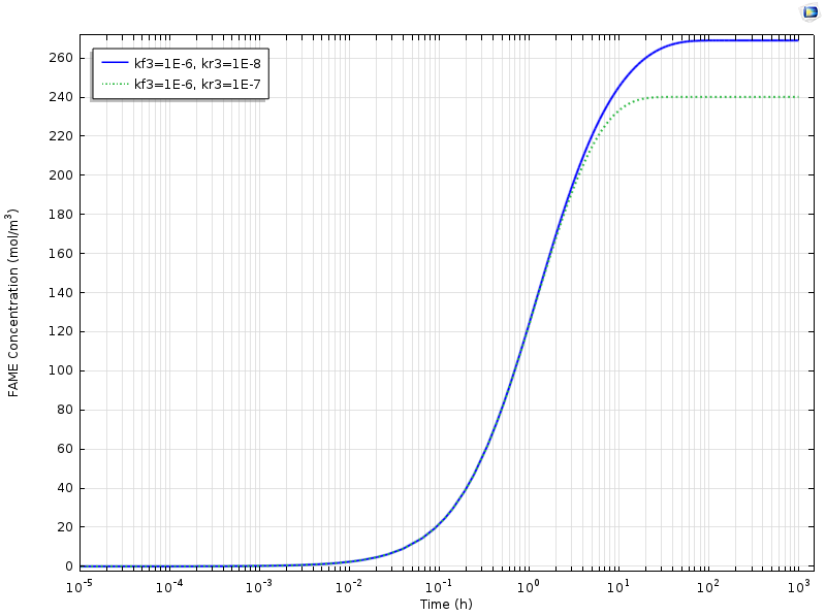

Figure 54 Comparison of kf3 and kr3 pairs effect on FAME concentration.

Once the two pairs are isolated for comparison, it can be noticed that for an initial concentration of [$O\cdot$]=281.25 mol/m^3, the FAME concentration reaches equilibrium at [FAME]=240.06 mol/m^3 when *kf3*=1x10^{-6} and *kr3*=1x10^{-7} m^3/(s·mol). On the other hand, for a value of *kf3*=1x10^{-6} and *kr3*=1x10^{-8}

m^3/(s·mol) the FAME concentration reaches equilibrium at [FAME]=268.99 mol/m^3. In order to achieve a higher conversion of the species $O\cdot$, the pair *kf3*=1x10^{-6} and *kr3*=1x10^{-8} m^3/(s·mol) is selected for the fitting of the model. This pair achieves a higher conversion since the rate constant *kr3* has a smaller value by one order of magnitude, *kr3*=1x10^{-7} and 1x10^{-8} m^3/(s·mol). Therefore, the competition for species $HO\cdot$ between the last two steps is favoured for the second step due to the orders of magnitude. The pair *kf3*=1x10^{-6} and *kr3*=1x10^{-8} m^3/(s·mol) is then selected because of its time scale in the correct order of magnitude and a higher conversion reached at equilibrium.

The effect of varying the initial concentration of $O\cdot$ on the FAME production is illustrated in Figure 55. For the five different initial concentrations of [$O\cdot$]= 10, 100, 281.45, 400 and 500 mol/m^3 studied in the sweep, the FAME concentration at equilibrium is 9.99, 99.86, 268.99, 286.02 and 287.3 mol/m^3 respectively. Increasing the initial concentration of $O\cdot$ results in an increase of the FAME production to a certain extent, being the increase smaller when the initial concentration of $O\cdot$ is similar to the initial concentration of [FFA]. The $O\cdot$ conversion is inversely proportional to its initial concentration. This means that at low initial concentrations of $O\cdot$ a higher conversion for the limiting reagent is achieved. This behaviour can be attributed to the reverse rate constant *kr3*. Increasing the initial concentration for $O\cdot$ above the initial [FFA]=301.53 mol/m^3, will only result in a small change in the FFA conversion due to the reverse rate constant *kr3* and the competition for the $HO\cdot$ as a reagent for the last two steps in the reversible mechanism. Therefore, there is no need to input more $O\cdot$ since it would only incur in an elevated cost for its production making the first stage of this mechanism not economically feasible.

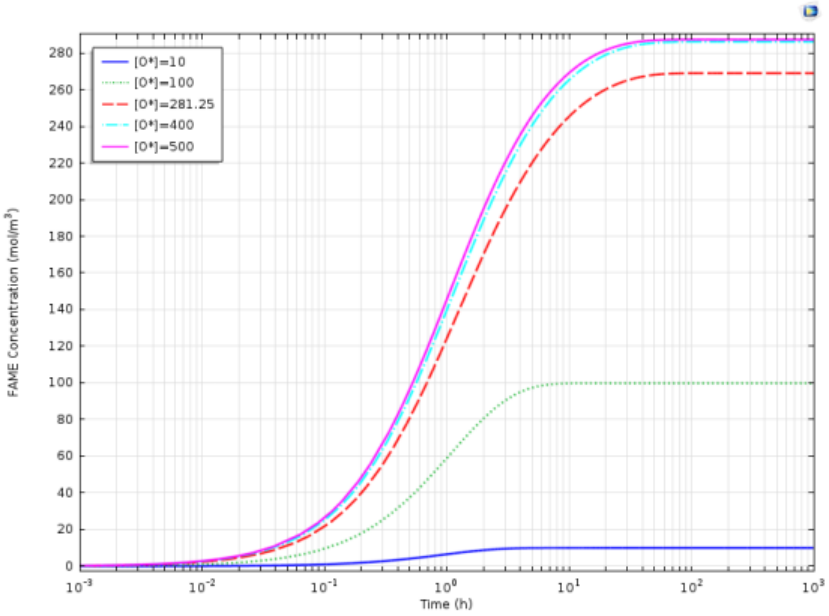

Figure 55 O· initial concentration effect on FAME production.

The concentration profile for FFA, FAME and water is shown in Figure 56. This profile is obtained using an initial concentration for water, FFA and [$O\cdot$] of 1x10^{-4}, 301.53 and 281.25 mol/m^3. The value

for the forward rate constant *kf2* is 1x10^{5} m^{3}/(s·mol), the forward rate constant *kf3* has a value of 1x10^{-6} m^{3}/(s·mol) and the reverse rate constant *kr3* has a value of 1x10^{-8} m^{3}/(s·mol).

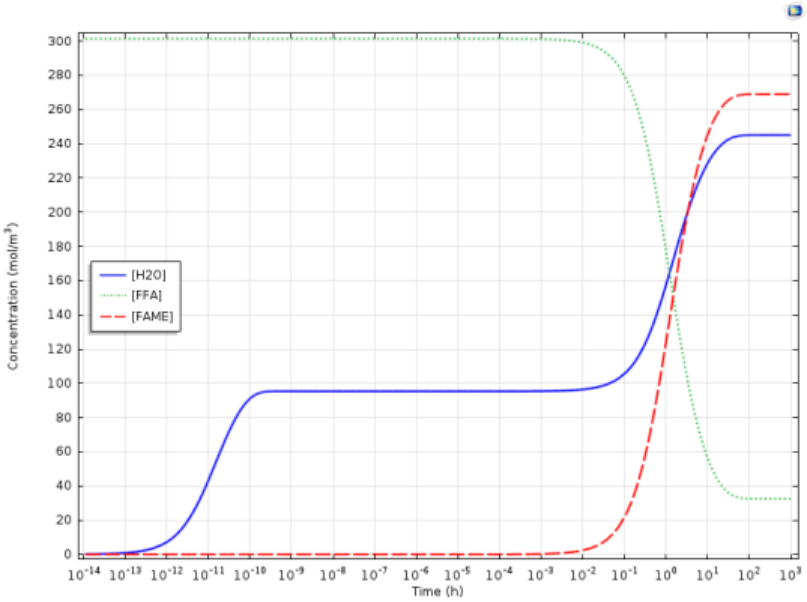

Figure 56 FAME, FFA and water concentration profile in time for the reversible mechanism.

The resulting reversible reaction mechanism reaches equilibrium between 1-100 h, which is the correct order of magnitude for the experimental data. In terms of water production, the concentration profile exhibits two plateaus, the first one for the spontaneous reactions at 1x10^{-10} h and the second one for the third step between 1-100 h, same orders of magnitude are obtained for the irreversible mechanism. For these two plateaus the concentration reached at equilibrium is 95.29 and 245.11 mol/m^{3} respectively. The first spontaneous equilibrium reaches the same concentration of water obtained in the irreversible mechanism, meaning the reaction happens so fast compared to the reverse reaction on the third step that no effect on $HO\cdot$ competition as a reagent for these last two reactions.

The production of FAME reaches a plateau at equilibrium with a concentration of 269.99 mol/m^{3}. With the parameters previously mentioned, a conversion of 89.21% of FFA is achieved at equilibrium resulting in a production of 24.694 and 22.502 g for FAME and H_2O respectively.

6.3.Least squares fitting for 0-D reversible model

The reversible 0-D model here discussed follows a reaction rate for FAME described by the following equation:

$$r_{FAME} = k_f[FFA][MeO\cdot] - k_r[FAME][HO\cdot] \quad (96)$$

$$r_{FAME} = k_{f3}k_1k_2^{\frac{1}{2}}[FFA]\frac{[MeOH][O\cdot]}{[H_2O]^{\frac{1}{2}}[O_2]^{\frac{1}{4}}} - \frac{k_{r3}}{k_2^{\frac{1}{2}}}[FAME][H_2O]^{\frac{1}{2}}[O_2]^{\frac{1}{4}} \quad (97)$$

where *kf* and *kr* are the combination of different rate constants for both the forward and reverse reaction. The procedure describing how these rate constants are calculated is described in Chapter 7 in more detail. The forward and reverse rate constant for the reversible reaction of the slowest step are therefore defined by:

$$k_f = k_{f3} k_1 k_2^{\frac{1}{2}} \tag{98}$$

$$k_r = \frac{k_{r3}}{k_2^{\frac{1}{2}}} \tag{99}$$

In Figure 43, the experimental data is shown, these curves belong to the FFA content of 20% at 20, 40 and 60°C. In order to facilitate the fitting of the reversible model, the value obtained for the forward rate constant in the previous chapter is used here as a set value, given by the equation:

$$k_f = k_{f3} k_1 k_2^{\frac{1}{2}} = 0.020127 e^{\frac{-1526.7}{T}} \tag{100}$$

For each one of the treatments here studied, the reverse rate constant *kr3* is calculated using the curve of each treatment and the respective value found for the forward rate constant *kf3* in Chapter 5.

6.4. Results and discussion

The least squares method is carried out to fit the predicted data from COMSOL Multiphysics to match the experimental data. COMSOL with MATLAB is used to perform the fitting of the curves following the code found in Appendix B, but some amendments are needed to label the reverse rate constant properly. It is important to mention that before running the code for each treatment, the initial concentration of [FFA] and the y^m are set to the respective value. The same code used for the fitting of the irreversible model is here utilised but with modifications in terms of the new parameter to be fitted *kr3.*

For the iterations used in this method, a condition to find only positive numbers is used since the order of magnitude is $1x10^{-7}$ and the solver could return negative values. The tolerance for the parameter *kr3* in the iterations is set to $1x10^{-10}$ to return values with significant figures. Once the code is run, it gives the value for *kr3* that satisfies the condition of having the least squared error and the values for the new predicted y^p.

The values for the rate constant *kr3* for each treatment are found in Table 26. In Section 6.1 a prediction for the right order of magnitude when the reaction mechanism reached equilibrium gave a value for the forward rate constant *kf3* of $1x10^{-6}$ $m^3/(s \cdot mol)$ and *kr3* $1x10^{-8}$ $m^3/(s \cdot mol)$ with a set value of *kf2* of $1x10^5$ $m^3/(s \cdot mol)$. This prediction was the first one to be run but since it did not return a decent fit, the forward rate constant from the irreversible mechanism is then used as a set value. The value for *kf3* reported for the irreversible reaction is here used as an initial guess for the fitting. The

resulting order of magnitude for majority of the reverse rate constants here studied is $1x10^{-8}$ $m^3/(s \cdot mol)$ as predicted in Section 6.1. In Table 26, the resulting values for *kr3* are shown in ($M^{-1}s^{-1}$) to ease further calculations. The effect on temperature can be easily notice in Table 26, an increase in temperature results in an increase in the reverse rate constant across the three different FFA contents here studied.

Table 26 Rate constant kr3x10^{-5} (1/M.s) values for each treatment.

		Free Fatty Acid %		
		10%	**15%**	**20%**
Temperature (K)	**293.15**	1.8908	1.9981	1.8922
	313.15	3.1010	3.3081	1.4901
	333.15	2.9403	2.9983	2.8824

Once the values for the reverse rate constant are found for all the treatments, the least square analysis is carried out to discuss the overall quality of the fit. Table 27 is comprised of the different terms calculated for the least squares method and its respective quality. *Sxx* and *Syy* are the corrected sum of squares for y^p and y^m respectively. *Sxy* corresponds to the corrected sum of cross products, *Cov(x,y)* is the covariance and S_{error} is the standard deviation of the error. The correlation coefficient R^2 is the parameterised value for the overall quality of the fit.

Table 27 Least squares analysis for the fitted curves.

FFA %	Temperature (K)	Sxx x10^2	Syy x10^2	Sxy x10^2	Cov (x,y)	R^2	S_{error}
10	293.15	5.047	8.040	6.161	68.459	0.9672	2.7218
	313.15	7.608	7.916	7.612	84.580	0.9808	2.0734
	333.15	10.707	10.052	10.308	114.536	0.9935	1.3569
15	293.15	5.014	6.980	5.763	64.038	0.9741	2.2576
	313.15	10.981	10.853	10.700	118.891	0.9801	2.4698
	333.15	23.624	21.755	22.475	249.732	0.9914	2.3044
20	293.15	221.504	216.010	216.807	2408.970	0.9911	7.3689
	313.15	414.677	425.115	417.517	4639.080	0.9944	8.2278
	333.15	602.933	592.301	597.430	6638.120	0.9997	2.1470

All the fitted curves have a correlation coefficient greater than 0.97 which suggests that the method used to fit the curves has a high overall quality. For each FFA content (10, 15 and 20%), the highest value for R^2 is achieved at 60°C, since the experimental data shows the plateau behaviour at higher temperatures and a more pronounced curvature for the FAME production over time. This behaviour could be attributed to the effect of temperature in a chemical reaction, since it is known that a higher

temperature a reaction occurs more rapidly. In other words, the exponential growth in terms of production of FAME at the beginning of the reaction is more noticeable at higher temperatures.

The best fit throughout the curves was obtained at a FFA content of 20% and 60°C with a correlation coefficient of R^2=0.994. Using a forward rate constant of 2.6740×10^{-4} $M^{-1}s^{-1}$, the calculated reverse rate constant had a value of 2.882×10^{-5} $M^{-1}s^{-1}$. In terms of comparison, the curve with the lowest R^2 was the 10 FFA% at 293.15 K. The treatment 10 FFA% at 293.15 K obtained a forward rate constant of 1.6631×10^{-4} $M^{-1}s^{-1}$(R^2=0.980). The treatment with the lowest R^2 (10 FFA% at 293.15 K) is then used to have a better comparison to be made between models. The reversible mechanism model shows an improvement in the fitting of the curves when compared to the irreversible model. This would suggest that the reversible model describes the experimental data in a better way.

As mentioned in Chapter 5, from the FAME production curves obtained in Figure 43 and the rest found in Chapter 4, an increase in temperature causes an increase in the FAME production and therefore an increase in the rate constants. The one-way ANOVA is then used in this section to determine if there is a significant difference between the reverse rate constants obtained across the FFA contents used in this model (10, 15 and 20%). The statistical test is run with a significance level of α=0.05, and considers the same null hypothesis used in Chapter 5. The alternative hypothesis states that at least one of the means is different from each other.

The results obtained for the one-way ANOVA are shown in Table 28, in this case the reverse rate constant across the FFA content are not significantly different since $F_{value}<F_{crit}$ (0.0782<5.14). In other words, we fail to reject the null hypothesis meaning there is no significant difference between the three groups for the FFA content 10, 15 and 20% but there is a noticeable difference between the temperatures considered in this model. The F_{value} calculated for the reverse rate constant is relatively smaller than the one obtained for the forward rate constant, this could be credited to the fact that the reverse rate constant are calculated using the forward rates which have already been proven to not show any significant difference across the FFA content.

Table 28 ANOVA results for the reverse rate constant.

	df	SS $x10^{-8}$	MS $x10^{-9}$	F	F_{crit}
Treatment	2	0.03017	0.1508	0.0782	5.14
Residuals	6	1.1568	1.9281		
Total	8	1.1870			

Once the statistical analysis across the FFA is completed and it is concluded there is no significant different between the groups accounting for the Free Fatty Acid%, the average values for the reverse rate constant *kr3* are used in the Arrhenius equation to obtain the activation energy (E_a) and pre-exponential factor (*A)* for the reverse reaction of the third step. The values for the average reverse rate

constant at each temperature are shown in Table 29, these values are then processed to be used in the Arrhenius equation. When plotting ln(*k*) against 1/T, a straight line is then obtained where the E_a and *A* can be calculated from the y-intercept and the slope of the line.

Table 29 Average rate constants used for Arrhenius equation parameters.

Temperature (K)	Rate constant x10^{-5} ($M^{-1}s^{-1}$)	1/T x10^{-3} (K^{-1})	ln(k)
293.15	1.9270	3.4112	-10.857
313.15	2.6331	3.1934	-10.545
333.15	2.9404	3.0017	-10.434

Once the plot is generated from the rate constants gathered at different temperatures, the curve shown in Figure 57 can be fitted by a linear regression to calculate the activation energy and the pre-exponential factor. The linear regression has a slope m=-1040.7 and an y-intercept= -7.2795.

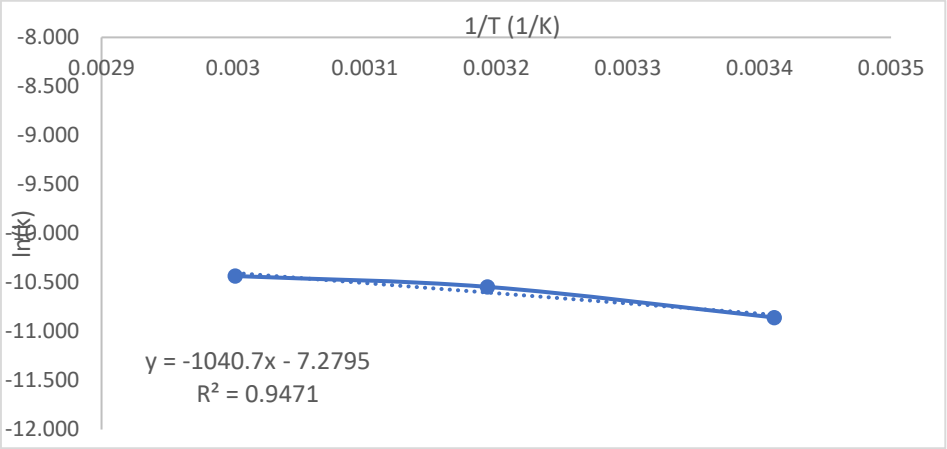

Figure 57 Ln(k) against 1/T plot for the reverse rate constant.

Having said this, the reverse reaction for the third step has an activation energy of E_a = 8.562 kJ/mol and a pre-exponential factor of *A* = 6.895x10^{-4} $M^{-1}s^{-1}$. These values were calculated using the linear regression with a R^2=0.9711. The reverse rate constant for the third reversible reaction can be expressed then using the Arrhenius equation, when this expression is combined with the reaction rate for the third step, it is possible to define a new equation for the forward rate constant that contains the parameters previously calculated in the Arrhenius equation, defined by:

$$k_r = \frac{k_{r3}}{k_2^{\frac{1}{2}}} = 6.895\text{x}10^{-4} e^{\frac{-1040.7}{T}} \quad (101)$$

It is important to point out that the first reaction in the proposed mechanism is in equilibrium (k_{eq}=k_{eq0}) with an equilibrium constant k_{eq0}=1, the second reaction is set to be reversible with a forward rate constant *kf2*=1x10^5 $m^3/(s\cdot mol)$, and the third step has a predicted reverse rate constant that could be included in the reaction rate at any temperature given by the equation:

$$r_{FAME} = (0.20127e^{\frac{-1526.7}{T}})[FFA]\frac{[MeOH][O\cdot]}{[H_2O]^{\frac{1}{2}}[O_2]^{\frac{1}{4}}} - (6.895\text{x}10^{-4}e^{\frac{-1040.7}{T}})[FAME][H_2O]^{\frac{1}{2}}[O_2]^{\frac{1}{4}} \quad (102)$$

The Arrhenius equation used to show the dependence of the rate constants at different temperatures has an exponential decay which accounts for the ratio of the activation energy to the average kinetic energy. As mentioned before a larger ratio will give a smaller rate constant which is the case for the proposed reverse mechanism.

For the esterification reaction here proposed, the forward reaction is considerably more thermodynamically favourable than its reverse reaction. Consequently, the forward rate constant is greater than the reverse constant, in other words *kf3 > kr3.* It is relevant to consider that this relationship can only be made since the rate constants have the same units. As mentioned before, the esterification reaction here proposed show an endothermic behaviour (Laidler, 1984).

The effect of temperature on both the forward and reverse rate constants is then studied. It is known that the effect of temperature on the rate constants is proportional to the activation energy. If the activation energy increases, then the effect of changing the temperature would increase. For the esterification reaction here proposed, the forward reaction (esterification) is endothermic and the reverse reaction (hydrolysis) is exothermic. The endothermic direction is known to have a larger activation energy, in other words $Ea_f > Ea_r$. The reversible model here studied follows this pattern and has an activation energy for the forward and reverse reaction of 12.692 and 8.652 kJ/mol respectively.

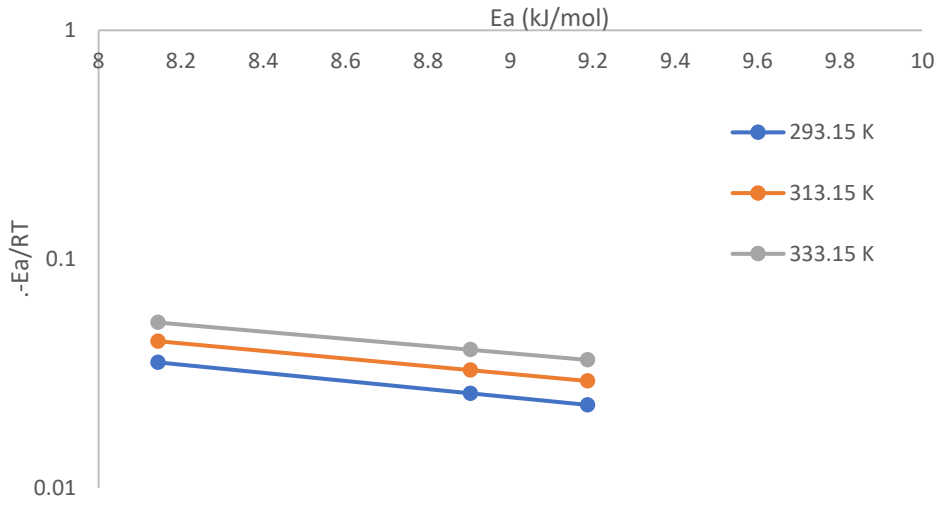

Figure 58 Semi-log plot of -Ea/RT against Ea for the reverse reaction.

In Figure 58, the effect of the activation energy on the reverse rate constant can be depicted. For the reverse reaction, an activation energy difference of 1 kJ/mol reduces the rate constant by a factor of 10^{-1}. The exponential term (-Ea/RT) suggests that the reverse rate constant decreases exponentially when the activation energy increases, and the rate of reaction would decrease as well. A reaction with

a low activation energy should proceed faster when compared with one that considers a larger activation energy. Having said this, the reverse reaction in this mechanism has an activation energy of E_a = 8.652 kJ/mol. Mandake et al reported similar activation energies for the forward and reverse reaction when studying the catalysed esterification of acetic acid with methanol using a 1:1 molar ratio at 308-328 K. Singh et al ported an activation energy of 30 kJ/mol for the esterification of butyric acid with ethanol at a molar ratio 1:5 to 1:15 and a temperature 328.15 to 348.15 K (Mandake, et al., 2013; Singh, et al., 2013).

In order to compare both the forward and reverse mechanism, the effect of the reverse rate constant is illustrated in Figure 59. The plot is generated using an initial concentration of $[O\cdot]$=281.25 mol/m^3 and [FFA]=301.54 mol/m^3 at 60°C. The irreversible mechanism reaches a final concentration for both water and oxygen of 254.43 and 127.2 mol/m^3 respectively. On the other hand, the reversible mechanism reaches a final concentration for water and oxygen of 207.97 and 103.98 mol/m^3 respectively. The reversible mechanism produces 18.26% less water and oxygen when compared to the irreversible one, this is attributed to the fact that hydroxyl radical is used in the reverse mechanism to carry out the hydrolysis of the esters. The hydrolysis of esters competes with the second step of the mechanism which explains why the water and oxygen productions decreases in the reversible reaction.

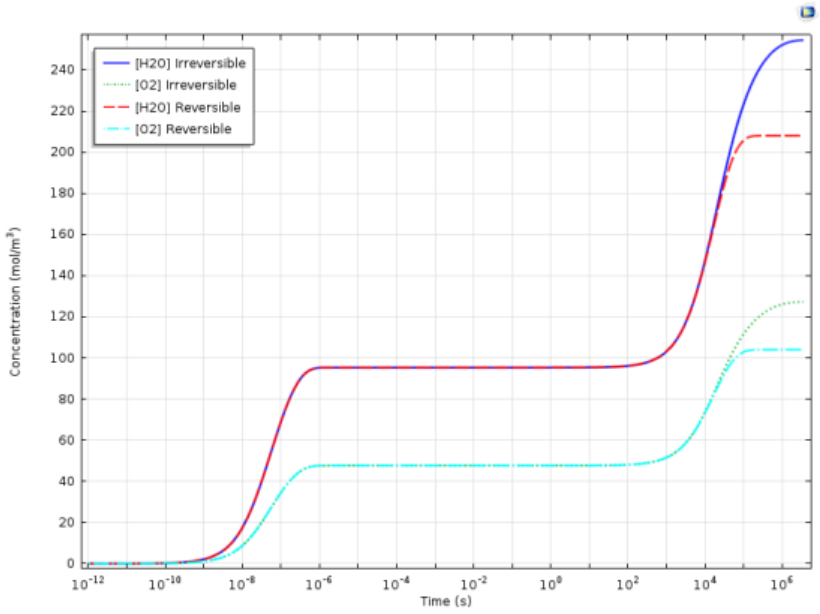

Figure 59 Comparison of the mechanisms in water and oxygen production.

The reversible mechanism involves the hydroxyl radical to carry out the hydrolysis of esters. This is the main driver to explore what happens to both the methoxy and hydroxyl radical between the irreversible and reversible mechanisms here studied, this is illustrated in Figure 60.

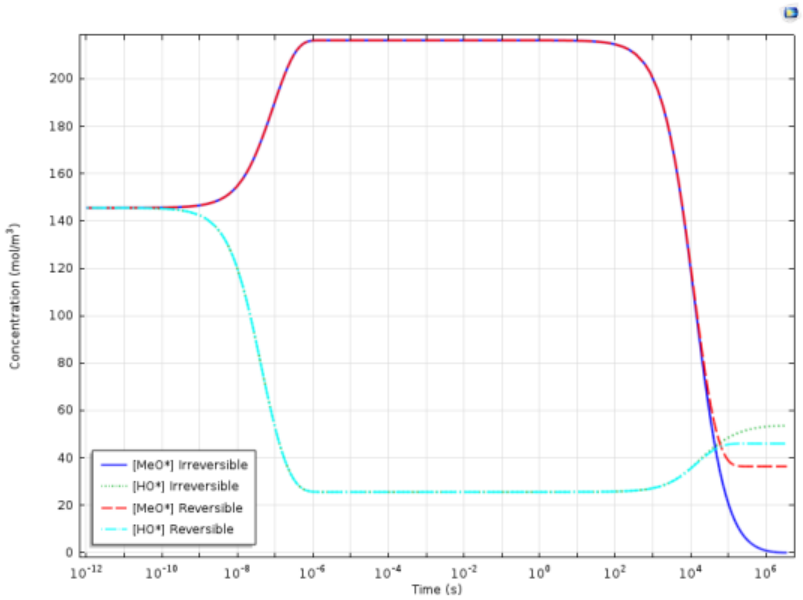

Figure 60 Comparison of the mechanisms in methoxy and hydroxyl radicals production.

The irreversible mechanism reaches a final concentration for both the methoxy and hydroxyl radical of 0 and 53.57 mol/m^3 respectively. On the other hand, the reversible mechanism reaches a final concentration for the methoxy and hydroxyl radical of 36.4 and 46.05 mol/m^3 respectively. The reversible mechanism produces 18.26% less hydroxyl radicals, which matches with the water and oxygen production. In terms of the methoxy radical production, the reverse reaction produces methoxy radicals which are found when the third step reaches equilibrium. The methoxy radicals could then react with more FFA if present in liquid mixture to react. Having said this, the reverse mechanism produces less water and oxygen since the hydroxyl radicals are used in both the forward reaction of the second step and the reverse reaction of the third step. These two reactions compete for the hydroxyl radicals, but it is important to acknowledge the fact that the forward reaction of the second step has a higher rate constant than the reverse reaction of the third step.

The esterification of free fatty acids is known to be a reversible reaction of second order shown in Figure 61. In order to validate this, the solution of the direct kinetic problem for the second order reaction is shown below. In this case, an inequality of the reactant's initial concentrations is observed. The forward reaction in the third step is given by:

$$FFA + MeO\cdot \leftrightarrow FAME + HO\cdot \tag{103}$$

$$r_{FAME} = k_f[FFA][MeO\cdot] - k_r[FAME][HO\cdot] \tag{104}$$

To ease and simplify calculations, the reverse term is neglected since the rate constant order of magnitude is smaller when compared to the forward rate constant. The forward rate constant has a value of $k_f = 2.6740x10^{-7}$ m^3/(s·mol). Therefore, the second term of the rate of reaction for FAME production is relatively smaller when compared to the forward term. Having said this, the rate of reaction is here described by:

$$r_{FAME} = 0.20127e^{\frac{-1526.7}{T}}[FFA][MeO\cdot] \quad (105)$$

At 60°C, the initial concentration of FAME at t(0)=0 mol/m^3 and the rate of reaction is given by the equation below:

$$\frac{d}{dt}FAME(t) = 2.6740x10^{-7}[FFA_0 - FAME(t)][MeO\cdot_0 - FAME(t)] \quad (106)$$

To integrate the equation is necessary to locate the terms on the right side, giving:

$$\int_0^{FAME} \frac{1}{[FFA_0 - FAME(t)][MeO\cdot_0 - FAME(t)]} dFAME = \int_0^t 2.6740x10^{-7} dt \quad (107)$$

Solving for $FAME(t)$ and simplifying the expression results in the equation below:

$$\frac{\ln(FAME(t) - FFA_0) - ln(FAME(t) - MeO\cdot_0) + \ln(FFA_0) - \ln(MeO\cdot_0)}{FFA_0 - MeO\cdot_0} = 2.6740x10^{-7}\cdot t \quad (108)$$

The following initial conditions are considered for this esterification for $[FFA_0]$=3.0154x10^2 mol/m^3 and $[MeO\cdot_0]$=2.162x10^2 mol/m^3 which result in the following expression:

$$FFA(t) = FFA_0 - FAME(t) \qquad MeO\cdot(t) = MeO\cdot_0 - FAME(t) \quad (109)$$

$$FAME(t) = [FFA_0][MeO\cdot_0]\frac{e^{([FFA_0]kt - [MeO\cdot_0]kt)}}{e^{([FFA_0]kt - [MeO\cdot_0]kt)}\cdot[FFA_0] - [MeO\cdot_0]} \quad (110)$$

For second order reaction with different initial concentration for the reactants, the previous equation can be modified to give a straight line, if so it validates the fact that the third step is second order in respect to the free fatty acid and the methoxy radical. The linearization results from plotting $ln\frac{[MeO\cdot_0]*([FFA_0]-FAME(t))}{[FFA_0]*([MeO\cdot_0]-FAME(t))}$ against time.

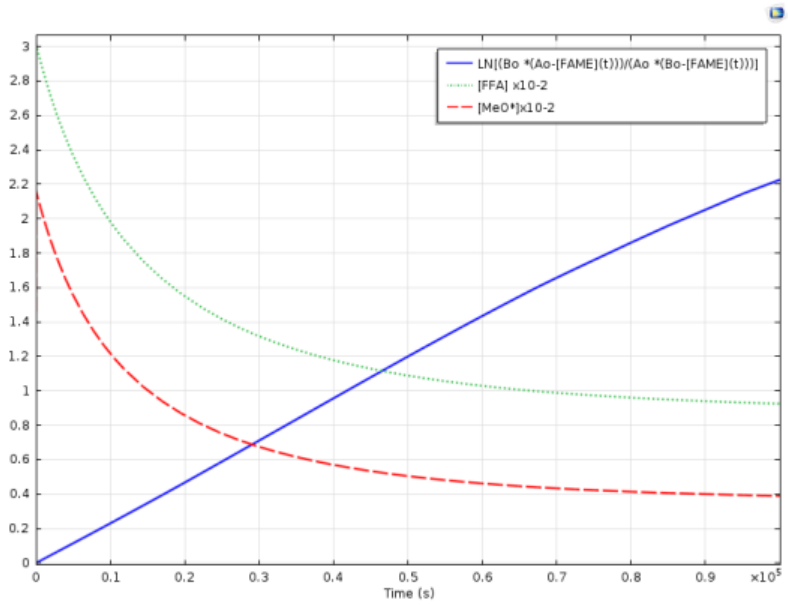

Figure 61 Linearization of the second order reaction.

The kinetic study of FFA esterification here proposed was performed using the three-step reversible kinetic model, COMSOL with MATLAB was then used to calculate the molar balances describing the concentration of FFA in the system. The Arrhenius equation was then used to determine the influence of temperature on the kinetic constants. The experimental data was successfully fitted by the least squares model and a good agreement is observed between the predicted and measured data points. The activation energies for the esterification and hydrolysis reactions were found to be 12.692 and 8.652 kJ/mol, respectively.

6.4.1. Variation of temperature

Once both the forward and the reverse rate constants are obtained, the effect of the temperature on the FAME production can be studied in more detail using the Arrhenius equation. COMSOL is then used to run the reversible mechanism to explore the temperature effect on FFA, FAME and water production. A parametric sweep is then performed ranging the temperature (283.15-343.25 K) and the Arrhenius parameters previously calculated for both reactions are implemented.

Increasing the temperature results in a higher FAME production mainly caused by the kinetic energy of the molecules. It is known that increasing the temperature speeds up a reaction. Before the third step in the reversible mechanism ($t<1x10^{-4}$ s), there is no discernible difference between the curves since the Arrhenius equation is only considered for the forward and reverse reaction in the third step.

In Figure 62, a noticeable difference between esterification at the highest and lowest temperature can be appreciated. When compared at a same time, the highest temperature always shows a higher FAME production right after the third step takes place. An initial concentration of $[O\cdot]$=281.25 mol/m^3 and [FFA]=301.54 mol/m^3 are used in this sweep.

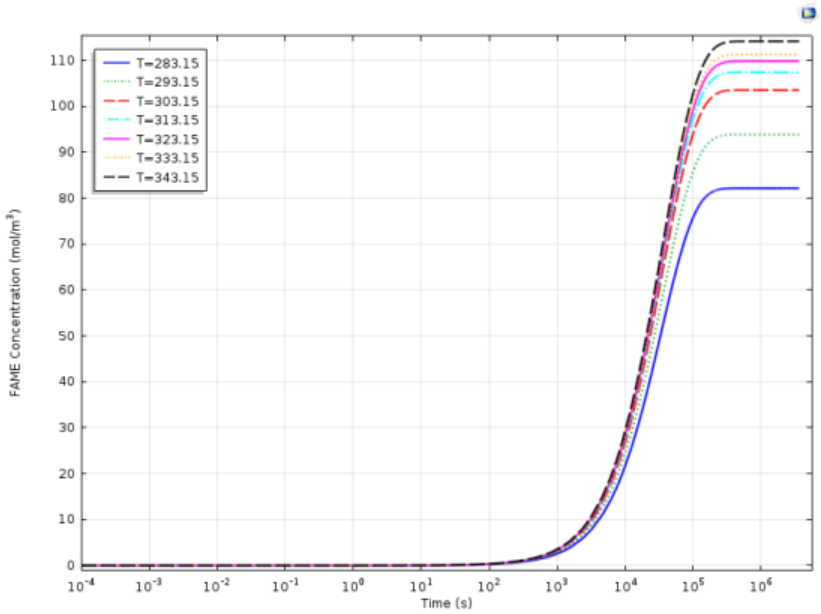

Figure 62 Temperature effect on FAME production for reversible mechanism.

When the temperature is varied in the range 283.15-343.15 K, intervals of 10 K, the reaction mechanism reaches a final FAME concentration of 82.16, 93.85, 103.55, 107.41, 109.83, 111.26 and 114.15 mol/m^3 respectively. As soon as the third reaction takes place, the curves for each temperature start separating in the exponential phase. It is the curve at 70°C the one showing the highest FAME production. With the parameters previously mentioned, a FAME percentage yield of 31.124, 35.621 and 36.898% is obtained at 273.15, 293.15 and 313.15 K respectively. These yields are relatively similar to the ones gathered with the experimental data since the fitted curves showed a better correlation coefficient across the treatments. Having said this, the reversible mechanism is then used in the next chapter to fit the 2-D axisymmetric model to the experimental data. It is known that esterification reactions are reversible 2nd order, this validates the proposed model.

From the different temperatures modelled, the highest FAME percentage yield is obtained at 70°C. Jagadeeshbabu et al reported the esterification of acetic acid at a temperature of 333-353 K using a molar ratio 1:1 in the presence of an ion exchange resin catalyst, the experimental data showed that the acetic acid conversion is increased with increasing the reaction temperature. Lucena et al reported the esterification of oleica cid with methanol using a water adsorption apparatus, the temperature was the variable with the greatest effect on the FAME production yield with high temperature (100-110°C) resulting in conversions ranging from 96.5 to 99.7%. As mentioned before, increasing the temperature showed an increase in the rate of reaction and a typical behaviour of reaction with a high activation energy that are generally favoured by higher temperatures (Jagadeeshbabu, et al., 2011; Lucena, et al., 2008).

Figure 63 shows the rate constants obtained for both the forward and reverse reaction in the proposed mechanism. The values obtained between these two rate constants differ from each other

by a factor of 10. The values obtained for the reverse rate constant are considered to be relatively small when compared to the forward rate constants, this indicates that the reverse reaction (hydrolysis) hardly takes place in the reversible mechanism.

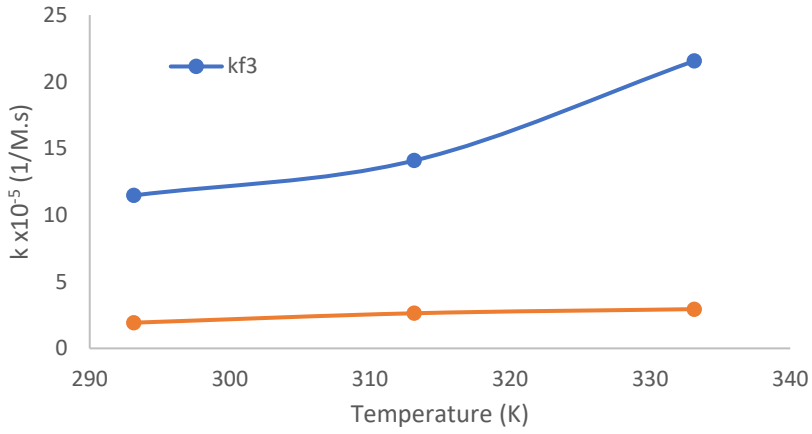

Figure 63 Comparison of the values obtained for kf3 and kr3 against temperature.

In Figure 63, the effect of temperature on the rate constants is depicted. An increase in temperature causes an increase in both the forward and reverse rate constants, but the rate of the endothermic reaction increases more. In the temperature range of 293.15-333.15 K, the forward rate constant varies from 1.147×10^{-4} to 2.155×10^{-4} $M^{-1}s^{-1}$ which means a difference of 1.008×10^{-4} $M^{-1}s^{-1}$. On the other hand, the reverse rate constant varies from 1.927×10^{-5} to 2.940×10^{-5} $M^{-1}s^{-1}$ which means a difference of 1.013×10^{-5} $M^{-1}s^{-1}$. This is attributed to the fact that equilibrium shifts in the endothermic (forward) direction since the added heat is consumed according to LeChatelier's principle. Additionally, for an endothermic reaction (esterification), raising the temperature would increase the equilibrium constant K_{eq} and would increase the equilibrium constant for the exothermic reaction (hydrolysis) (Jagadeeshbabu, et al., 2011).

For the reaction mechanism here proposed, the reverse rate constant has a value of 1.927×10^{-5}, 2.633×10^{-5} and 2.940×10^{-5} $M^{-1}s^{-1}$ at 273.15, 313.15 and 333.15 K. The behaviour followed by the reverse rate constants is in agreement with the effect of temperature on rate constants.

$$FFA + MeOH + O \cdot \leftrightarrow FAME + H_2O + \frac{1}{2}O_2 \qquad \Delta H_{rxn} = -441.116\ \text{kJ/mol} \tag{111}$$

Considering that the third step in this mechanism, the esterification, has a heat of reaction of $\Delta H_{rxn} = 57.21$ kJ/mol. It is important to mention that the three-step mechanism overall follows the general equation found above and has a heat of reaction of -441.116 kJ/mol which means overall the mechanism is exothermic.

In terms of water production, the concentration profile exhibits two plateaus, one for the first two spontaneous reactions and the last one for the third step (esterification). After the first plateau is

reached, when the temperature is varied in the range 293.15-343.15 K, intervals of 10 K, the reaction mechanism reaches a water concentration of 33.55, 38.29, 42.17, 43.71, 44.67, 45.24 and 46.37 mol/m^3 respectively. When the same temperature values are used, the final water concentration reaches a value of 72.13, 83.83, 91.73, 95.29, 97.51, 98.84 and 101.51 mol/m^3 respectively.

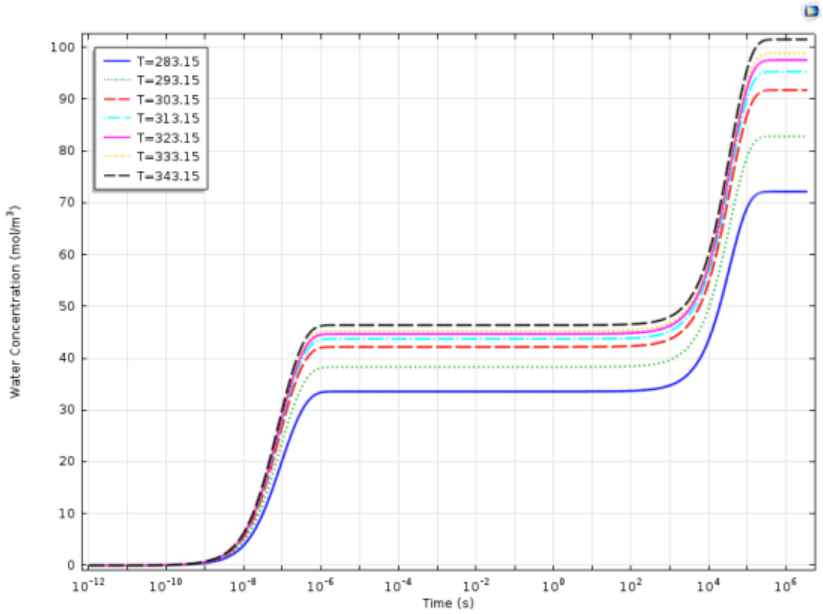

Figure 64 Effect of temperature on water production for reversible reaction.

Figure 64 shows the effect of temperature on the water production for the irreversible mechanism. This figure illustrates how the water production starts varying as soon as the second step takes place. The water production is relatively smaller when compared to the values obtained for the irreversible reaction, this is explained because the increase in temperature means an increase in both the forward and reverse reaction, but the forward reaction increases more. At 333.15 K, the final water concentration for both the irreversible and reversible mechanism was 98.84 and 99.41 mol/m^3. This behaviour is related to the fact that the forward reaction is in the endothermic direction.

6.4.2. Variation of initial methanol concentration

In order to study the effect of the initial concentration of methanol on the FAME production, a parametric sweep for different concentrations of methanol is carried out. Figure 65 illustrates the effect of the initial methanol concentration on the FFA conversion and FAME production. The plot is generated using an initial concentration of [$O\cdot$]=281.25 mol/m^3 and [FFA]=301.54 mol/m^3 at 60°C. This figure shows a comparison between the theoretical FAME production and the experimental data at different initial concentrations of methanol. For an initial methanol concentration of 200, 300, 400, 500 and 600 mol/m^3, the FAME percentage yield achieved has a value of 57.97, 70.48, 73.51, 74.46 and 74.90%. Therefore, increasing the initial methanol concentration increases dramatically the FAME production to a certain extent.

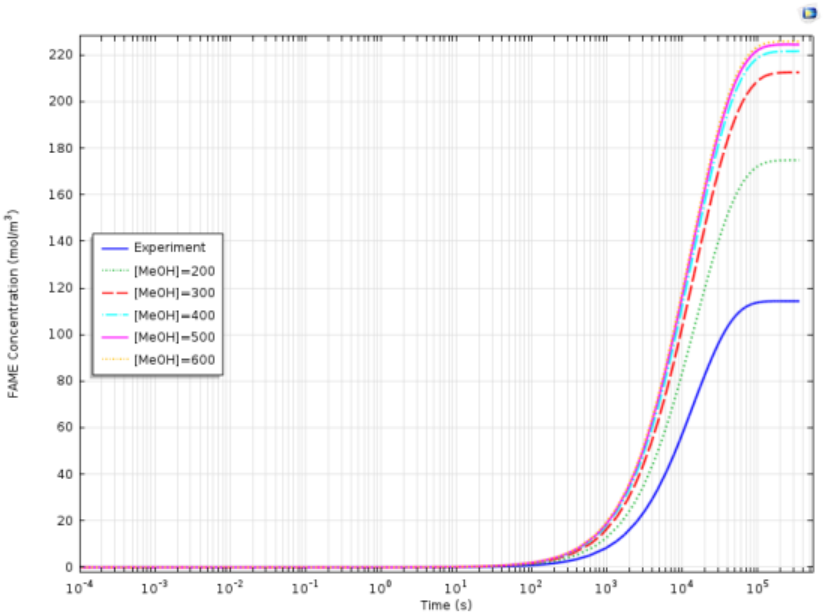

Figure 65 Methanol concentration effect on FAME production and FFA conversion.

At initial methanol concentrations higher than 400-600 mol/m^3, the increase in FAME production only varies 1.89%. This suggests that a further increase in the molar concentration of methanol above 400 mol/m^3 would only incur in an increase of the material cost due to the excess used for the process. When comparing the molar ratio, the proposed 1:1 ratio of oil:methanol achieves a FAME percentage yield of 70.48% and a molar ratio of 1:2 would increase the FAME percentage yield only by 4.42%. Having said this, considering an excess of methanol in for the proposed reaction could mean an increase in the FAME production but more importantly would ease the reaction taking it to completion.

6.4.3. Variation of initial O· concentration

The effect of the initial concentration of the oxygen singlet on the FFA conversion and FAME production is illustrated in Figure 66. This figure shows a comparison between the theoretical FAME production and the experimental data at different initial concentrations of the oxygen singlet. The plot is generated using an initial concentration of [FFA]=301.54 mol/m^3 at 60°C, the ratio oil:methanol used is 1:1. This figure shows a comparison between the theoretical FAME production and the experimental data at different initial concentrations of the oxygen singlet. For an initial $O\cdot$ concentration of 200, 300, 400, 500 and 600 mol/m^3, the FAME percentage yield achieved has a value of 58.27, 72.07, 75.87, 77.05 and 77.57%. Therefore, increasing the initial $O\cdot$ concentration increases the FAME production to a certain extent. The effect of the $O\cdot$ on the FAME production is more significant than varying the initial methanol concentration.

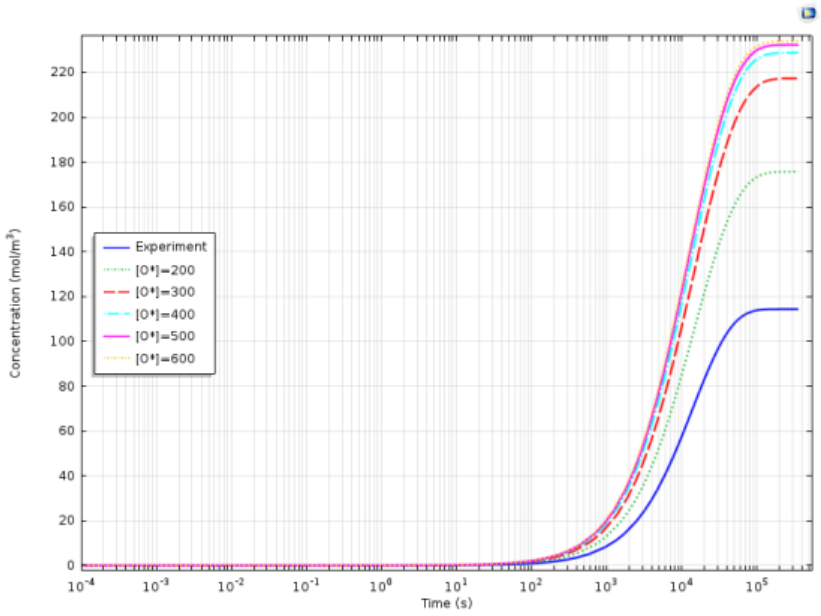

Figure 66 O· Initial concentration effect on FAME production.

At initial $O\cdot$ concentrations higher than 400-600 mol/m^3, the increase in FAME production varies 2.23%. This suggests that a further increase in the molar concentration of the oxygen singlet above 600 mol/m^3 would only incur in an increase of the material cost due to the excess used for the process. When comparing the molar ratio, the proposed 1:1 ratio of oil: $O\cdot$ achieves a FAME percentage yield of 72.07% and a molar ratio of 1:2 would increase the FAME percentage yield only by 5.49%. Varying the initial $O\cdot$ means a more significant increase in the FAME production, this is the main driver to explore its effect on the 2-D model proposed in the next chapter. The results here obtained are in agreement with the hypothesis that the production rate of the biodiesel could be maximised by increasing the initial concentration of oxygen singlet ($O\cdot$) which is thought to enhance the proposed reaction mechanism and take the reaction to completion.

6.5.Conclusions

Some of the key features found when studying the reversible reaction mechanism proposed in this chapter are here presented. For the esterification reaction here proposed, the forward reaction (esterification) is endothermic and the reverse reaction (hydrolysis) is exothermic. The endothermic direction is known to have a larger activation energy, in other words $Ea_f > Ea_r$. The reversible model here studied follows this pattern and has an activation energy for the forward and reverse reaction of 12.692 and 8.652 kJ/mol respectively. The reverse reaction for the third step has an activation energy of E_a = 8.562 kJ/mol and a pre-exponential factor of A = 6.895x10^{-4} M^{-1}s^{-1}. The forward reaction is considerably more thermodynamically favourable than its reverse reaction.

The irreversible mechanism reaches a final concentration for both water and oxygen of 254.43 and 127.2 mol/m^3 respectively. On the other hand, the reversible mechanism reaches a final concentration

for water and oxygen of 207.97 and 103.98 mol/m^3 respectively. The reversible mechanism produces 18.26% less water and oxygen when compared to the irreversible one, this is attributed to the fact that hydroxyl radical is used in the reverse mechanism to carry out the hydrolysis of the esters. The hydrolysis of esters competes with the second step of the mechanism which explains why the water and oxygen productions decreases in the reversible reaction. An increase in temperature causes an increase in both the forward and reverse rate constants, but the rate of the endothermic reaction increases more. This is attributed to the fact that equilibrium shifts in the endothermic (forward) direction since the added heat is consumed according to LeChatelier's principle. Additionally, for an endothermic reaction (esterification), raising the temperature would increase the equilibrium constant K_{eq} and would increase the equilibrium constant for the exothermic reaction (hydrolysis).

Increasing the initial methanol concentration increases dramatically the FAME production to a certain extent. A further increase in the molar concentration of methanol above 400 mol/m^3 would only incur in an increase of the material cost due to the excess used for the process. At initial $O\cdot$ concentrations higher than 400-600 mol/m^3, the increase in FAME production varies 2.23%. This suggests that a further increase in the molar concentration of the oxygen singlet above 600 mol/m^3 would only incur in an increase of the material cost due to the excess used for the process. Varying the initial $O\cdot$ means a more significant increase in the FAME production, this is the main driver to explore its effect on the 2-D model proposed in the next chapter.

7. 2-D axisymmetric model for ozone free radical initiated esterification

Having studied the effect of parameters such as, temperature and the initial concentration of both methanol and the oxygen singlet in the two 0-D models presented in previous chapters. It is necessary to include the heat and mass transfer, surface reactions, transport of diluted species and reaction engineering modules available in the software previously mentioned. The relevant data calculations and estimations presented in both chapter 3 and 4 are here considered. When comparing the 0-D and 2-D axisymmetric inferred rate constants, it is important to stress that the 2-D axisymmetric model is for interfacial interaction only. The 0-D model presumes homogeneous reaction and the 2-D model is heterogeneous. Inherently, this distinction is a massively different mechanistic approach.

Conceptually, the 2-D model can make predictions that are testable to distinguish between heterogeneous and homogeneous catalysis. For instance, the layer depth is extremely important to avoid re-condensation in the 2-D model, whereas the 0-D model has no such mechanism so would be monotonically varying with layer depth. Having said this, in this chapter the reversible mechanism is considered since esterification is known to be a reversible reaction of second order. In this chapter the reader can find the model description, the numerical method used, least squares fitting of the model, the rate constants estimation and the appropriate results and discussion for the simulation profiles and variation of different parameters in order to analyse their effect on the key features. The variation of bubble size, liquid mixture temperature, bubble temperature and initial oxygen singlet concentration are discussed in this chapter.

7.1.Model description

In order to model the physical and chemical properties of the intensified esterification process, COMSOL Multiphysics is used. This is a platform software for modelling engineering applications comprised of add-on modules for simulating processes based on fluid flow, mass and heat transfer, chemistry and reaction engineering.

One of the main purposes of this model is to understand and explore the effects of water production and its respective removal. This thesis explores a hypothesis that forces the esterification reaction of FFAs to completion via the microbubble mediated reactive distillation. In this case, ozone-rich bubbles provide the catalyst to this reaction and remove the water product, driving the reaction to completion following Le Chatelier's principle. This approach uses $O\cdot$, produced in the ozone free radical initiation process, as free radical initiator for the three-step reaction mechanism proposed which takes place on the bubble interface (gas-liquid). The microbubble removes the vapour phase products (water) avoiding product inhibition.

The microbubbles containing a free radical rich atmosphere and dry-to-bone air are injected at the bottom of the esterification unit and rise due to buoyancy force in the liquid phase, stripping one of the resultant by-products like water in the process. The chemical reactions for the esterification of the FFAs take place on the skin bubble in the presence of methanol. Figure 67 illustrates the reactants and reactions taking place according to the proposed model.

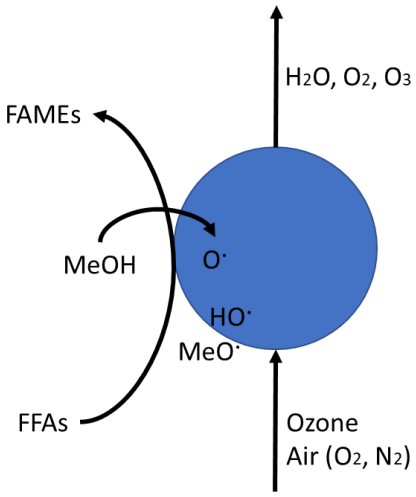

Figure 67 Schematic diagram for the esterification reaction mediated by microbubbles.

In order to simplify the system described above, the proposed model is based on several assumptions: (1) The bubble is always rising in the reservoir at its terminal velocity, making emphasis and focusing only on the heat and mass transfer dynamics. (2) Due to a small residence time of the bubble in the liquid, the pressure inside the bubble is assumed to be constant. (3) The spherical shape of the bubble is maintained since it is sufficiently small that the surface tension around it assures no deformation from the spherical shape takes place. (4) The relevant chemical reactions of the model take place on the skin of the microbubble (Abdulrazzaq, et al., 2016).

7.2.Numerical method

The numerical simulations in this study were carried out using the Galerkin finite element method (FEM) with the software COMSOL Multiphysics 5.3a in order to solve the governing equations. The simulations were performed using both a personal computer and the University server. The first one had an Intel Core i3-7100U Intel HD Graphics 620 running at 2.4 GHz with 8 GB of installed memory and the second one had 12 processors and 94 GB of installed memory.

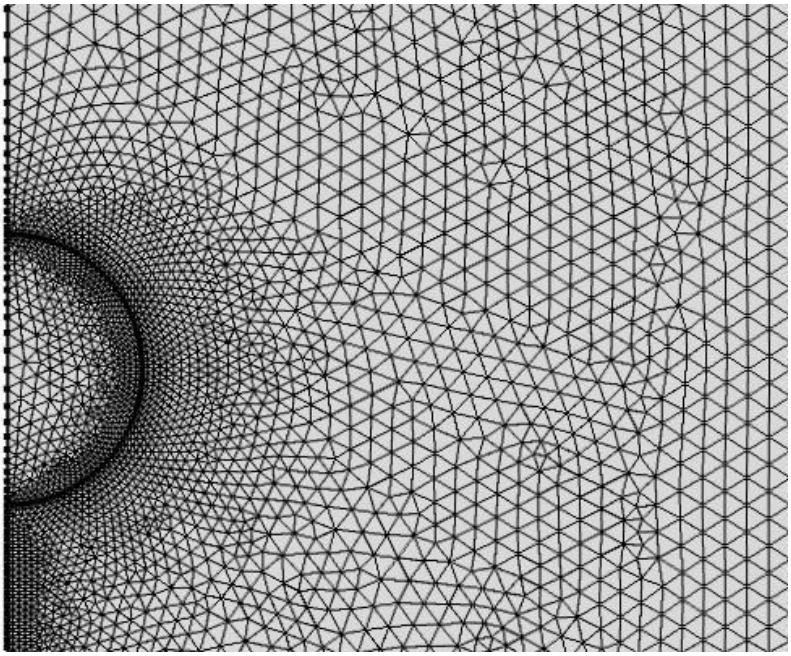

Figure 68 Triangular mesh used for the model.

The mesh used in this computational model is defined by the user. The element size is set to calibrate for general physics. Some of the element size parameters are a maximum element growth rate of 1.1, a maximum element size of 0.5×10^{-5} m, a minimum element size of 4×10^{-8} m, a curvature factor of 0.2 and a resolution of narrow regions of 1. This setting is applied to the gas-liquid interface where majority of the physical and chemical features take place. There are 19,275 triangular mesh elements with an average element quality of 0.9461 and a mesh area of 2×10^{-6} m^2. In Figure 68 is shown the triangular mesh used in this computational model after being refined in order to achieve a higher resolution of the problem at a lower computational cost.

7.3.Results and discussion

The results obtained in the numerical simulations for the ozone free radical initiated esterification are presented in this section. The trends observed by the temperature and concentration profiles of the species of interest over time in this process are here discussed. Several parametric sweeps are presented in order to explore the physics and kinetics of this process by varying parameters such as the radius of the bubble, the temperature of the liquid and the bubble, and the initial oxygen singlet concentration.

7.3.1. Simulation profiles

Firstly, the microbubble profile of water concentration distribution inside the bubble with the respective temperature field and velocity vectors is studied. For the simulation profiles, a radius of 100 μm, an initial temperature of the liquid of 333.15 K, an initial temperature of the bubble of 293.15 K, an initial oxygen singlet concentration of 281.25mol/m^3, and an initial concentration for both methanol

and FFA of 301.54 mol/m^3 are used. It is important to mention that for the purpose of presenting the results in a more detailed and organised structure, the figures in this section have been adapted to the appropriate time scale of up to 1 s, where most of the physical and chemical changes are taking place inside the bubble and in its surroundings.

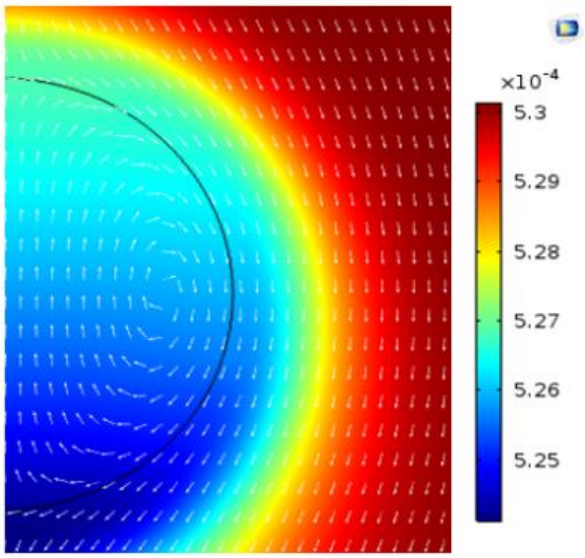

Figure 69 Microbubble profile for the water concentration (mol/m³) after t=0.0 09 s.

Figure 69 shows the microbubble profile for the concentration of water after 0.009 s. The arrows represent the steady state velocity field for a bubble rising through the liquid according to Hadamard and Rybcynski equation. It can be depicted from the figure that the water concentration is constant across the bubble at around 5.26x10^{-4} mol/m^3. This pattern is mainly due to the intensive internal mixing found in the inside of the microbubble which favours the homogenisation of both the thermal and chemical fields at short residence times when the bubble rises through the liquid (Zimmerman, et al., 2013; Abdulrazzaq, et al., 2016).

Regarding the behaviour of the microbubble rising through the liquid, it was noticed that that both the mass and heat transfer dynamics have a strong dependence on time. In terms of the average microbubble temperature, this profile is shown in Figure 70. From this figure it can be depicted that there are two different regimes happening. Firstly, a rapid increase in temperature is noticed followed by a slow increase can be depicted which reaches the liquid temperature T_∞. This would suggest that vaporisation and sensible heat transfer are dominating the first and second regime respectively.

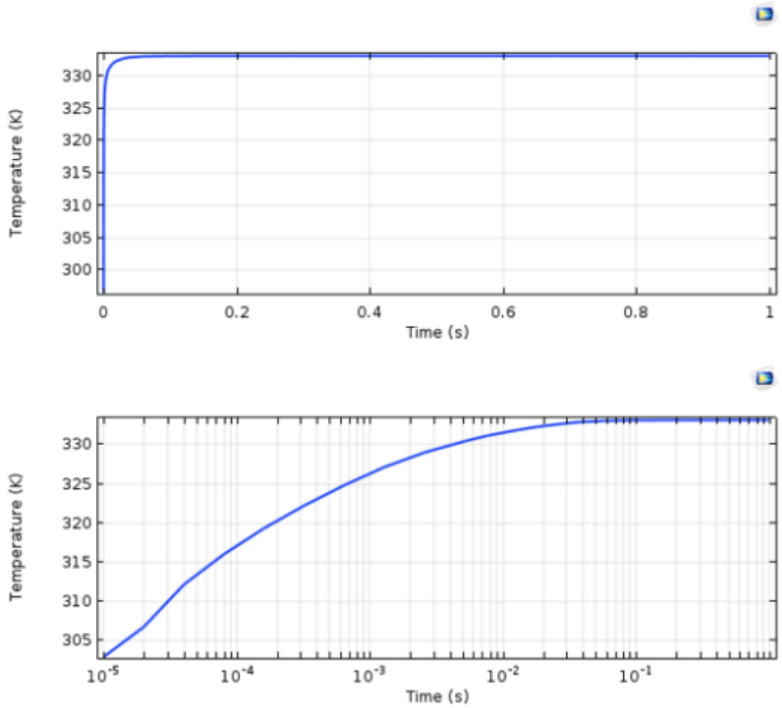

Figure 70 Average microbubble temperature for a bubble T0=293.15 K. Bottom: semilogx plot.

The semilog plot found at the bottom of Figure 70 shows that the average microbubble temperature displays an exponentially faster increase up to $3x10^{-3}$ s compared with the next 10^{-1} s. This could suggest that evaporative cooling happens at least one to two orders of magnitude faster than sensible heat transfer for this process. In other words, this could be explained as an effect caused by the evaporation of the liquid into the bubble. The latent heat of vaporisation is lost causing the bubble temperature to increase rapidly at short contact time. The value of $3x10^{-3}$ s is considered as the turning point where the process changes of regime. This turning point is one order of magnitude different to the one reported by Zimmerman et al of $1x10^{-4}$ s. The difference could be attributed to the discrepancy in the initial microbubble temperature used in both studies, of nearly 100°C (Zimmerman, et al., 2013; Abdulrazzaq, et al., 2016).

The microbubble temperature profile at the turning point (T=330 K) is illustrated in Figure 71. A heat transfer coefficient of 0.1 W/m^2K is used in this simulation, the arrows represent the steady state velocity field and the shading represents temperature. It can be depicted from the figure that at this specific time, the microbubble is relatively isothermal at 330 K. The purpose of this figure is to point out that at this turning point is where the maximum internal humidity is achieved.

The physical properties for both the liquid and gas phase are shown in Table 10 and Table 11. Properties like heat capacity and thermal conductivity are defined by polynomial empirical correlations since they depend on temperature. Whereas, from Figure 71 can be noticed that the temperature variation across the microbubble is not considerably significant, properties like density, viscosity and molecular diffusivity are considered constant.

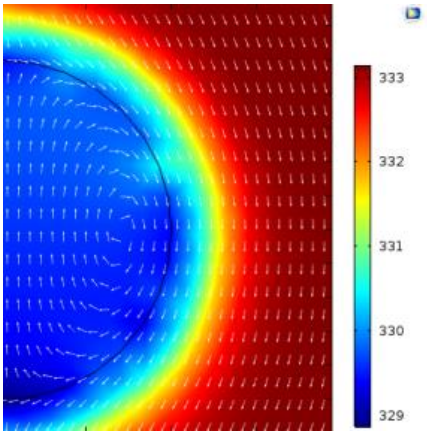

Figure 71 Microbubble temperature profile (K) at the turning point.

For the heat transfer coefficient value, Kumar et al reported a value of 1080 W/m^{2}K for bubble of approximately 1 cm. For the purpose of this simulation, since the radius of the microbubble is 100 times smaller, a value for the heat transfer coefficient of 0.1 W/m^{2}K is considered. This value has been used by Zimmerman et al when studying the evaporation dynamics of microbubbles (Zimmerman, et al., 2013; Kumar, et al., 1992).

In order to fully understand the correlation between the ozone free radical initiated esterification and the water vaporisation and further removal, it is necessary to analyse the concentration profile of the different species found in this reaction mechanism. Firstly, the average oxygen singlet concentration profile inside the bubble found in Figure 72 shows the behaviour of this species over time. It can be noticed from the graph that the oxygen singlet starts being consumed after 1x10^{-4} s, showing an exponential decay around 1x10^{-2} s. The concentration reached after one second is approximately 275.5 mol/m^3. This difference in oxygen singlet concentration could be then correlated to the FAME production in the reaction mechanism.

The decrease in the oxygen singlet concentration means the reaction mechanism here proposed has already started and that the subsequent second reaction would take place right after.

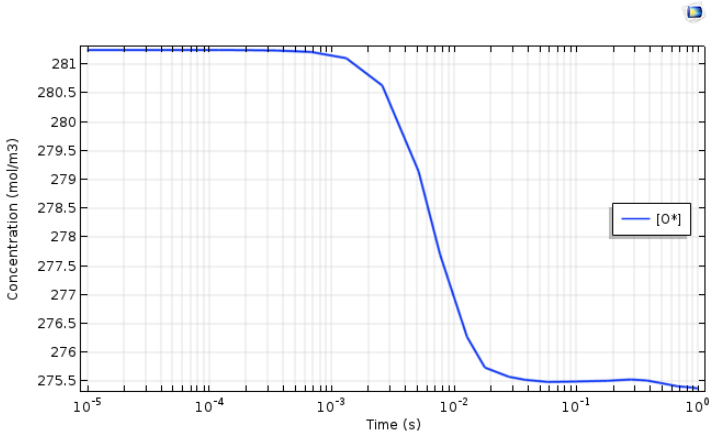

Figure 72 Oxygen singlet concentration profile in time.

For the average concentration profile of the hydroxyl radical and FAME in the gas-liquid interface, it can be noticed that both species show the same exponential behaviour in the first regime, followed by a slow increase due to the reaction kinetics of the third step. The concentration profile for both species is found in Figure 73. It is assumed for this reaction mechanism that the third step is the slowest one. Therefore, the oxygen singlet species reaches an equilibrium concentration and is consumed rapidly in less than $1x10^{-1}$ s, while the products for the third step would take longer to reach an equilibrium in both the liquid and gas domain.

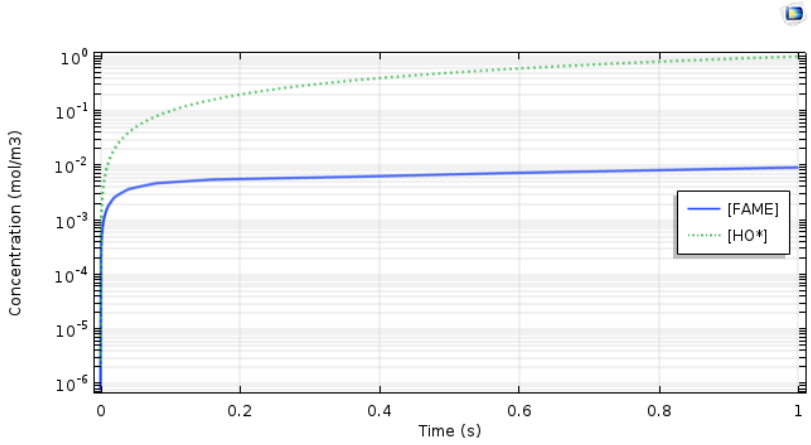

Figure 73 FAME and hydroxy radical concentration on the surface profile over time.

As expected the concentration of FAME is relatively lower compared to the hydroxyl radical for this case. After one second, the FAME and hydroxyl radical concentration reach a value of $1.46x10^{-2}$ and 1.041 mol/m^3. There are nearly two orders of magnitude between the concentrations of these two species. This suggests the radical species is being produced by the forward reaction in the first step of the mechanism and but not been consumed fully by the third reaction (esterification). This would suggest that there is room for improvement so most of the radical species produced in the gas-liquid interface is fully used. In order to explore the behaviour of the product of interest in this study, the FAME production, a concentration profile for FAME over time is presented in Figure 74. In this figure, the arrows represent the steady state velocity field and the shading represents concentration profile. It can be noticed that time at $1x10^{-3}$ s, the FAME concentration on the microbubble surface has a value of around $2.5x10^{-3}$ mol/m^3 across the surface. A thin layer of the FAME produced is observed around the microbubble surface. At $1x10^{-2}$ s, the FAME concentration reaches a value nearly 4 times greater compared to the first time analysed. It is clear that the layer thickness increases in time suggesting more FAME is being produced on the gas-liquid interface.

At $1x10^{-1}$ s, it can be depicted from the figure that majority of the FAME produced migrates to the bottom of the microbubble and reaches a concentration of $3x10^{-3}$ mol/m^3. This behaviour is attributed to the outflow condition previously mentioned in this chapter in order to emulate the rising of the

bubble through the liquid. At 1 s, the FAME produced continues to migrate to the bottom of the microbubble and achieves a concentration of $4x10^{-2}$ mol/m^3.

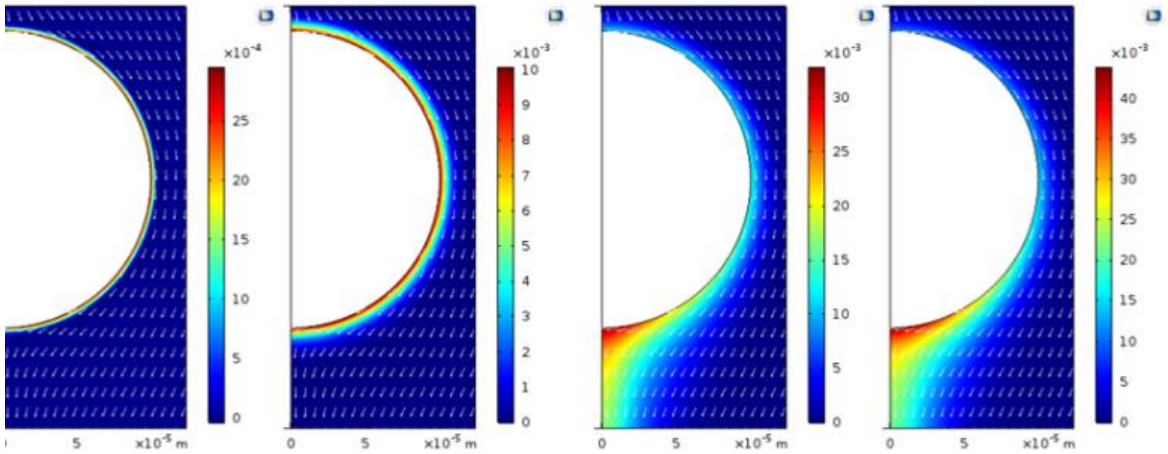

Figure 74 FAME concentration profile (mol/m^3) over time (From left to right t=$1x10^{-3}$, $1x10^{-2}$, $1x10^{-1}$ and 1 s).

It is important to mention that these concentrations may differ from the ones reported in Figure 73, since in Figure 73 the average concentration on the surface for both species was plotted whereas in Figure 74 the whole gradient is shown and the values reported are the maximum at each time analysed.

7.3.2. Variation of the bubble size

One of the most important parameters when studying microbubbles is the bubble size since it is strongly related to the gas-liquid interface, which is responsible for the heat and mass transfer dynamics. In Figure 75, the variation of the average bubble temperature with the bubble size is shown. In this case four different radius were used to illustrate the effect of the bubble size from top to bottom, R= $5x10^{-5}$, $1x10^{-4}$, $3x10^{-4}$ and $5x10^{-4}$ m. The initial bubble temperature is T0= 293.15 K and an initial FFA concentration of 301.54 mol/m^3. It can be noticed that a smaller bubble reaches the thermal equilibrium faster compared to a bubble with a larger radius. In the case of R=$1x10^{-4}$ m, this thermal equilibrium is reached around $9x10^{-3}$ s compared to $4x10^{-2}$ s for a bubble five times its size (r=$5x10^{-4}$ m). This is mainly attributed to the fact that smaller bubbles deliver majority of their enthalpy at shorter residence times in the liquid mixture, whereas larger bubbles take considerably longer to reach the mentioned thermal equilibrium since they possess a weaker internal convection (Zimmerman, et al., 2013).

The plot here discussed has a maximum value on the x-axis of 0.1 in order to magnify the differences between the simulations here studied. This behaviour is in agreement with results reported by Abdulrazzaq et al when studying the purification of bioethanol using microbubbles generated by fluidic oscillation. Their results indicate smaller bubbles deliver their enthalpy relatively faster and reach

equilibrium, hence promoting the stripping efficiency of ethanol in binary mixtures (Abdulrazzaq, et al., 2016).

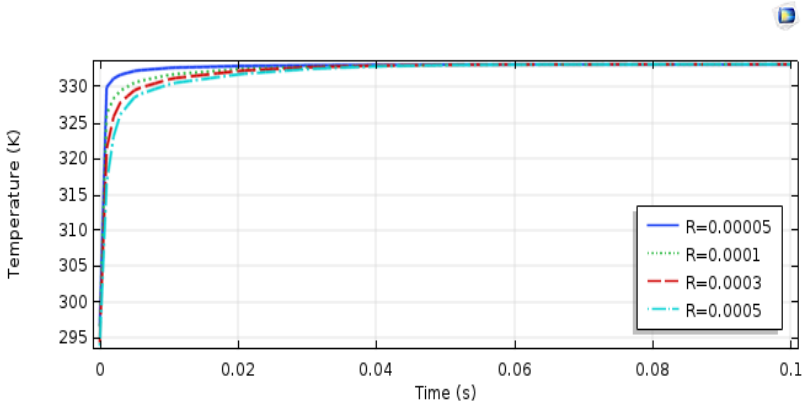

Figure 75 Variation of the average bubble temperature with bubble size (m).

Once the effect of the bubble size on the average bubble temperature has been analysed. It is important to explore the effect of the same parameter but in the FAME concentration. Figure 76 illustrates the effect of the bubble size on the average FAME concentration found in the liquid mixture for different radius, from top to bottom R= $5x10^{-5}$, $1x10^{-4}$, $3x10^{-4}$ and $5x10^{-4}$ m.

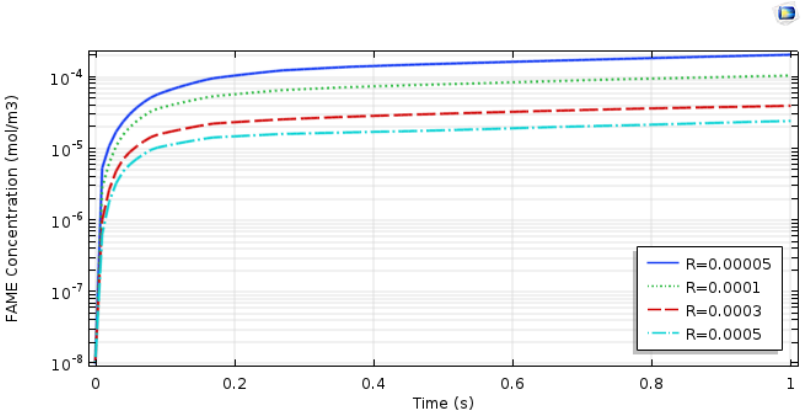

Figure 76 Variation of the average FAME concentration in the liquid mixture with bubble size (m).

The initial bubble temperature is T0= 293.15 K and an initial FFA concentration of 301.54 mol/m^3. It can be depicted from Figure 76 that a higher FAME concentration is found in the liquid mixture at a smaller bubble size. This behaviour could be attributed mainly to several factors: i) An enhanced mass and heat transfer by the enhanced gas-liquid interface when reducing the size of the bubble, ii) the increased vaporisation and stripping of the produced water, iii) a combination of both scenarios previously mentioned.

After 1 s at a radius of R= $5x10^{-5}$, $1x10^{-4}$, $3x10^{-4}$ and $5x10^{-4}$ m, the average FAME concentration in the liquid mixture has a value of $3.07x10^{-5}$, $5.15x10^{-5}$, $1.32x10^{-4}$ and $2.32x10^{-4}$ mol/m^3 respectively. These results suggest that small bubbles are more efficient in terms of FAME production due to an

enhanced mass and heat transfer related to a higher surface area to volume ratio. This behaviour is best exploited at short residence times within the liquid in order to avoid recondensation. Microbubbles have higher residence times and a more intensive internal velocity rate, these attributes here mentioned lead to a faster vapour concentration of water inside the microbubble at short residence time. At higher residence times, the concentration inside a microbubble tend be similar compared to larger bubbles. This pattern is explained because the microbubbles loses most of its contents when it cools down due to the recondensation process (Zimmerman, et al., 2013).

7.3.3. Variation of liquid mixture temperature

In the esterification process, the liquid mixture temperature is the parameter that mainly establishes the temperature at which the reaction kinetics are happening. It is known from the data gathered in the previous chapters that an increase in the liquid mixture temperature would result in an increase of the FAME concentration in the liquid mixture due to an increase in the rate constants. For the conventional esterification reaction, the increase in temperature is mainly limited by the boiling point of the solvent used in the reaction. In the case of methanol, the boiling point is 64.7°C. As mentioned before in this thesis, the approach considered in the reaction mechanism in order to avoid this limitation states that methanol is found to be highly reactive in the presence of the oxygen singlet radical which then react to produce the methoxy and hydroxyl radical, therefore initiating the free radical chain reaction.

Having said this, the effect of the liquid mixture temperature on the average water concentration inside the bubble is here studied and showed Figure 77. From the figure a few features can be noticed, an increase in the liquid mixture temperature results in an increase in the average water concentration found in the bubble. In theory, the bubble reaches a maximum concentration in the first regime at the turning point previously mentioned, to then decrease until it reaches the thermal and chemical equilibrium. In this model, five different temperatures were studied (T=293.15-373.15 K) in order to explore and understand if increasing the liquid temperature has an impact on the bubble average water concentration. It is important to mention that the experimental data to which the model is compared to then be validated considers runs only at 293.15 to 333.15 K.

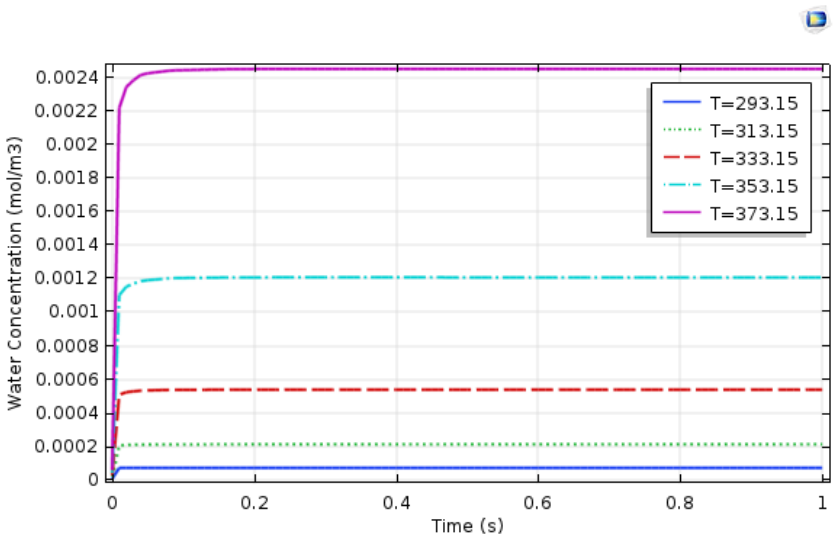

Figure 77 Variation of the bubble average water concentration with liquid mixture temperature (K).

In Figure 77 can be seen that at a liquid mixture temperature of 293.15-373.15 K, the average water concentration in the bubble is $7.17x10^{-5}$, $2.12x10^{-4}$, $5.38x10^{-4}$, $1.23x10^{-3}$ and $2.45x10^{-3}$ mol/m^3 respectively. This suggests that increasing the liquid mixture temperature would increase dramatically the vaporisation of water and therefore favour the FAME production, only if the produced water is stripped before it undergoes recondensation after the turning point (Abdulrazzaq, et al., 2016).

The vaporisation parameter of water in this system is described as (*KL*). In order to understand the influence of this parameter in the reaction mechanism here proposed, a sensitivity study of the average bubble temperature to several values of this *KL* was performed. Figure 78 shows a lack of sensitivity to the parameter *KL* on the average bubble temperature. A small value of the water vaporisation parameter ($2x10^{-7}$) would result in a slower mass transfer, mainly found in isothermal systems.

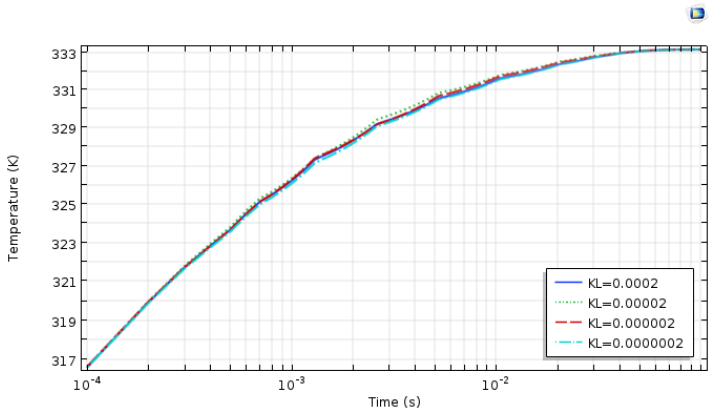

Figure 78 Double log plot of the variation the average bubble temperature with mass transfer coefficient.

A large value of this parameter would result in systems that flash to equilibrium characterised by a rapid vaporisation followed by recondensation as the bubble reaches the second regime. In this study a value of $2x10^{-5}$ has been used in order to guarantee nonequilibrium dynamics that are rapid enough.

This value is in agreement with previous values reported by Abdulrazzaq et al in the purification of bioethanol in binary mixtures (Abdulrazzaq, et al., 2016; Zimmerman, et al., 2013).

As mentioned in previous chapters, an increase in temperature would mean an increase in the rate constants. And in the case of the esterification reaction (endothermic process) the rate constants in the endothermic direction would always suffer a higher impact by this increase in temperature.

The effect of the liquid mixture temperature on the average FAME concentration is then analysed as well. This parameter is analysed in order to understand its impact on the product of interest. Figure 79 shows the effect of the liquid temperature at five different temperatures (T=293.15-373.15 K) on the FAME concentration found in the liquid. It can be noticed that the behaviour followed by the FAME species is similar to the water produced. An increase in the liquid mixture temperature results in an increase on the FAME concentration in the liquid mixture. The curves here generated are possible thanks to the use of the Arrhenius equation which describes the temperature dependence of the rate constants in the reaction mechanism.

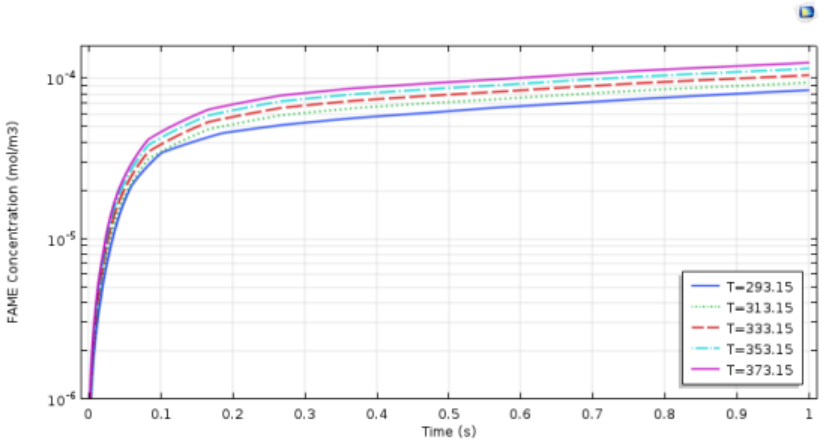

Figure 79 Variation of the average FAME concentration with liquid mixture temperature (K).

This is the explanation for an increase of the FAME concentration from the kinetic side of the process. In terms of the vaporisation of water, this process is thermodynamically favoured with an increase in temperature and therefore would cause an increase in the FAME production. Having said this, the increase of the FAME concentration in the liquid mixture could be attributed to the sum of these two factors which address both the reaction kinetics in the proposed mechanism and the physical advantage posed by the stripping of the produced water. In Figure 79 can be seen that at a liquid mixture temperature of 293.15-373.15 K, the average FAME concentration in the liquid mixture reaches a value of $1.05x10^{-4}$, $1.18x10^{-4}$, $1.32x10^{-4}$, $1.44x10^{-4}$ and $1.57x10^{-4}$ mol/m^3 respectively.

7.3.4. Variation of the bubble temperature

The variation of the average bubble water concentration with bubble temperature is here studied in order to explore the effect of this parameter. It is important to point out that the experimental data was carried out at initial bubble temperature of 293.15 K.

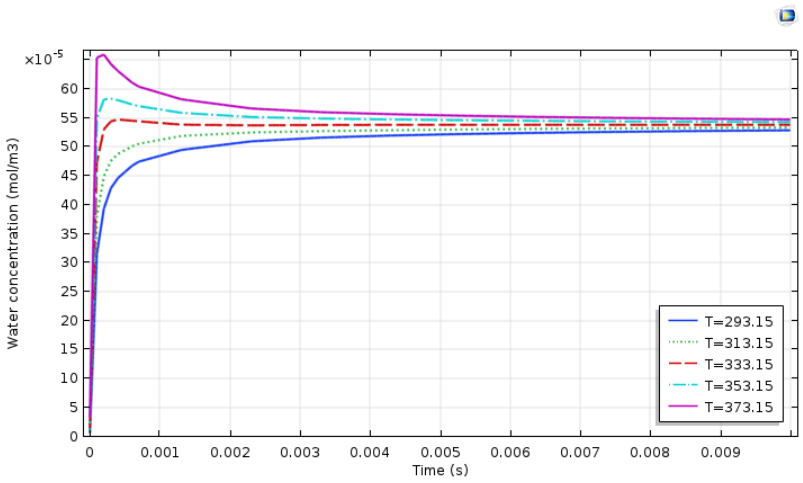

Figure 80 Variation of the average water concentration with bubble temperature (K).

This is one of the main reasons why the model here proposed is used to explore the behaviour in the average bubble water concentration shown in Figure 80. An initial liquid mixture temperature for this simulation of 333.15 K and an initial FFA concentration of 301.54 mol/m^3 are used. It can be easily depicted from this figure, that for an initial bubble temperature above the initial liquid mixture temperature (T_0 bubble > T_0 liquid), a maximum in the water concentration is found at the turning point previously mentioned. The higher the difference in temperature between these two temperatures, the more rapidly the turning point is reached.

In other words, the maximum water concentration is achieved when the bubble temperature has a higher value. Decreasing the initial bubble temperature would slow the recondensation process. This could be understood as if the bubble temperature is increased, the vapour pressures of the species in the liquid mixture would increase leading to an increase in the fraction of the evaporated species into the inside of the bubble. The results here obtained are in agreement with study reported by Zimmerman et al when analysing the evaporation dynamics of microbubbles. This suggests that increasing the initial bubble temperature in this process would improve the water vaporisation and therefore the FAME production (Zimmerman, et al., 2013).

The turning point separates the two regimes, the exponential decay caused by the vaporisation of the water followed by the sensible heat transfer. in order to maximise the water vaporisation and therefore enhance the FAME production, the residence time of the microbubble should always be lower than this point. This would mean a maximum in the water vaporisation but without

compromising the reaction kinetics for the FAME production. After the turning point, the recondensation of the produced water is observed and the water is then returned to the liquid mixture allowing the bubble to cool down and give away its enthalpy by slowly increasing the temperature of the liquid (sensible heat transfer). It can be noticed that the low heat transfer coefficient used in this model leads to a pronounced and long plateau in the water concentration in the bubble while the recondensation process slowly takes place, this plateau in time would reach a value of $5.38x10^{-4}mol/m^3$ (Zimmerman, et al., 2013).

In Figure 80 can be seen that at a bubble temperature of 333.15-373.15 K with intervals of 10 K, the maximum water concentration in the bubble is $5.417x10^{-4}$, $5.623x10^{-4}$, $5.868x10^{-4}$, $6.225x10^{-4}$ and $6.649x10^{-4}$ mol/m^3 respectively. Once the data from the simulation is gathered, it is possible to generate a plot in order to find a correlation between the maximum water concentration against the difference in temperature between the gas and liquid domain, this correlation is illustrated in Figure 81. It is clear there is a linear correlation between the difference in temperature between the initial bubble and liquid mixture temperature and the maximum water concentration in the bubble achievable, described by the following expression $C_{max}=5.3432 + 0.0307\Delta T$ ($R^2=0.9774$).

It is important to mention that the initial condition for this simulation is that the bubble enters dry into the liquid mixture. This plot was generated considering an initial liquid mixture temperature of T=333.15 K, a heat transfer coefficient of 0.1 W/m^2K and a radius of $1x10^{-4}$ m. This correlation could then be used in order to calculate the maximum water concentration inside the bubble that would be achievable without the need to carry out an experiment.

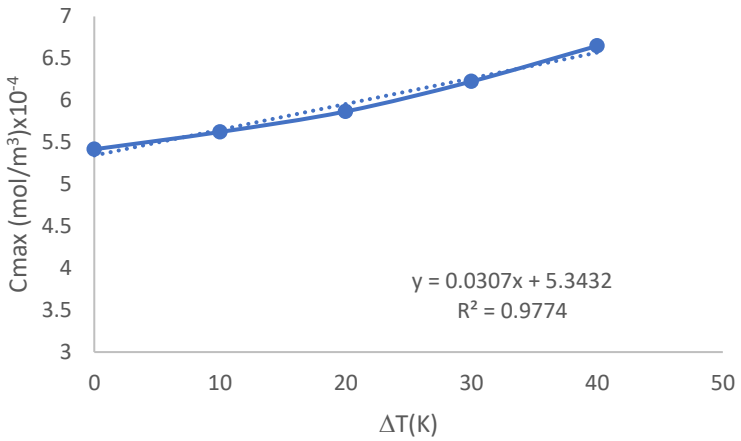

Figure 81 Maximum water concentration against ΔT=T0-T∞ (K).

As seen in Figure 80, for every different initial bubble temperature used in the parametric sweep, a chemical equilibrium is reached in terms of the water concentration. At a residence time longer than the turning point, a thermal equilibrium would be reached by all the different treatments. Figure 82 shows the thermal equilibrium reached by different average bubble temperatures (T=293.15-373.15)

with the surrounding liquid mixture. An initial liquid mixture temperature of 333.15 K and an initial FFA concentration of 301.54 mol/m^3 are used for this simulation. It can be noticed that the thermal equilibrium is reached by all the different temperatures before 0.1 s. A larger temperature difference between the initial bubble temperature and the liquid mixture temperature results in a longer period of time required to reach this equilibrium.

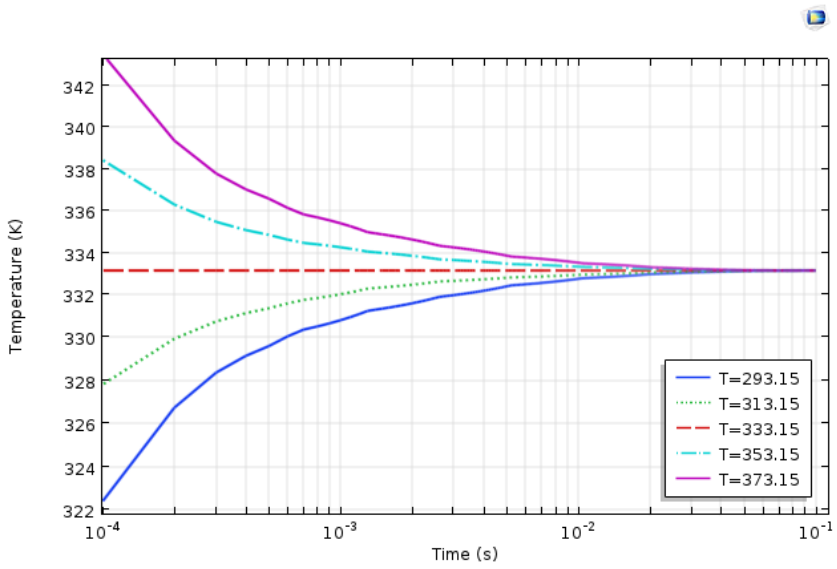

Figure 82 Double log plot of the variation of the average bubble temperature over time.

It is fair to say that the additional evaporation achieved when injecting higher bubble temperatures could be neglected for the purpose of this simulation mainly because of the volumetric heat capacity of the liquid and the size of this computational model. In other words, the product of the density of a species by its heat capacity is nearly three orders of magnitude higher that of the vapour phase, and the liquid domain is only one order of magnitude large than the radius of the microbubble (Abdulrazzaq, et al., 2016).

7.3.5. Variation of the oxygen singlet concentration

One of the main features in this thesis is to explore the effect of the oxygen singlet radical on the FAME production. It has been hypothesised that increasing its initial concentration would suggest an increase in the overall FAME production found in the liquid mixture.

As mentioned before, the microbubbles generated with a fluidic oscillator have an initial concentration for the free radical $O\cdot$ of [$O\cdot$]= 4500 ppm which corresponds to the initial concentration of [$O\cdot$]= 281.25 mol/m^3 used in these models. The production rate of the biodiesel could be potentially maximised by producing a high amount of $O\cdot$ using an advanced oxidation plasma reactor. It has been reported by Zimmerman and Lozano Parada that it is possible to tune a plasma reactor under specific conditions, so a maximum of $O\cdot$ at 1x10^{-3} s it then produced. This means there is no need to form the

ozone species for then to be decomposed in $O\cdot$, but by tuning the device a set amount of this species can be produced (Lozano-Parada & Zimmerman, 2010).

The importance of this species relies on the fact that it is one of the initiators in the proposed reaction mechanism. Figure 83 shows the effect of different initial concentrations of the oxygen singlet radical on the average FAME concentration in the liquid mixture. It can be noticed that increasing the concentration of the $O^{\cdot}$ radical results in an increase in the FAME concentration in the liquid domain. For the initial molar ratio $O^{\cdot}$:FFA of 2:1 and 3:1, the FAME concentration reaches a maximum value at 0.1 s of 1.156 and 1.775×10^{-4} mol/m^3.

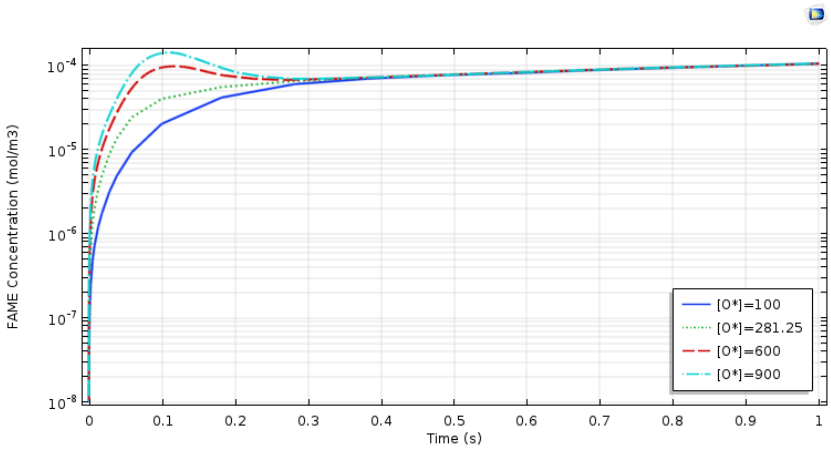

Figure 83 Variation of the average FAME concentration with oxygen singlet concentration (mol/m^3).

It can be noticed from this figure, that for the curves when the $O^{\cdot}$ concentration is higher than the initial FFA concentration ($[O^{\cdot}]_i > [FFA]_i$) the curves reach a maximum around 0.1 s. All the curves reach a chemical equilibrium right after 4×10^{-1} s. These findings would suggest that the residence time of the microbubble (τ_{res}) rising though the liquid with the respective rate constants would necessarily be lower than 0.1 s, in other words (τ_{res}<0.1 s), when the maximum FAME concentration in the liquid is reached before it reaches the chemical equilibrium.

In order to maximise the FAME production and optimise the kinetics of this reaction mechanism, one approach would be estimating the maximum vaporisation layer thickness. This refers to the maximum thickness that ensures a maximum in the FAME concentration by tuning the residence time of the microbubble rising through the liquid in terms of the layer thickness. This vaporisation layer is estimated to be a few hundred microns (~438 μm) for the case of the mechanism here proposed. If this design feature is relevant when studying a vaporising system which would achieve maximum water removal and FAME production at a cost of the minimum heat transfer. The modelling work here presented could be potentially considered for the ozone free radical initiated esterification. The simulations analysed in this chapter are informed in experimental data and validated using the least square fitting of the curves (Zimmerman, et al., 2013).

7.3.6. Rate constants estimation

In order to validate the results presented in this chapter, the least square method was carried out to fit the curves of the product of interest over time. The modelling approach considered the amount of FAME produced of the single bubble size to predict the amount of FAME produced that was obtained in the experimental data. The assumption of a single bubble size is sensible for microbubbles generated by a fluidic oscillator since the interactions between them could be neglected and the size distribution is very narrow (Zimmerman, et al., 2008; Abdulrazzaq, et al., 2016).

In order to compute the residence time of the microbubble in the liquid mixture for the experimental data, a few factors need to be taken into account in order to estimate this parameter. The residence time is a combination of three regimes: i) the generation of the bubble from the pore in the diffuser, ii) the rising time through the liquid mixture, and iii) the time for the bubble to burst at the top of the liquid mixture layer. According to the numerical results calculated for this esterification unit, the residence time of the microbubbles rising through the liquid mixture has a value of 19.26 s. Having said this, the model was run using MATLAB with COMSOL in order to generate an appropriate time step that would describe the curves obtained in the experimental data. The information from the model is used to generate a gradient for both FFA and FAME over time, based on the gradient of production/consumption and the bubble flux over time is possible to generate the plot found in Figure 84. The code used for this regression is found in Appendix B.

Figure 84 gives an example of the least squares fitting for the FAME production curves obtained in the experimental data. The best fit throughout the curves was obtained at a FFA content of 20% and 60°C with a correlation coefficient of R^2=0.999. Using a forward rate constant of 11.03×10^{-6} $M^{-1}s^{-1}$, the calculated reverse rate constant had a value of 6.317×10^{-7} $M^{-1}s^{-1}$. The computational model fit is joined up by a trend curve, as it is presumed continuous and monotonic, so that one can interpolate if needed. For a brief explain of the fitting method refer to Section 3.2 in Chapter 3.

In terms of comparison, the curve with the lowest R^2 was the 10 FFA% at 293.15 K. The treatment 10 FFA% at 293.15 K obtained a forward rate constant of 1.6631×10^{-4} $M^{-1}s^{-1}$(R^2=0.998). The 2-D reversible mechanism considering mass and heat transfer, surface reactions and the reaction kinetics in the gas-liquid interface shows an improvement in the fitting of the curves when compared to the irreversible model. This would suggest that the 2-D reversible model describes the experimental data in a better way since it acknowledges the physico-chemical properties of the compounds involved in the esterification reaction. Consequently, the 2-D reversible model represents a more solid and reliable model that could be used for further modelling since it considers every aspect of the reaction kinetics happening in the interface and the transport of the species that are being both produced or consumed.

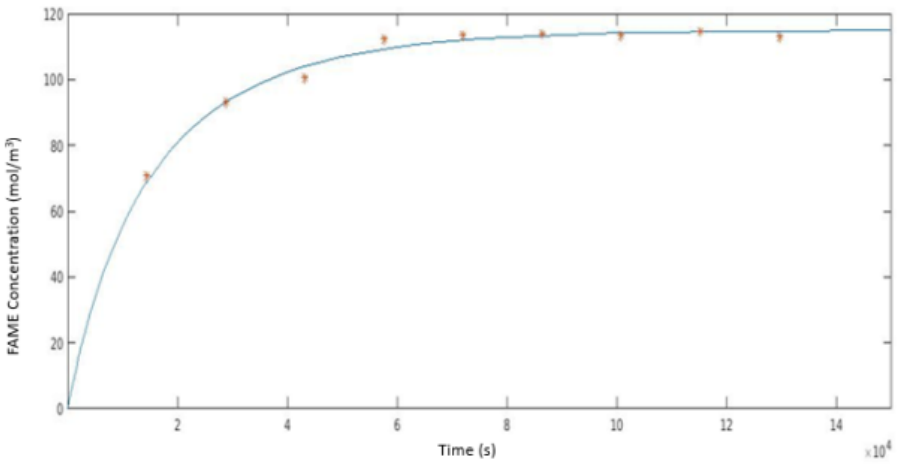

Figure 84 Comparison between model and experimental data for the amount of FAME produced over time.

For the iterations used in this method, a condition to find only positive numbers is used since the order of magnitude is $1x10^{-7}$ and the solver could return negative values. The tolerance for the rate constants in the iterations is set to $1x10^{-10}$ to return values with significant figures. Once the code is run, it gives the value that satisfies the condition of having the least squared error and the values for the new predicted y^p.

The values for the rate constant *kf3* for each treatment are found in Table 30. It can be noticed that compared to the forward rate constants estimated in Chapter 5 for the 0-D, these values differ by one order of magnitude. It is important to point out that the rate constants calculated in both Chapter 5 and 6 only consider the reaction mechanism in the reactor, the forward rate constants here presented consider the heat and mass transfer across the gas-liquid interface as well as the temperature dependence of the reaction kinetics. The difference in the orders of magnitude could be attributed to the residence time of the microbubble rising in the liquid mixture. In Table 30, the resulting values for *kf3* are shown in ($M^{-1}s^{-1}$) to ease further calculations. The effect on temperature can be easily noticed, an increase in temperature results in an increase in the forward rate constant across the three different FFA contents here studied.

Table 30 Rate constant kf3x10^{-6} (1/M.s) values for each treatment.

		Free Fatty Acid %		
		10%	**15%**	**20%**
Temperature (K)	**293.15**	3.569	3.739	3.931
	313.15	3.201	4.175	4.818
	333.15	9.287	10.69	11.03

The values for the rate constant *kr3* for each treatment are found in Table 31. The difference in the orders of magnitude pattern is observed for the reverse rate constants as well.

Table 31 Rate constant kr3x10^{-7} (1/M.s) values for each treatment.

		Free Fatty Acid %		
		10%	**15%**	**20%**
Temperature (K)	**293.15**	3.872	4.028	4.217
	313.15	4.293	4.628	4.912
	333.15	5.846	6.026	6.317

All the fitted curves have a correlation coefficient greater than 0.97 which suggests that the method used to fit the curves has a high overall quality. For each FFA content (10, 15 and 20%), the highest value for R^2 is achieved at 60°C, since the experimental data shows the plateau behaviour at higher temperatures and a more pronounced curvature for the FAME production over time. This behaviour could be attributed to the effect of temperature in a chemical reaction, since it is known that a higher temperature a reaction occurs more rapidly. In other words, the exponential growth in terms of production of FAME at the beginning of the reaction is more noticeable at higher temperatures.

The results obtained for the one-way ANOVA are shown in Table 32, in this case the forward rate constant across the FFA content are not significantly different since $F_{value}<F_{crit}$ (0.0866<5.14). In other words, we fail to reject the null hypothesis meaning there is no significant difference between the three groups for the FFA content 10, 15 and 20% but there is a noticeable difference between the temperatures considered in this model. The F_{value} calculated for the reverse rate constant is relatively smaller than the one obtained for the forward rate constant, this could be credited to the fact that the reverse rate constant are calculated using the forward rates which have already been proven to not show any significant difference across the FFA content.

Table 32 ANOVA results for the forward rate constant.

	df	**SS x10^{-12}**	**MS x10^{-12}**	**F**	**F_{crit}**
Treatment	2	2.413	1.206	0.0866	5.14
Residuals within	6	83.531	13.921		
Total	8	85.944			

Once the statistical analysis across the FFA is completed and it is concluded there is no significant different between the groups accounting for the Free Fatty Acid%, the average values for both the forward and reverse rate constants are used in the Arrhenius equation to obtain the activation energy (E_a) and pre-exponential factor (*A)* for the reverse reaction of the third step. The values for the average forward and reverse rate constant at each temperature are shown in Table 33, these values are then

processed to be used in the Arrhenius equation. When plotting ln(*k*) against 1/T, a straight line is then obtained where the E_a and *A* can be calculated from the y-intercept and the slope of the line.

Table 33 Average rate constants used for Arrhenius equation parameters.

Temperature (K)	1/T x10^{-3} (K^{-1})	Forward rate constant x10^{-6} ($M^{-1}s^{-1}$)	ln(k)	Reverse rate constant x10^{-7} ($M^{-1}s^{-1}$)	ln(k)
293.15	3.4112	5.352	-12.137	4.670	-14.576
313.15	3.1934	6.201	-11.990	4.894	-14.530
333.15	3.0017	6.593	-11.929	5.149	-14.479

Once the plot is generated from the rate constants gathered at different temperatures, the data can be fitted by a linear regression to calculate the activation energy and the pre-exponential factor for both the forward and reverse rate constant. For the forward rate constant, the linear regression has a slope m=-512.78 and an y-intercept= -10.377 (R^2=0.9617). On the other hand, the linear regression for the reverse rate constant has a slope m=-237.54 and an y-intercept= -13.768 (R^2=0.996).

Having said this, the forward reaction for the third step has an activation energy of E_a = 4.263 kJ/mol and a pre-exponential factor of *A* = 3.114x10^{-5} $M^{-1}s^{-1}$. The reverse reaction for the third step has an activation energy of E_a = 1.974 kJ/mol and a pre-exponential factor of *A* = 1.048x10^{-6} $M^{-1}s^{-1}$. Having calculated both rate constants, it is possible to substitute these terms in the reaction rate at any temperature given by the equation:

$$r_{FAME} = (3.114x10^{-5}e^{\frac{-512.78}{T}})[FFA]\frac{[MeOH][O\cdot]}{[H_2O]^{\frac{1}{2}}[O_2]^{\frac{1}{4}}} - (1.048\text{x}10^{-6}e^{\frac{-237.54}{T}})[FAME][H_2O]^{\frac{1}{2}}[O_2]^{\frac{1}{4}} \quad (112)$$

For the esterification reaction here proposed, the forward reaction is considerably more thermodynamically favourable than its reverse reaction. Consequently, the forward rate constant is greater than the reverse constant, in other words *kf3 > kr3.* As mentioned before, the esterification reaction here proposed show an endothermic behaviour (Laidler, 1984).

It is known that the effect of temperature on the rate constants is proportional to the activation energy. If the activation energy increases, then the effect of changing the temperature would increase. For the esterification reaction here proposed, the forward reaction (esterification) is endothermic and the reverse reaction (hydrolysis) is exothermic. The endothermic direction is known to have a larger activation energy, in other words $Ea_f > Ea_r$. The reversible model here studied follows this pattern and has an activation energy for the forward and reverse reaction of 4.263 and 1.974 kJ/mol respectively.

7.4.Conclusions

Some relevant features for this 2-D model can be concluded after the respective analysis. The temperature profile is nearly isothermal at 333 K and the water concentration is constant across the bubble at around 5.26×10^{-4} mol/m^3. This pattern is mainly due to the intensive internal mixing found in the inside of the microbubble which favours the homogenisation of both the thermal and chemical fields at short residence times when the bubble rises through the liquid. A rapid increase in temperature is noticed with an turning point around T=330 K. Secondly, a slow increase can be depicted which reaches the liquid temperature T_∞. This would suggest that vaporisation and sensible heat transfer are dominating the first and second regime respectively.

A smaller bubble reaches the thermal equilibrium faster compared to a bubble with a larger radius. In the case of R=1×10^{-4} m, this thermal equilibrium is reached around 9×10^{-3} s compared to 4×10^{-2} s for a bubble five times its size. A higher FAME concentration is found in the liquid mixture at a smaller bubble size. This behaviour could be attributed mainly to several factors: i) An enhanced mass and heat transfer by the enhanced gas-liquid interface when reducing the size of the bubble, ii) the increased vaporisation and stripping of the produced water, iii) a combination of both scenarios previously mentioned. Increasing the liquid mixture temperature would increase dramatically the vaporisation of water and therefore favour the FAME production, only if the produced water is stripped before it undergoes recondensation after the turning point.

An increase of the FAME concentration from the kinetic side of the process. In terms of the vaporisation of water, this process is thermodynamically favoured with an increase in temperature and therefore would cause an increase in the FAME production. Having said this, the increase of the FAME concentration in the liquid mixture could be attributed to the sum of these two factors which address both the reaction kinetics in the proposed mechanism and the physical advantage posed by the stripping of the produced water. An initial bubble temperature above the initial liquid mixture temperature (T_0 bubble > T_0 liquid), a maximum in the water concentration is found at the turning point previously mentioned. The higher the difference in temperature between these two temperatures, the more rapidly the turning point is reached.

These findings would suggest that the residence time of the microbubble (τ_{res}) rising though the liquid would necessarily be lower than 1×10^{-4} s, in other words ($\tau_{res} < 1 \times 10^{-4}$ s), when the maximum water concentration in the bubble is reached before it reaches the chemical equilibrium. Increasing the concentration of the $O^{\cdot}$ radical results in an increase in the FAME concentration in the liquid domain. The forward reaction for the third step has an activation energy of E_a = 4.263 kJ/mol and a pre-exponential factor of A = 3.114×10^{-5} $M^{-1}s^{-1}$. The reverse reaction for the third step has an activation energy of E_a = 1.974 kJ/mol and a pre-exponential factor of A = 1.048×10^{-6} $M^{-1}s^{-1}$.

8. 2-D model for the intensified esterification of *Jatropha platyphylla* oil

In this chapter a computational model is proposed for the ozone free radical initiated esterification using *Jatropha platyphylla* oil. The main reason for the election of this Mexican species relies on the special interest from the postgraduate student who is carrying out this research as well as the Mexican government sponsoring this project in order to find a sustainable use for this species in the pacific coast from Sinaloa to Michoacán states in Mexico. In this chapter, the use of *Jatropha platyphylla* oil is the main difference when compared to the previous chapter. In order to use the same model as in the previous chapter adaptations to the properties of the oil are conveniently updated. A brief comparison of the physicochemical properties between the oils used are illustrated in Table 5 found in section 2.1.4. The production of biodiesel via the intensified esterification is here analysed as an alternative for this vegetable oil. The relevant data calculations and estimations presented in both chapter 3 and 4 are here considered.

It is important to mention that the model proposed in this chapter is informed by the experimental data described in Chapter 3 and the model described in Chapter 7 but is yet to be validated with experimental runs which are then considered as potential future work in this thesis. In this chapter the reader can find the model description, a brief description of the proposed feedstock, the numerical method used, rate constants estimation and the appropriate results and discussion for the simulation profiles and variation of different parameters in order to analyse their effect on the key features. The variation of bubble size, liquid mixture temperature, bubble temperature and initial oxygen singlet concentration are discussed in this chapter.

8.1.Model description

The computational model used in this chapter uses the same reaction mechanism as the one proposed in the previous chapters. The main difference is that in this chapter a shorter residence time and enhanced reaction kinetics are estimated in order to assess the performance of the ozone free radical initiated esterification in a thin layer thickness of a few hundred microns based solely on the assumption that it is possible to maximise the FAME production and optimise the kinetics of this reaction mechanism. This could be understood as estimating the maximum vaporisation layer thickness. This refers to the maximum thickness that ensures a maximum in the FAME concentration by tuning the residence time of the microbubble rising through the liquid in terms of the layer thickness.

This vaporisation layer is estimated to be a few hundred microns (~438 μm) for the case of the mechanism here proposed. If this design feature is relevant when studying a vaporising system which would achieve maximum water removal and FAME production at a cost of the minimum heat transfer. The modelling work here presented could be potentially considered for the ozone free radical initiated

esterification using the vegetable oil from *J. platyphylla*. It is important to mention that the heat and mass transfer modules, transport of diluted species, chemistry, surface reactions and reaction engineering used in the previous chapter are here considered as the backbone for this computational model.

One of the main purposes of this model is to understand and explore the effects of water production and its respective removal. This chapter explores the hypothesis that forces the esterification reaction of FFAs to completion via the microbubble mediated reactive distillation. In this case, ozone-rich bubbles provide the catalyst to this reaction and remove the water product, driving the reaction to completion following Le Chatelier's principle. This approach uses $O\cdot$, produced in the ozone free radical initiation process, as free radical initiator for the three-step reaction mechanism proposed which takes place on the bubble interface (gas-liquid). The microbubble removes the vapour phase products (water) avoiding product inhibition.

A 2-D axisymmetric computational model of a dry-to-bone air and ozone microbubble is developed using COMSOL Multiphysics. The system to be investigated is comprised of a dispersed phase being the single fluidic oscillator air microbubble with a diameter of 200 μm rising in an infinite reservoir of methanol-oil mixture due to a buoyancy force. A simulation study is carried out for the system previously described using a time dependent model for the concentration and temperature profile inside the microbubble, considering circulation patterns inside and around the bubble correlated to the bubble motion. According to the operating conditions set in Chapter 3, the liquid bed height is 0.027 cm which corresponds to a residence time of 1 s for the microbubble to rise at terminal velocity through the liquid mixture.

In order to simplify the system described above, the proposed model is based on several assumptions: (1) The bubble is always rising in the reservoir at its terminal velocity, making emphasis and focusing only on the heat and mass transfer dynamics. (2) Due to a small residence time of the bubble in the liquid, the pressure inside the bubble is assumed to be constant. (3) The spherical shape of the bubble is maintained since it is sufficiently small that the surface tension around it assures no deformation from the spherical shape takes place. (4) The relevant chemical reactions of the model take place on the skin of the microbubble (Abdulrazzaq, et al., 2016).

8.2.Jatropha platyphylla species

The most famous species and also widely promoted as a feedstock source for biodiesel production is *Jatropha curcas*. In this chapter, *J. platyphylla* is briefly described in order to point out its feasibility as feedstock sources for biodiesel production.

Jatropha platyphylla is a species in the family of the Euphorbiaceae, found in the pacific coast from Sinaloa to Michoacan states in Mexico. *J. platyphylla* is restricted to warm areas with temperatures fluctuating around 20-29ºC and is normally found around deciduous forests. Concerning to the fat profile of *J. platyphylla* oil, it has been reported a content of 58% oil similar to the one found in *J. curcas* and the kernels of both of these species. Regarding the amino acid compositions, *J. platyphylla* kernel meal had a higher crude protein of 75% against 60% in *J. curcas*, but similar amino acid composition. Except lysine, all the essential amino acids found in the kernel meal were more abundant than in the FAO reference protein or the soybean meal (Makkar, et al., 2010).

Regarding the oil and protein contents, in *J. platyphylla* kernels the oil and crude protein content do not differ significantly. But the high oil content in *J. platyphylla* (60%) makes this species a valuable and suitable source for oil and therefore biodiesel production. Although the oil content is slightly higher in *J. platyphylla*, since the proportion of kernels in its seeds is lower than that in *J. curcas* the oil content would be lower; the same would be true for the crude protein content (Oyeleye, et al., 2011; Gosselink, et al., 2004).

Regarding the fatty acid composition, in *J. platyphylla* the saturated fatty acid levels are similar to that of *J. curcas*. Oil in both species is composed mainly of unsaturated fatty acids (linoleic and oleic acid), a higher linoleic acid level is found in *J. platyphylla* which could be beneficial for human consumption but at the same time shows the potential of this plant as a suitable feedstock source in the semi-arid coastal areas of Mexico. As mentioned before, *J. platyphylla* contains more than 50% of polyunsaturated fatty acids from which the predominant one is linoleic acid, 18:2n-6. The monounsaturated fatty acids comprise 25% of the total being the most predominant oleic acid 18:1n-9 and, oleic acid 18:1n-7 and palmitoleic acid, 16:1n-7 respectively. Lastly, the monosaturated fatty acids are found in less proportion of around 21%, from which palmitic, 16:0 and stearic acid 18:0 are the most predominant ones. *J. platyphylla* in comparison to *J. curcas* has a higher amount of polyunsaturated fatty acids due to the abundance of linoleic acid, which is higher than that of *J. curcas*. But concerning monounsaturated fatty acids, *J. platyphylla* has a lower composition than *J. curcas* due to the lower presence of oleic acid, 18:1n-9. Depending on the season, the FFA content found in *J. platyphylla* usually fluctuates between 12-21%, which is convenient in this case so this model can be used to propose an enhanced mechanism for the intensified esterification (Oyeleye, et al., 2011; Makkar, et al., 1998).

Having said this, this species has potential and could be used to produce biofuels due to the high levels of oil contained in this plant and its abundance in the semi-arid coastal areas of Mexico, *J. platyphylla* would be a suitable Mexican feedstock source for village-level and small scale biodiesel production (Makkar & Becker, 2009; Kumar, et al., 2010; Akinleye , et al., 2011)

8.3.Numerical method

The numerical simulations in this study were carried out using the Galerkin finite element method (FEM) with the software COMSOL Multiphysics 5.3a in order to solve the governing equations. The simulations were performed using both a personal computer and the University server. The first one had an Intel Core i3-7100U Intel HD Graphics 620 running at 2.4 GHz with 8 GB of installed memory and the second one had 12 processors and 94 GB of installed memory.

The mesh used in this computational model is defined by the user. The element size is set to calibrate for general physics. Some of the element size parameters are a maximum element growth rate of 1.1, a maximum element size of $0.5x10^{-5}$ m, a minimum element size of $4x10^{-8}$ m, a curvature factor of 0.2 and a resolution of narrow regions of 1. This setting is applied to the gas-liquid interface where majority of the physical and chemical features take place. There are 19,275 triangular mesh elements with an average element quality of 0.9461 and a mesh area of $2x10^{-6}$ m^2.

8.4.Results and discussion

The results obtained in the numerical simulations for the ozone free radical initiated esterification are presented in this section. The trends observed by the temperature and concentration profiles of the species of interest over time in this process are here discussed. Several parametric sweeps are presented in order to explore the physics and kinetics of this process by varying parameters such as the radius of the bubble, the temperature of the liquid and the bubble, and the initial oxygen singlet concentration.

8.4.1. Simulation profiles

For the simulation profiles, a radius of 100 μm, an initial temperature of the liquid of 333.15 K, an initial temperature of the bubble of 393.15 K, an initial oxygen singlet concentration of 281.25mol/m^3, and an initial concentration for both methanol and FFA of 301.54 mol/m^3 are used. According to the operating conditions set in Chapter 3, the liquid bed height is 278.1 μm which corresponds to a residence time of 1 s for the microbubble to rise through the liquid mixture. It is important to mention that for the purpose of presenting the results in a more detailed and organised structure, the figures in this section have been adapted to the appropriate time scale of up to 1 s, where most of the physical and chemical changes are taking place inside the bubble and in its surroundings.

From the simulation results obtained for the intensified esterification proposed for *J. platyphylla*, it was noticed that that both the heat and mass transfer dynamics have a strong dependence on time. The average bubble temperature profile over time is shown in Figure 85. From this figure it can be depicted that there are two different regimes happening. Firstly, a rapid decay in temperature is noticed with an turning point around T=337 K. The turning point previously described is reached in this

system around 2x10^{-4} s, which is in agreement with the one reported by Zimmerman et al of 1.5x10^{-4} s when studying the evaporation dynamics of microbubbles. The discrepancy between these two values could be attributed to the difference in temperature between the gas and liquid phase used in both models. The temperature difference between the bubble and the liquid reported by Zimmerman et al and this model is 130 and 60 K respectively (Zimmerman, et al., 2013).

Secondly, a slow increase can be depicted which reaches the liquid temperature T_{∞}. This would suggest that vaporisation and sensible heat transfer are dominating the first and second regime respectively.

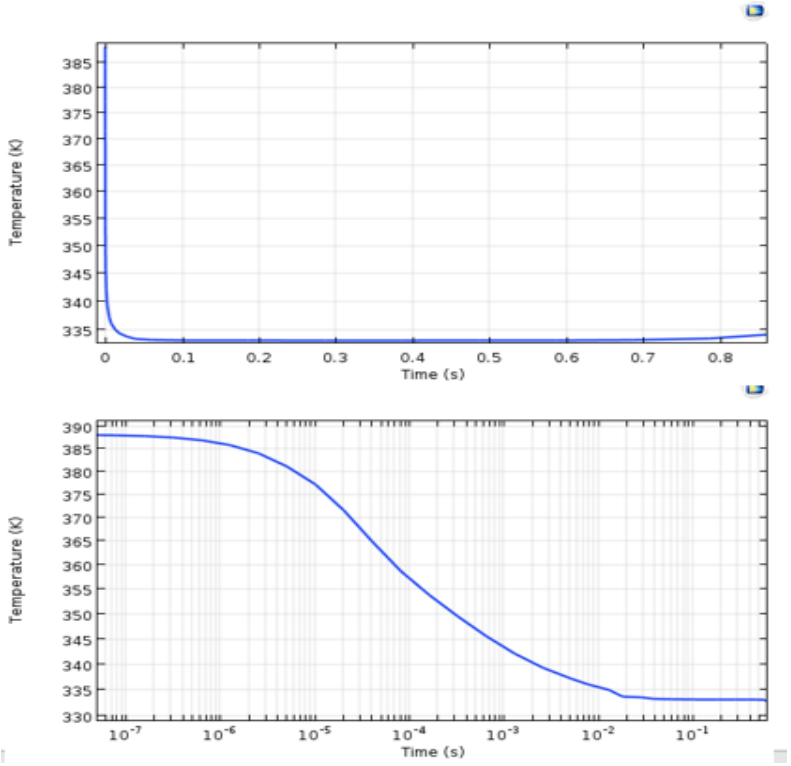

Figure 85 Average microbubble temperature for a bubble T_0=393.15 K. Bottom: semilogx plot.

The semilog plot found at the bottom of Figure 85 shows that the average microbubble temperature displays an exponentially faster increase up to 2x10^{-4} s compared with the next 10^{-1} s. This could suggest that evaporative cooling happens at least three orders of magnitude faster than sensible heat transfer for this process. In other words, this could be explained as an effect caused by the evaporation of the liquid into the bubble. The latent heat of vaporisation is lost causing the bubble temperature to increase rapidly at short contact time (Abdulrazzaq, et al., 2016).

In order to understand the importance of this turning point, Figure 86 shows the average water concentration found in the bubble over time. It can be easily depicted from this graph that water concentration rapidly increases reaching a maximum water concentration at 2x10^{-4} s of 1.14x10^{-3} mol/m^3. This value corresponds to the maximum in the absolute humidity which would mean the maximum efficiency in terms of heat transfer from the bubble to the liquid mixture in order to vaporise

the water without falling into the sensible heat transfer regime. The value for this absolute humidity would fall off from the maximum value more rapidly when the temperature driving force rises. At long residence times, the microbubble will achieve both thermal and chemical equilibrium. In this case the thermal equilibrium is reached at T=333.15 K and the chemical equilibrium for the bubble is a water concentration of 5.38×10^{-4} mol/m^3.

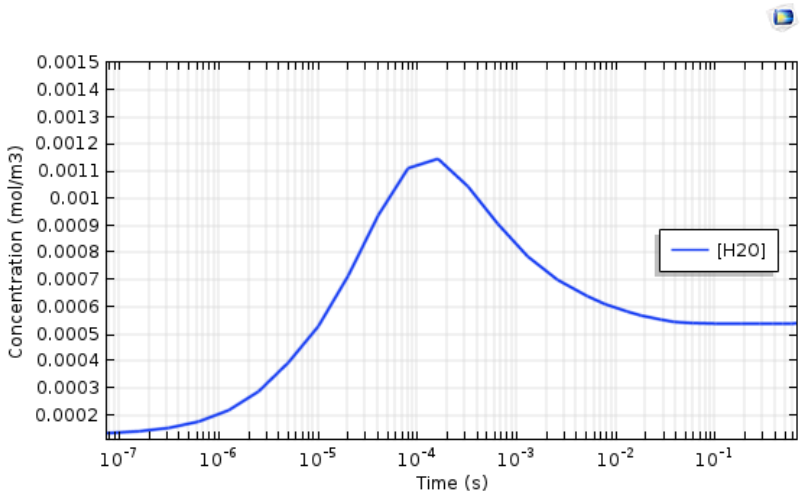

Figure 86 Average water concentration in bubble over time.

The microbubble temperature profile at the turning point (T=337 K) is illustrated in Figure 86. A heat transfer coefficient of 0.1 W/m^{2}K is used in this simulation, the arrows represent the steady state velocity field and the shading represents temperature. It can be depicted from the figure that at this specific time, the microbubble is relatively isothermal at 336-337 K.

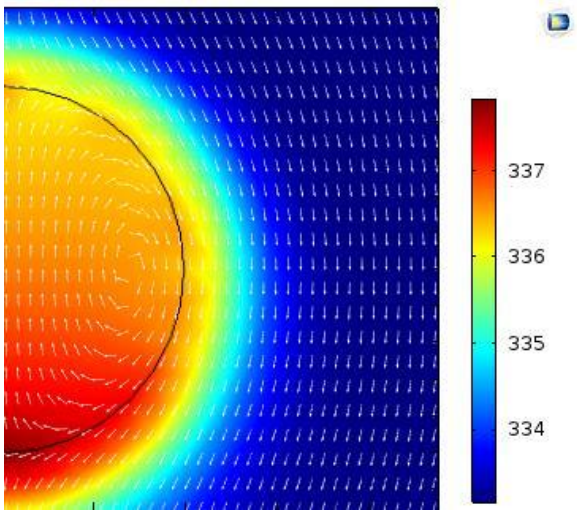

Figure 87 Microbubble temperature profile (K) at the turning point.

In order to fully understand the correlation between the ozone free radical initiated esterification and the water vaporisation and further removal, it is necessary to analyse the concentration profile of the different species found in this reaction mechanism. Firstly, the average oxygen singlet

concentration profile inside the bubble found in Figure 88 shows the behaviour of this species over time. The same pattern was found to be followed in this system compared to the one studied in Chapter 7. This is mainly because the enhanced reaction kinetics only consider the third reaction and not the first one, where the oxygen singlet is being consumed. It can be noticed from the graph that the oxygen singlet starts being consumed after $1x10^{-4}$ s, showing an exponential decay around $1x10^{-2}$ s. The concentration reached after one second is approximately 275.5 mol/m^3. This difference in oxygen singlet concentration could be then correlated to the FAME production in the reaction mechanism.

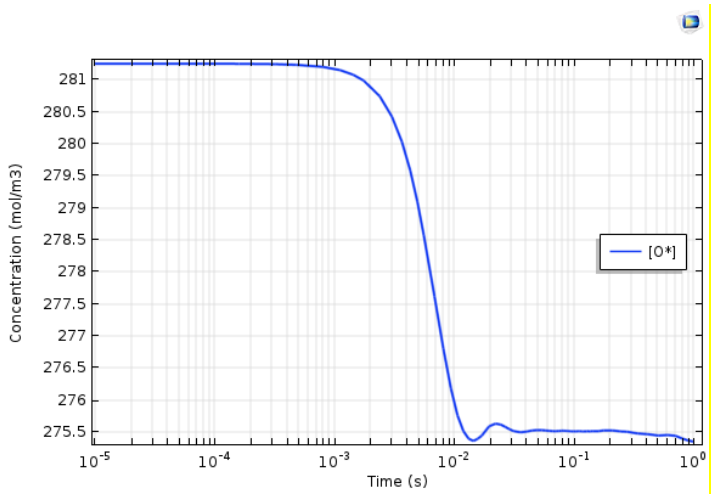

Figure 88 Oxygen singlet concentration profile in time.

For the average concentration profile of the hydroxyl radical and FAME in the gas-liquid interface, it can be noticed that both species show the same exponential behaviour in the first regime, followed by a slow increase due to the reaction kinetics of the third step. The concentration profile for both species is found in Figure 89. It is assumed for this reaction mechanism that the third step is the slowest one. Therefore, the oxygen singlet species reaches an equilibrium concentration and is consumed rapidly in less than $1x10^{-1}$ s, while the products for the third step would take longer to reach an equilibrium in both the liquid and gas domain. After 1 s, the average concentration on the surface for both FAME and the hydroxyl radical is 123.39 and 1.041 mol/m^3 respectively.

As expected the concentration of FAME is relatively higher compared to the hydroxyl radical. There are nearly two orders of magnitude between the concentrations of these two species. This suggests the radical species is being produced by the forward reaction in the first and third step of the mechanism and then consumed by forward reaction in the second step so it reaches an equilibrium.

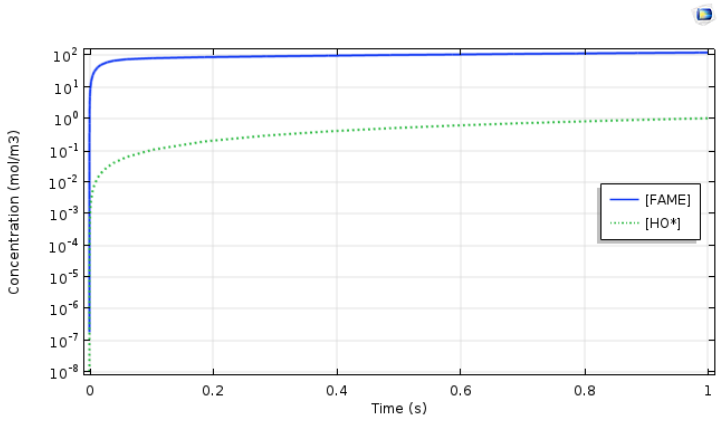

Figure 89 FAME and hydroxy radical concentration on the surface profile over time.

In order to explore the behaviour of the product of interest in this study, a concentration profile for FAME over time is presented in Figure 90. In this figure, the arrows represent the steady state velocity field and the shading represents concentration profile. It can be noticed that time at $1x10^{-3}$ s, the FAME concentration on the microbubble surface fluctuates around 10-15 mol/m^3 across the surface. A thin layer of the FAME produced is observed around the microbubble surface. At $1x10^{-2}$ s, the FAME concentration reaches a value nearly 3-4 times greater compared to the first time analysed. It is clear that the layer thickness increases in time suggesting more FAME is being produced on the gas-liquid interface, and some of this product is migrating to the bottom of the microbubble.

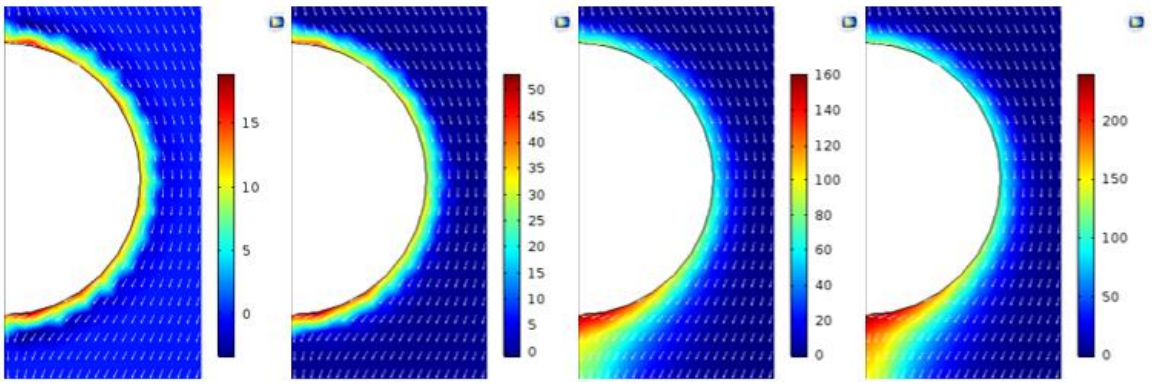

Figure 90 FAME concentration profile (mol/m^3) over time (From left to right t=$1x10^{-3}$, $1x10^{-2}$, $1x10^{-1}$ and 1 s).

At $1x10^{-1}$ s, it can be depicted from the figure that majority of the FAME produced migrates to the bottom of the microbubble and reaches a concentration of 140-160 mol/m^3. This behaviour is attributed to the outflow condition previously mentioned in chapter 7 in order to emulate the rising of the bubble through the liquid. At 1 s, the FAME produced continues to migrate to the bottom of the microbubble and achieves a concentration around 200 mol/m^3.

8.4.2. Variation of the bubble size

The bubble size is strongly related to the gas-liquid interface, which is responsible for the heat and mass transfer dynamics. In Figure 91, the variation of the average bubble temperature with the bubble

size is shown. In this case four different radius were used to illustrate the effect of the bubble size from top to bottom, R= $5x10^{-5}$, $1x10^{-4}$, $3x10^{-4}$ and $5x10^{-4}$ m. The initial bubble temperature is T0= 393.15 K and an initial FFA concentration of 301.54 mol/m^3. It can be noticed that a smaller bubble reaches the thermal equilibrium faster compared to a bubble with a larger radius. Smaller bubbles deliver majority of their enthalpy at shorter residence times in the liquid mixture, whereas larger bubbles take considerably longer to reach the mentioned thermal equilibrium since they possess a weaker internal convection. The same pattern is reported in Chapter 7 for the intensified esterification (Zimmerman, et al., 2013).

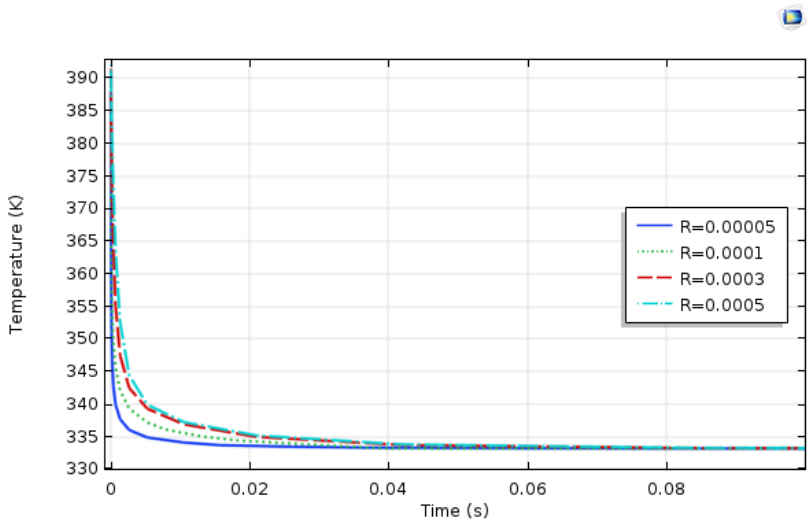

Figure 91 Variation of the average bubble temperature with bubble size (m).

Once the effect of the bubble size on the average bubble temperature has been analysed. It is important to explore the effect of the same parameter but in the FAME concentration. Figure 92 illustrates the effect of the bubble size on the average FAME concentration found in the liquid mixture for different radius, from top to bottom R= $5x10^{-5}$, $1x10^{-4}$, $3x10^{-4}$ and $5x10^{-4}$ m. The initial bubble temperature is T0= 293.15 K and an initial FFA concentration of 301.54 mol/m^3. It can be depicted from Figure 92 that a higher FAME concentration is found in the liquid mixture at a smaller bubble size. This behaviour could be attributed mainly to several factors: i) An enhanced mass and heat transfer by the enhanced gas-liquid interface when reducing the size of the bubble, ii) the increased vaporisation and stripping of the produced water, iii) a combination of both scenarios previously mentioned. After 1 s at a radius of R= $5x10^{-5}$, $1x10^{-4}$, $3x10^{-4}$ and $5x10^{-4}$ m, the average FAME concentration in the liquid mixture has a value of 2.311, 1.375, 0.379, and 0.262 mol/m^3 respectively. These results suggest that small bubbles are more efficient in terms of FAME production due to an enhanced mass and heat transfer related to a higher surface area to volume ratio.

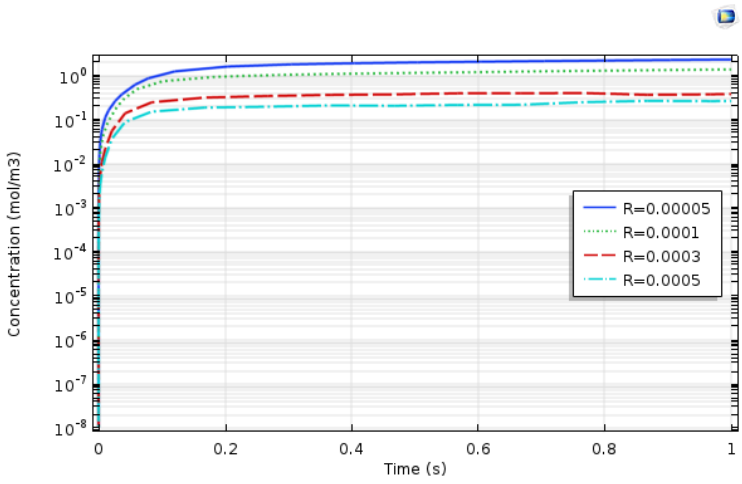

Figure 92 Variation of the average FAME concentration in the liquid mixture with bubble size (m).

This behaviour is best exploited at short residence times within the liquid in order to avoid recondensation. Microbubbles have higher residence times and a more intensive internal velocity rate, these attributes here mentioned lead to a faster vapour concentration of water inside the microbubble at short residence time. At higher residence times, the concentration inside a microbubble tend be similar compared to larger bubbles. This pattern is explained because the microbubbles loses most of its contents when it cools down due to the recondensation process (Zimmerman, et al., 2013; Abdulrazzaq, et al., 2016).

8.4.3. Variation of the liquid mixture temperature

It is known from the data gathered in the previous chapters that an increase in the liquid mixture temperature would result in an increase of the FAME concentration in the liquid mixture due to an increase in the rate constants. The effect of the liquid mixture temperature on the average water concentration inside the bubble is here studied and showed in Figure 93. An increase in the liquid mixture temperature results in an increase in the average water concentration found in the bubble.

In this model, five different temperatures were studied (T=293.15-373.15 K) in order to explore and understand if increasing the liquid temperature has an impact on the bubble average water concentration. It can be noticed in this figure that for all the different temperatures, a maximum in the water concentration in reached at an early stage. This is the maximum absolute humidity reached due to the vaporisation taking place in the first regime, using up all the enthalpy from the hot bubbles to vaporise the water present in the liquid mixture. In Figure 93 can be seen that at a liquid mixture temperature of 293.15-373.15 K, the maximum water concentration at the turning point is 4.46×10^{-4}, 7.28×10^{-4}, 1.14×10^{-3}, 1.78×10^{-3} and 2.89×10^{-3} mol/m^3 respectively.

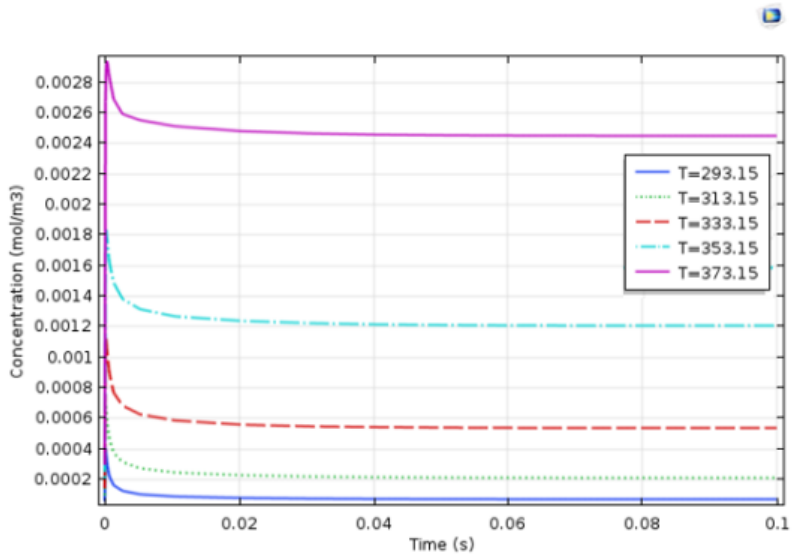

Figure 93 Variation of the bubble average water concentration with liquid mixture temperature (K).

This suggests that increasing the liquid mixture temperature would increase dramatically the vaporisation of water and therefore favour the FAME production, only if the produced water is stripped before it undergoes recondensation after the turning point (Abdulrazzaq, et al., 2016).

The effect of the liquid mixture temperature on the average FAME concentration is then analysed as well. Figure 94 shows the effect of the liquid temperature at five different temperatures (T=293.15-373.15 K) on the FAME concentration found in the liquid. It can be noticed that the behaviour followed by the FAME species is similar to the water produced. An increase in the liquid mixture temperature results in an increase on the FAME concentration in the liquid mixture.

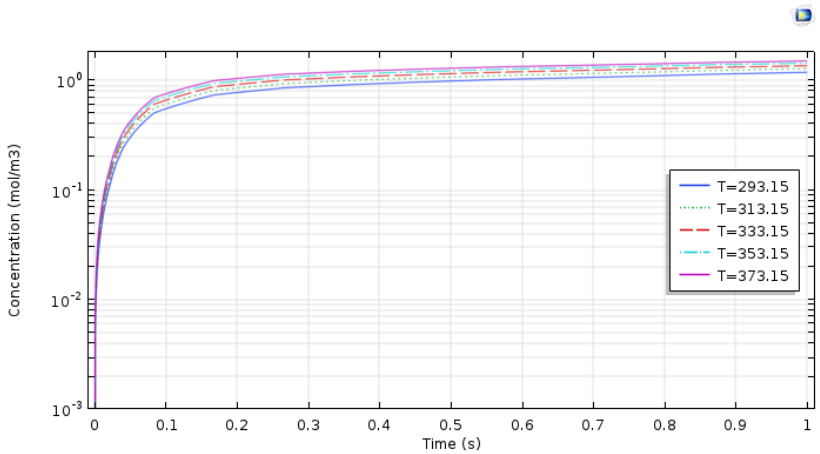

Figure 94 Variation of the average FAME concentration with liquid mixture temperature (K).

As mentioned in previous chapters, an increase in temperature would mean an increase in the rate constants. And in the case of the esterification reaction (endothermic process) the rate constants in the endothermic direction would always suffer a higher impact by this increase in temperature.

This is the explanation for an increase of the FAME concentration from the kinetic side of the process. In terms of the vaporisation of water, this process is thermodynamically favoured with an increase in temperature and therefore would cause an increase in the FAME production. Having said this, the increase of the FAME concentration in the liquid mixture could be attributed to the sum of these two factors which address both the reaction kinetics in the proposed mechanism and the physical advantage posed by the stripping of the produced water. In Figure 94 can be seen that at a liquid mixture temperature of 293.15-373.15 K, the average FAME concentration in the liquid mixture reaches a value of 1.191, 1.283, 1.375, 1.44 and 1.51 mol/m^3 respectively.

8.4.4. Variation of the bubble temperature

The variation of the average bubble water concentration with bubble temperature is here studied in order to explore the effect of this parameter. It is important to point out that the experimental data was carried out at initial bubble temperature of 393.15 K.

The effect of the bubble temperature on the average bubble water concentration shown in Figure 95. An initial liquid mixture temperature for this simulation of 333.15 K and an initial FFA concentration of 301.54 mol/m^3 are used. It can be easily depicted from this figure, that for an initial bubble temperature above the initial liquid mixture temperature (T_0 bubble > T_0 liquid), a maximum in the water concentration is found at the turning point previously mentioned. The higher the difference in temperature between these two temperatures, the more rapidly the turning point is reached.

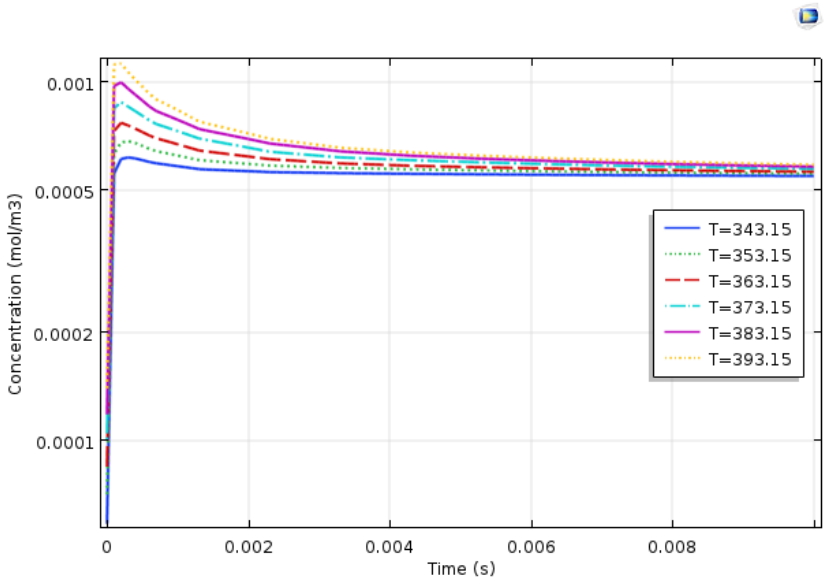

Figure 95 Variation of the average water concentration with bubble temperature (K).

In Figure 95 can be seen that at a bubble temperature of 343.15-393.15 K with intervals of 10 K, the maximum water concentration in the bubble is 6.16x10^{-4}, 6.38x10^{-4}, 7.68x10^{-4}, 8.76x10^{-4}, 9.97x10^{-4} and

$11.14x10^{-4}$ mol/m^3 respectively. At long residence times, all these curves would tend to reach the thermal equilibrium in the microbubble when the water concentration is $5.38x10^{-4}$ mol/m^3.

Once the data from the simulation is gathered, it is possible to generate a plot in order to find a correlation between the maximum water concentration against the difference in temperature between the gas and liquid domain, this correlation is illustrated in Figure 96. It is clear there is a linear correlation between the difference in temperature between the initial bubble and liquid mixture temperature and the maximum water concentration in the bubble achievable, described by the following expression $C_{max}=4.8787 + 0.1012\Delta T$ ($R^2=0.989$). This plot was generated considering an initial liquid mixture temperature of T=333.15 K, a heat transfer coefficient of 0.1 W/m^2K and a radius of $1x10^{-4}$ m. This correlation could then be used in order to calculate the maximum water concentration inside the bubble that would be achievable without the need to carry out an experiment.

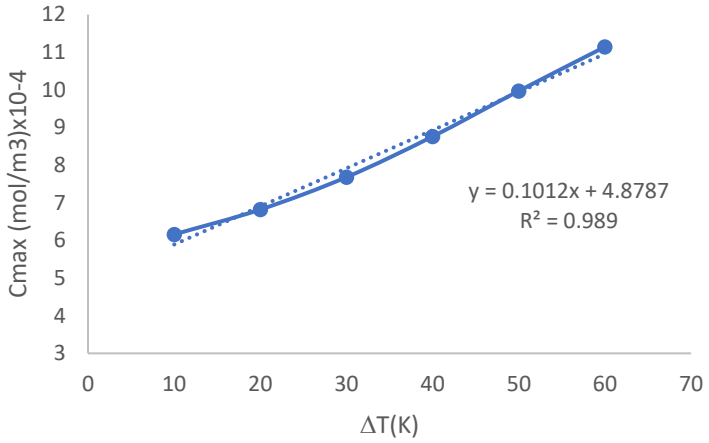

Figure 96 Maximum water concentration against ΔT=T0-T∞ (K).

Figure 97 shows the thermal equilibrium reached by different average bubble temperatures (T=343.15-393.15) with the surrounding liquid mixture.

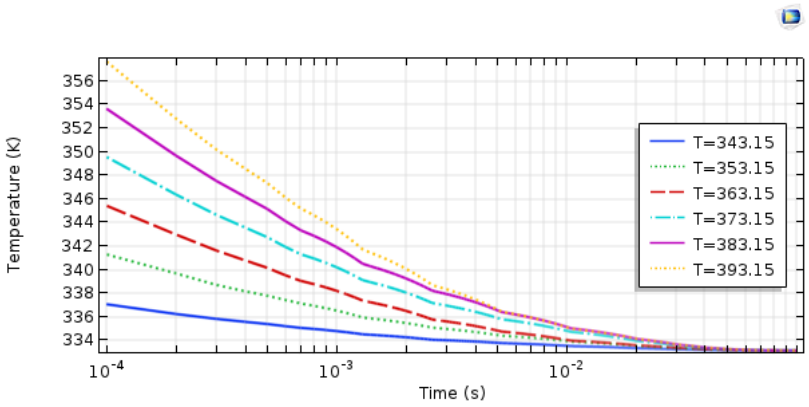

Figure 97 Double log plot of the variation of the average bubble temperature over time.

An initial liquid mixture temperature of 333.15 K and an initial FFA concentration of 301.54 mol/m^3 are used for this simulation. It can be noticed that the thermal equilibrium is reached by all the different temperatures before 0.1 s. A larger temperature difference between the initial bubble temperature and the liquid mixture temperature results in a longer period required to reach this equilibrium.

8.4.5. Variation of the oxygen singlet concentration

One of the main features in this thesis is to explore the effect of the oxygen singlet radical on the FAME production. It has been hypothesised that increasing its initial concentration would suggest an increase in the overall FAME production found in the liquid mixture.

The importance of this species relies on the fact that it is one of the initiators in the proposed reaction mechanism. Figure 98 shows the effect of different initial concentrations of the oxygen singlet radical on the average FAME concentration in the liquid mixture. It can be noticed that increasing the concentration of the $O^{\cdot}$ radical results in an increase in the FAME concentration in the liquid domain. For the initial molar ratio $O^{\cdot}$:FFA of 2:1 and 3:1, the FAME concentration reaches a maximum value at 0.1 s of 1.662 and 2.427 mol/m^3.

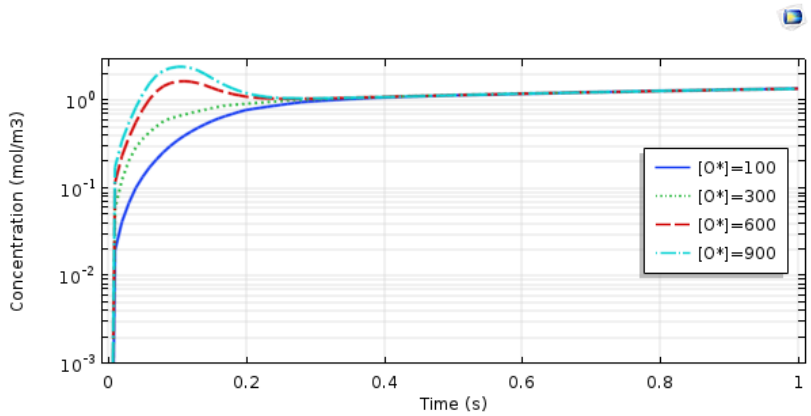

Figure 98 Variation of the average FAME concentration with oxygen singlet concentration (mol/m^3).

It can be noticed from this figure, that for the curves when the $O^{\cdot}$ concentration is higher than the initial FFA concentration ($[O^{\cdot}]_i > [FFA]_i$) the curves reach a maximum around 0.1 s. All the curves reach a chemical equilibrium right after 0.3 s. After 1s, the FAME concentration reaches a value of 1.375 mol/m^3. These findings would suggest that the residence time of the microbubble (τ_{res}) rising though the liquid with the respective rate constants would necessarily be lower than 0.1 s, in other words (τ_{res}<0.1 s), when the maximum FAME concentration in the liquid is reached before it reaches the chemical equilibrium.

8.4.6. Rate constants estimation

The values for the rate constant kf3 for each treatment are found in Table 34. It can be noticed that compared to the forward rate constants estimated in Chapter 5 for the 0-D, majority of these values have the same order of magnitude. It is important to point out that the rate constants calculated in both Chapter 5 and 6 only consider the reaction mechanism in the reactor, the forward rate constants here presented consider the heat and mass transfer across the gas-liquid interface as well as the temperature dependence of the reaction kinetics. The effect on temperature can be easily notice in Table 34, an increase in temperature results in an increase in the forward rate constant across the three different FFA contents here studied.

Table 34 Rate constant kf3x10^{-5} (1/M.s) values for each treatment.

		Free Fatty Acid %		
		10%	**15%**	**20%**
Temperature (K)	**293.15**	7.237	7.547	7.956
	313.15	6.457	8.461	9.743
	333.15	18.74	21.59	23.31

The values for the rate constant *kr3* for each treatment are found in Table 35. The effect on temperature can be easily notice in this table, an increase in temperature results in a slight increase in the reverse rate constant compared to the forward rate constants.

Table 35 Rate constant kr3x10^{-5} (1/M.s) values for each treatment.

		Free Fatty Acid %		
		10%	**15%**	**20%**
Temperature (K)	**293.15**	3.374	3.562	3.821
	313.15	3.912	4.182	4.361
	333.15	4.827	5.394	5.726

The average values for both the forward and reverse rate constants are used in the Arrhenius equation to obtain the activation energy (E_a) and pre-exponential factor (A) for the reverse reaction of the third step. The values for the average forward and reverse rate constant at each temperature are shown in

Table 36, these values are then processed to be used in the Arrhenius equation. When plotting ln(*k*) against 1/T, a straight line is then obtained where the E_a and *A* can be calculated from the y-intercept and the slope of the line. For the forward rate constant, the linear regression has a slope m=-575.14 and an y-intercept= -7.1633 (R^2=0.9875). On the other hand, the linear regression for the reverse rate constant has a slope m=-338.19 and an y-intercept= -8.9612 (R^2=0.995).

Table 36 Average rate constants used for Arrhenius equation parameters.

Temperature (K)	1/T x10^{-3} (K^{-1})	Forward rate constant x10^{-4} (M^{-1}s^{-1})	ln(k)	Reverse rate constant x10^{-5} (M^{-1}s^{-1})	ln(k)
293.15	3.4112	1.081	-9.132	4.038	-10.117
313.15	3.1934	1.253	-8.984	4.379	-10.036
333.15	3.0017	1.367	-8.897	4.636	-9.979

Having said this, the forward reaction for the third step has an activation energy of E_a = 4.7817 kJ/mol and a pre-exponential factor of A = 7.744x10^{-4} M^{-1}s^{-1}. The reverse reaction for the third step has an activation energy of E_a = 2.8117 kJ/mol and a pre-exponential factor of A = 1.282x10^{-4} M^{-1}s^{-1}. Having calculated both rate constants, it is possible to substitute these terms in the reaction rate at any temperature given by the equation:

$$r_{FAME} = (7.744x10^{-4}e^{\frac{-575.14}{T}})[FFA]\frac{[MeOH][O\cdot]}{[H_2O]^{\frac{1}{2}}[O_2]^{\frac{1}{4}}} - (1.282\text{x}10^{-4}e^{\frac{-338.19}{T}})[FAME][H_2O]^{\frac{1}{2}}[O_2]^{\frac{1}{4}} \quad (113)$$

For the esterification reaction here proposed, the forward reaction is considerably more thermodynamically favourable than its reverse reaction. Consequently, the forward rate constant is greater than the reverse constant, in other words *kf3 > kr3.* As mentioned before, the esterification reaction here proposed show an endothermic behaviour. If the activation energy increases, then the effect of changing the temperature would increase. For the esterification reaction here proposed, the forward reaction (esterification) is endothermic and the reverse reaction (hydrolysis) is exothermic. The endothermic direction is known to have a larger activation energy, in other words $Ea_f > Ea_r$. The reversible model here studied follows this pattern and has an activation energy for the forward and reverse reaction of 4.781 and 2.811 kJ/mol respectively (Laidler, 1984).

8.5.Conclusions

The intensified esterification mechanism here proposed for the use of *J. platyphylla* as feedstock for the biodiesel production has several relevant features. Firstly, evaporative cooling happens at least three orders of magnitude faster than sensible heat transfer for this process. Water concentration rapidly increases reaching a maximum water concentration at 2x10^{-4} s of 1.14x10^{-3} mol/m^3. This value corresponds to the maximum in the absolute humidity which would mean the maximum efficiency in terms of heat transfer from the bubble to the liquid mixture to vaporise the water without falling into the sensible heat transfer regime.

The concentration of FAME is relatively higher compared to the hydroxyl radical. There are nearly two orders of magnitude between the concentrations of these two species. This suggests the radical species is being produced by the forward reaction in the first and third step of the mechanism and then consumed by forward reaction in the second step, so it reaches an equilibrium. A higher FAME concentration is found in the liquid mixture at a smaller bubble size. This behaviour could be attributed mainly to several factors: i) An enhanced mass and heat transfer by the enhanced gas-liquid interface when reducing the size of the bubble, ii) the increased vaporisation and stripping of the produced water, iii) a combination of both scenarios previously mentioned.

At a bubble temperature of 343.15-393.15 K with intervals of 10 K, the maximum water concentration in the bubble is 6.16×10^{-4}, 6.38×10^{-4}, 7.68×10^{-4}, 8.76×10^{-4}, 9.97×10^{-4} and 11.14×10^{-4} mol/m^3 respectively. At long residence times, all these curves would tend to reach the thermal equilibrium in the microbubble when the water concentration is 5.38×10^{-4} mol/m^3. A larger temperature difference between the initial bubble temperature and the liquid mixture temperature results in a longer period required to reach this equilibrium. Increasing the concentration of the $O^{\cdot}$ radical results in an increase in the FAME concentration in the liquid domain. For the initial molar ratio $O^{\cdot}$:FFA of 2:1 and 3:1, the FAME concentration reaches a maximum value at 0.1 s of 1.662 and 2.427 mol/m^3.

In the case of the esterification reaction (endothermic process) the rate constants in the endothermic direction would always suffer a higher impact by this increase in temperature. Majority of both forward and reverse rate constants have the same order of magnitude compared to the ones obtained in Chapter 5 and 6. An increase in temperature results in a slight increase in the reverse rate constant compared to the forward rate constants. The forward reaction for the third step has an activation energy of E_a = 4.7817 kJ/mol and a pre-exponential factor of A = 7.744×10^{-4} $M^{-1}s^{-1}$. The reverse reaction for the third step has an activation energy of E_a = 2.8117 kJ/mol and a pre-exponential factor of A = 1.282×10^{-4} $M^{-1}s^{-1}$. All these results are in agreement with the hypothesis that reducing the liquid layer thickness and therefore the residence time of the microbubble rising through the liquid would result in maximising the vaporisation of the produced water. This would then result in an enhanced FAME production, which is an appealing feature when designing an esterification unit.

9. Conclusions and future work

From this research project, it can be concluded that a high-volume process for the production of biodiesel comes from esterification, but it suffers from an inherent problem related to not being able to go to completion and requiring at least two downstream purification steps to purify the ester product. In order to avoid these last purification steps, the proposed microbubble mediated esterification using ozone-rich microbubbles could potentially be an alternative to solve this issue. This new approach works as an alternative to the traditional biodiesel production as a pre-treatment stage.

Since up to 80% of the production costs are related to the feedstock sources, this novel approach considers the use of unconventional sources remarkably improving profitability of biodiesel. One of the main advantages of the esterification process is that cheaper organic oils are used as feedstock sources. The great majority of the cheapest organic oils are found above this saponification threshold.

The proposed approach uses microbubbles in order to remove water vapour produced from the esterification reaction driving the reaction to completion, as stated by LeChatelier's principle. Liquid methanol is found in solution with the FFA, both of them reacting with ozone rich microbubbles from air plasma injection. As a result, the liquid components in the vessel are removed and taken away by the microbubbles leaving only biodiesel in the vessel when reaction is completed. Therefore, no downstream separations are needed saving operating costs related to purification steps.

This research project is based around the hypothesis that the chemical kinetics of microbubble intensified esterification is mainly controlled by the average bubble size and the interfacial area. Microbubbles are known to support spontaneous generation of free radicals on their interface, at the same time ozone plasma injection increases the supply and density of free radicals. As hypothesized, if the mechanism of intensified esterification is free radical catalysed, then lab bench experiments can be modelled to predict esterification rates under the bubble flux conditions at pilot scale. If valid this hypothesis, a design for full scale implementation can be based on lab bench kinetics measurements for any organic oil. If not, lab scale data can be extrapolated to industrial scale with some confidence at a feasible operating regime.

A kinetics model of reaction on the bubble interface is built using information from fine bubble and microbubble experiments in COMSOL Multiphysics® Software in order to relate both experimental and modelling data. In this research project using computational modelling supported by experimental evidence, both evaporation and heat transfer on the microbubble interface are explored. Some of the key results obtained in the computational models here studied explained in further detail. An increase in the FFA content means an increase in the activation energy since the esterification is needed to reach the activation stage. A reaction with a low activation energy should proceed faster when compared with one that considers a larger activation energy. The forward reaction for the third step

has an activation energy of E_a = 12.692 kJ/mol and a pre-exponential factor of A = 2.0127x10^{-2} M^{-1}s^{-1}. The highest temperature always shows a higher FAME production right after the third step takes place. Considering that the third step in this mechanism, the esterification, has a heat of reaction of $\Delta H_{rxn} =$ 57.21 kJ/mol, the reaction is defined as endothermic which means the system absorbs energy from the surroundings. If the forward reaction of the esterification is endothermic, the other direction (reverse reaction) is exothermic.

When the methanol concentration is lower than the initial concentration of $O\cdot$, all the methanol is used and turned into methoxy radicals which then react to form FAME, in other words $[MeOH]_i = [FAME]_f$. But when the initial concentration of methanol is higher than the one of $O\cdot$, $[O\cdot]_i = [FAME]_f$. This suggests that the $O\cdot$ is the limiting reactant in the three-step mechanism. When the $O\cdot$concentration is comparatively lower than the initial concentration of FFA, all the $O\cdot$ is used and turned into methoxy and hydroxyl radicals which then react to form FAME, in other words $[O\cdot]_i = [FAME]_f$. When the initial concentration of $O\cdot$ is fairly similar or higher to the initial concentration of FFA, the reaction tends to completion.

Therefore, increasing the initial $O\cdot$ concentration increases dramatically the FAME production to a certain extent. For initial concentrations higher than 500 mol/m^3, the room for improvement is less than 0.51% so there is no need to input more $O\cdot$ since it would only incur in an elevated cost for its production making the first stage of this mechanism fairly feasible. Having analysed the key features of the irreversible mechanism, it is important to explore the effect of the reverse reaction in the third step. This is the main driver to develop a new 0-D model to understand the influence of the reverse reaction in terms of the produced water but mainly the production of FAME.

For the esterification reaction here proposed, the forward reaction (esterification) is endothermic and the reverse reaction (hydrolysis) is exothermic. The endothermic direction is known to have a larger activation energy, in other words $Ea_f > Ea_r$. The reversible model here studied follows this pattern and has an activation energy for the forward and reverse reaction of 12.692 and 8.652 kJ/mol respectively. The reverse reaction for the third step has an activation energy of E_a = 8.562 kJ/mol and a pre-exponential factor of A = 6.895x10^{-4} M^{-1}s^{-1}. The forward reaction is considerably more thermodynamically favourable than its reverse reaction.

The irreversible mechanism reaches a final concentration for both water and oxygen of 254.43 and 127.2 mol/m^3 respectively. On the other hand, the reversible mechanism reaches a final concentration for water and oxygen of 207.97 and 103.98 mol/m^3 respectively. The reversible mechanism produces 18.26% less water and oxygen when compared to the irreversible one, this is attributed to the fact that hydroxyl radical is used in the reverse mechanism to carry out the hydrolysis of the esters. The hydrolysis of esters competes with the second step of the mechanism which explains why the water

and oxygen productions decreases in the reversible reaction. An increase in temperature causes an increase in both the forward and reverse rate constants, but the rate of the endothermic reaction increases more. This is attributed to the fact that equilibrium shifts in the endothermic (forward) direction since the added heat is consumed according to LeChatelier's principle. Additionally, for an endothermic reaction (esterification), raising the temperature would increase the equilibrium constant K_{eq} and would increase the equilibrium constant for the exothermic reaction (hydrolysis).

Some relevant features for the 2-D model can be concluded after the respective analysis. The temperature profile is nearly isothermal at 333 K and the water concentration is constant across the bubble at around 5.26×10^{-4} mol/m^3. This pattern is mainly due to the intensive internal mixing found in the inside of the microbubble which favours the homogenisation of both the thermal and chemical fields at short residence times when the bubble rises through the liquid. A rapid increase in temperature is noticed with an turning point around T=330 K. Secondly, a slow increase can be depicted which reaches the liquid temperature T_∞. This would suggest that vaporisation and sensible heat transfer are dominating the first and second regime respectively.

A smaller bubble reaches the thermal equilibrium faster compared to a bubble with a larger radius. In the case of R=1×10^{-4} m, this thermal equilibrium is reached around 9×10^{-3} s compared to 4×10^{-2} s for a bubble five times its size. A higher FAME concentration is found in the liquid mixture at a smaller bubble size. An increase of the FAME concentration from the kinetic side of the process. In terms of the vaporisation of water, this process is thermodynamically favoured with an increase in temperature and therefore would cause an increase in the FAME production. Having said this, the increase of the FAME concentration in the liquid mixture could be attributed to the sum of these two factors which address both the reaction kinetics in the proposed mechanism and the physical advantage posed by the stripping of the produced water. An initial bubble temperature above the initial liquid mixture temperature (T_0 bubble > T_0 liquid), a maximum in the water concentration is found at the turning point previously mentioned. The higher the difference in temperature between these two temperatures, the more rapidly the turning point is reached.

These findings would suggest that the residence time of the microbubble (τ_{res}) rising though the liquid would necessarily be lower than 1×10^{-4} s, in other words ($\tau_{res} < 1 \times 10^{-4}$ s), when the maximum water concentration in the bubble is reached before it reaches the chemical equilibrium. Increasing the concentration of the $O^{\cdot}$ radical results in an increase in the FAME concentration in the liquid domain. For the initial molar ratio $O^{\cdot}$:FFA of 2:1 and 3:1, the FAME concentration reaches a maximum value at 0.1 s of 1.156 and 1.775×10^{-4} mol/m^3. The forward reaction for the third step has an activation energy of E_a = 4.263 kJ/mol and a pre-exponential factor of A = 3.114×10^{-5} $M^{-1}s^{-1}$. The reverse reaction for the

third step has an activation energy of E_a = 1.974 kJ/mol and a pre-exponential factor of A = 1.048x10^{-6} M^{-1}s^{-1}.

The intensified esterification mechanism here proposed for the use of *J. platyphylla* as feedstock for the biodiesel production has several relevant features. Firstly, evaporative cooling happens at least three orders of magnitude faster than sensible heat transfer for this process. Water concentration rapidly increases reaching a maximum water concentration at 2x10^{-4} s of 1.14x10^{-3} mol/m^3. This value corresponds to the maximum in the absolute humidity which would mean the maximum efficiency in terms of heat transfer from the bubble to the liquid mixture to vaporise the water without falling into the sensible heat transfer regime. The concentration of FAME is relatively higher compared to the hydroxyl radical. There are nearly two orders of magnitude between the concentrations of these two species. This suggests the radical species is being produced by the forward reaction in the first and third step of the mechanism and then consumed by forward reaction in the second step, so it reaches an equilibrium.

At a bubble temperature of 343.15-393.15 K with intervals of 10 K, the maximum water concentration in the bubble is 6.16x10^{-4}, 6.38x10^{-4}, 7.68x10^{-4}, 8.76x10^{-4}, 9.97x10^{-4} and 11.14x10^{-4} mol/m^3 respectively. At long residence times, all these curves would tend to reach the thermal equilibrium in the microbubble when the water concentration is 5.38x10^{-4} mol/m^3. A larger temperature difference between the initial bubble temperature and the liquid mixture temperature results in a longer period required to reach this equilibrium. Increasing the concentration of the O$^{\cdot}$ radical results in an increase in the FAME concentration in the liquid domain. For the initial molar ratio O$^{\cdot}$:FFA of 2:1 and 3:1, the FAME concentration reaches a maximum value at 0.1 s of 1.662 and 2.427 mol/m^3. The forward reaction for the third step has an activation energy of E_a = 4.7817 kJ/mol and a pre-exponential factor of A = 7.744x10^{-4} M^{-1}s^{-1}. The reverse reaction for the third step has an activation energy of E_a = 2.8117 kJ/mol and a pre-exponential factor of A = 1.282x10^{-4} M^{-1}s^{-1}. All these results are in agreement with the hypothesis that reducing the liquid layer thickness and therefore the residence time of the microbubble rising through the liquid would result in maximising the vaporisation of the produced water. This would then result in an enhanced FAME production, which is an appealing feature when designing an esterification unit.

It is important to mention that the experimental data obtained for this thesis do not consider the use of a thin liquid layer and operate under a low bubble flux. The experiments are indeed slow since the time scale for the esterification reaction carried out lasts around 36 h, the samples were collected every 4 hours. In terms of the computational model, it is clear that the physics and the reaction kinetics happen in the order of magnitude of 1x10^{-3} s. This has several implications when modelling the single bubble esterification reaction. One of them was the mentioned stiff system detected by COMSOL

Multiphysics which caused the model to change the initial conditions in order to find an appropriate solution for the problem. This could suggest that a more appropriate design of the experiments to be carried out would improve the fitting and description of the intensified esterification. Having said this, a consideration for future work could be a set of experiments with an online sampling for the species of interest in order to gather experimental data with enough sensitivity in the exponential stage of the reaction of around $1x10^{-3}$ s. Although this experimental data considers samples every 4 h, it is the "first word" on the subject and it is important to point out that we are a long way from the "last word". This would pose an engineering problem to be solved and understood scientifically. Even though there were some constraints to model the process here studied, the kinetic modelling proposed in this thesis aims to explore the parameter space that was not experimentally explored.

Another important aspect to be considered for future work could be a new set of experiments for the utilisation of the Mexican *J. platyphylla* species in order to properly inform and validate the computational model proposed in chapter 8. This matter is of particular interest for the Mexican government since it exists in abundancy in the coastal region of Mexico and several alternatives have been explored in order to use this plant in a sustainable but economically feasible way. The set of experiments would need to consider the right time scale in terms of sampling and the use of a thin liquid layer to enhance the reaction kinetics and promote the maximum evaporation of the produced water. To mention, the experimental data presented in this thesis was analysed using GC, which is sparse temporally; and did not consider enough data in the rapidly changing regime. The main drawback of sampling is that is a guess work to know the timescales. This is the main reason to suggest the use of an online method to quantify the species of interest in the liquid mixture, so we have readings in the rapidly changing regime.

Another consideration for future work is the appropriate analysis of the microbubbles using a bubble size distribution method to quantify its diameter. A feasible option could be the use of a high-speed camera able to capture 2000 frames/second which could be used for the bubble characterisation in order to determine the size distribution. The experimental data only considered a bubble temperature of 293.15 K, but it has been reported that an increase in the bubble temperature increases the evaporation of the produced water in the esterification reaction. This aspect of the process could potentially be exploited by using a process air heater to increase the temperature of the gas phase up to 393.15 K. Therefore, achieving a maximum stripping of the water in the liquid mixture which would mean an increase in the FAME production following LeChatelier's principle.

The recondensation process is connected to a release of sensible heat to the liquid mixture leading to an increase in temperature. In order to control these features, the residence time of bubbles is determined by the liquid bed height through which the microbubbles rise through. In the case of a thin

liquid layer, vaporisation is favoured leading to maximum separation efficiency. On the other hand, if the bed height is increased then the sensible heat transfer becomes more relevant to the process and leads to a reduced vaporisation and increase of the liquid mixture. In order to achieve a maximum removal of vapour with minimum heat transfer, both the vaporisation layer thickness (few hundred microns) and the contact time need to be accurately estimated. Reducing the liquid layer thickness and therefore the residence time of the microbubble rising through the liquid would result in maximising the vaporisation of the produced water. This would then result in an enhanced FAME production, which is an appealing feature when designing an esterification unit.

vii. References

Abbas , A. & Abbas, S., 2013. Kinetic Study and Simulation of Oleic Acid Esterification in Different Type of Reactors. *Iraqi Journal of Chemical and Petroleum Engineering,* 14(2), pp. 13-20.

Abdul-Majeed, W., AA-Thani, G. & Al-Sabahi, J., 2016. Application of Flying Jet Plasma for Production of Biodiesel Fuel from Wasted Vegetable Oil. *Plasma Chemistry and Plasma Processing,* 36(6), pp. 1517-1531.

Abdulrazzaq, N., Al-Sabbagh, B., Rees, J. & Zimmerman, W., 2015. Separation of azeotropic mixtures using air microbubbles generated by fluidic oscillation. *AICHE Journal,* 62(4), pp. 1192-1199.

Abdulrazzaq, N., Al-Sabbagh, B., Rees, J. & Zimmerman, W., 2016. Purification of Bioethanol Using Microbubbles Generated by Fluidic Oscillation: A Dynamical Evaporation Model. *Industrial & Engineering Chemistry Research,* 55(50), pp. 12909-12918.

Abidin, S., Vladisavljevic, G. & Saha, B., 2016. Kinetics of Free Fatty Acid Esterification in Used Cooking Oil Using Hypercrosslinked Exchange Resin as Catalyst. *International Journal of Chemical Engineering and Applications,* 7(5), pp. 295-298.

Achten, W. et al., 2008. Jatropha biodiesel production and use. *Biomass and bioenergy,* Volume 32, pp. 1063-1084.

Ahmed, N., Al-Hassani, M. & Al-Jendeel, H., 2010. Kinetic Study of Esterification Reaction. *Al-Khwarizmi Engineering Journal,* 6(2), pp. 33-42.

Akinleye , A. et al., 2011. Jatropha platyphylla kernel meal as feed ingredient for Nile tilapia (Oreochromis niloticus L): growth, nutrient utilization and blood parameters. *Animal Physiology and Animal Nutrition,* Volume 96, pp. 119-129.

AL-Mashhadani, M., Wilkinson , S. & Zimmerman WB, 2015. Airlift bioreactor for biological applications with microbubble mediated transport processes. *Chemical Engineering Science,* Volume 137, pp. 243-253.

Antolin, G. et al., 2002. Optimisation of biodiesel production by sunflower oil transesterification. *Bioresource Technology,* 83(2), pp. 111-114.

Aransiola , E. et al., 2014. A review of current technology for biodiesel production: state of the art. *Biomass Bioenergy,* Volume 61, pp. 276-297.

Baber, T., Graiver, D., Lira, C. & Narayan, R., 2005. Application of catalytic ozone chemistry for improving biodiesel product performance. *Biomacromolecules,* 6(3), pp. 1334-1344.

Becker, K., 2005. *Non-equilibrium air plasmas at atmospheric pressure.* Bristol: Institute of Physics Publishing.

Beltran, F., 2003. *Ozone Reaction Kinetics for Water and Wastewater Systems.* 1st ed. Boca Raton: CRC Press.

Berchmans, H. & Hirata , S., 2008. Biodiesel production from crude Jatropha curcas L seed oil with a high content of free fatty acids. *Bioresource Technology,* Volume 99, pp. 1716-1721.

Berrios, M., Siles, J., Martin, M. & Martin, M., 2007. A kinetic study of the esterification of free fatty acids (FFA) in sunflower oil. *Fuel,* 86(15), pp. 2383-2388.

Bharathiraja, B. et al., 2014. Biodiesel production using chemical and biological methods – A review of process, catalyst, acyl acceptor, source and process variables. *Renewable and Sustainable Energy Reviews,* 38(C), pp. 368-382.

Boocock, D., Konar, S., Mao, V. & Sidi, H., 1996. Fast one-phase oil-rich processes for the preparation of vegetable methyl esters. *Biomass Bioenergy,* Volume 11, pp. 43-50.

Borges, M. & Diaz, L., 2012. Recent developments on heterogeneous catalysts for biodiesel production by oil esterification and transesterification reactions: A review. *Renewable and Sustainable Energy Reviews,* Volume 16, pp. 2839-2849.

BP, 2013. *Statistical Review of World Energy ,* s.l.: Energy BSRoW British Petroleum.

Brittle, S. et al., 2015. Minimising microbubble size through oscillation frequency control. *Chemical Engineering Research and Design,* Volume 104, pp. 357-366.

Burns, S., Yiacoumi, S. & Tsouris, C., 1997. Microbubble generation for environmental and industrial separations. *Separation and Purification Technology,* Volume 11, pp. 221-232.

Camara, L. & Aranda, D., 2011. Reaction Kinetic Study of Biodiesel Production from Fatty Acids Esterification with Ethanol. *Industrial & Engineering Chemistry Research,* 50(5), pp. 2544-2547.

Canakci, M. & Van Gerpen, J., 2001. Biodiesel production from oils and fats with high free fatty acids. *American Society of Agricultural Engineers,* 44(6), pp. 1429-1436.

Chai, M., Tu, Q., Lu, M. & Yang , Y., 2014. Esterification pretreatment of free fatty acid in biodiesel production, from laboratory to industry. *Fuel Processing Technology,* Volume 125, pp. 106-113.

Chalmers, I., Baird, R. & Kelly, T., 1998. Control of an ozone generator- Theory and practice. *Measurement Science and Technology,* Volume 9, p. 983.

Chu, L. et al., 2007. Enhanced ozonation of simulated dyestuff wastewater by microbubbles. *Chemosphere,* Volume 68, pp. 1854-1860.

Climate Change Central, 2006. Biofuels industry: Present and Future.

Conrads, H. & Schmidt, M., 2000. Plasma generation and plasma sources. *Plasma Sources Science and Technology,* 9(4), p. 441.

Cox, J., Wagman, D. & Medvedev, V., 1989. *CODATA Key Values for Thermodynamics.* New York: Hemisphere Publishing Corp.

Crabtree, J. & Bridgewater, J., 1969. Chain bubbling in viscous liquids. *Chemical Engineering Science,* Volume 24, pp. 1755-1768.

Criegee, R., 1975. Mechanism of Ozonolysis. *Angewandte Chemie,* 14(11), pp. 745-752.

Cvetkovic, I., Milic, J., Ionescu, M. & Petrovic, Z., 2008. Preparation of 9-Hydroxynonanoic Acid Methyl Ester by Ozonolysis of Vegetable Oil and its Polycondensation. *Hemijska Industrija,* Volume 62, pp. 319-328.

Davis, M. & Davis, R., 2003. *Fundamentals of chemical reaction engineering.* 1st ed. New York: McGraw-Hill Higher Education.

Dawodu, F. et al., 2014. Effective conversion of non-edible oil with high free fatty acid into biodiesel by sulphonated carbon catalyst. *Applied Energy,* Volume 114, pp. 819-826.

de Araujo, C., de Andrade, C., de Souza , E. & Dupas, F., 2013. Biodiesel production from used cooking oil: A review. *Renewable and Sustainable Energy Reviews,* Volume 27, pp. 445-452.

Demirbas, A., 2002. Biodiesel from vegetable oils via transesterification in supercritical methanol. *Energy Conversion and Management,* 43(17), pp. 2349-2356.

Demirbas, A., 2003. Biodiesel fuels from vegetable oils via catalytic and non-catalytic supercritical alcohol transesterifications and other methods. *Energy conversion and Management,* Volume 44, pp. 466-487.

Demirbas, A., 2008. Biofuel sources, biofuel policy, biofuel economy and global biofuel projections. *Energy conversion and management,* Volume 49, pp. 2106-2116.

Demirbas, A., 2008. Current technologies in biodiesel production. *Biodiesel,* pp. 161-173.

Department for Transport, 2015. Renewable Transport Fuel Obligation statistics: obligation period 7, 2014/15, report 4.

Desphande, K. & Zimmerman, W., 2005. Experimental study of mass transfer limited reaction—Part II: Existence of cross-over phenomenon. *Chemical Engineering Science,* Volume 60, pp. 4147-4156.

Devi, A., Kumar, C., Naidu Y & Rao, M., 2006. Production and evaluation of biodiesel from Sunflower (Helianthus annus) and Nigerseed oil (Guizotia abyssinica). *Asian Journal of Chemistry,* Volume 18, pp. 2951-2958.

Di Serio, M., Tesser, R., Pengemei, L. & Santacesaria, E., 2008. Heterogeneous catalysts for biodiesel production. *Energy Fuel,* Volume 22, pp. 207-217.

Dizge, N. et al., 2009. Biodiesel production from sunflower. soybean and waste cooking oils by transesterification using lipase immobilized onto a novel microporous polymer. *Bioresource Technology,* 100(6), pp. 1983-1991.

Eliasson, B. & Kogelschatz, U., 1991. Modeling and applications of silent discharge plasmas. *IEEE Transactions on Plasma Science,* 19(2), pp. 309-323.

Eriksson, M., 2004. *Ozone chemistry in aqueous solution –Ozone decomposition and stabilisation,* Stockholm: KTH Chemistry.

European Biodiesel Board, 2014. Sector reference document on the manufacturing of safe feed materials from biodiesel processing.

Evans , R., Dal Poggetto, G., Nilsson, M. & Morris , G., 2018. Improving the Interpretation of Small Molecule Diffusion Coefficients. *Analytical chemistry,* 90(6), pp. 3987-3994.

Evans , R. et al., 2013. Quantitative Interpretation of Diffusion-Ordered NMR Spectra: Can We Rationalize Small Molecule Diffusion Coefficients?. *Angewandte Chemie,* Volume 52, pp. 3199-3202.

Fridman, A., 1953. *Plasma Chemistry.* Cambridge: Cambridge University Press.

Fukuda, H., Kondo, A. & Noda , H., 2001. Biodiesel fuel production by transesterification of oils. *Journal of Bioscience and Bioengineering,* Volume 92, pp. 405-416.

Gonsalves, J., 2006. An assessment of the Biofuels Industry in India.

Gosselink, R., de Jong, E., Guran , B. & Abacherli, A., 2004. Coordination network for lignin: Standardisation, production and applications adapted to market requirements. *Industrial Crops products,* Volume 20, pp. 121-129.

Government of India Planning Commission, 2005. Report of the Committee on Development of Biofuel.

Gui, M., Lee, K. & Bhatia, S., 2008. Feasibility of edible oil vs non-edible oil vs waste edible oil as biodiesel feedstock. *Energy,* Volume 33, pp. 1646-1653.

Haas, M. & Scott, K., 2007. Moisture Removal Substantially Improves the Efficiency of In Situ Biodiesel production from soybeans. *Journal of the American Oil Chemists Society,* 84(2), pp. 197-204.

Han , S., Ichikawa, K. & Utsumi, H., 1998. Quantitative analysis for the enhancement of hydroxyl radical generation by phenols during ozonation of water. *Water Research,* Volume 32, pp. 3261-3266.

Hanotu, J., Bandulasena, H. & Zimmerman, W., 2012. Microflotation performance for algal separation. *Biotechnology and Bioengineering,* 109(7), pp. 1663-1673.

Hanotu, J., Bandulasena, H. & Zimmerman, W., 2017. Aerator design for microbubble generation. *Chemical Engineering Research and Design,* Volume 123, pp. 367-376.

Harrington, K. & D'Arcy, C., 1985. Transesterification in situ of sunflower seed oil. *Industrial & Engineering Chemistry Product Research and Development,* 24(2), pp. 314-318.

Helwani, Z. et al., 2009. Technologies for production of biodiesel focusing on green catalytic techniques: A review. *Fuel Processing Technology,* Volume 90, pp. 1502-1514.

Helwani, Z. et al., 2009. Solid heterogeneous catalysts for transesterification of triglycerides with methanol: A review. *Applied Catalysis A: General,* Volume 363, pp. 1-10.

Himus , G. & Hinchley, A., 1924. The effect of a current of air on the rate of evaporation of water below the boiling point. *Journal of the Society of Chemical Industry,* Volume 43, p. 840.

Hool, K. & Schuchardt, B., 2011. A new instrument for the measurement for the measurement of interfacial tension and the dynamics of interfacial tension reduction. *Measurement Science and Technology ,* 16(4), pp. 350-356.

Huaping, Z. et al., 2006. Preparation of biodiesel catalyzed by solid super base of calcium oxide and its refining process. *Chinese Journal of Catalysis,* 27(5), pp. 391-396.

Ivanov, A. et al., 2007. OH, HO2, and ozone gaseous diffusion coefficients. *Journal of Physical Chemistry A,* 111(9), pp. 1632-1637.

Jagadeeshbabu, P., Sandesh, K. & Saidutta, M., 2011. Kinetics of Esterification of Acetic Acid with Methanol in the Presence of Ion Exchange Resin Catalysts. *Industrial & Engineering Chemistry Research,* Volume 50, pp. 7155-7160.

Jerabek, K., Hankova, L. & Holub, L., 2010. Working-state morphologies of ion exchange catalysts and their influence on reaction kinetics. *Journal of Molecular Catalysis A: Chemical,* Volume 333, pp. 109-113.

Johnston, M. & Holloway, T., 2007. A Global Comparison of National Biodiesel Production Potentials. *Environmental Science & Technology,* 41(23), pp. 7967-7973.

Join Nature Conservation Committee, 2009. The global biodiversity footprint of UK biofuel consumption. *JNCC.*

Kansedo, J., Lee, K. & Bhatia, S., 2009. Cerbera odollam (sea mango) oil as a promising non-edible feeedstock for biodiesel production. *Fuel,* Volume 88, pp. 1148-1150.

Kastratović, V. & Bigović, M., 2017. *Esterification of stearic acid with lower monohydroxylic alcohols,* Podgorica: University of Montenegro.

Kim , M. et al., 2011. Performance of heterogeneous ZrO2 supported metaloxide catalysts for brown grease esterification and sulfur removal. *Bioresource Technology,* Volume 102, pp. 2380-2386.

Kogelschatz, U., 2003. Dielectric-barrier Discharges: Their History, Discharge Physics, and Industrial Applications. *Plasma Chemistry and Plasma Processing,* Volume 23, pp. 1-46.

Kogelschatz, U., Eliasson, B. & Hirth, M., 1988. Ozone Generation from Oxygen and Air: Discharge Physics and Reaction Mechanisms. *Ozone: Science & Engineering,* 10(4), pp. 367-377.

Kokoo, R. & Zimmerman , W., 2018. Esterification for biodiesel production with a phantom catalyst: Bubble mediated reactive distillation. *Applied Energy,* Volume 221, pp. 28-40.

Kossyi, I., 1992. Kinetic scheme of the non-equilibrium discharge in nitrogen-oxygen mixtures. *Plasma Sources Science and Technology,* 1(207), pp. 207-220.

Kulkarni, M., Gopinath, R., Meher, L. & Dalai , A., 2006. Solid acid catalyzed biodiesel production by simultaneous esterification and transesterification. *Green Chem,* Volume 8, pp. 1056-1062.

Kumar, S., Kusakabe, K., Raghunathan,, K. & Fan, L., 1992. Mechanism of heat transfer in bubbly liquid and liquid–solid systems: injection single bubble. *AIChE Journal,* 38(5), p. 733.

Kumar, V. et al., 2010. Growth performance and metabolic efficiency in Nile tilapia (Oreochromis niloticus L) fed on a diet containing Jatropha platyphylla kernel meal as protein source. *Animal Physiology and Animal Nutrition,* Volume 96, pp. 37-46.

Laidler, K., 1984. The Development of the Arrhenius Equation. *Journal of Chemical Education,* 61(6), p. 494.

Lane, J., 2014. *Biofuels mandates around the world,* s.l.: Biofuels Digest.

Lee, A., Bennett, J., Manayil, J. & Wilson, K., 2014. Heterogeneous catalysis for sustainable biodiesel production via esterification and transesterification. *Chemical Society Reviews,* Volume 43, pp. 7887-7916.

Lee, J. & Saka, S., 2010. Biodiesel production by heterogeneous catalysts and supercritical technologies. *Bioresource Technology,* Volume 101, pp. 7191-7200.

Lefevre, H., Meagher, J. & Timmons , R., 1972. The kinetics of the reactions of O(3P) atoms with dimethyl ether and methanol. *International Journal of Chemical Kinetics,* 4(1), pp. 103-116.

Leh, F., 1973. Ozone: Properties, toxicity and applications. *Journal of Chemical Education,* 50(6), pp. 404-405.

Leung, D., Wu , X. & Leung, M., 2010. A review on biodiesel production using catalyzed transesterification. *Applied Energy,* Volume 87, pp. 1083-1095.

Levich, B., 1962. *Physicochemical hydrodynamics.* Englewood Cliffs, NJ: Prentice-Hall.

Lewis , W. & Whitman, W., 1924. Principles of gas transfer absorption. *Industrial & Engineering Chemistry,* Volume 16, p. 1215.

Liger-Belair, G., Topgaard, D., Voisin, C. & Jeandet, P., 2004. Is the wall of a cellulose fiber saturated with liquid whether or not permeable with co2 dissolved molecules? Application to bubble nucleation in champagne wine. *Langmuir,* 20(10), pp. 4132-4138.

Lim, S. & Teong, K., 2013. Process intensification for biodiesel production from Jatropha curcas L. seeds: Supercritical reactive extraction process parameters study. *Applied Energy,* Volume 103, pp. 712-720.

Li, P., Takahasho, M. & Chiba, K., 2009. Degradation of phenol by the collapse of microbubbles. *Chemosphere,* 75(10), pp. 1371-1375.

Logan, S., 1982. The orgin and status of the Arrhenius Equation. *Journal of Chemical Education,* 59(4), p. 279.

Lozano-Parada, J. & Zimmerman, W., 2010. The role of kinetics in the design of plasma microreactors. *Chemical Engineering Science,* 65(17), pp. 4925-4930.

Lucena, I., Silva, G. & Fernandes, F., 2008. Biodiesel Production by Esterification of Oleic Acid with Methanol Using a Water Adsroption apparatus. *Industrial & Engineering Chemistry Research,* Volume 47, pp. 6885-6889.

Lu, H. et al., 2009. Production of biodiesel from Jatropha curcas L oil. *Computers and Chemical Engineering,* Volume 33, pp. 1091-1096.

Maccines, J., Pitt, M., Allen, R. & Prietsman, G., 2012. Analysis of two-phase contacting in a rotating spiral channel. *Chemical Engineering Science,* Volume 69, pp. 304-315.

Ma, D., Liu, M., Zu, Y. & Tang, C., 2012. Two-dimensional volume of fluid simulation studies on single bubble formation and dynamics in bubble columns. *Chemical Engineering Science,* Volume 72, pp. 61-77.

Ma, F. & Hanna, M., 1999. Biodiesel production: A review. *Bioresource Technology,* Volume 70, pp. 1-15.

Makkar, H., Aderibigbe, A. & Becker, K., 1998. Comparative evaluation of non-toxic and toxic varieties of Jatropha curcas for chemical composition, digestibility, protein degradability and toxic factors. *Food Chemistry,* 62(2), pp. 207-215.

Makkar, H., Angulo-Escalante, M. & Becker , R., 2010. Traditional wisdom confirmed by scientific research: Jatropha species from Mexico is nontoxic. *Nature precedings,* pp. 1-2.

Makkar, H. & Becker, K., 2009. Jatropha curcas, a promising crop for the generation of biodiesel and value-added coproducts. *European Journal of Lipid Science and Technology,* 111(8), pp. 773-787.

Makuta, T. et al., 2006. Generation of micro gas bubbles of uniform diameter in an ultrasonic field. *Journal of Fluid Mechanics,* Volume 548, pp. 113-131.

Mandake, M., Anekar, S. & Walke, S., 2013. Kinetic Study of Catalyzed and Uncatalyzed Esterification Reaction of Acetic acid with Methanol. *American International Journal of Research in Science, Technology, Engineering & Mathematics,* 3(1), pp. 114-121.

Marchetti, J. & Errazu, A., 2008. Esterification of free fatty acids using sulfuric acid as catalyst in the presence of triglycerides. *Biomass and Bioenergy,* 32(9), pp. 892-895.

Marchetti, J., Miguel, V. & Errazu , A., 2007. Heterogeneous esterification of oil with high amount of free fatty acids. *Fuel,* 86(5), pp. 906-910.

Martinez-Herrera, J. et al., 2006. Chemical composition, toxic/antimetabolic constituents, and effects of different treatments on their levels, in four provenances of Jatropha curcas L from Mexico. *Food Chemistry,* Volume 96, pp. 80-89.

Mittelbach, M. & Remschmidt, C., 2004. Biodiesel, the comprehensive Handbook.

Mondala, A. et al., 2009. Biodiesel production by in situ transesterification of municipal primary and secondary sludges. *Bioresource Technology,* 100(3), pp. 1203-1210.

Morgan, J. & Schiff, H., 1964. Diffusion coefficients of O and N atoms in inert gases. *Canadian Journal of Chemistry,* 42(10), pp. 2300-2306.

Mulakhudair, A., Hanotu, J. & Zimmerman, W., 2017. Exploiting ozonolysis-microbe synergy for biomass processing: Application in lignocellulosic biomass pretreatment. *Biomass and Bioenergy,* Volume 105, pp. 147-154.

Narayan, G. et al., 2013. Bubble columns for condensation at high concentrations of noncondensable gas: Heat transfer model and experiments. *AIChE,* 59(5), pp. 1780-1790.

Nemes, A., Fabian, I. & Gordon, G., 2008. Experimental Aspects of Mechanistic Studies on Aqueous Ozone Decomposition in Alkaline Solution. *Ozone Science & Engineering,* Volume 22, pp. 287-304.

Nest, M., 2013. *Steady state approximation,* Munich: Technische Universität München.

Owens, C. & Roscoe, J., 1976. The reactions of atomic oxygen with methanol and ethanol. *Journal of Chemistry,* Volume 54, pp. 984-989.

Oyeleye, O. et al., 2011. Jatropha platyphylla, a new non-toxic Jatropha species: Physical properties and chemical constituents including toxic and antinutritional factors of seeds. *Food Chemistry,* Volume 125, pp. 63-71.

Pan , L., Takahashi, M. & Chiba, K., 2009. Enhanced free-radical generation by shrinking microbubbles using a copper catalyst. *Chemosphere,* Volume 77, pp. 1157-1160.

Park, Y. et al., 2010. Tungsten oxide zirconia as solid superacid catalyst for esterification of waste acid oil (dark oil). *Bioresource Technology,* Volume 101, pp. 6589-6593.

Pietsch, G. & Gibalov, V., 1998. Dielectric barrier discharges and ozone synthesis. *Pure and Applied Chemistry,* 70(6), pp. 1169-1174.

Prabaningrum, N., Subbarao, D. & Ismail, L., 2011. *In-situ transesterification of Jatropha curcas seeds using the mixture of methanol and isopropanol.* Malaysia, National Postgraduate Conference, pp. 1-6.

Qian, J., Wang, F., Liu, S. & Yun, Z., 2008. In situ alkaline transesterification of cottonseed oil for production of biodiesel and nontoxic cottonseed meal. *Bioresource Technology,* 99(18), pp. 9009-9012.

Ragnar, M., Eriksson, T. & Reitberger, T., 1999. Radical formation in ozone reactions with lignin and carbohydrate model compounds. *Holzforschung,* Volume 53, pp. 292-298.

Rathore, V. & Madras, G., 2007. Synthesis of biodiesel from edible and non-edible oils in supercritical alcohols and enzymatic synthesis in supercritical carbon dioxide. *Fuel,* Volume 86, pp. 2650-2659.

Rattanaphra, D., Harvey, A., Thanapimmetha, A. & Srinophakun, P., 2011. Kinetic of myristic acid esterification with methanol in the presence of triglycerides over sulfated zirconia. *Renewable Energy,* Volume 36, pp. 2679-2686.

Rehman, F., Liu, Y. & Zimmerman , W., 2016. The role of chemical kinetics in using O3 generation as proxy for hydrogen production from water vapour plasmolysis. *International Journal of Hydrogen Energy,* 41(15), pp. 6180-6192.

Rehman, F., Medley, G., Bandulasena, H. & Zimmerman, W., 2015. Fluidic oscillator-mediated microbubble generation to provide cost effective mass transfer and mixing efficiency to the wastewater treatment plants. *Environmental Research,* Volume 137, pp. 32-39.

RS, 2016. *Air Heater, NPT Fitting, 750 W, 240 V Ac..* [Online] Available at: http://uk.rs-online.com/web/p/air-heaters/2002547 [Accessed 10 02 2019].

Russbueldt, B. & Hoelderich, W., 2009. New sulfonic acid ionexchange resins for the pre-esterification of different oils and fats with high content of free fatty acids. *Applied Catalysis A: General,* Volume 362, pp. 47-57.

Rutz, D. & Janssen, R., 2007. Biofuel Technology Handbook. *Renewable Energies.*

Sahoo, P. & Das, L., 2009. Process optimization for biodiesel production from Jatropha, Karanja and Polanga oils. *Fuel,* Volume 88, pp. 1588-1594.

Saka, S. & Kusdiana, D., 2001. Biodiesel fuel from rapeseed oil as prepared in supercritical methanol. *Fuel,* Volume 80, pp. 225-231.

San Jose Alonso, J., Lopez Sastre, J., Romero-Avila, C. & Lopez , E., 2008. A note on the combustion of blends of diesel and soya, sunflower and rapeseed vegetable oils in a light boiler. *Biomass Bioenergy,* Volume 32, pp. 880-886.

Sathyaselvabala, V. et al., 2010. Removal of free fatty acid in Azadirachta indica (Neem) seed oil using phosphoric acidmodified mordenite for biodiesel production. *Bioresource Technology,* Volume 101, pp. 5897-5902.

Schinas, P. et al., 2009. Pumpkin (Cucurbita pepo L) seed oil as an alternative feedstock for the production of biodiesel in Greece. *Biomass Bioenergy,* Volume 33, pp. 44-49.

Shi, H., 2006. *Novel Bubble Aerator Performance.* MSc in Environmental and Energy Engineering ed. s.l.:University of Sheffield.

Singh, N., Kumar, R. & Kumar, P., 2013. Kinetic Study of Catalytic Esterification of Butyric Acid and Ethanol over Amberlyst 15. *ISRN Chemical Engineering,* Volume 2013, pp. 1-6.

Singh, S. & Singh, D., 2009. Biodiesel production through the use of different sources and characterization of oils and their esters as the substitute of diesel: a review. *Renewable and Sustainable Energy Reviews,* Volume 14, pp. 200-216.

Soriano , N., Venditti, R. & Argyropoulos, D., 2009. Biodiesel synthesis via homogeneous Lewis acid-catalyzed transesterification. *Fuel,* Volume 88, pp. 560-565.

Srivastava, A. & Prasad, R., 2000. Triglycerides-based diesel fuels. *Renewable and Sustainable Energy Reviews,* 4(2), pp. 111-133.

Stacy, C., Melick, C. & Cairncross, R., 2014. Esterification of free fatty-acids to biodiesel in a bubble column reactor. *Fuel Processing Technology,* Volume 124, pp. 70-77.

Su, C., 2013. Recoverable and reusable hydrochloric acid used as a homogeneous catalyst for biodiesel production. *Applied Energy,* Volume 104, pp. 503-509.

Su, E. & Wei, D., 2008. Improvement in lipase-catalyzed methanolysis of triacylglycerols for biodiesel production using a solvent enginnering method. *Jornal of Molecular Catalysis B: Enzymatic,* Volume 55, pp. 118-125.

Takahashi, M., Chiba, K. & Li, P., 2007. Free-radical generation from collapsing microbubbles in the absence of a dynamic stimulus. *Journal of Physical Chemistry B,* Volume 111, pp. 1343-1347.

Talebian, A., Aishah, N. & Mazaheri, H., 2013. A review on novel processes of biodiesel production from waste cooking oil. *Applied Energy,* Volume 104, pp. 683-710.

Talebian-Kiakalaieh, A., Aishah, N., Zarei, A. & Noshadi, I., 2013. Transesterification of waste cooking oil by heteropoly acid (HPA) catalyst: Optimization and kinetic model. *Applied Energy,* 102(C), pp. 283-292.

Tavassoli, M., Foley, P., Kharraz, E. & Curtis, J., 2016. Quantification of Nonanal and Oleic Acid Formed During the Ozonolysis of Vegetable Oil Free Fatty Acids or Fatty Acid Methyl Esters. *Journal of the American Oil Chemists Society,* 93(3), pp. 303-310.

Tesar, V., 2014. Microbubble generator excited by fluidic oscillator's third harmonic frequency. *Chemical Engineering Research,* Volume 92, pp. 1603-1615.

Tesar, V., Hung, C. & Zimmerman , W., 2006. No-moving-part hybrid-synthetic jet actuator. *Sensors and Actuators A:Physical ,* 125(2), pp. 159-169.

Tesser, R. et al., 2010. Acid exchange resins deactivation in the esterification of free fatty acids. *Chemical Engineering Journal ,* Volume 161, pp. 212-222.

Timberlake, J. & Hodges, M., 1970. Substituent effects and free radical stability. The methoxy group. *Tetrahedron Letters,* 11(48), pp. 4147-4150.

Tiwari, A., Kumar, A. & Raheman, H., 2007. Biodiesel production from jatropha oil (jatropha curcas) with high free fatty acids: An optimized process. *Biomass and Bioenergy,* Volume 31, pp. 569-575.

Tran, D., Chang, J. & Lee, D., 2017. Recent insights into continuous-flow biodiesel production via catalytic and non-catalytic transesterification processes. *Applied Energy,* Volume 185, pp. 376-409.

Tropilab, 2006.

United Nations, 2008. Biofuel production technologies: Status, prospects and implications for trade and development.

Upham, P., Thornley, P., Tomei, J. & Boucher, P., 2009. Sustainable biodiesel feedstocks for the UK: a review of sustainability issues with reference to the UK RFTO. *Journal of Cleaner Production,* Volume 17, pp. 537-545.

Vallance, C., 2016. *Reaction Kinetics ,* s.l.: University of Oxford.

Van Gerpen, J. et al., 2004. Biodiesel production technology: August 2002 - January 2004.

Vitiello, R. et al., 2017. Catalysis for esterification reactions: a key step in the biodiesel production from waste oils. *Rendiconti Lincei,* Volume 28, pp. 117-123.

Wang, J., Wang, L., Hanotu, J. & Zimmerman, W., 2017. Improving the performance of coal flotation using oscillatory air supply. *Fuel Processing Technology,* Volume 165, pp. 131-137.

Woo, A. et al., 2016. Developments in in-situ (trans) esterification for biodiesel production: A critical review. *Renewable and Sustainable Energy Reviews,* Volume 60, pp. 284-305.

Worldwatch Institute, 2006. Biofuels for transportation: Global potential and Implications for sustainable agriculture and energy in the 21st century. *Federal Ministry of Food.*

Zatta, L., da Costa Gardolinski, J. & Wypych, F., 2011. Raw halloysite as reusable heterogeneous catalyst for esterification of lauric acid. *Applied Clay Science,* Volume 51, pp. 165-169.

Zhang , J., Costa, A., Tao, W. & Cooks, R., 2011. Direct detection of fatty acid ethyl esters using low temperature plasma (LTP) ambient ionization mass spectrometry for rapid bacterial differentiation. *Analyst,* Volume 136, pp. 3091-3097.

Zhang, F., Fang, Z. & Wang , Y., 2015. Biodiesel production direct from high acid value oil with a novel magnetic carbonaceous acid. *Applied Energy,* Volume 155, pp. 637-647.

Zhang, Y., Dube, M., Mclean, D. & Kates, M., 2003. Biodiesel production from waste cooking oil: Economic assessment and sensitivity analysis. *Bioresource Technology,* Volume 90, pp. 229-240.

Zimmerman , W. & Tesar , V., 2013. *Bubble generation for aeration and other purposes,* s.l.: US Patent 20,130,092,626,.

Zimmerman, W., 2011. Electrochemical microfluidics. *Chemical Engineering Science,* 66(7), pp. 1412-1425.

Zimmerman, W., Al-Mashhadani, M. & Bandulasena, H., 2013. Evaporation dynamics of microbubbles. *Chemical Engineering Science,* Volume 101, pp. 865-877.

Zimmerman, W. et al., 2009. On the design and simulation of an airlift loop bioreactor with microbubble generation by fluidic oscillation. *Food and Bioproducts Processing,* 87(3), pp. 215-227.

Zimmerman, W. & Rees, J., 2004. The wavelength of solitary internal waves in a stably stratified fluid layer. *Nonlinear Processes Geophysics,* 11(2), pp. 165-180.

Zimmerman, W. & Rees, J., 2009. Optimal modelling and experimentation for the improved sustainability of microfluidic chemical technology design. *Chemical Engineering Research and Design,* 87(6A).

Zimmerman, W., Tesar , V. & Bandulasena, H., 2011. Towards energy efficient nanobubble generation with fluidic oscillation. *Current Opinion in Colloid & Interface Science,* 16(4), pp. 350-356.

Zimmerman, W., Tesar, V., Butler, S. & Bandulasena, H., 2008. Microbubble generation. *Recent Patents on Engineering,* Volume 2, pp. 1-8.

Zimmerman, W. et al., 2011. Design of an airlift loop bioreactor and pilot scales studies with fluidic oscillator induced microbubbles for growth of a microalgae Dunaliella salina. *Applied Energy,* 88(10), pp. 3357-3369.

viii. Appendices

In this section of this thesis, the relevant appendices are found in order to ease understanding of the calculations and show the remaining features of the findings in this study.

viii.1. Appendix A. FFA and FAME content and molar concentration

Table 37 Values for content and molar concentration at FFA 20%.

	Acid number (mg of KOH/g)			FFA (mol) x10^{-2}			[FAME] (mol/m^3)		
Time (h)	**273.15 K**	**313.15 K**	**333.15 K**	**273.15 K**	**313.15 K**	**333.15 K**	**273.15 K**	**313.15 K**	**333.15 K**
0	43.63	43.63	43.63	10.743	10.743	10.743	0	0	0
4	42.18	40.57	34.3	10.386	9.989	8.445	10.985	23.183	70.687
8	37.62	34.76	31.29	9.263	8.558	7.704	45.533	67.202	93.492
12	35.68	33.45	30.34	8.785	8.236	7.470	60.231	77.127	100.689
16	34.53	30.93	28.81	8.502	7.615	7.093	68.944	96.219	112.281
20	33.47	30.12	28.63	8.241	7.416	7.049	76.975	102.356	113.645
24	33.31	29.88	28.57	8.201	7.357	7.034	78.187	104.174	114.099
28	32.25	29.53	28.66	7.940	7.271	7.056	86.218	106.826	113.417
32	32.23	29.22	28.52	7.936	7.194	7.022	86.370	109.175	114.478
36	31.07	29.18	28.69	7.650	7.185	7.064	95.158	109.478	113.190

Table 38 Values for content and molar concentration at FFA 15%.

	Acid number (mg of KOH/g)			FFA (mol) x10^{-2}			[FAME] (mol/m^3)		
Time (h)	**273.15 K**	**313.15 K**	**333.15 K**	**273.15 K**	**313.15 K**	**333.15 K**	**273.15 K**	**313.15 K**	**333.15 K**
0	31.13	31.13	31.13	7.665	7.665	7.665	0	0	0
4	30.05	29.54	28.72	7.399	7.273	7.071	8.182	12.046	18.258
8	29.46	28.41	27.36	7.253	6.995	6.736	12.652	20.607	28.562
12	28.99	27.92	26.94	7.138	6.874	6.633	16.213	24.320	31.744
16	28.72	27.54	26.51	7.071	6.781	6.527	18.258	27.199	35.002
20	28.14	27.09	26.03	6.928	6.670	6.409	22.653	30.608	38.639
24	27.47	26.65	25.53	6.763	6.562	6.286	27.729	33.942	42.427
28	27.21	26.01	25.22	6.699	6.404	6.209	29.699	38.790	44.776
32	27.07	25.57	24.76	6.665	6.296	6.096	30.759	42.124	48.261
36	26.8	25.48	24.61	6.598	6.273	6.059	32.805	42.806	49.397

Table 39 Values for content and molar concentration at FFA 10%.

	Acid number (mg of KOH/g)			FFA (mol) $x10^{-2}$			[FAME] (mol/m^3)		
Time (h)	**273.15 K**	**313.15 K**	**333.15 K**	**273.15 K**	**313.15 K**	**333.15 K**	**273.15 K**	**313.15 K**	**333.15 K**
0	21.11	21.11	21.11	5.197	5.197	5.197	0	0	0
4	19.96	19.36	18.86	4.914	4.767	4.643	8.712	13.258	17.046
8	19.21	18.73	17.94	4.730	4.611	4.417	14.395	18.031	24.017
12	18.7	18.01	17.3	4.604	4.434	4.259	18.258	23.486	28.865
16	18.27	17.37	16.96	4.498	4.277	4.176	21.516	28.335	31.441
20	17.62	16.99	16.32	4.338	4.183	4.018	26.441	31.214	36.290
24	16.95	16.46	16.17	4.173	4.052	3.981	31.517	35.229	37.427
28	16.66	16.3	16.04	4.102	4.013	3.949	33.714	36.442	38.412
32	16.4	16.17	15.87	4.038	3.981	3.907	35.684	37.427	39.700
36	16.28	16.05	15.79	4.008	3.952	3.887	36.593	38.336	40.306

viii.2. Appendix B. MATLAB code for the least squares method

For the editor code, here are some instructions:

When working at different FFA%, the new value needs to be changed using COMSOL and saved before the code is run. As well as the new set of values for y^m from the experimental data.

```
function Mario_new();
    close all force;
    addpath('version_50');
    model=mphload('irrev_matlab_11092018.mph');
    options=optimset('display','iter','tolX',1e-10,'tolFun',1e-9);
    [xval fval]=fmincon(@(X) Mario_forward(model,X),1e-6,[],[],[],[],0,
    1e-5,[],options);
end

function dif=Mario_forward(model,x)
    model.param.set('kf3',x);
    x
    model.study('std1').run;
    out=mphglobal(model,'comp1.re.c_fame');
    t=mphglobal(model,'t');
    %out=interp1(t,out,[t1 t2 t3 ...])
    dif=1;
    tdata=[14400 28800 43200 57600 72000 86400 100800 115200 129600];
    out=interp1(t,out,tdata) ;
    target=[70.68728257 93.49207576 100.6896019 112.281407 113.6451488
    114.0997294 113.4178585 114.4785466 113.1905682];
    plot(tdata,out,'o'); hold on; plot(tdata,target,'*'); hold off;
    drawnow;
    dif= sum((out-target).^2);
    %target=[y1 y2 y3 ...];
    %dif=sum((out-target).^2);
    % [kf error]=fminsearch(@(x) Mario_new(x),100000);
end
```

```
function Hardwork();
    firstvalue=1.0;
    [gradient_fame1 gradient_ro1]=MarioA(firsvalue);
    step rO;
    step FAME;
    secondvalue= is steppedvalue
    out2=MarioA(secondvalue);
    step FAME
end

function rateFAME=Mario_anything(rado)
    model=mphload('2dmodel2709.mph');
    model.param.set('rado',rado);
    model.study('std1').run;
    fin=1.926
    fame=mphglobal(model,'intop1(cfame)');
    t=mphglobal(model,'t');
    FAMEf=interp1(t,fame,fin)
    rateFAME=FAMEf*3.979E+05
end
```

To retrieve the values for y^p at the fitted rate constant

The function below needs to be run in MATLAB

```
function dif=Mario_forward2(x)

    model=mphload('irrev_matlab_11092018.mph');
    model.param.set('kf3',x);
    x
    model.study('std1').run;
    out=mphglobal(model,'comp1.re.c_fame');
    t=mphglobal(model,'t');
    %out=interp1(t,out,[t1 t2 t3 ...])
    dif=1;
    tdata=[14400 28800 43200 57600 72000 86400 100800 115200 129600];
    out=interp1(t,out,tdata) ;
    target=[70.68728257 93.49207576 100.6896019 112.281407 113.6451488
    114.0997294 113.4178585 114.4785466 113.1905682];
    plot(tdata,out,'o'); hold on; plot(tdata,target,'*'); hold off;
    drawnow;
    dif=out;
    %target=[y1 y2 y3 ...];
    %dif=sum((out-target).^2);
    %[kf error]=fminsearch(@(x) Mario_new(x),100000);
end
```

In the command window, the following function is typed so it returns the interpolated values at the new fitted parameter. It should return a value that looks like the one below.

A=Mario_forward2(2.67e-7)

x = 2.6700e-07

A = 68.7725 93.1002 103.9786 109.2880 111.9945 113.4086 114.1537 114.5490 114.7591